

## Final Report

# Performance Evaluation of Glass Fiber Reinforced Polymer (GFRP) Reinforcing Bars Embedded in Concrete Under Aggressive Environments

Contract Number BDV30 TWO 977-18

FSU Project ID: 038558

---

*Submitted to:*

**Florida Department of Transportation**  
Research Center  
605 Suwannee Street  
Tallahassee, Florida 32399-0450



**Chase C. Knight, Ph.D.**  
Project Manager  
FDOT State Materials Office



**FAMU-FSU**  
**Engineering**



---

*Prepared by:*

**Raphael Kampmann, Ph.D.**  
Principal Investigator  
**Francisco De Caso, PhD, LEED A.P.**  
Co-Principal Investigator  
**Michelle Roddenberry, Ph.D., P.E.**  
Co-Principal Investigator  
**Alvaro Ruiz Emparanza**  
Ph.D. Candidate and Research Assistant

FAMU-FSU College of Engineering  
Department of Civil and Environmental Engineering  
2525 Pottsdamer Street  
Tallahassee, FL 32310

University of Miami  
Department of Civil, Architectural & Environmental Engineering  
1251 Memorial Drive — McArthur Engineering Building 308  
Coral Gables, Florida 33146

# Table of Contents

- List of Figures . . . . . v
- List of Tables . . . . . x
  
- 1 Introduction . . . . . 1**
- 1.1 Background . . . . . 1
- 1.2 Problem Statement . . . . . 3
- 1.3 Research Objective . . . . . 4
- 1.4 Research Scope . . . . . 5
- 1.5 Report Overview . . . . . 6
  
- 2 Background . . . . . 9**
- 2.1 Resin . . . . . 10
  - 2.1.1 Epoxies . . . . . 11
  - 2.1.2 Polyester . . . . . 11
  - 2.1.3 Vinyl Ester . . . . . 11
- 2.2 Fiber Reinforcement . . . . . 12
  - 2.2.1 Glass Fibers . . . . . 12
- 2.3 GFRP Rebar Manufacturing . . . . . 15
  - 2.3.1 FRP Rebar Cross-Sectional Shapes . . . . . 16
  - 2.3.2 Surface Enhancement Features . . . . . 17
  - 2.3.3 Bending Process for FRP Stirrups . . . . . 19
  - 2.3.4 Bending FRP Bars On Site . . . . . 20
  - 2.3.5 Quality Control for GFRP Manufacturing . . . . . 21
- 2.4 Degradation of Bond Between FRP Bars and Concrete . . . . . 23
- 2.5 GFRP Rebar Applications Overview . . . . . 25

<b>3</b>	<b>GFRP Market and Rebar Manufacturers</b>	<b>29</b>
3.1	Worldwide FRP Rebar Manufacturing . . . . .	29
3.2	GFRP Products Database . . . . .	34
<b>4</b>	<b>Experimental Program</b>	<b>39</b>
4.1	Introduction . . . . .	39
4.2	Experimental Concept . . . . .	39
4.2.1	Virgin Material Properties . . . . .	41
4.2.2	Material Properties after Saltwater Exposure . . . . .	41
4.3	Materials: Glass FRP Rebars . . . . .	42
4.4	Equipment and Test Devices . . . . .	44
4.4.1	Cutting Saw . . . . .	45
4.4.2	Precision Saw . . . . .	46
4.4.3	Caliper . . . . .	47
4.4.4	Precision Balance . . . . .	48
4.4.5	Drying Oven . . . . .	48
4.4.6	Muffle Furnace . . . . .	49
4.4.7	Scanning Electron Microscope . . . . .	50
4.4.8	Sputter Coater . . . . .	52
4.4.9	Load Frame . . . . .	53
4.4.10	Test Fixture for Transverse Shear Tests . . . . .	56
4.4.11	Test Fixture for Horizontal Shear Tests . . . . .	59
4.4.12	Test Fixture for Tensile Tests . . . . .	61
4.5	Test Procedures . . . . .	64
4.5.1	Measurements of Cross-Sectional Area . . . . .	65
4.5.2	Measurements of Fiber Content . . . . .	68
4.5.3	Measurements of Moisture Absorption . . . . .	70
4.5.4	Measurements of Micro Defects (SEM) . . . . .	71
4.5.5	Measurements of Transverse Shear Strength . . . . .	72
4.5.6	Measurements of Apparent Horizontal Shear Strength . . . . .	74
4.5.7	Measurements of Tensile Properties . . . . .	76
4.5.8	Measurement of Bond-to-Concrete Strength . . . . .	82
4.5.9	Accelerated Conditioning Protocols — Specimen Aging . . . . .	84

<b>5</b>	<b>Experimental Results</b>	<b>87</b>
5.1	Introduction . . . . .	87
5.2	Test Results from Measurements of Physical Properties . . . . .	87
5.2.1	Cross-Sectional Dimensions Results . . . . .	87
5.2.2	Fiber Content Results . . . . .	88
5.2.3	Moisture Absorption Results . . . . .	90
5.2.4	Microstructure via SEM Imagery . . . . .	90
5.3	Test Results from Measurements of Strength Properties . . . . .	91
5.3.1	Transverse Shear Strength Results . . . . .	94
5.3.2	Horizontal Shear Strength Results . . . . .	95
5.3.3	Tensile Properties Results . . . . .	97
5.3.4	Bond-to-Concrete Strength Results . . . . .	103
5.4	Summary of Material Characterization Tests . . . . .	108
5.5	Test Results from Measurements of Durability Properties . . . . .	109
5.5.1	Durability of Microstructure via SEM Imagery . . . . .	110
5.5.2	Durability of Strength Properties . . . . .	117
<b>6</b>	<b>Durability Modeling</b>	<b>125</b>
6.1	Introduction . . . . .	125
6.2	Durability Model . . . . .	125
6.2.1	Degradation Laws . . . . .	128
6.2.2	Degradation Rate Alternative . . . . .	134
6.3	Summary and Conclusions . . . . .	138
<b>7</b>	<b>Discussion</b>	<b>144</b>
7.1	Research Significance . . . . .	144
7.2	Critical Analysis of Major Findings . . . . .	145
7.3	Supplementary Findings . . . . .	147
7.4	Limitations . . . . .	149
7.5	Future Directions and Follow-up Research . . . . .	150
<b>8</b>	<b>Conclusions</b>	<b>152</b>
8.1	Summary . . . . .	152
8.2	Conclusions . . . . .	153
8.3	Recommendations . . . . .	155

<b>Bibliography</b>	<b>159</b>
<b>Appendices</b>	<b>164</b>
<b>A Manufacturer Survey</b>	<b>165</b>
<b>B Visual Rebar Documentation</b>	<b>169</b>
B.1 Introduction . . . . .	169
B.2 GFRP straight bars . . . . .	170
B.3 GFRP bent bars . . . . .	190
B.4 Basalt FRP straight bars . . . . .	195
B.5 Basalt FRP bent bars . . . . .	199
<b>C Quality Control Plans</b>	<b>201</b>
<b>D Individual Experimental Results</b>	<b>204</b>
D.1 Density and Cross-Sectional Dimension Test . . . . .	204
D.2 Fiber Content Test . . . . .	206
D.3 Transverse Shear Test . . . . .	208
D.4 Horizontal Shear Test . . . . .	213
D.5 Tensile Test . . . . .	219
D.6 Bond-to-Concrete Test . . . . .	225

# List of Figures

1.1	Corrosion of reinforced concrete structure in marine environment . . . . .	1
2.1	Thermosetting polymeric resin used for GFRP rebars . . . . .	10
2.2	Tensile stress and strain of different types of fibers according to Busel (2012) . . . . .	12
2.3	Glass fibers . . . . .	13
2.4	Pultrusion process for the manufacture of GFRP rebars . . . . .	16
2.5	GFRP bars with different cross-sectional shapes . . . . .	17
2.6	Parallelism defects in bent sections of FRP bars . . . . .	19
2.7	Bare fibers of bent section after removing the resin . . . . .	20
2.8	Stresses at the bend zone of stirrups according to Ahmed et al. (2010) . . . . .	21
2.9	Typical failure of FRP stirrups Ahmed et al. (2010) . . . . .	22
3.1	Distribution of GFRP rebar manufacturers . . . . .	30
3.2	Production rate for different GFRP Manufacturers . . . . .	34
3.3	Production planning for different GFRP Manufacturers . . . . .	35
4.1	Experimental concept . . . . .	40
4.2	Cross-sectional features of tested GFRP rebar products . . . . .	43
4.3	Miter saw used to cut raw materials to specimen length . . . . .	45
4.4	Saw blade . . . . .	46
4.5	Precision saw . . . . .	47
4.6	Electronic caliper . . . . .	48
4.7	Precision scale, used to meet ASTM D792–13 requirements . . . . .	49
4.8	Drying oven VWR Scientific Products Oven Model 1690 . . . . .	50
4.9	Conditioning container for small-size specimens . . . . .	50
4.10	Muffled furnace used for high temperature experiments (fiber content) . . . . .	51
4.11	Scanning Electron Microscope — JEOL JSM-7401F . . . . .	52

4.12	Scanning Electron Microscope — Work station . . . . .	53
4.13	Sputter coater SC7640 . . . . .	53
4.14	Load frame and laboratory setup for rebar strength tests . . . . .	54
4.15	MTS load frame control panel . . . . .	55
4.16	MTS test works interface — Used to control all strength test experiments . . . . .	55
4.17	MTS extensometer for tensile tests . . . . .	56
4.18	Transverse shear test concept . . . . .	57
4.19	Transverse shear test fixture — Individual components . . . . .	58
4.20	Transverse shear test fixture — T-plate support . . . . .	59
4.21	Transverse shear test fixture — Final test setup . . . . .	60
4.22	Horizontal shear test — Test methodology . . . . .	60
4.23	Horizontal shear test — Internal forces . . . . .	61
4.24	Horizontal shear test fixture — Components . . . . .	62
4.25	Horizontal shear test fixture — Mounted in load frame . . . . .	63
4.26	Schematic drawing of tensile test anchor according to ASTM D 7205–06 . . . . .	63
4.27	Support frame for anchor installation of tensile test specimens . . . . .	64
4.28	Tensile test fixture — Schematic drawing . . . . .	65
4.29	Tensile test fixture — Details . . . . .	66
4.30	Test setup for measurement of cross-sectional properties . . . . .	67
4.31	Specimens for fiber content test . . . . .	69
4.32	Moisture absorption specimens . . . . .	70
4.33	Specimens for transverse shear testing . . . . .	72
4.34	Specimen after completion of transverse shear test . . . . .	74
4.35	Specimens for apparent horizontal shear test . . . . .	75
4.36	Expansive grout . . . . .	77
4.37	Fitting of plastic bumper . . . . .	78
4.38	Potting of the anchors for tensile test specimens . . . . .	79
4.39	Test Setup . . . . .	81
4.40	Bond-to-concrete strength experiment test setup . . . . .	83
4.41	Specimen conditioning according to accelerated conditioning protocol . . . . .	86
5.1	Fiber content results — relative material proportions . . . . .	89
5.2	Moisture absorption results — relative weight gain (average values for all rebar types and sizes)	90
5.3	SEM pictures of virgin rebar materials — Rebar-surface enhancement interface . . . . .	91

5.4	SEM pictures of virgin rebar materials — Cross section . . . . .	92
5.5	SEM pictures of virgin rebar materials — Surface enhancement . . . . .	93
5.6	Transverse shear behavior of virgin material . . . . .	94
5.7	Transverse shear test — failure mode of all tested rebar sizes . . . . .	95
5.8	Transverse shear test — failure mode in detail . . . . .	96
5.9	Horizontal shear behavior of virgin material . . . . .	97
5.10	Horizontal shear test — failure mode . . . . .	98
5.11	Horizontal shear test — failure mode in detail . . . . .	99
5.12	Tensile behavior of virgin material . . . . .	100
5.13	Stress-strain behavior of virgin material (elastic modulus) . . . . .	101
5.14	Tensile failure of tensile tested rebars — Type-A . . . . .	102
5.15	Tensile failure of tensile tested rebars — Type-B . . . . .	103
5.16	Tensile failure of tensile tested rebars — Type-C . . . . .	104
5.17	Bond-to-concrete behavior of virgin material . . . . .	105
5.18	Bond failure at rebar interface of all rebar types in virgin state . . . . .	106
5.19	Bond failure at rebar interface of all rebar types after 365 day of exposure to 60 °C saltwater . . . . .	106
5.20	Bond failure at concrete interface of all rebar types in virgin state . . . . .	107
5.21	Bond failure at concrete interface of all rebar types after 365 day of exposure to 60 °C saltwater . . . . .	107
5.22	Individual SEM pictures for Type-A rebars after saltwater exposure . . . . .	113
5.23	Individual SEM pictures for Type-B rebars after saltwater exposure . . . . .	114
5.24	Individual SEM pictures for Type-C rebars after saltwater exposure . . . . .	115
5.25	Combined SEM pictures for Type-A rebars after saltwater exposure . . . . .	116
5.26	Combined SEM pictures for Type-B rebars after saltwater exposure . . . . .	117
5.27	Combined SEM pictures for Type-C rebars after saltwater exposure . . . . .	118
5.28	Retention of transverse shear strength . . . . .	119
5.29	Retention of horizontal shear strength . . . . .	120
5.30	Retention of tensile strength . . . . .	120
5.31	Retention of elastic modulus . . . . .	121
5.32	Retention of bond-to-concrete strength . . . . .	122
5.33	Bond strength slippage . . . . .	123
5.34	Summary of strength retention of GFRP rebars throughout exposure to accelerated conditioning . . . . .	124
6.1	Bond retention over time in a double logarithmic scale according to (Yan and Lin, 2017) . . . . .	129
6.2	Transverse shear strength retention over time in a double logarithmic scale . . . . .	131



6.3	Horizontal shear strength retention over time in a double logarithmic scale . . . . .	132
6.4	Tensile strength retention over time in a double logarithmic scale . . . . .	133
6.5	Elastic modulus retention over time in a double logarithmic scale . . . . .	134
6.6	Bond-to-Concrete strength retention over time in a double logarithmic scale . . . . .	134
6.7	Graphical representation of the degradation rate, ‘k’ . . . . .	137
6.8	Arrhenius plots for different reaction orders . . . . .	139
6.9	Service life prediction for different temperatures . . . . .	140
6.10	Long-term prediction based on Arrhenius relationship — Summary . . . . .	143
B.1	AFR # 4 Bar . . . . .	171
B.2	AFR # 6 Bar . . . . .	172
B.3	ASL # 3 Bar . . . . .	173
B.4	ASL # 4 Bar . . . . .	174
B.5	ASL # 5 Bar . . . . .	175
B.6	ASL # 6 Bar . . . . .	176
B.7	ASL # 8 Bar . . . . .	177
B.8	ATP # 3 Bar . . . . .	178
B.9	ATP # 5 Bar . . . . .	179
B.10	MAR # 4 Bar . . . . .	180
B.11	CRT # 6 Bar . . . . .	181
B.12	CRT # 7 Bar . . . . .	182
B.13	RAW # 4 Bar . . . . .	183
B.14	RAW # 6 Bar . . . . .	184
B.15	PAL # 5 Bar . . . . .	185
B.16	PAL # 6 Bar . . . . .	186
B.17	PAL # 8 Bar . . . . .	187
B.18	SIR # 8 Bar . . . . .	188
B.19	SIR # 10 Bar . . . . .	189
B.20	MAR # 3 Bar . . . . .	191
B.21	ATP # 5 Bar . . . . .	192
B.22	ASL # 5 Bar . . . . .	193
B.23	PAL # 5 Bar . . . . .	194
B.24	RAWBas # 3 Bar . . . . .	196
B.25	RAWBas # 4 Bar . . . . .	197

B.26 RAWBas # 6 Bar . . . . .	198
B.27 RAWBas # 4 Bar . . . . .	200

# List of Tables

2.1	Chemical compositions of different glass fiber types in % . . . . .	14
2.2	Mechanical properties of different types of glass fibers . . . . .	15
2.3	Coefficient of thermal expansion (CTE) of different materials (Balázs and Borosnyói, 2001) . . . . .	23
2.4	Design guidelines for GFRP reinforcement bars . . . . .	27
3.1	Location of GFRP manufacturers . . . . .	31
3.2	GFRP bars produced by different manufacturers . . . . .	32
3.3	Manufacturer production . . . . .	33
3.4	Manufacturer specifications of GFRP rebar #3 . . . . .	36
3.5	Manufacturer specifications of GFRP rebar #5 . . . . .	37
3.6	Manufacturer specifications of GFRP rebar #8 . . . . .	38
4.1	Conducted test methods to evaluate virgin material properties of GFRP rebars . . . . .	41
4.2	Conducted test methods to evaluate material properties of GFRP rebars after saltwater exposure . . . . .	42
4.3	GFRP rebar materials — Physical features . . . . .	43
4.4	GFRP rebar materials — Mechanical Properties (reported by the manufacturers) . . . . .	44
5.1	Average cross-sectional properties results for all rebars . . . . .	88
5.2	Acceptance criteria evaluation for Type-A #3 rebars . . . . .	108
5.3	Acceptance criteria evaluation for Type-A #5 rebars . . . . .	109
5.4	Acceptance criteria evaluation for Type-A #8 rebars . . . . .	109
5.5	Acceptance criteria evaluation for Type-B #3 rebars . . . . .	110
5.6	Acceptance criteria evaluation for Type-B #5 rebars . . . . .	110
5.7	Acceptance criteria evaluation for Type-B #8 rebars . . . . .	111
5.8	Acceptance criteria evaluation for Type-C #3 rebars . . . . .	111
5.9	Acceptance criteria evaluation for Type-C #5 rebars . . . . .	112
5.10	Acceptance criteria evaluation for Type-C #6 rebars . . . . .	112

6.1	Existing durability modeling research projects . . . . .	130
6.2	Integrated Rate Equations . . . . .	135
6.3	Calculation of degradation rate, $k$ . . . . .	138
6.4	Calculation of the activation energy . . . . .	139
6.5	Sum of Squares of Errors (SSE) for all the reaction orders and rebar types . . . . .	141
6.6	Coefficients of determination ‘ $R^2$ ’ and slopes of trend lines for all rebar types, temperatures, and mechanical properties . . . . .	141
D.1	Density and cross-sectional property test results for each individual specimen . . . . .	205
D.1	Density and cross-sectional property test results for each individual specimen . . . . .	206
D.2	Fiber content test results for each individual specimen . . . . .	207
D.2	Fiber content test results for each individual specimen . . . . .	208
D.3	Transverse shear test results (ultimate values) for each individual specimen . . . . .	209
D.3	Transverse shear test results (ultimate values) for each individual specimen . . . . .	210
D.3	Transverse shear test results (ultimate values) for each individual specimen . . . . .	211
D.3	Transverse shear test results (ultimate values) for each individual specimen . . . . .	212
D.4	Transverse shear test statistical values for each sample group . . . . .	212
D.4	Transverse shear test statistical values for each sample group . . . . .	213
D.5	Horizontal shear test results (ultimate values) for each individual specimen . . . . .	214
D.5	Horizontal shear test results (ultimate values) for each individual specimen . . . . .	215
D.5	Horizontal shear test results (ultimate values) for each individual specimen . . . . .	216
D.5	Horizontal shear test results (ultimate values) for each individual specimen . . . . .	217
D.6	Horizontal shear test statistical values for each sample group . . . . .	218
D.6	Horizontal shear test statistical values for each sample group . . . . .	219
D.7	Tensile strength test results (ultimate values) for each individual specimen . . . . .	219
D.7	Tensile strength test results (ultimate values) for each individual specimen . . . . .	220
D.7	Tensile strength test results (ultimate values) for each individual specimen . . . . .	221
D.7	Tensile strength test results (ultimate values) for each individual specimen . . . . .	222
D.8	Tensile strength test statistical values for each sample group (Imperial Units) . . . . .	222
D.8	Tensile strength test statistical values for each sample group (Imperial Units) . . . . .	223
D.9	Tensile strength test statistical values for each sample group (Metric Units) . . . . .	224
D.10	Bond-to-Concrete strength test results for each individual specimen (Imperial Units) . . . . .	225
D.10	Bond-to-Concrete strength test results for each individual specimen (Imperial Units) . . . . .	226
D.10	Bond-to-Concrete strength test results for each individual specimen (Imperial Units) . . . . .	227

D.11 Bond-to-Concrete strength test results for each individual specimen (Metric Units) . . . . .	227
D.11 Bond-to-Concrete strength test results for each individual specimen (Metric Units) . . . . .	228
D.11 Bond-to-Concrete strength test results for each individual specimen (Metric Units) . . . . .	229
D.11 Bond-to-Concrete strength test results for each individual specimen (Metric Units) . . . . .	230
D.12 Bond-to-Concrete strength test statistical values for each sample group . . . . .	230
D.12 Bond-to-Concrete strength test statistical values for each sample group . . . . .	231

# Chapter 1

## Introduction

### 1.1 Background

Our infrastructure continues to deteriorate due to growing traffic and rising environmental impacts. Corrosion of steel is one of the main deteriorating mechanisms that significantly degrades traditionally reinforced concrete elements (Portland Cement Association, 2002), leading to a reduced service-life of infrastructure components. Specifically, pitting corrosion caused by saltwater chlorides is a major problem, as these concentrated attacks are difficult to detect but lead to a structural failure without previous warning, possibly causing human disaster (Lowe’s Motor Speedway Bridge Collapse). In general, chloride rich environments lead to accelerated degradation of reinforcing steel and significant structural damage as shown in Figure 1.1. Because this is a particular problem for coastal states in which many structures are exposed to saltwater and



(a) Destruction of longitudinal reinforcement



(b) Destruction of transverse reinforcement

Figure 1.1: Corrosion of reinforced concrete structure in marine environment

123.3 million people, or 39% of the U.S. population, live in counties directly on shorelines, it is an urgent national interest to develop resilient materials for structural applications that better withstand the demands

of harsh environments. In the United States, 54,007 bridges (9.1% of the nation's bridges) were considered structurally deficient in 2016, which is estimated to cost \$128 billion for repair and reconstruction efforts (American Society of Civil Engineers, 2016). To reduce these costs for the infrastructure of tomorrow and because improved durability of concrete structures is becoming more important for many civil applications, non-corrosive materials such as fiber reinforced polymer (FRP) reinforcing bars (rebars) — in substitution of steel — are a viable option (Inmana et al., 2017). Because Florida is a coastal state that is currently home to 12 358 bridges (Florida Department of Transportation Forecasting and Trends Office, 2018) — 6929 bridges are maintained by the Florida Department of Transportation (FDOT) — and a significant number of those bridges are exposed to various aggressive environments<sup>1</sup>, the FDOT owns numerous structures and concrete elements exposed to aggressive conditions (e.g. the splash zone for bridge piers). Accordingly, the FDOT is currently working toward an implementation of FRP rebars to officially allow alternative reinforcing materials for future publicly funded construction projects and to promote more resilient structures, specifically in harsh environments.

The considerably new FRP rebar technology is based on pultruded composite products, which are made from longitudinally bundled fibers — along the bar axis — embedded in a resin matrix. The fibers are the main load carrying component and the resin binds the fibers together, and therefore, transfers the load between individual fibers while protecting them from chemical and physical attacks. Currently, the most widely used fiber type for FRP rods in the United States is glass based for the production of Glass Fiber Reinforced Polymer (GFRP) rebars. E- and E-CR (Electrical/Chemical Resistant) glass fibers are the most commonly used ones because they possess high tensile strength, offer high chemical resistance, and feature low production cost. Drawbacks include low elastic modulus, sensitivity to abrasion, and low fatigue strength. Thermosetting resins typically form the protective matrix, and vinyl ester based resins are most dominant due to its high mechanical toughness and excellent corrosion resistance.

Rooted in the nature of the fibers, the tensile behavior of GFRP rebars is characterized by a linear elastic stress-strain relationship up to failure. Compared to steel rebars, GFRP rebars offer a higher tensile strength but a lower ultimate tensile strain and a lower elastic modulus in tension. The main factors affecting the characteristics of a GFRP rebar include fiber volume, dimensional effects, rate of curing, manufacturing process, and quality control measures during manufacturing. The unit weight of GFRP rebars varies from about one-sixth to one-fourth of that of steel, which reduces transportation costs and makes the rebars easy to handle at the job site, yielding additional benefits to its implementation. However, the main advantage of GFRP rebars for construction projects is a presumably high corrosion resistance when exposed to harsh environments like seawater. Nevertheless, the mechanical properties of a GFRP rebar are affected by the en-

---

<sup>1</sup>According to email correspondence with the State Material Research Specialist, 2429 FDOT maintained concrete structures are situated in water or in soil, and the provided FDOT Bridge Environmental Data revealed that 1643 *bridges* are exposed to moderately aggressive chloride concentrations above 500 ppm.

vironment, where the presence of water, saline solution, alkaline (e.g. concrete) or acidic solutions, ultraviolet exposure, and high temperature may affect the mechanical and bond properties of GFRP rebars.

Due to the inherent material properties and the predominant benefits, the number of reinforced concrete (RC) structures specifying GFRP rebars for improved durability has increased significantly throughout recent years. Accordingly, the market demand for GFRP rebars around the world continues to grow. In response, numerous GFRP rebar manufacturers have emerged in various countries, mainly within the past decade, and based on the growing market demand, it is assumed that new manufacturers will emerge quickly. While the demand for these products has been recognized by the industry, the production of GFRP rebars is not yet standardized — in contrast to traditional steel rebars — and guidelines that define the mechanical characteristics of the final products are just now emerging. Accordingly, products may differ significantly from one another because each rebar manufacturer produces proprietary rebars from different raw materials, with various material proportions, via dissimilar pultrusion processes, and in consequence, with numerous geometric features and physio-mechanical properties. In addition, manufacturers have developed different surface enhancement methods to create and improve the bond with concrete, which is one of the most important aspects if these rods are used as rebar. Because standardization efforts for civil engineering applications are lagging behind industry implementations and because various products with dissimilar properties already exist and are in use for structures that do not require uniform material approval, it is difficult to comprehensively implement this new technology.

## 1.2 Problem Statement

Before a new technology can be used in tax payer funded infrastructure projects, it is indispensable to evaluate the performance characteristics of GFRP rebar that are representative of the currently available products. Individual material characteristics such as physical, mechanical, and bond-to-concrete properties must be clearly identified and evaluated against the current state-of-the-art and (if available) applicable acceptance criteria. Because GFRP technology is generally thought of as an alternative solution for reinforcement of concrete elements in aggressive environments and local environmental challenges are unique due to the exceptional climate conditions in Florida, durability aspects must be carefully analyzed. The compatibility of GFRP rebars with the aggressive environments generally found in Florida has not been fully evaluated yet, and research is needed to address the accelerated degradation of infrastructure elements and structures in Florida. Dangerous consequences may be suffered if the time dependent degradation of the mechanical properties and the interface between the GFRP rebar and concrete in aggressive environments (saltwater) is not fully understood. To make progress toward safe and long-term infrastructure solutions via GFRP rebars, the material performance must be experimentally evaluated for various conditions and the resulting data used



to develop durability prediction models. For GFRP reinforcement, different studies have separately verified the durability of individual GFRP reinforcement characteristics (Robert and Benmokrane, 2013; Micelli and Nanni, 2004; Dong et al., 2016). However, studies that target a wide array of material properties and the bond behavior simultaneously are rare. A multi-parametric approach is needed to identify the sensitivity of all relevant engineering properties and to compare the individual property retention characteristic. Based on such experimentally derived information, data-driven prediction models can be evaluated for a more robust implementation of GFRP rebars.

### 1.3 Research Objective

The first project objective was an extensive literature review to target the current state-of-the-art for GFRP rebar production and to establish a worldwide industry profile based on the major manufacturers that currently produce relevant composite rebars. Based on the review and a market analysis, it was the goal to identify non-corrosive GFRP rebar technologies for concrete reinforcement with suitable surface enhancements for the construction of durable and sustainable infrastructure in aggressive environments. To fully embrace and implement the composite rebar technology by the FDOT, it was the aim to select representative GFRP rebars with various differentiating features (cross-sectional shape, constituent materials, surface enhancement, etc.) for full characterization of these products to evaluate if pre-approval requirements for GFRP rebar can be avoided or minimized in the future. Accordingly, it was the goal to test a variety of GFRP rebar products and measure the most common physical and strength properties to compare the material performance to the prevailing acceptance criteria for GFRP rebars. In addition to the virgin material performance, the characterization of the long-term behavior of the chosen glass composite rebars was of interest for this project, specifically from a durability and sustainability standpoint. The intent was to mimic conditions comparable to the environment and climate generally found in Florida and to provide a systematic experimental approach through various accelerated aging temperatures and periods (based on commonly accepted accelerated aging protocols for FRPs). Therefore, the purpose of the experimental phase was also to test and evaluate the material performance of GFRP rebars after exposure to severe environments to collect additional test data and to quantify durability and property retention of the selected/tested rebar types. Based on the full characterization of virgin and aged properties and with a data-driven understanding of property retention after exposure, a major aim of this project was to mathematically model the durability behavior of the selected GFRP rebar technology for a better prediction of the long-term performance in concrete members or real-world construction projects. The experimental data and the mathematical modeling efforts ultimately targeted recommendations and relevant updates for existing FDOT guidelines and specifications to improve and simplify the adoption or implementation of GFRP rebar in concrete.

In short, the main objectives of this research work were to provide a general overview of the GFRP rebar technology and market, to provide data and suggestions for material specifications, to experimentally address durability concerns, to offer additional quality control/assurance measures, and to ultimately provide recommendations for the integration of GFRP technology in existing guidelines, specifications, and design. This project aims to directly benefit the State by providing missing data and knowledge for the reliable use of GFRP rebar technologies for concrete reinforcement as a resilient solution for infrastructure projects. This study intends to provide additional data and information for a more efficient design of reinforced concrete structures with non-corrosive reinforcement.

## 1.4 Research Scope

In this research project, GFRP rebar products from three major composite rebar producers were extensively and comprehensively tested to characterize these materials and to evaluate the usability of these products under current FDOT guideline constraints. Three manufacturers were chosen to capture a variety of different physical rebar features (various fiber types, different resins, dissimilar surface enhancements and forms, etc.) and to test commonly available products, which are produced in various locations via individual and proprietary methods. For each product type, three rebar sizes were selected to evaluate the current, most typical GFRP rebar diameters and a suitable size range for FDOT construction projects. Specifically, rebar sizes #3, #5, and #6 or #8 (diameters 10 mm, 15 mm, and 19 mm or 25 mm) were tested in pristine condition (as received from the manufacturer) and after exposure to saltwater. First, each rebar type and size was characterized in its virgin state to define reference values for four physical properties and four strength characteristics. Physical rebar analyses included density measurements or measurement of cross-sectional dimensions, fiber content, moisture absorption, and scanning electron microscopy imaging, while strength measurements were conducted to determine the transverse shear strength, horizontal shear strength, tensile strength including elastic modulus properties, as well as the bond-to-concrete characteristics. As these virgin properties were determined, companion specimens were exposed to saltwater (representative of conditions generally expected in Florida seawater) at three different elevated temperatures for accelerated aging. Only #3 (10 mm) were conditioned because aggressive environments were expected to impact small-size rebars more severely as the percentage of degradation effects is intensified for smaller cross sections. Aging temperatures ranged from 73 °F (23 °C), through 105 °F (40 °C), to 140 °F (60 °C) and the specimens were conditioned inside the storage solutions for 60 days, 120 days, 240 days, and 365 days. At the end of each aging period, the needed material was removed from the conditioning solutions, dried, and tested. Except for cross-section and fiber content measurements, the same experiments that were conducted for the virgin materials were conducted for the aged specimens. Based on the experimental measurements and an in-depth comparison

between the virgin and the aged material properties, the retention of each tested property was determined throughout the four aging periods. All test data were statistically reduced and compared to the prevailing material specifications or acceptance criteria for FRP rebars (AC454, ASTM D 7957, etc.) with a special focus on FDOT Developmental Specification Section 932 (Florida Department of Transportation, 2017). The analyzed and statistically evaluated test data were used to predict the durability behavior of GFRP rebars in saltwater based on a multi-parameter Arrhenius approach. Finally, the findings made throughout the experimental phase and the theoretical analyses provided a foundation for recommendations toward future implementation of GFRP rebars in FDOT construction projects and adjustments or refinements for FDOT Developmental Specification Section 932 (Florida Department of Transportation, 2017) were proposed.

## 1.5 Report Overview

This report presents the completed research in eight chapters. While the general introduction and an overview of the project is presented in this Chapter, the following Chapter 2 provides important background information about the GFRP rebar technology, describing raw materials, production processes, and various properties of composite material. Furthermore, relevant studies that evaluated the strength and durability behavior of GFRP rebars are reviewed. A market analysis that targeted the worldwide production of GFRP rebars was conducted and the findings are presented in Chapter 3. For a detail description of the experimental concepts and the general approach to the laboratory work, the experimental program is presented in Chapter 4. This chapter details the material characteristics and the mechanical properties — according to the manufacturer — of the evaluated GFRP rebar products, and also lists all additional materials that were needed to prepare the specimens for testing. Moreover, the equipment and test devices, which were used to conduct the tests, are listed and described in detail. To ensure repeatability for future research projects, the relevant test protocols (ASTM, ACI, etc.) as they were interpreted for the purpose of this project are described. Accordingly, all required procedural steps and test sequences are explained in detail. The gathered test data from all experiments are concisely represented via graphs and tables in Chapter 5 to provide an overview and explanation for the empirical findings. Failure patterns and material characteristics for the virgin and aged materials (accelerated conditioning) are pictured and described. The empirical data presented in Chapter 5 were used to model the long-term behavior of GFRP rebars in aggressive environments, and the approach to the model and the applicability of the data and model are discussed in Chapter 6 to offer additional insight for durability modeling of GFRP rebars. A detailed discussion follows in Chapter 7 for a critical analysis of the experimental results, durability modeling, and all related research findings. The importance of the research findings — in the context of the available literature — with a focus on GFRP rebars applications in FDOT construction projects is contemplated, but not without considering the limitations or applicability

of this study. Finally, in Chapter 8, the project is summarized and all conclusions for this study are listed, before final recommendations for the implementation of GFRP rebars in FDOT construction projects are presented.

In addition to the main text, this report offers four appendices to substantiate the claims made throughout this report. Appendix A presents a model survey that was used to gather most of the data presented in Chapter 3. A visual database containing numerous GFRP rebars with various shapes, forms, and sizes from different manufacturers from around the globe is illustrated throughout Appendix B. A GFRP rebar production quality control plan is listed in Appendix C to supplement the discussion laid out in Chapter 3. Finally, Appendix D lists the most relevant test data for every single specimen that was tested for the purpose of this project. In addition to the individual specimen results, Appendix D also lists statistical results for relevant data sets (specimen groups) to provide a detailed but concise interpretation of the data shown and used in Chapters 5 and 6, respectively.

# Contents

## Chapter 2

# Background

The number of reinforced concrete (RC) structures in recent years specifying GFRP rebars has increased exponentially, and so has the number of GFRP rebar manufacturers. Additionally, manufacturers have developed different GFRP rebar types, where the surface enhancement to create the bond with concrete varies. Furthermore, the nature of the GFRP manufacturing pultrusion process (Nanni et al., 2014) requires a marginal investment to set up (compared to traditional steel mills), while strict control measures, which are necessary to assure quality and consistency of the produced GFRP rebar, may not always be fully implemented.

The main factors affecting the characteristics of a GFRP rebar include fiber volume, dimensional effects, rate of curing, manufacturing process, and quality control measures during manufacturing. The unit weight of GFRP rebar varies from about one-sixth to one-fourth that of steel, which reduces transportation costs and makes the rebars easier to handle at the job site, yielding additional benefits. The tensile behavior of GFRP rebars is characterized by a linear elastic stress-strain relationship up to failure. Compared to steel rebars, GFRP rebars offer higher tensile strength but lower ultimate tensile strain and lower tensile modulus of elasticity. Unlike steel, the tensile strength of a GFRP rebar varies with its diameter, while the longitudinal modulus does not change appreciably. This phenomenon is primarily due to the effects of shear lag. The mechanical properties of a GFRP rebar are influenced by the environment, where the presence of water, saline solution, alkaline (e.g. concrete) or acidic solutions, ultraviolet exposure, and high temperature may affect the mechanical and bond properties of GFRP rebars.

GFRP rebars are made of continuous glass fibers embedded in a polymeric resin matrix. The fibers have the function of carrying the load; the resin binds and transfers the load to the fibers while protecting the fibers. A surface treatment ensures bond between the GFRP rebar and the concrete. The combination of the constituents leads to a composite technology with superior properties. The constituents of the GFRP

rebars are discussed briefly in the following sections.

## 2.1 Resin

The three primary functions of the resin matrix include, i) to protect the fibers from mechanical and environmental attacks; ii) to maintain the alignment of fibers; and iii) to guarantee load transfer between individual fibers. The chemical stability, diffusivity, and toughness determine the suitability of resins for use in fiber reinforced polymer (FRP) reinforcing bars (Benmokrane et al., 2002).

Resins can be classified into two main categories: thermosetting and thermoplastic. Thermoplastic resins can change reversibly from solid to liquid state through variations in temperature. Hence, thermoplastics are not desirable for FRP rebar and structural applications.

Thermosetting polymeric resins are most commonly used to manufacture FRP bars (Nanni et al., 2014). Initially, in an unreacted state, thermosetting resins are liquid (as shown in Figure 2.1). To saturate the



Figure 2.1: Thermosetting polymeric resin used for GFRP rebars

fibers, resins are heated to temperatures of approximately  $177^{\circ}\text{C}$  (Joshi et al., 2003). Heat treatment and catalysts are used to cure the resin. After curing, the material is permanently solidified. The main type of thermosetting resins are polyesters, vinyl esters, and epoxies (Nanni et al., 2014). Each type of thermosetting resin is discussed briefly below.

### **2.1.1 Epoxies**

The main epoxies used in composites are phenolic glycidyl ethers, aromatic glycidyl amines, and cycloaliphatics. Epoxies have a high chemical resistance, low diffusivity, good adhesion to many fiber types, and low shrinkage during curing; they are compatible with glass, carbon, aramid, basalt fibers, etc. These resins also have high corrosion resistance and good resistivity to moisture. Their main disadvantage is high viscosity, which limits their use in some processes such as pultrusion. Moreover, these resins are relatively more expensive and require a relatively longer curing process, generally including a post-curing phase. Because of this, epoxies are usually found in automotive, marine, electrical, building and appliance applications (Nanni et al., 2014; Bagherpour, 2012).

### **2.1.2 Polyester**

Polyester resins are usually made of a dihydric alcohol and a dibasic organic acid. They are classified as saturated or unsaturated polyesters, depending on the amount of acid and alcohol used. Worldwide, 75 % of the polyester used is unsaturated (Bagherpour, 2012). The usage of polyesters for FRP rebars usually requires a curing and a post-curing process. Curing is done at high temperatures with the use of catalysts. After the polyester resin has turned from a liquid state to a brittle solid, it is usually post-cured at higher temperatures to achieve the final properties (Bagherpour, 2012). Polyesters mainly benefit from balanced properties: good mechanical, chemical, and electrical performance, at competitive costs and ease of production. However, for the manufacturing of FRP bars, its use is discouraged because they are not as chemically resistant as vinyl ester resins (Nanni et al., 2014).

### **2.1.3 Vinyl Ester**

Vinyl ester resins are created through the reaction of epoxies with methacrylic acid, called esterification. This type of resin takes advantage of the beneficial properties of polyester resins, such as fast curing and viscosity, but also of the superior characteristics of epoxy; high strength and high chemical resistance. Because the product is a combination of the two previously mentioned resins, the material and production costs of vinyl ester are between those of epoxy and polyester resins. Vinyl ester resins are preferred for GFRP composites because of their good alkali resistance and strong adhesion to glass fibers (Nanni et al., 2014; Benmokrane et al., 2002). Moreover, vinyl ester offers strong resistance to microcrack development (Benmokrane et al., 2002).



## 2.2 Fiber Reinforcement

Fibers are the structural load-carrying component in FRP rebars, where the fiber volume in FRP rebars is typically above 70% by weight. Different types of fibers are currently used for FRP rebar manufacturing. The most commonly used fiber types for FRP rebar is fiberglass, followed by basalt and some aramid. Carbon is also used, but typically for pre-stressed applications. As shown in Figure 2.2, the engineering properties of FRP rebars highly depend on the utilized fiber type. According to Busel (2012), the tensile strain capacity

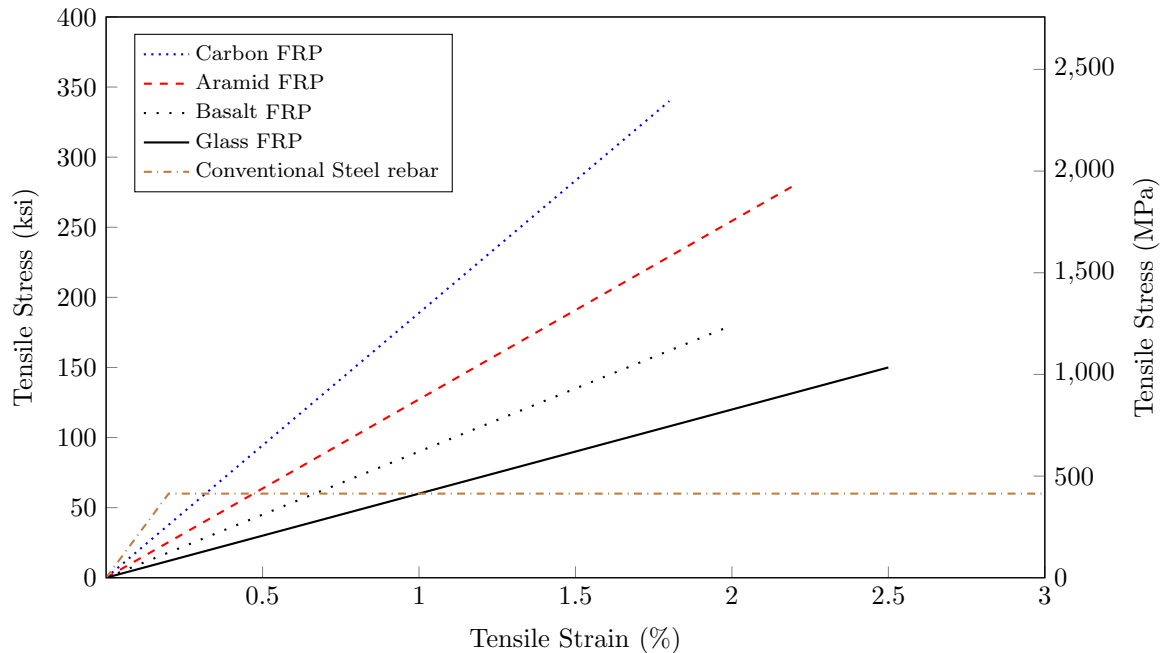


Figure 2.2: Tensile stress and strain of different types of fibers according to Busel (2012)

of glass FRP rebars is higher than the tensile strain capacity of carbon or aramid FRP rebars, while the reverse is true for the tensile strength. In addition, glass fibers are among the most economic along with basalt, while carbon fibers are the most expensive. The cost of aramid fibers are comparable to the price of low grade carbon fibers (Bagherpour, 2012).

There are other types such as boron, but currently, they are not economically competitive compared to the other three major types (Bagherpour, 2012).

### 2.2.1 Glass Fibers

Glass fibers are white as shown in Figure 2.3, with filament diameters ranging from  $2\ \mu\text{m}$  to  $13\ \mu\text{m}$  (Bagherpour, 2012). The three main classes of glass fiber used for GFRP reinforcement are E-glass, C-glass, and S-glass. E-glass (“E” for its initial electrical application) is the first glass type used to produce continuous filaments and was first used in electrical applications due to its low conductivity and its permeability to

magnetic fields. C-glass (“C” for its chemical resistance) is mainly used in aggressive environments, and S-glass (“S” for stiff) is used in applications where high-strength (and modulus) is necessary, such as aircraft manufacturing <sup>1</sup>. Glass fibers contain silicate or silica and varying amounts of calcium oxide, magnesium, and sometimes boron. Glass fiber filaments have to be almost entirely free of defects to be used in FRP composites, to ensure high quality product and avoid a premature deterioration of the rebar (Bagherpour, 2012).

High corrosion resistance is the main characteristic of C-glass, S-glass typically has the highest strength properties, and E-glass is generally designated for electrical applications. E-glass is generally the most used type of glass fiber for civil engineering and industrial applications due to the ease of its production (Bagherpour, 2012). E-glass can be produced from calcium-alumina-borosilicate that is abundantly available in raw materials like sand. Furthermore, there is an extensive variety of glass fibers that are used for the production



Figure 2.3: Glass fibers

of GFRP rebars (Bagherpour, 2012) including:

- ECR-glass: has a high electrical and chemical resistance and it is composed of calcium alumino-lime silicate with a maximum alkali content of 2% of the total mass. This class of fiber is normally used when high strength, electrical resistivity, and acid corrosion resistance are needed.

<sup>1</sup> Information retrieved on October 13, 2016  
from: <http://www.redorbit.com/reference/fiberglass/>

- A-glass: Alkali soda lime silicate glass with little or no boron oxide. The use of these fibers is restricted to cases where the durability, strength, and good electrical resistivity of E-glass are not necessary.
- AR-glass: These alkali-resistant fibers are principally used in cement substrates and fiber-reinforced concrete and are composed of alkali zirconium silicates. They are more resistant to alkaline environments than normal E-glass fibers (Benmokrane et al., 2002).
- D-glass: Borosilicate glass used for electrical applications due to its low dielectric constant.
- R-glass: Used for applications in which high strength and corrosion resistance are desired. It is made of calcium alumino silicate.
- S-2-glass: Magnesium alumino silicate glasses used in structural applications that require high resistance to corrosion and high temperatures.

Table 2.1 presents the chemical composition for the different type of glass fibers. The main component

Table 2.1: Chemical compositions of different glass fiber types in %

	SiO <sub>2</sub>	Al <sub>2</sub> O <sub>3</sub>	B <sub>2</sub> O <sub>3</sub>	CaO	Na <sub>2</sub> O + K <sub>2</sub> O	MgO	ZrO <sub>2</sub>	TiO <sub>2</sub>	Others*
A-glass	63–72	0–6	0–6	6–10	14–16	0–4	-	0–0.6	0–0.9
C-glass	64–68	3–5	4–6	11–15	7–10	2–4	-	-	0–1.8
D-glass	72–75	0–1	21–24	0–1	0–4	-	-	-	0–0.3
E-glass	52–56	12–16	5–10	16–25	0–2	0–5	-	0–4	0–0.8
ECR-glass	54–62	9–15	-	17–25	0–2	0–4	-	0–4	2–5.8
AR-glass	55–75	0–5	0–8	1–10	11–21	-	1–18	0–12	0–2.5
R-glass	55–60	23–28	0–0.35	8–15	0–1	4–7	-	-	0–1.8
S-2-glass	64–66	24–25	-	0–0.2	0–0.2	9.5–10	-	-	0–0.1

\* BaO, ZnO, Li<sub>2</sub>O, Fe<sub>2</sub>O<sub>3</sub>, F<sub>2</sub>

in all types of glass fiber is silicon dioxide (SiO<sub>2</sub>) with around 50 % to 75 % of the total mass. The remaining components provide specific desired mechanical or chemical properties at different proportions (Bagherpour, 2012).

Table 2.2 outlines the main mechanical properties for the different fiberglass types. The table shows that among these different glass types, S-2-glass has the greatest tensile strength and the highest modulus of elasticity throughout all listed temperatures. Per unit volume, D-glass fibers are the lightest and also have the lowest tensile strength and modulus of elasticity (Bagherpour, 2012).

**Fiber Sizing** The sizing is a formulation of chemicals, generally diluted in water, that is used to coat (i.e. size) each individual fiber. The sizing formulation varies with fiber producers. All fiber producers develop their proprietary sizing and apply it to the fiber relative to the needs of the targeted fiber application.

Sizing is a complex and specialized procedure. Many of the chemical structure-property and process-property relationships involved in sizing performance remain proprietary knowledge. Furthermore, there are

Table 2.2: Mechanical properties of different types of glass fibers

	Density $\frac{\text{g}}{\text{cm}^3}$	Tensile Strength MPa				E-Modulus GPa		Elongation %
		at 23 °C	at 196 °C	at 371 °C	at 538 °C	at 23 °C	at 538 °C	
A-glass	2.44	3310	-	-	-	68.9	-	4.8
C-glass	2.52	3310	5380	-	-	68.9	-	4.8
D-glass	2.12	2415	-	-	-	51.7	-	4.6
E-glass	2.58	3445	5310	2620	1725	72.3	81.3	4.8
ECR-glass	2.72	3445	5310	2165	1725	80.3	81.3	4.8
AR-glass	2.70	3241	-	-	-	73.1	-	4.4
R-glass	2.54	4135	-	2930	2140	85.5	-	4.8
S-2-glass	2.46	4890	8275	4445	2415	86.9	88.9	5.7

no standard tests for sizing stability, where sizing stability is a key characteristic that glass fiber producers must consider when selecting raw materials for their sizing formulations. Sizing stability is the ability of a formulation to stay in a homogeneous state from the moment it is mixed to the time it is delivered and applied to the fiber. Maintaining the quality and consistency of the sizing throughout production is also critical, as sizing problems can cause significant losses in efficiency during glass fiber production. For example, increasing the loss of ignition; increasing fiber breakage during application; changing the pH, which affects the sizing pickup; and foaming, which results in uneven coating.

In summary, sizing is a critical element as it determines how fibers will handle during processing, as well as how they perform as part of FRP rebars. Sizing development for fiber production will ensure proper bond and stress transfer between the resin matrix and the fibers. Thus, ensuring that the fibers within an FRP rebar are sourced from a producer with established experience and sound quality processes would be highly advantageous. This would require a continuously well-documented production process, and possibly a fact sheet that identifies the individual components that were used throughout the production process. For example, agencies could develop white-lists for acceptable GFRP components, and stipulate that products with different source materials are not acceptable for publicly funded projects.

## 2.3 GFRP Rebar Manufacturing

Pultrusion is a continuous manufacturing process used to make a diverse range of FRP composite profiles with consistent cross-sections. In this process, the fibers are impregnated with resin and pulled through a heated stationary die to shape the product before it is cut to the desired length. It is a cost-efficient process that efficiently accommodates the exponentially growing market of FRP products, which allows for consistent and potentially high-quality profiles with low error margins if proper production and quality procedures are adopted.

Generally, all pultrusion techniques follow the same basic steps and production sequence, schematically

explained in Figure 2.4. The process begins by feeding the fibers into the machine from rolls of continuous

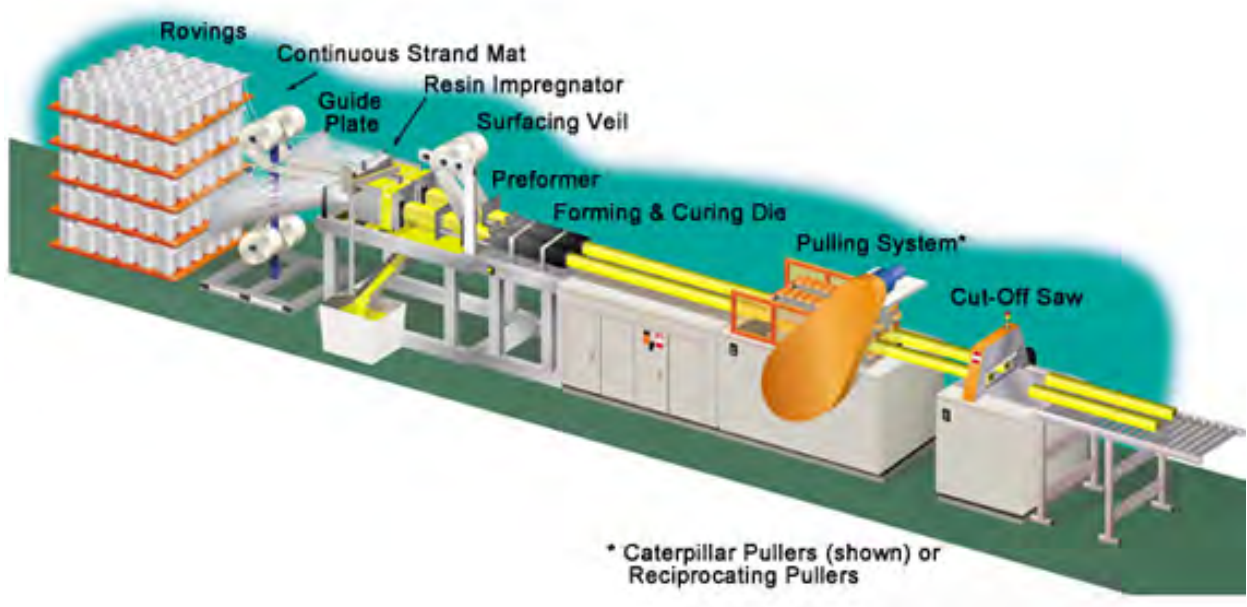


Figure 2.4: Pultrusion process for the manufacture of GFRP rebars <sup>a</sup>

<sup>a</sup>Information retrieved on October 10, 2016  
from: <http://www.creativepultrusions.com>

reinforced filaments or fabric. Before impregnating the fibers with resin, the reinforcement fibers are threaded into a tension roller. This roller is the first component in the production line that prepares the product for its final shape by grouping them accordingly. Once the fibers are appropriately grouped, they pass through a resin bath for impregnation. Catalysts may be added to the bath to assist the curing or solidifying process of the resin matrix. This part of the production sequence is vital, because it guarantees that the final product is properly protected (e.g.; against corrosion, UV rays, etc.). Additionally, color pigments can be added during this production step to enhance the appearance of the product. A pull mechanism extracts the cured product and advances it to the cutting station where the pultruded product is cut to the desired lengths. In addition to the physio-mechanical elements (type of fibers, fiber content, etc.) that will determine the properties of GFRP rebars, the manufacturing process will also directly affect its performance based on the rate of resin polymerization, the manufacturing process, and the quality control procedures.

### 2.3.1 FRP Rebar Cross-Sectional Shapes

Solid round (or quasi-circular) is the FRP rebar cross-section that has been most extensively researched, tested, and experimentally validated, where the existing design models assume this is the type of composite reinforcement used for concrete. In addition, due to the versatility of composites and innovative manufacturing techniques, GFRP rebars can be, and are produced in a variety of different cross-sectional shapes. Some

of the available rebar cross-sections in addition to the solid round include oval, flat (rectangular or square), star-shaped, and round hollow rebars. The shape may vary due to the application (eg. anchoring) to improve the effectiveness of the components reinforcement due to shear lag effects. In the past years, different studies and research projects have been conducted (Wang and Belarbi, 2012; Fava et al., 2016; Claire, 2015; Micelli and Nanni, 2004; Benmokrane et al., 2002; High et al., 2015) to evaluate the advantages and disadvantages of each type, and to determine the most suitable application for each individual shape. Generally, most companies will have conducted extensive material characterization so that the products can be commercially marketable with established characteristics. This project will consider only the evaluation and manufacturing



Figure 2.5: GFRP bars with different cross-sectional shapes, reprinted with permission from Claire (2015)

of solid round (or quasi-circular) GFRP rebars.

**2.3.2 Surface Enhancement Features**

Reinforced concrete relies on the transfer of stresses from the concrete to the internal reinforcement, where a perfect bond is assumed. With steel, the bond is provided via mechanical means by deformations or lugs. For GFRP rebars, the surface enhancement to ensure appropriate bond to concrete is achieved by techniques, which vary according to manufacturer preference.

The most commonly manufactured surface enhancements in FRP rebars include: i) sand-coating increasing the friction and interlocking with concrete, ii) the use of an external helical wrap to create an undulating surface, which increases mechanical interlock; iii) surface deformation or lugs, similar to steel rebars; and lastly iv) using fiber tows twisted externally around the rebar increasing mechanical interlock. To date, there is no standard test method to determine the most appropriate surface enhancement (Wang and Belarbi, 2012;

Fava et al., 2016; Claire, 2015), however an ACI test method has been generally accepted to determine if a minimum acceptable level of bond is provided by the rebar to the concrete based on the rebar nominal diameter.

A research project completed in 2005 (Okelo and Yuan, 2005) evaluated four different types of rebars for concrete bonding properties via the pullout method similar to the procedure outlined in ASTM D7913 (ASTM International, 2014). GFRP, AFRP (aramid fiber reinforced polymer), CFRP (carbon fiber reinforced polymer) and steel, with diameters of 6, 8, 10, 16, and 19 mm were tested. The bond improvement methods that were analyzed in this research included sand coating, helical wrapping, ribs and surface undulations. 151 rebars were tested using the pullout test, in which 762 mm long FRP rebars were pulled out of 203 mm concrete cubes with embedment lengths of five, seven, and nine times the rebar diameter. Special round specimen wedges with alloy at the surface interface were used for this study due to the low transverse strength of the GFRP rebars. It is noted that at the time gripping methods for composite rebars were not fully developed. However, anchors for tensile testing of composite rebars are now well established. The round shapes were mounted via “vee” wedges in conjunction with copper sleeves at the gripping end of the rebar. For each of the tested rebars, the average bond stress slip relationship and the failure mode were experimentally determined (Okelo and Yuan, 2005). The test results showed that in general, the bond of FRP rebars varied between 40 % to 100 % the bond strength of steel rebars for pullout failure mode. The ribbed FRP rebars (similar to the ones used for steel bars) were found to be very effective surface enhancements. Other solutions such as helical wrapping or similar surface deformations were also determined to be acceptable. Sand coating or other surface textures produced better bonding characteristics than smooth GFRP surfaces (Okelo and Yuan, 2005). The pullout failure modes were also analyzed, and it was determined that the type of failure depends on: 1) the shape and the surface type of the rebars; ii) the compressive strength of the concrete; iii) the concrete-cover; and iv) the embedment length. When using low compressive strength concrete and short embedment lengths, the bar was usually pulled out. On the other hand, splitting failures occurred for short embedment lengths and higher compressive strength or for longer embedment lengths and low compressive strength concrete. The average bond strength decreases with increased embedment lengths, because the pullout load and the embedment length are not proportional to each other. Similar to steel bars, the bond strength of FRP rebars decreases with increasing bar diameters (Okelo and Yuan, 2005). It has been found that the use of sand coatings reduces the occurrence of both micro and macro cracking on the FRP rebar surface due to the chemical reaction between alkali ions and the coating resins (Benmokrane et al., 2002).

### 2.3.3 Bending Process for FRP Stirrups

The most common production method to produce bended FRP reinforcement bars is based on the above mentioned pultrusion process, which is normally used to manufacture straight continuous FRP reinforcement bars. Because pultrusion is a continuous process, its not feasible to produce closed stirrups with this method. Furthermore, since the resinous matrix is cured during the usual pultrusion process, it is also not possible to bend the bars without destroying the composite material due to the brittle characteristics of the components. Therefore, polymerization of the resin must be prevented throughout the pultrusion process for (at least) the sections that are ought to be bend. Those sections of the rod can then be bent by hand and placed in an oven to complete the polymerization. The fibers are initially lined up to be parallel, but upon bending, the innermost fibers tend to crinkle and relieve the tension such that only the fibers along the outermost radius can be fully activated as illustrated in Figure 2.6 (a) (Ahmed et al., 2010). In addition, the fibers in the bent section also tend to concentrate in the centerline of the bar, as it is illustrated in Figure 2.6 (b).

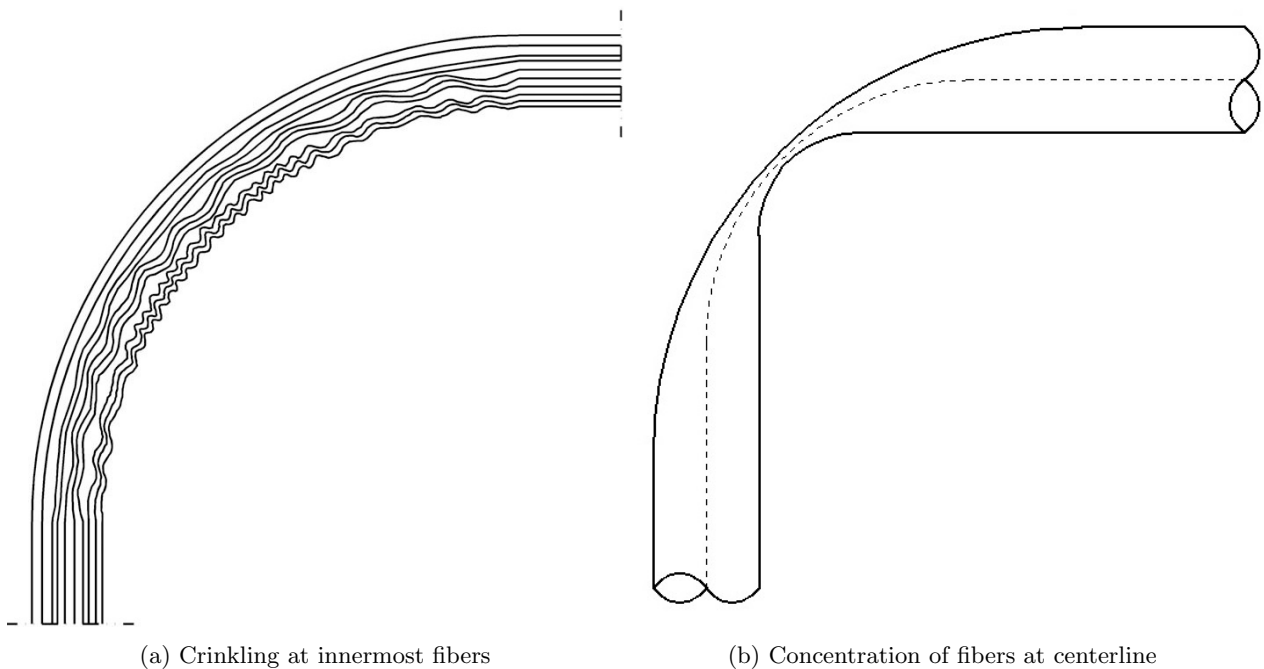


Figure 2.6: Parallelism defects in bent sections of FRP bars

This concentration causes a significant reduction of the shear strength throughout the bent zone. To demonstrate the defect in the initially parallel fibers, Figure 2.7 shows a photo of the fibers after the resin was removed and the fibers were bent. One possibility to reduce this issue could be local twisting of the fibers such that they are rotated about the longitudinal axis of the (initially straight) bar<sup>2</sup>. But this rotation

<sup>2</sup>As suggested in “Comments on the efficiency of closed stirrups” made available by ATP Srl  
Information retrieved on December 24, 2016  
from: [http://www.atp-frp.com/Marco\\_Pisani\\_Comportamento\\_staffe\\_chiuse\\_eng.pdf](http://www.atp-frp.com/Marco_Pisani_Comportamento_staffe_chiuse_eng.pdf)





Figure 2.7: Bare fibers of bent section after removing the resin

may lead to helical patterns at the inner part of the curved zone, while the fibers at the center of the cross section would be wavy. Apart from the geometrical problems that stem from bending of parallel fibers, the anisotropic characteristics of FRP material also cause difficulties, because the lateral strength of the FRP is marginal compared to their longitudinal one. But as Figure 2.8 illustrates, in addition to the stresses along the longitudinal direction (parallel to the fiber axis), stirrups have to resist lateral loads due to bearing stresses that arise at the inner bent, where the stirrup is pushed against concrete. These strength/stress related issues and the geometrical difficulties that occur during bending of parallel fibers lead to a significantly reduced design shear strength, which generally ranges between 40% to 60% of the longitudinal strength (Ahmed et al., 2010).

The typical failure of FRP stirrups is shown in Figure 2.9. The photo emphasizes that the failure of non-straight FRP bars occurs at the bent section, due to the reasons mentioned above. Because the strength of the stirrups depends on the geometric properties, or the radius of the bend, a minimum radius must be considered and respected — similar to the requirements for stirrup radii of steel bars.

#### **2.3.4 Bending FRP Bars On Site**

As mentioned above, it is not possible to simply bend FRP reinforcement bars after polymerization of the thermosetting resin occurs because of the brittle characteristics of the resinous matrix after hardening. After such resins thermally set, they cannot be restored into their original liquid state. However, as mentioned in Section 2.1, there are other categories of resin, and some of them have thermoplastic characteristics. These

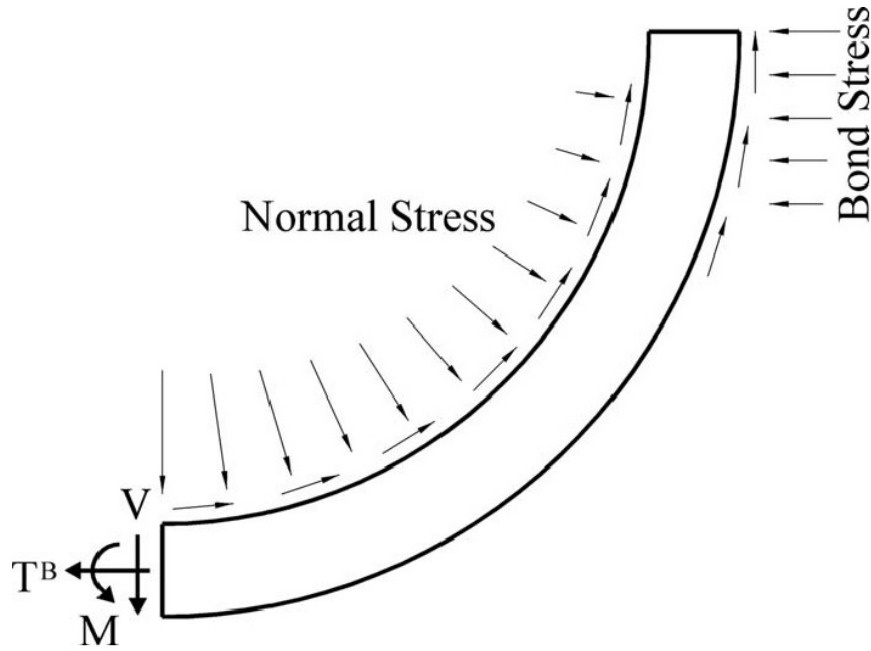


Figure 2.8: Stresses at the bend zone of stirrups according to Ahmed et al. (2010)

resins can change reversibly from a liquid state to a solid state (and back) through temperature variations. Consequently, thermoplastic resins seem to be promising for the development of FRP bars that can be bent at the construction site via heat treatment. But it is emphasized that thermoplastic characteristics also have some serious disadvantages: A change in temperature may cause significant variations in the material properties. For example, too much heat may lead to a complete loss of the load carrying capacity. Hence, FRP rebars made from thermoplastics are not considered desirable for structural applications (Nanni et al., 2014). Besides durability issues that result from bending thermoplastics, bending fibers encased in thermoplastics (on site) would still suffer from parallelism defects as shown above in Figure 2.6.

### 2.3.5 Quality Control for GFRP Manufacturing

Though GFRP rebars are considerably new and a technology under development, a few standards have been established to ensure consistency and quality of the material, as explained in Section 2.5. However, quality control is not just important for the final product, but instead has to be a continuous process throughout the entire manufacturing process. Accordingly, the quality control process can be divided into four different phases: i) inspection of the raw materials and the installations that are used in their production, ii) control of the start of the production, iii) quality control during the production of the rebars, and iv) the final inspection of the produced rebars. In each phase, different tests are conducted. Each manufacturer has its own proprietary quality control plan, which — depending on the capacities of the company — is fulfilled internally or via external testing companies.



Figure 2.9: Typical failure of FRP stirrups Ahmed et al. (2010)

Initially, before any type of production, all installations and devices, as well as the raw materials, have to be inspected and checked for possible deficiencies. This inspection covers different tests and controls of different characteristics, such as i) the viscosity or reactivity of the resin, ii) the linear weight of the fiber roving, iii) the resin mix ratio if different types of resin are mixed, iv) the fiber/resin ratio, v) the heating temperature of the die, vi) the proper running of the pultrusion machine, and possibly other aspects. After it has been ensured that both materials and installation comply with the relevant quality standards, the production sequence can be prepared. For that, other tests and quality control processes have to be taken into account. Among the control tests for the production sequence, the following can be named: i) the setup for the length and wicking of the rebars, ii) the cure ratio, iii) the temperature, and if necessary other details of the production sequence have to be monitored. Throughout the control process, the necessary adjustments and changes are implemented to ensure a high quality product.

During production, i) the pultrusion temperature, ii) the pulling speed, iii) the pultrusion length and wicking, and iv) the cure ratio of the resin are controlled to ensure that the production results match the target characteristics (that were established before — see above). Moreover, in this phase, the uniformity of the coating is also inspected. Finally, once the rebars are produced, a final inspection of the manufactured GFRP product is conducted. Some of these quality tests include the inspection of the following characteristics:

i) number of produced rebars , ii) strength characteristics (tensile, transverse shear, etc.), iii) cross-sectional area, iv) fiber content, and v) water absorption. If the rebars comply with all quality standards, they are ready to be sold, shipped, and used.

All of the tests described above are conducted with different instruments, following various norms, at different intervals — depending on the production company, tests, and the recorded results. For more information, an example of a quality control plan, provided by the manufacturer “Pultrall,” can be found in Appendix C.

## 2.4 Degradation of Bond Between FRP Bars and Concrete

In the last two decades, many research projects have been conducted to study the deterioration process of GFRP rebars and their bond to concrete (Benmokrane et al., 2002; Balázs and Borosnyói, 2001; Wang and Belarbi, 2012). Though it is commonly believed that GFRP rebars do not suffer any type of deterioration, it is a false assumption because the GFRP rebar properties degrade over time. This process of degradation is considered to be a consequence of three possible reasons (Wang and Belarbi, 2012):

1. For GFRP rebars, the thermal actions may influence both the mechanical characteristics of the bar itself, as well as the bond behavior between the rebar and the concrete. Table 2.3 shows that FRP rebars along the longitudinal direction measure lower or similar CTE values than concrete, however, in the transverse direction (mostly governed by the resin), the CTE of FRP rebars reach 5 to 8 times greater values than that of concrete. Though glass fibers and concrete behave similarly under heat

Table 2.3: Coefficient of thermal expansion (CTE) of different materials (Balázs and Borosnyói, 2001)

Material	Coefficient of thermal expansion (CTE) ( $10^{-6} \frac{1}{K}$ )	
	Longitudinal direction	Transverse direction
Glass fiber	5 to 15	5 to 15
Carbon fiber	-0.9 to 0.7	8 to 18
Aramid fiber	-6 to -2	55 to 60
Resin	60 to 140	60 to 140
GFRP	7 to 12	9 to 20
CFRP	-0.5 to 1	20 to 40
AFRP	-2 to -1	60 to 80
Steel	12	12
Concrete	6 to 13	6 to 13

changes, the combination of glass fibers and resin (with a 10-times higher CTE) leads to FRP rebars with a greater CTE value than concrete. Accordingly, with high temperature variations, the large differences between the CTE of FRP rebars and concrete may lead to high radial pressures at the FRP rebars’ surface, which causes the surrounding concrete to crack if the developed stresses are higher than

the tensile strength of the concrete (Balázs and Borosnyói, 2001). This may cause longitudinal splitting of the concrete cover. On the other hand, under negative temperature gradients, FRP rebars contract more than the surrounding concrete, which leads to micro-gaps along the interface.

2. The FRP rods themselves suffer deterioration too. They are not waterproof, and moisture or alkaline ions can penetrate into the polymer resin by diffusion. Water molecules become resin plasticizers and destroy the Van der Waals bonds of the polymer chain, which leads to degradation. Furthermore, infiltrated water expands during freeze-thaw cycles, which generates cracks in the resin matrix. Because the surface of the GFRP bar is more susceptible, the bond between the bars and concrete is also affected. The damage caused depends on: the type of resin, stress level, diameter, manufacturing process, and the pH of the alkali environment (Benmokrane et al., 2002).
3. During FRP rebar fabrication, micro-voids form between the FRP and concrete, preventing a full contact between both components. According to Benmokrane et al. (2002), when a section of rebar is exposed to (or drowned in) a solution, these micro-voids fill up gradually. During freezing cycles, the water in the voids expands 10 %, leading to microcracks at locations where the generated stresses are higher than the tensile strength of the concrete. Successive freeze-thaw cycles create bigger microcracks and possibly severe damages, for this reason. Freeze-thaw cycles may not be a major concern in Florida, but it has to be taken into account in northern states with colder climates.

Multiple research projects have been conducted to model the long-term durability of GFRP rods (Benmokrane et al., 2002; Balázs and Borosnyói, 2001; Wang and Belarbi, 2012). Many of these efforts concluded that the best method to analyze the degradation of GFRP rebars was not to submerge them directly in an alkali solution, but instead to apply certain stresses to the bars when embedded in moist/wet concrete. In 2002, at the Université de Sherbrooke (Quebec), Benmokrane et al. (2002) conducted more than 400 accelerated aging tests on 20 different GFRP rebar types. The rebars were exposed to three different alkaline environments (NaOH, simulated solution of pore-water, and embedded in concrete) and tested under various tensile loads (22 % to 68 % of ultimate strength). The aim was to determine the applicable time of rupture or residual strength after the aging process. The results showed that the most realistic durability analysis was based on rebars embedded in moist concrete. Benmokrane et al. (2002) suggested that high temperatures (under the glass transition temperature of the matrix) could be used to accelerate the process, specifically 60 °C was proposed.

## 2.5 GFRP Rebar Applications Overview

GFRP rebars are spreading into many different applications (Markets and Markets, 2016) because of their numerous advantages. GFRP rebars are considered beneficial for use in concrete members susceptible to chloride ions or chemicals due to their high resistance to corrosion. For example, in reinforced concrete exposed to marine salts such as water breaks, seawalls, structures and buildings near waterfront, floating marine docks, etc., GFRP rebars are also used to reinforce concrete near electromagnetic fields because of the magnetic transparency; e.g. MRI rooms in hospitals, toll booths in road pavements and airport radio towers. Moreover, GFRP reinforcements can be found in concrete structures near high voltage cables, substations, and transformers since they are not conductive (thermally and electrically). Mining and tunneling applications also benefit from GFRP bars — since the bars are easily cut due to a low transverse strength as compared to the longitudinal strength — when reinforced soft-eyes or provisional walls have to be “consumed” by tunneling machinery. Although usually not a concern in Florida, in many other states and countries with colder climatic conditions, GFRP rebars are used for reinforced concrete structures exposed to de-icing salts. For instance, in bridge decks, median barriers, salt storage facilities, parking garage elements and various other applications (Purdue ECT Team, 2007).

Over the last two decades, numerous buildings and structures have been constructed with concrete elements that have utilized GFRP rebars. Initially, these types of rebars gained importance as an alternative to steel for the restoration of old buildings, but nowadays, new construction projects also take advantage of the beneficial properties of glass fiber rebars. The following list itemizes some of the high-profile worldwide projects that implemented GFRP rebars in concrete for different infrastructure applications:

- Burj Al Arab — Dubai, UAE (2015): 1500 wave energy dissipating shed units of this iconic 7 star hotel were reinforced with GFRP bars. GFRP was used because the service life requirements were 50+ years.
- Reinforced concrete (RC) water tank — Quebec, Canada (2013): Was the first water treatment tank that was completely reinforced with GFRP reinforcement bars. The tank was designed for a volume capacity of 2500 m<sup>3</sup> with 4.7 meter tall walls, and GFRP rebars were used because a required chemical resistance could not be guaranteed with conventional reinforcement methods. Fiber-optic sensors were installed on critical points, and they have been used to verify the performance of the tank and the GFRP reinforcements.
- El Ain El Sokhna Supercritical Power Plant — Egypt (2012): The water intake of this 2 x 650 MW gas/oil fired power station was secured with GFRP rods because there was a need for corrosion resistance to protect the structure from the surrounding marine environment. These rods were designed to prevent flow-induced vibration and resist wave loads, impact loads from large objects, and entrance of fish and

people. The service life requirements of 100 years prompted the utilization of GFRP.

- Dibba Harbour — Sharjah, UAE (2011): This marina development for a housing project, accessed through a 600 m canal, is located near the beaches of Dibba Harbour. The 6 m deep walls of the excavated canal were stabilized with GFRP reinforced concrete to avoid corrosion induced through chlorides from sea water near the canal.
- Northside Storage Tunnel — Sydney, Australia (1998 – 2000): This 20 km long tunnel, with diameters from 2.8 m to 6.6 m, connects the suburb of Lane Cove with the North Head in Sydney. GFRP rebars were used in lieu of steel because of the corrosive chemicals present in the sewage overflow and in the storm-water.

Along with the developments of manufacturing FRP rebars for the construction industry, the experimental behavior of GFRP-RC elements has also been documented during the last two decades. To this end, guidelines, specifications, and standard test methods relevant to GFRP rebars for concrete have been developed and are readily available. To ensure that engineers have the necessary tools to design safe and durable structures, different agencies and entities have developed guiding documents. For example, in North America, the Association of State Highway and Transportation Officials (AASHTO), American Concrete Institute (ACI), and Canadian Standards Association (CSA) have generated specific design guidelines. Also the International Organization for Standardization (ISO) has developed guidelines, while the International Code Council Evaluation Service (ICC-ES) has approved the acceptance criteria for the implementation FRP rebars as part of the building code. The design guidelines for the use of FRP rebars in concrete members are listed in Table 2.4. It should be noted that the documents reference primarily the design and specification of solid round (or quasi-circular) GFRP rebar for concrete and carbon strands since these technologies have been extensively investigated and developed. The only exception is ICC-ES AC454 document, which includes the use of solid round basalt FRP rebars.

Table 2.4: Design guidelines for GFRP reinforcement bars

Design Guidelines	Title
AASHTO	
GFRP-1	AASHTO LRFD Bridge Design Guide Specifications for GFRP- Reinforced Concrete Bridge Decks and Traffic Railings
FDOT	
DEV932	Nonmetallic Accessory Materials for Concrete Pavement and Concrete Structures
ACI	
440.1R-15	Guide for the Design and Construction of Structural Concrete Reinforced with Fiber-Reinforced Polymer Bars
440.3R-12	Guide Test Methods for Fiber-Reinforced Polymers (FRPs) for Reinforcing or Strengthening Concrete Structures
440.5-08	Specification for Construction with Fiber-Reinforced Polymer Reinforcing Bars
440.6-08	Specification for Carbon and Glass Fiber-Reinforced Polymer Bar Materials for Concrete Reinforcement
440.9R-15	Guide to Accelerated Conditioning Protocols for Durability Assessment of Internal and External Fiber-Reinforcement
CSA	
CAN/CSA-S06-15	Fiber Reinforced Structures, Canadian Highway Bridge Design Code, Page 693-728
CAN/CSA-CSA-S806-12	Design and Construction of Building Components with Fiber-Reinforced Polymers
CAN/CSA-S807-10	Specification for Fiber-Reinforced Polymers
Design Manual No. 3	Reinforcing Concrete Structures with Fiber Reinforced Polymers
Design Manual No. 4	FRP Rehabilitation of Reinforced Concrete Structures
Design Manual No. 5	Prestressing Concrete Structures with FRPs
ISO	
14484:2013 ED1	Performance guidelines for design of concrete structures using fiber reinforced polymer(FRP) materials.
ICC-Evaluation Service	
AC454	International Code Council, Evaluation Service, Acceptance Criteria for Fiber Reinforced Polymner (FRP) bars for Internal Reinforcement of concrete members, June 2016.



# Contents

## Chapter 3

# GFRP Market and Rebar Manufacturers

### 3.1 Worldwide FRP Rebar Manufacturing

The global market of FRP rebars is growing and could reach \$91.0 million by 2021, based on a predicted Compound Annual Growth Rate (CAGR) of 11.4 % between 2016 and 2021 (Markets and Markets, 2016). Currently, North America is leading the world market with the fastest-growing demand, in part due to increased spending on built infrastructure. Figure 3.1 provides a visualization of GFRP rebar manufacturer density around the world; this density was determined by the market analysis done within the scope of this project. The highest concentration is in North America, where there are 9 manufacturers (6 in the USA and 3 in Canada). A total of 6 GFRP rebar producers are located in Europe (2 in Germany, 2 in Italy, 1 in Switzerland, and 1 in the Czech Republic), while 6 Asian manufacturers exist (6 in India, 2 in Thailand, 1 in Russia, 1 in the United Arab Emirates, and 1 in Saudi Arabia). Finally, 2 Oceanian manufacturers produce in South Australia and New Zealand.

All manufacturers in these countries were contacted and surveyed with GFRP production specific questionnaires. A copy of the survey that was sent out to all known GFRP rebar producers can be found in Appendix ???. In addition, email contact was established and phone interviews were conducted. Manufacturers that produce solid round (or quasi-circular) GFRP rebars were prioritized, given that the design and specification for this type of rebars have been fully developed. Additional rationale aspects targeted full scale (industrial) manufacturing production capabilities, established manufacturing quality program and policies, fully developed material specifications (either via internal or external laboratory testing), and the capability to manufacture three or more different size rebars. Based on the provided information, the state

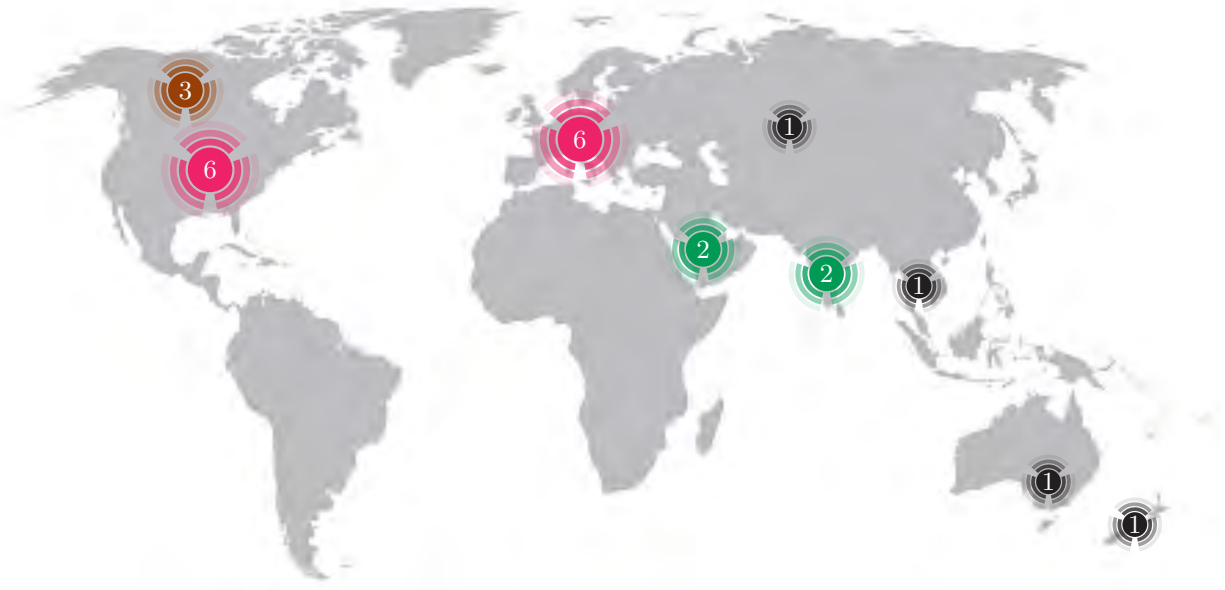


Figure 3.1: Distribution of GFRP rebar manufacturers

of the market was analyzed and the data is presented below to provide context of the technology, nationally and internationally. Table 3.1 lists all main GFRP manufacturers and provides detailed information about the production location, for a comprehensive summary of the main GFRP producers that are in business today. These companies have been established mainly throughout the last two decades. Each of the listed manufacturers uses different materials, produces various cross-sectional shapes, and/or takes advantage of a variety of surface enhancements when producing GFRP rebars. Table 3.2 provides a summary of the currently produced GFRP rebars and their reported specifications — per manufacturer. As reported in the table, round rebars are the most common, while helical wrapping appears to be the most popular surface bond enhancement feature. In addition, most GFRP rebar manufacturers produce a large variety of bars — ranging in sizes from # 3 bars to # 18 bars.

Due to these manufacturer specific and unique products, the GFRP market appears rather broad and dispersed, without unified standardization requirements across different producers — as is usual for the steel rebar industry. While this might still pose an additional difficulty for design engineers, standard specifications are currently being developed by ASTM committee D30, which may provide a solution to these shortcomings in the near future.

Depending on the bar sizes and the specific bar features, as well as the factory size and capabilities, different companies produce their products at varying rates and use different strategies to distribute their products. Table 3.3 lists the production planning and rate for each manufacturer. Table 3.3 also shows the range of GFRP rebar production experience for the surveyed manufacturers. To clarify and emphasize these differences, the following Figures 3.2 and 3.3 visualize the numbers shown in Table 3.3. Figure 3.2 visually

Table 3.1: Location of GFRP manufacturers

Manufacturer		Nearest Office to Florida			Web-page
ID	Name	Country	State	City	
AFR	American Fiberglass Rebar	USA	Nevada	Henderson	www.americanfiberglassrebar.com
CRT	Composite Rebar Technologies, Inc.	USA	Wisconsin	Madison	www.hollowrebar.com
ASL	Asland, Hughes Brothers, Inc.	USA	Nebraska	Seward	www.aslanfrp.com
INF	INFUS Advanced Construction Solutions	USA	North Carolina	Walnut Creek	www.infus.com
KOD	KODIAK Fiberglass Rebar	USA	Texas	Houston	www.fiberglassrebar.us
MAR	Marshall Composite Technologies, LLC	USA	Oregon	Salem	www.marshallcomposite.com
RAW	Raw Energy Materials Corporation	USA	Florida	Pompano Beach	www.newrebar.com
PAL	Pultrall, Inc.	USA (Canada) †	North Carolina	Sumnerfield	www.vrod.ca
BBM	B&B FRP Manufacturing Inc.	Canada	Ontario	Toronto	www.bandbfrp.com
BPC	BP Composites, Ltd.	Canada	Alberta	Edmonton	www.bpcposites.com
ATP	ATP srl	Italy	Salerno	Angri	www.atp-frp.com
SIR	Sireg Geotech Srl	Italy	Milan	Arcore	www.sireggeotech.it
FIX	Fibrolux GmbH	USA (Germany) †	California	Orangevale	www.fibrolux.com
SCH	Schoeck Bauteile	USA (Germany) †	New Jersey	Princeton	www.schoeck-combar.com
FIR	Firep Inc.	Switzerland	St. Gallen	Rapperswil	www.firepworld.com
ARM	Armaastek	Czech Republic	Prague	Prague	www.armaastekcz.cz
ARO	Applied Research of Australia (AROA)	USA (South Australia) †	Georgia	Savannah	www.aroa.com.au
PUN	Pultron Composites	USA (New Zealand) †	Michigan	Grosse Pointe Woods	www.matcon-bar.com
ARC	ARC Insulations & Insulators (P) LTD.	India	West Bengal	Bishnupur	www.arcinsulations.com
CSK	CSK Technologies	India	Telangana	Hyderabad	www.csksktechnologies.com
DXT	Dextra Group	USA (Thailand) †	California	Simi Valley	www.dextragroup.com
CHK	Composite Group Chelyabinsk	Russia	Chelyabinsk Region	Chelyabinsk	www.compositgroupworld.com
ING	International Grating Inc.	United Arab Emirates	Ras al-Khaimah	Abu Dhabi	www.igi-ugt.com
AFJ	AL-APFAJ Group	Saudi Arabia	Eastern Province	Al-Khobar	www.al-arfaajgroup.com

† Manufacturers headquartered in a different location, noted in parenthesis

Table 3.2: GFRP bars produced by different manufacturers

Manufacturer	Cross-Sectional Shape	Surface Enhancement	Glass Fiber Type	Resin Type	Produced Diameters
AFR	Round (solid)	Helical wrap + Sand coat	N/A	Vinyl Ester	#2, 3, 4, 5, 6, 7, 8, 9, 10
CRT	Round (hollow)	Helical wrap	N/A	N/A	N/A
ASL	Round (solid)	Helical wrap + Sand coat	E-CR glass	Vinyl ester	#2, 3, 4, 5, 6, 7, 8, 9, 10, 11, 12, 13
INF	Round (Solid)	Helical groove	N/A	N/A	N/A
KOD	Round (solid)	Helical ribs + hard silicate impregnation	E-CR Glass	N/A	#2, 3, 4, 5, 6, 7, 8, 9
MAR	Round (solid)	Helical rib	E-glass	Urethane modified vinyl ester	#2, 3, 4, 5, 6, 7, 8, 9
RAW	Round (solid)	Helical wrap + Sand coat	N/A	N/A	#2, 3, 4, 5, 6, 8, 10
PAL	Round, Y-Shape (solid)	Sand coat	Glass fibers	N/A	#2, 3, 4, 5, 6, 7, 8, 9, 10, 11, 14, 18
BBM	Round (solid)	Helical rib	E-Glassfiber	Vinyl ester	#2, 3, 4, 5, 6, 7, 8, 9, 10
BPC	Round (solid)	Helical thread + Sand coat	E-Glass or E-CR Glass	N/A	#2, 3, 4, 5, 6, 7, 8
ATP	Round, oval (solid)	Helical ribs + Sand coat	N/A	Vinyl Ester Resin	#3, 4, 5, 6, 7, 8, 9, 10, 11
SIR	Round, oval, quadratic, Y Shape(solid/hollow)	Quartz sand coat	N/A	Vinyl Ester /Thermoset polyester	#1, 2, 3, 4, 5, 6, 7, 8, 9, 10, 11, 12
FIX	Round (solid)	Helical thread	N/A	N/A	N/A
SCH	Round (solid)	Helical ribs	E-CR glass	Vinyl ester	#3, 4, 5, 6, 8, 10
FIR	N/A	Helical thread + Sand coat	N/A	N/A	N/A
ARM	Round (solid)	Helical ribs	N/A	Polymeric epoxy resin	N/A
ARO	Round (solid)	Helical thread or ribs	N/A	Vinyl ester	N/A
PUN	Round (solid/hollow)	Helical wrap or surface ground ribs	N/A	N/A	#2, 3, 4, 5, 6, 7, 8, 10, 11, 13
ARC	N/A	N/A	N/A	N/A	N/A
CSK	Round (solid)	N/A	N/A	N/A	N/A
DXT	N/A	Surface deformation + Sand coat	N/A	N/A	N/A
CHK	Round (solid)	Helical wrap + Sand coat	Glass roving	Epoxy resin based polymer	#2, 3, 4, 5, 6, 7, 8, 9, 10, 13, 16
ING	N/A	N/A	N/A	N/A	#3, 4, 5, 6, 7, 8, 9, 10, 11
AFJ	N/A	N/A	N/A	N/A	N/A

† N/A: multiple attempts were made to contact the manufacturer for detailed information, but it was difficult to get specific responses

Table 3.3: Manufacturer production

Manufacturer	First GFRP bars Year	Production Planning	Production Rate	
			$\frac{m}{d}$	$\frac{ft}{d}$
AFR	2013	Stock in large quantities	684	2,244
CRT	AR <sup>†</sup>	AR	AR	AR
ASL	1993	Stock in large quantities	12,200	40,000
INF	AR	AR	AR	AR
KOD	1984	AR	AR	AR
MAR	1995	Stock in large quantities	9,150	30,000
RAW	1988	Production on demand	4,575	15,000
PAL	AR	Stock in large quantities	30,000	98,425
BBM	2013	Production on demand	3,000	9,845
BPC	2007	Stock in small quantities	AR	AR
ATP	1985	Production on demand	7,000	22,965
SIR	1992	Production on demand	15,000	49,215
FIX	1980	AR	AR	AR
SCH	AR	AR	AR	AR
FIR	2004	Production on demand	9,000	29,528
ARM	2007	AR	AR	AR
ARO	1990	AR	AR	AR
PUN	1985	Production on demand	10,000	32,810
ARC	2003	AR	AR	AR
CSK	2008	AR	AR	AR
DXT	1997	AR	AR	AR
CHK	2012	Stock in large quantities	40,000	131,234
AFJ	AR	AR	AR	AR

<sup>†</sup> AR: Awaiting Response; multiple attempts have been made to contact the manufacturer for detailed information, but no specific response has been provided so far.

compares the production capacity of different companies (for those companies that have responded to the survey, emails, and/or phone calls so far). The company identifier is listed along the x-axis and the production rate (output per time) is graphed along the y-axis. It appears that most companies produce no more than  $50\,000 \frac{ft}{d}$  ( $15\,240 \frac{m}{d}$ ) of GFRP rebars, except for Pultrall, Inc., which seems to produce six times faster than most other companies. However, not only the production rate plays an important role for product availability, but also the production planning—on demand production vs. pre-production for material stocking—defines how quickly a specific product can be obtained. The relative production planning information is provided in Figure 3.3, which distinguishes and categorizes the production strategies based on small quantity stock, large quantity stock, and on-demand production. While one half of GFRP producers manufacture their products on demand, the other half is capable to pre-stock the produced rebars. Only 16.7% of all surveyed producers stock in small quantities, with less than 1640 ft (500 m) of any produced rebar size, while 33.3% of producers have the means to stock multiple rebar sizes with a total length of more than 1640 ft (500 m).

In addition to the market and production details, the manufacturers were also surveyed for material and

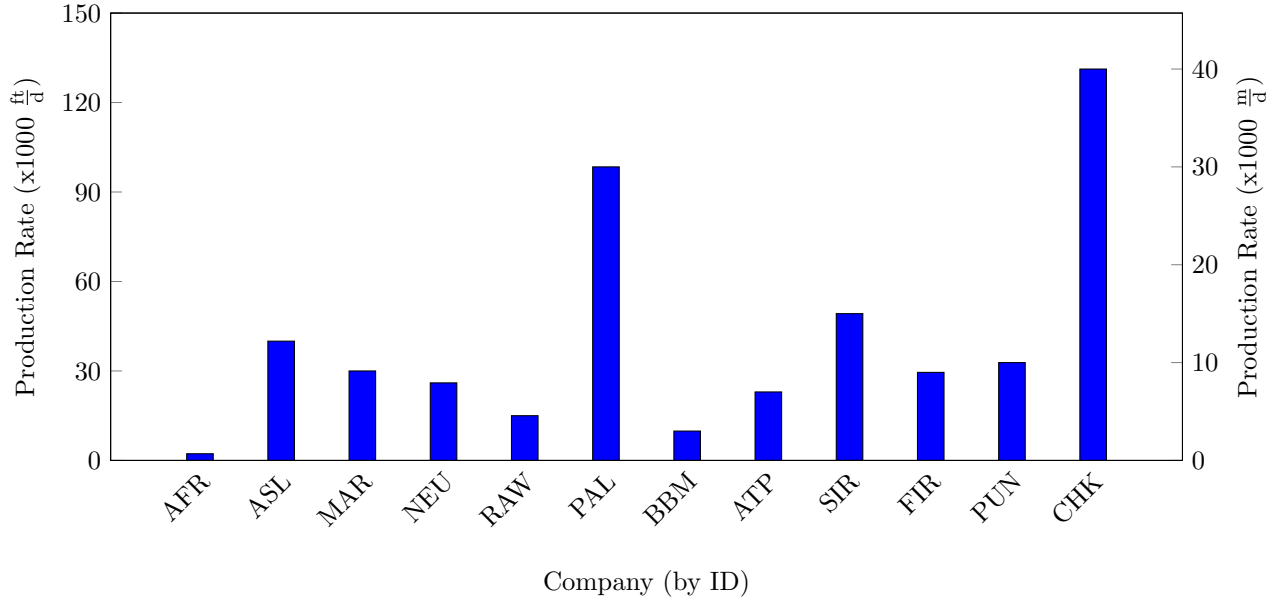
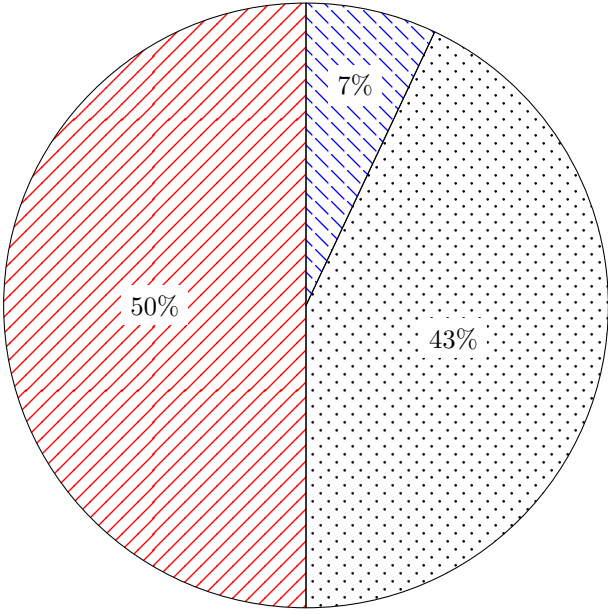


Figure 3.2: Production rate for different GFRP Manufacturers

product specific data. This information is detailed in the following subsection.

### 3.2 GFRP Products Database

As seen in Appendix ??, product-specific details were also requested from all surveyed manufacturers to target the engineering properties of each individual product. The collected information and data was unified and consolidated to produce a centralized state-of-practice database that summarizes the currently available GFRP rebar products. The parameters compiled in the database include cross-sectional shape, surface-enhancement features, materials used, production rate, main advantages of each rebar type, and quality control measures. Moreover, mechanical test data and details about physical characteristics were collected to provide simplified access to design-based properties; these include load capacity, maximum tensile strength, ultimate elongation, modulus, and unit weight for each rebar produced per manufacturer (as available). All data are summarized in Tables 3.4 through Tables 3.6 for specific bar sizes (# 3, # 5, and # 8). Furthermore, sample rebars were requested from all listed manufacturers to visually document the different features. Photos were taken at specific distances and angles to visually present the information shown in Appendix B.




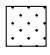

-  Production on demand
-  Stock in large quantities  $\Rightarrow$  multiple bar sizes with  $> 500$  m (1640 ft)
-  Stock in small quantities  $\Rightarrow$  any bar sizes with  $< 500$  m (1640 ft)

Figure 3.3: Production planning for different GFRP Manufacturers



Table 3.4: Manufacturer specifications of GFRP rebar #3

Manufacturer		Unit Weight		Area		Load Capacity		Max. Stress		Elastic Modulus		Strain
ID <sup>†</sup>	Type	$\frac{\text{kg}}{\text{m}}$	$\frac{\text{lbs.}}{\text{ft}}$	mm <sup>2</sup>	in. <sup>2</sup>	kN	kip	MPa	ksi	GPa	10 <sup>6</sup> psi	%
AFJ												
AFR		0.149	0.100	72.3	0.112	59.0	13.25	821.0	119.1	46.0	6.67	1.81
ARC												
ARM												
ARO												
ASL		0.174	0.117	71.0	0.110	58.7	13.20	827.4	120.0	44.8	6.50	1.79
ATP		0.190	0.128	71.0	0.110	91.0	20.46	958.0	139.0	47.0	6.82	2.03
BBM		0.150	0.101	71.0	0.110	71.0	15.96	1000.0	145.0	72.0	10.44	1.50
BPC	TUF 40GPa	0.149	0.100	71.0	0.110	69.8	15.70	983.8	142.7	49.1	7.12	2.30
BPC	TUF 60GPa	0.193	0.130	71.0	0.110	86.1	19.36	1370.5	198.8	63.7	9.24	2.20
CHK												
CRT												
CSK				78.5	0.122							1.66
DXT	GR45P			71.0	0.110	59.0	13.26	834.0	121.0	45.0	6.53	1.85
DXT	GR50P			71.0	0.110	65.0	14.61	910.0	132.0	50.0	7.25	1.82
FIR												
FIX												
INF												
ING												
KOD		0.159	0.107	86.0	0.121			800.0	116.0	40.8	5.92	
MAR		0.149	0.100	80.0	0.124	113.0	25.40	855.6	124.1	52.0	7.54	1.78
PAL	Standard	0.182	0.122	71.3	0.111			1100.0	159.0	52.5	7.61	2.10
PAL	Low Modulus	0.135	0.091	71.3	0.111			880.0	128.0	42.5	6.16	2.07
PAL	High Modulus	0.243	0.163	71.3	0.111			1372.0	199.0	65.1	9.44	2.11
PUN		0.233	0.157	95.0	0.147	103.0	23.16	1085.0	157.4	63.2	9.17	1.86
REM												
SCH												
SIR		0.150	0.101	71.0	0.110	75.0	16.86	1000.0	145.0	46.0	6.67	2.00

<sup>†</sup> Manufacturer ID according to table XY

Table 3.5: Manufacturer specifications of GFRP rebar # 5

Manufacturer		Unit Weight		Area		Load Capacity		Max. Stress		Elastic Modulus		Strain
ID <sup>†</sup>	Type	$\frac{\text{kg}}{\text{m}}$	$\frac{\text{lbs.}}{\text{ft}}$	mm <sup>2</sup>	in. <sup>2</sup>	kN	kip	MPa	ksi	GPa	10 <sup>6</sup> psi	%
AFJ												
AFR		0.432	0.290	200.6	0.311	158.4	35.60	715.0	103.7	46.0	6.67	1.63
ARC												
ARM												
ARO												
ASL		0.446	0.300	198.1	0.307	142.3	32.00	689.5	100.0	44.8	6.50	1.57
ATP		0.440	0.296	200.0	0.310	206.0	46.31	932.0	135.2	47.0	6.82	2.01
BBM		0.500	0.336	100.0	0.155	200.0	44.96	1000.0	145.0	70.0	10.15	1.60
BPC	TUF 40GPa	0.432	0.290	199.0	0.308	183.3	41.21	921.0	133.6	48.8	7.08	2.10
BPC	TUF 60GPa	0.521	0.350	199.0	0.308	223.9	50.33	1287.3	186.7	62.6	9.08	2.10
CHK												
CRT												
CSK				201.0	0.311							1.69
DXT	GR45P			199.0	0.308	144.0	32.37	725.0	105.2	45.0	6.53	1.61
DXT	GR50P			199.0	0.308	177.0	39.79	890.0	129.1	50.0	7.25	1.78
FIR												
FIX												
INF												
ING												
KOD		0.421	0.283	211.0	0.327			717.0	104.0	40.8	5.92	
MAR		0.417	0.280	205.8	0.319	95.0	21.36	695.7	100.9	49.2	7.14	1.60
PAL	Standard	0.488	0.328	197.9	0.307			1130.0	163.9	52.5	7.61	2.15
PAL	Low Modulus	0.379	0.255	197.9	0.307			940.0	136.3	42.5	6.16	2.21
PAL	High Modulus	0.558	0.375	197.9	0.307			1184.0	171.7	62.6	9.07	1.89
PUN		0.492	0.331	211.2	0.327	218.9	49.21	1036.0	150.3	60.6	8.79	1.71
REM												
SCH												
SIR		0.390	0.262	198.0	0.307	190.0	42.71	1000.0	145.0	46.0	6.67	2.00

<sup>†</sup> Manufacturer ID according to table XY

Table 3.6: Manufacturer specifications of GFRP rebar # 8

Manufacturer		Unit Weight		Area		Load Capacity		Max. Stress		Elastic Modulus		Strain
ID <sup>†</sup>	Type	$\frac{\text{kg}}{\text{m}}$	$\frac{\text{lbs.}}{\text{ft}}$	$\text{mm}^2$	$\text{in.}^2$	kN	kip	MPa	ksi	GPa	$10^6$ psi	%
AFJ												
AFR		1.012	0.680	512.9	0.795	310.0	69.69	643.0	93.3	46.0	6.67	1.36
ARC												
ARM												
ARO												
ASL		1.116	0.750	506.5	0.785	314.3	70.65	620.0	89.9	44.8	6.50	1.34
ATP		1.060	0.712	509.7	0.790	426.0	95.77	802.0	116.3	48.0	6.96	1.66
BBM		1.300	0.874	510.0	0.791	490.0	110.16	960.0	139.2	69.0	10.01	1.40
BPC	TUF 40GPa	1.101	0.740	510.0	0.791	417.5	93.86	818.6	118.7	52.0	7.54	1.80
BPC	TUF 60GPa	1.310	0.880	510.0	0.791	510.7	114.81	1201.0	174.2	61.7	8.95	1.90
CHK												
CRT												
CSK				490.6	0.760							1.33
DXT	GR45P			510.0	0.791	324.0	72.84	635.0	92.1	45.0	6.53	1.41
DXT	GR50P			510.0	0.791	428.0	96.22	840.0	121.8	50.0	7.25	1.68
FIR												
FIX												
INF												
ING												
KOD		1.060	0.712	521.9	0.809			552.0	80.1	40.8	5.92	
MAR												
PAL	Standard	1.132	0.761	506.7	0.785			800.0	116.0			1.52
PAL	Low Modulus	0.926	0.622	506.7	0.785			960.0	139.2			2.26
PAL	High Modulus	1.524	1.024	506.7	0.785			1000.0	145.0			1.51
PUN		1.146	0.770	547.4	0.848	543.7	122.23	993.0	144.0	61.5	8.92	1.60
REM												
SCH												
SIR		0.950	0.638	507.0	0.786	400.0	89.92	830.0	120.4	46.0	6.67	1.90

<sup>†</sup> Manufacturer ID according to table XY

# Chapter 4

## Experimental Program

### 4.1 Introduction

The experimental program detailed throughout this chapter targeted the material performance of various Glass Fiber Reinforced Polymer (FRP) rebar products. Benchmark values were obtained and compared to the material performance after saltwater exposure at different temperatures for extended time periods.

This chapter provides background information about the general research approach in the following Section 4.2, and specifies the tested materials in Section 4.3. All equipment and test devices that were needed to conduct the experiments are described in Section 4.4, which includes specialized fixtures needed to test specific strength properties of FRP rebars. Finally, the test procedures based on the relevant and applicable ASTM standard documents are outlined in Section 4.5.

### 4.2 Experimental Concept

This research project focused on an extensive evaluation of virgin and aged material properties of GFRP rebar products. For this study, products from three major GFRP rebar manufacturers were selected to measure the repeatability of virgin material characteristics throughout three different production lots. Because actual rebar dimensions vary between different manufacturers and each rebar size differs differently from the nominal dimensions, # 3, # 5, and # 8 rebars were targeted to cover a wide size range of the most commonly produced GFRP rebar sizes. For each of these manufacturers, production lots, and rebar sizes, four physical properties (e.g.; fiber content, cross-sectional dimensions, etc.) and four strength characteristics (e.g.; tensile strength, transverse shear strength, etc.) were tested. To attain reliability of the measured characteristics, it was the goal to test a minimum of five specimens per test group, but for some test procedures the sample size was

reduced to three specimens for economical reasons. Figure 4.1 illustrates the experimental approach and shows the methodology for the virgin material properties on the left. The right side of Figure 4.1 represents



Figure 4.1: Experimental concept

the experimental concept that was chosen to obtain results for material durability evaluations. To test GFRP rebars for resistance to harsh environments, the experimental design aimed to expose virgin material samples to saltwater at three different temperatures (23 °C, 40 °C, and 60 °C) for accelerated conditioning. This study was designed to test all strength characteristics after four different aging periods (60 d, 120 d, 210 d, and 360 d) to evaluate the material performance over time. However, the strength measurements on aged material samples were conducted for #3 rebars only because a potential degradation (most significant on the outer surface) would lead to most severe effects in smaller specimens as the percentage of the affected rebar cross section would be maximized (as compared to the other two rebar sizes tested in this study). In addition, it was the goal to test only two physical characteristics (moisture absorption and microstructure observations) after aging because the fiber content and the cross-sectional dimensions were not expected to change due to saltwater exposure.

### 4.2.1 Virgin Material Properties

The unaged GFRP rebars were experimentally tested as summarized in Table 4.1. The four physical proper-

Table 4.1: Conducted test methods to evaluate virgin material properties of GFRP rebars

Bar		Lot	Property <sup>†</sup>	Test
Type	Size			Method <sup>†</sup>
A, B, C	#3, #5, #6/#8	1, 2, 3	Cross-sectional area	ASTM D 798
			Fiber content	ASTM D 2584
			Moisture absorption / mass change	ASTM D 570
			Transverse shear properties	ASTM D 7617
			Horizontal shear properties	ASTM D 4475
			Tensile properties	ASTM D 7205
	#3	1	Bond to concrete strength	ACI 440.3R, B.3
	#8	1	Microstructure observation <sup>‡</sup>	SEM <sup>‡</sup>

<sup>†</sup> Each test was repeated three times for each lot, bar type, and size

<sup>‡</sup> Only one specimen for each bar type and size were tested

ties that were tested included cross-section dimensions, fiber content, moisture absorption, and microstructure observations via scanning electron microscopy (SEM). SEM analysis targeted two distinctive locations: GFRP rebar resin-fiber interface and the concrete-GFRP rebar surface interface. The strength properties that were tested for this study included the transverse shear strength, horizontal shear strength, tensile strength (and elastic modulus), and the bond-to-concrete strength. Three test repetitions from three different GFRP production lots resulted in a total of nine test repetitions for each selected GFRP rebar size per the test standards (as referenced in Table 4.1). This led to a total specimen count of 522 for the experiments conducted on virgin rebars. Testing GFRP specimens from different production lots provided quality assurance of the manufacturing process of the GFRP bar. The results from the tests listed in Table 4.1 (on virgin materials) provided benchmark values for the GFRP rebars and constituents properties including the resin, fibers, surface enhancement properties, and microstructure to reflect the quality of the pultrusion process. In addition, the obtained results were used as 100 %-reference values for a comparison against the material properties measured after exposure to harsh saltwater environments.

### 4.2.2 Material Properties after Saltwater Exposure

GFRP rebars from the first lot were aged via different accelerated conditioning protocols (ACP), by exposing specimens to saltwater from Key Biscayne to resemble the aggressive marine environment that is common in Florida, which often attacks substructures of FDOT-owned infrastructure. As seen in Table 4.2, the ACP included three temperatures at 23 °C, 40 °C, and 60 °C (74 °F, 104 °F, 140 °F) and four different time periods

(60 d, 120 d, 210 d, and 360 d). These temperatures were chosen because 23 °C reassembled standard labo-

Table 4.2: Conducted test methods to evaluate material properties of GFRP rebars after saltwater exposure

Bar		Exposure	ACP		Property <sup>†</sup>	Test Method <sup>†</sup>			
Type	Size		Temp				Days		
			°C	°F					
A, B, C	#3	Saline Solution	23, 40, 60	74, 104, 140	60, 120, 210, 365	Moisture absorption / mass change	ASTM D 570		
						Transverse shear properties	ASTM D 7617		
								Horizontal shear properties	ASTM D 4475
								Tensile properties	ASTM D 7205
								Concrete bond strength	ACI 440.3R, B.3
								Microstructure observation <sup>‡</sup>	SEM <sup>‡</sup>

<sup>†</sup> Each test was repeated three times for each bar type and size (randomly chosen from the first lot)

<sup>‡</sup> Only one specimen for each bar type and size was tested

ratory conditions, 60 °C is most commonly used in accelerated conditioning protocols for FRP rebars (Chen et al., 2007; Benmokrane et al., 2017) for aging of GFRP rebars in alkaline water, and 40 °C because it provided reference values in between. It was the ultimate aim to model long-term durability of the GFRP rebar based on the Arrhenius model (see Chapter 6), and therefore, the temperatures and exposure duration listed in Table 4.2 were selected to produce sufficient and extensive data for the model. Likewise, because it was the goal to establish a multi-property model based on various material characteristics, the four strength characteristics tested for the virgin materials were all evaluated for material specimens exposed to the AAP. To simulate a combined aggressive environment that included the salinity of saltwater and the high alkaline of saturated concrete, bond-to-concrete specimens were also prepared and tested via the pullout method.

### 4.3 Materials: Glass FRP Rebars

As mentioned above, GFRP reinforcement bars from three different manufacturers (Hughes Brothers, ATP S.r.L., and Marshall) were tested for this project to evaluate rebars with different (but comparable) characteristics. As extensively shown in Appendix B, the rebar had different shapes and surface properties. The following Table 4.3 provides a general overview of the differentiating aspects of the evaluated products and the naming convention used for this project. The “Aslan” rebars were named Type-A and were characterized as a round, solid GFRP bar with sand coating and helical wraps for surface enhancement to ensure proper bond to concrete. These bars were made from E-CR glass and vinyl-ester. Type-B (“ATP”) rebars were also solid and round, but the surface was enhanced via helical wraps (without any sand coating). This

Table 4.3: GFRP rebar materials — Physical features

ID	Name	Cross Section	Surface Enhancement	Material	
				Resin	Glas
Type-A	Aslan	Round and Solid	Helical Wraps + Sand Coating	Vinyl-Ester	E-CR Glass
Type-B	ATP	Round and Solid	Helical Wraps	Vinyl-Ester	E-CR Glass
Type-C	C-Bar	Oval and Solid	Rips	Vinyl-Ester	E Glass

composite rebar was also made from E-CR glass and vinyl-ester. Marshall produces the “C-Bar” with a solid cross-section that is oval and not perfectly round. This product was named Type-C for the purpose of this research paper and it used helical ribs like traditional steel rebars — without any sand coating — for the surface enhancement. As seen in Table 4.3, the only commonality between these three products was the resin (vinyl-ester), however, the individual source materials per manufacturer remain unknown (proprietary information) and it cannot be assumed that the same materials were used (although the same material types were used by all three manufacturers). The following Figure 4.2 provides an overview about the physical features of the three tested products, exemplified for # 3 rebars. Figure 4.2a shows the combination of sand

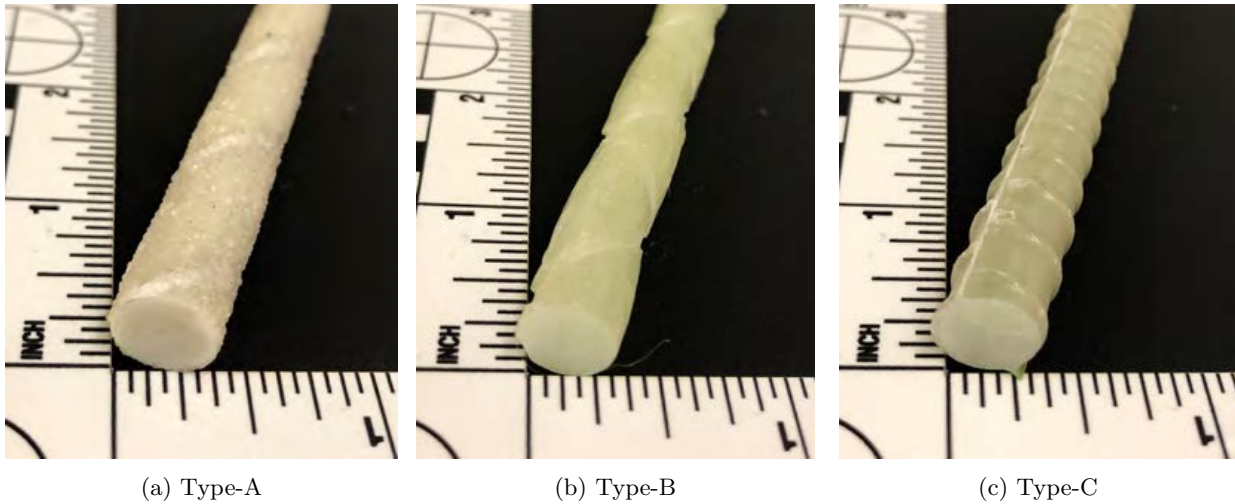


Figure 4.2: Cross-sectional features of tested GFRP rebar products

and helical fiber as surface enhancement for Type-A rebars, while Figure 4.2b illustrates the doubled helical wraps that signified Type-B rebars. The ribs and oval cross section of Type-C rebars is shown in Figure 4.2c.

The mechanical properties — as reported by the manufacturers — for the evaluated GFRP reinforcement bars are shown in Table 4.4. The numbering system for the GFRP rebars follows the standard convention and referred to the diameter, in which the number describes the nominal diameter in  $\frac{1}{8}$  in. increments, such that a # 8 rebar has a nominal diameter of 1 in. Therefore, the rebars # 3 ( $\frac{3}{8}$  in.) had a nominal cross-sectional area of  $71.0 \text{ mm}^2$  ( $0.110 \text{ in.}^2$ ), while # 5 ( $\frac{5}{8}$  in.) had a nominal area of  $197.9 \text{ mm}^2$  ( $0.307 \text{ in.}^2$ ). However, due to the different deformations on the outer surface for bond enhancement and due to different



Table 4.4: GFRP rebar materials — Mechanical Properties (reported by the manufacturers)

Size	ID	Unit Weight		Load Capacity		Max. Stress		Elastic Modulus		Ultimate Strain
		$\frac{\text{kg}}{\text{m}}$	$\frac{\text{lbs.}}{\text{ft}}$	kN	kip	MPa	ksi	GPa	$10^6$ psi	%
# 3	Type-A	0.174	0.117	58.7	13.20	827.4	120.0	46.0	6.70	1.79
	Type-B	0.190	0.128	58.9	13.24	830.0	120.4	40.0	5.83	1.50
	Type-C	0.148	0.100	59.6	13.40	840.0	121.0	42.0	6.00	2.00
# 5	Type-A	0.427	0.287	143.4	32.24	724.0	105.0	46.0	6.70	1.57
	Type-B	0.440	0.296	143.5	32.24	725.0	105.2	40.0	5.83	1.50
	Type-C	0.416	0.280	154.4	34.71	780.0	113.0	40.0	5.83	1.95
# 6	Type-C	0.610	0.410	406.6	91.40	644.7	93.5	47.6	6.91	1.61
# 8	Type-A	1.012	0.680	314.3	70.65	620.0	89.9	44.8	6.50	1.34
	Type-B	1.060	0.712	426.0	95.77	802.0	116.3	48.0	6.96	1.66

production methods, these numbers are not reliable for GFRP rebars and actually differ from manufacturer to manufacturer. Likewise, some manufacturers produce rebars above the actual nominal diameter and others produce below the reported nominal diameter. Hence, the actual dimensions should be measured and experimentally determined. Although all bars were made from similar raw materials, like E- or E-CR glass and vinyl-ester, each product had a different unit weight. But while the selected # 3 rebars had different unit weights, their load capacity and maximum tensile stress were comparable. According to the manufacturers, each # 3 product had a guaranteed load capacity of approximately 59 kN (13 kip) and a maximum tensile strength of about 830 MPa (120 ksi). As shown in Table 4.4 the larger rebars had a higher guaranteed load capacity than the smaller rebars (per manufacturer) because the larger cross sections fit more fibers. However, their ultimate tensile strength was reported with lower values (due to the shear-lag phenomena). While Type-A and Type-B rebars had a similar load capacity of approximately 143 kN (32 kip) and a maximum tensile strength of about 725 MPa (105 ksi) according to the manufacturer, the load capacity, and hence, the tensile strength of the # 5 Type-C was about 8% higher. The elastic modulus was different for each product, but seemed not to differ significantly between the rebar size within each manufacturer. The Type-A rebars had a reported elastic modulus of 46 GPa ( $6.70 \times 10^6$  psi), while it was about 40 GPa ( $5.83 \times 10^6$  psi) for the Type-B rebars and the Type-C bars. From the table it can be seen that the manufacturer reported ultimate strain values generally decreased with increasing bar size (per manufacturer). Finally, it is noted that none of the manufacturers officially reported the shear strengths of their products.

## 4.4 Equipment and Test Devices

This section details all test devices and equipment components that were necessary to prepare the specimens and to conduct each test. The following subsections provide general information and specifics for each tool, machine, test fixture, and other device that was used throughout this project. The usage of all these test

devices for the specimen preparation and the experimental procedures are explained step by step in a later Section 4.5 to describe how these devices were required to complete the experimental procedure for each individual test.

#### 4.4.1 Cutting Saw

The GFRP rebars samples that were provided by the manufacturers had a length of about 152 cm (60 in.). A saw was used to cut the raw materials to the required specimen lengths. The saw was a “heavy-duty single-bevel compound miter saw” that featured a machined base frame to ensure a straight cut. To provide a save and comfortable working position, the saw was placed on a level and stable working table as it is shown in Figure 4.3. A wooden template was designed to ensure a fast workflow while obtaining consistent



Figure 4.3: Miter saw used to cut raw materials to specimen length

lengths between individual specimens. Furthermore, the template ensured that the cut was properly angled with  $90^\circ$ , relative to the longitudinal axis of the rebars. It was fixed on the base frame of the saw via clamps and bolts, as shown in Figure 4.3, to avoid any movements of the template, and to prevent varying specimen lengths or different cutting angles. The round blade that was used to cut the GFRP was a diamond disk, which was designed for general-purpose cutting. This kind of saw was chosen to ensure a precise and clean cut specimen. Figure 4.4 shows the saw blade “Diamond Montage Y1-2 Series” before and after it was mounted to the saw according to the manufacturer’s instructions. Because the saw dust caused by the cutting process can be dangerous for human health (especially when cutting glass fibers), protective equipment (respiratory



(a) Diamond blade



(b) Diamond blade mounted to miter saw

Figure 4.4: Saw blade

masks, eye wear, and ear protection) was worn at any time the saw was used for this research project. While this kind of cut was sufficient to prepare the GFRP rebars for tensile strength testing, the specimens that were created to evaluate the physical properties of GFRP rebars (cross-sectional dimensions, fiber content, moisture absorption, and SEM) had to be further cut with a more precise instrument (cf. Subsection 4.4.2) to achieve a higher length precision.

#### 4.4.2 Precision Saw

A precise cut was required to ensure maximum accuracy of diameter results. To prepare a specimen of known length within plus/minus one thousandths of an inch, a precision saw was needed. The model used for this research was a “IsoMet 1000 Precision Cutter”<sup>1</sup> (shown in Figure 4.5) produced by Buehler (see Figure 4.5). It was designed to precisely cut various types of materials without significant deformation along the cut surface. The saw was equipped with a 5 in. (127 mm) diameter diamond blade, which allowed it to cut GFRP material. Because the friction between blade and specimen produced significant heat during cutting, the blade was partially submerged in a water bath for cooling. As it is shown in Figure 4.5, the machine was equipped with a “Sample Arm” to support the sample during the cutting process. To reduce deformation throughout the cutting process, the saw was designed with a gravity-fed system, in which the samples were simply guided over the blade via gravity (the specimen fell onto the blade, and not vice versa). However, the contact pressure was adjustable and could be increased through the addition of load to the lever arm, that was connected to the sample arm (see Figure 4.5). The control panel in the front of the machine had

<sup>1</sup> Information retrieved on April 15, 2017  
from: <https://www.buehler.com/Spanish/Brochures/English/Sectioning/IsoMet1000Brochure.pdf>

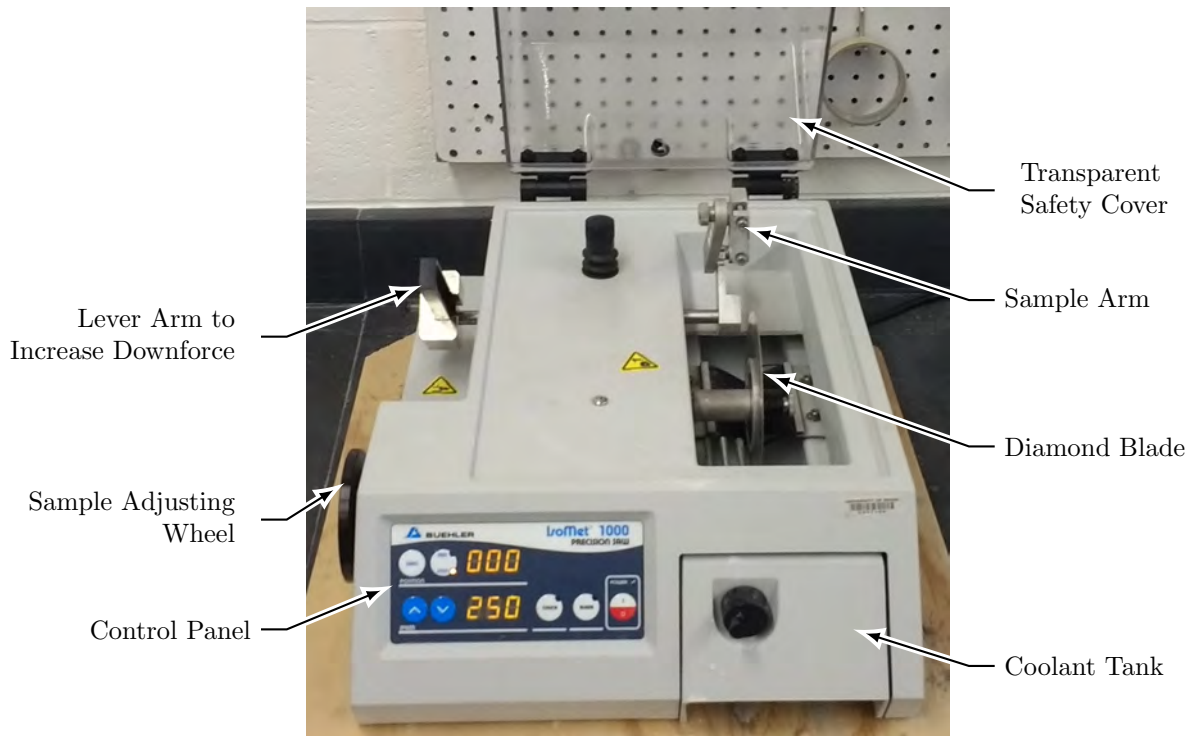


Figure 4.5: Precision saw

two LED displays to show the cutting length and the blade speed. While the blade speed (the saw offered blade speeds from 100 rpm to 975 rpm) was set through the bottom left buttons next to the display, the black wheel on the left hand side of the machine was used to adjust the length that was desired for the sample after the cutting process. The cover served as a splash guard to keep the water inside the self-contained coolant system. This saw was used to precisely prepare the GFRP specimens for all experiments that relied on accurate length measurements (fiber content, cross-sectional properties, moisture absorption). Although the saw cut the samples to a precise length, it was necessary to measure and verify the exact length of the sample with a caliper (see next paragraph) to use true length values when using and determining geometric properties.

#### 4.4.3 Caliper

To determine the exact measurements of the specimens, a digital caliper was used. Figure 4.6 shows the “Fowler” electronic caliper that was used to measure the precise lengths — within 0.01 mm (0.00039 in.) precision — of all tested rebar samples that were precision cut for the physical properties experiments. This specific caliper met the requirements for all applicable ASTM test methods in this project. The instrument was calibrated prior to the experimental phase, and it was properly nulled before each measurement.



Figure 4.6: Electronic caliper

#### 4.4.4 Precision Balance

The balance used for this project was a “Nimbus Precision Balance NBL 623e” produced by Adam Equipment Inc., and had a maximum capacity of 620 g. It featured a readability of 0.001 g ( $2.205 \times 10^{-6}$  lbs.) and it operated with a repeatability of 0.002 g ( $4.409 \times 10^{-6}$  lbs.), matching the requirements of ASTM D792 (ASTM International, 2013). As it is shown in Figure 4.7, the balance was equipped with a level indicator to ensure a proper and balanced setup for optimum measurements. Furthermore, this scale was equipped with a transparent and removable draft shield to reduce erroneous readings that may result from air flow. Because the included shield was not sufficient to accommodate the desired applications for this project, a customized extension was produced with 3D-printing technology. The measuring pan had a diameter of 160 mm (6.3 in.) and was made of grade 304 stainless steel to allow swift cleaning. A large LCD display and several operating keys were located on the control panel of the scale. Before measurement, the scale reading was tared (or nulled) via the button on the lower left, next to the level indicator<sup>2</sup>. The stabilization time of the balance was three seconds. A wave symbol was displayed on the LCD screen if the measurement pan was stable, so that the reading could be accurately obtained.

#### 4.4.5 Drying Oven

A drying oven was used to condition all small-size specimen that were designated for the characterization of physical rebar properties (cross-sectional dimensions, fiber content, moisture absorption, and SEM). The VWR Scientific Products Oven Model 1690 that was used is shown in Figure 4.8. This piece of equipment was set to maintain a temperature of 50 °C (120 °F) for all specimen conditioning purposes. Compartment boxes (see Figure 4.9) were used to store and organize the specimens inside the oven. To monitor the humidity inside the drying oven and the laboratory during testing, an AcuRite Humidity and Temperature Monitor

---

<sup>2</sup> Information retrieved on April 16, 2017  
from: <https://www.adamequipment.com/nbl-623e>

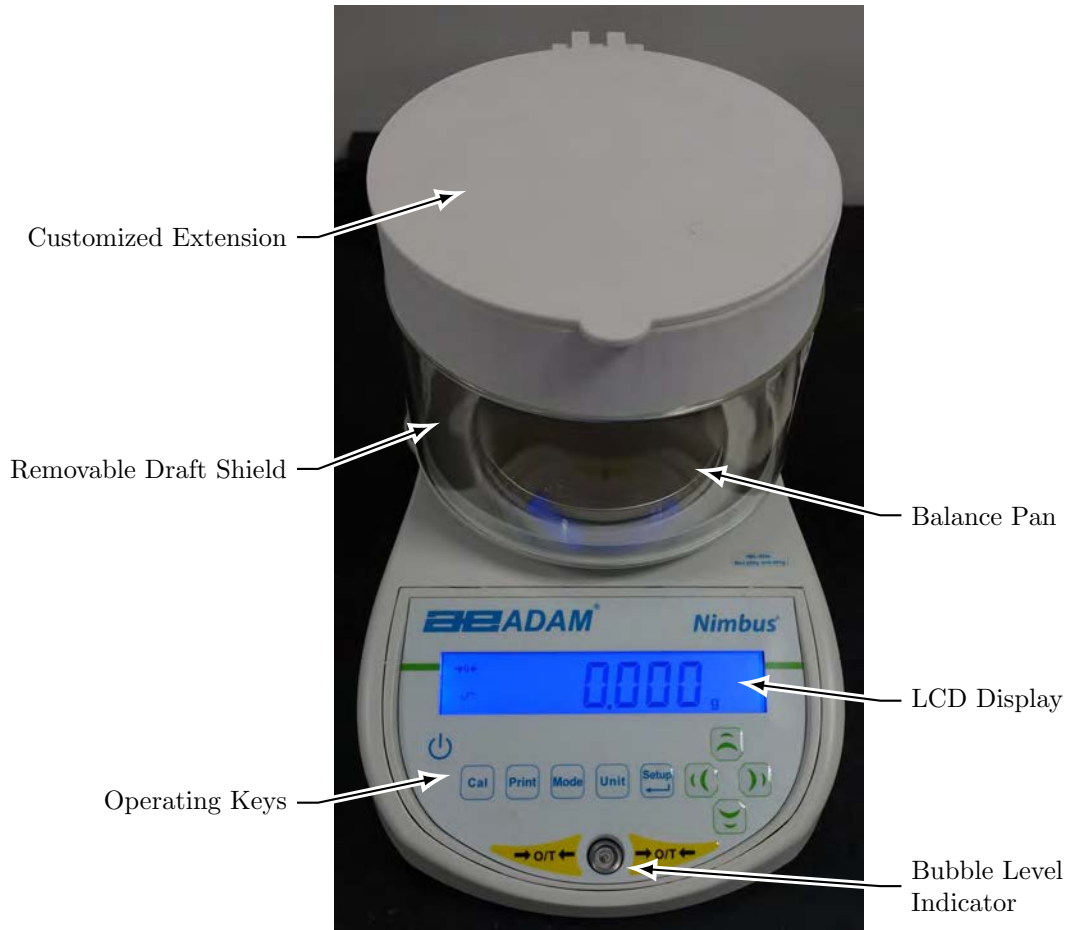


Figure 4.7: Precision scale, used to meet ASTM D792–13 requirements

was used. If the humidity did not reside within the limitations prescribed by ASTM (of the relevant test procedure), the experiment was not conducted and the specimens remained in the oven until all parameters were satisfying.

#### 4.4.6 Muffle Furnace

The furnace, a Thermo Fischer Scientific Instrument, was used for experiments with high temperature requirements. It aided in the characterization of the fiber contents for the tested FRP rebars because it reached the required temperatures for those experiments and was capable of holding the temperature at high levels for continued time periods. The furnace used in this research project is shown in Figure 4.10. While Figure 4.10a shows the furnace as it appears throughout an experiment, Figure 4.10b illustrates the heat resistant specimen holders inside the burning chamber. The device was equipped with an integrated scale that provides weight readings throughout the heating process. The metal cages (specimen holders) sat on a baseplate that was held in place by four ceramic tubes that were connected to the scale underneath the chamber. The cages were used to hold an array of  $3 \times 3$  crucibles, which were filled with individual rebar



Figure 4.8: Drying oven VWR Scientific Products Oven Model 1690



Figure 4.9: Conditioning container for small-size specimens

specimens. Thermocouple wire type K were connected to an Omega thermocouple temperature readout and inserted into the furnace chamber to monitor the precise temperature inside the chamber throughout the experiments.

#### 4.4.7 Scanning Electron Microscope

A Scanning Electron Microscope (SEM) is a microscope that operates under high vacuum and with an electron beam to analyze materials. It mainly consists of two parts: A vacuum chamber and a sample chamber, which are shown in Figure 4.11. The vacuum chamber contains all instruments necessary to produce the electron



(a) Instrument overview



(b) Heat resistant metal cages inside burning chamber

Figure 4.10: Muffled furnace used for high temperature experiments (fiber content)

beam, which is focused onto a specimen placed inside the sample chamber. As soon as the electron beam reaches the specimen, it generates different kinds of electrons and X-rays, which are recognized by several detectors located inside the chamber such as an LEI detector, an SEI detector, and an EDS detector. Software connected to the microscope and the detectors analyzes the electrons and X-rays to obtain information on optical and chemical features of a specimen.

The SEM model used in this research project (see Figure 4.11) was a JEOL JSM-7401F Field Emission Scanning Electron Microscope (FESEM) and had a supplemental EDS system from EDAX. The microscope magnified objects up to  $1\,000\,000\times$  of its original size. The maximum resolution was 1.0 nm at an accelerating voltage of 15 kV, and 1.5 nm at 1 kV. The accelerating voltage ranged from 0.1 kV to 30 kV.

The vacuum chamber provided the needed vacuum for operation and contained an electron field emission gun and various lenses. A sample, detectors, and cameras were located in the sample chamber, which was able to hold a specimen of 50 mm (2 in.) diameter. To determine the various electrons, the JSM-7401F had three electron detectors: an SEI detector, an LEI detector, and a retractable backscattered electrons detector (RBEI). The microscope and detectors were operated through the workstation shown in Figure 4.12. The interlock chamber on the left is the device that holds the specimen before it is loaded inside the sample chamber by using the lever and the control buttons. The *Z knob* on the right outer part of the SEM enables adjustments of the Z position (the vertical position) of the specimen inside the sample chamber. The left side of the figure shows the screen of the computer, the control panel, and the joystick to run the image analysis.



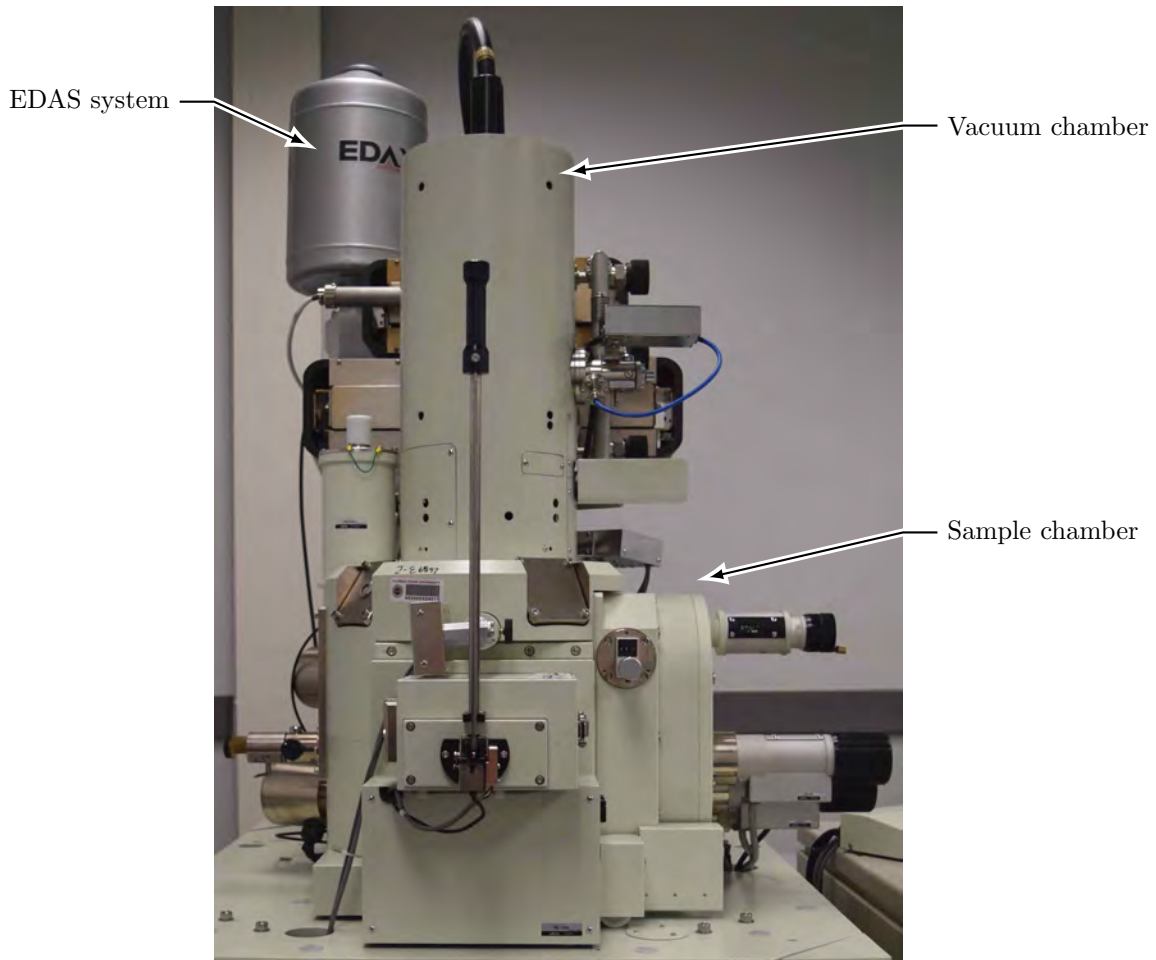


Figure 4.11: Scanning Electron Microscope — JEOL JSM-7401F

To operate the SEM or EDS and to analyze the detected electrons and X-rays, two different software packages were used. While EOS 7401 software was connected to the SEM to operate the SEM along with the LEI and SEI detector, Genesis software was linked to the EDS detector to control the detection and analysis of X-rays. X-rays were detected by the EDS system equipped with a thin polymer window and analyzed through a Genesis software package<sup>34</sup>.

#### 4.4.8 Sputter Coater

Before using the SEM, all specimens were coated to establish a conductive layer of gold or palladium on their surface. The SC7640, a sputter coater from Quorum Technologies Ltd., was applied. The sputter coater seen in Figure 4.13 was comprised of two parts: A cabinet assembly and a vacuum chamber. The front panel of the cabinet assembly was the part containing the switches and meters for operating the sputter coater. It

<sup>3</sup> Information retrieved on December 29, 2016  
from: <http://imel.demokritos.gr/docs/SEM-FACILITY.pdf>

<sup>4</sup> Information retrieved on December 29, 2016  
from: <http://www.jeol.co.jp/en/science/sem.html>

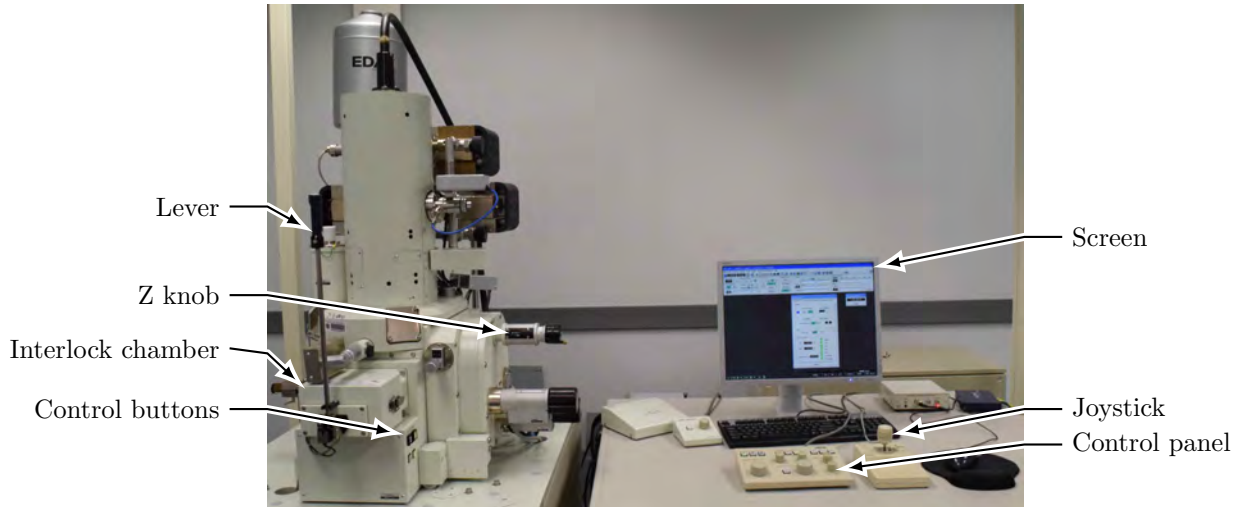


Figure 4.12: Scanning Electron Microscope — Work station

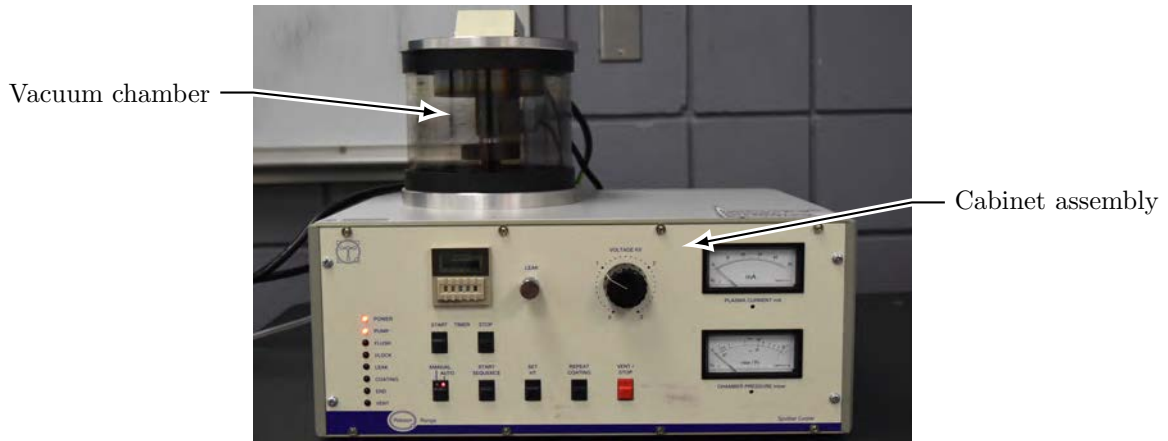


Figure 4.13: Sputter coater SC7640

also held a high voltage power supply, vacuum gauging, and manifold. The vacuum chamber consisted of a baseplate, which held specimens during the operation, along with a glass work chamber, which secured the chamber vacuum, and a top plate, which supported a cathode and ensured electrical and gas connections<sup>5</sup>.

#### 4.4.9 Load Frame

To test GFRP rebars for strength characteristics and engineering properties, a displacement controlled test frame was required. Accordingly, tests were conducted at both the High Performance Material Institute (HPMI) in Tallahassee, and at the Structures and Materials Laboratory (SML) at the University of Miami (Miami, Florida). An overview of the test machine and the laboratory setup at the High Performance Material Institute is shown in Figure 4.14. The load frame was a “MTS Landmark” Testing System (floor

<sup>5</sup> Information retrieved on December 15, 2017  
from: [https://www.quorumtech.com/\\_assets\\_/pdf/Manuals/OM-SC7640-Issue-3.pdf](https://www.quorumtech.com/_assets_/pdf/Manuals/OM-SC7640-Issue-3.pdf)

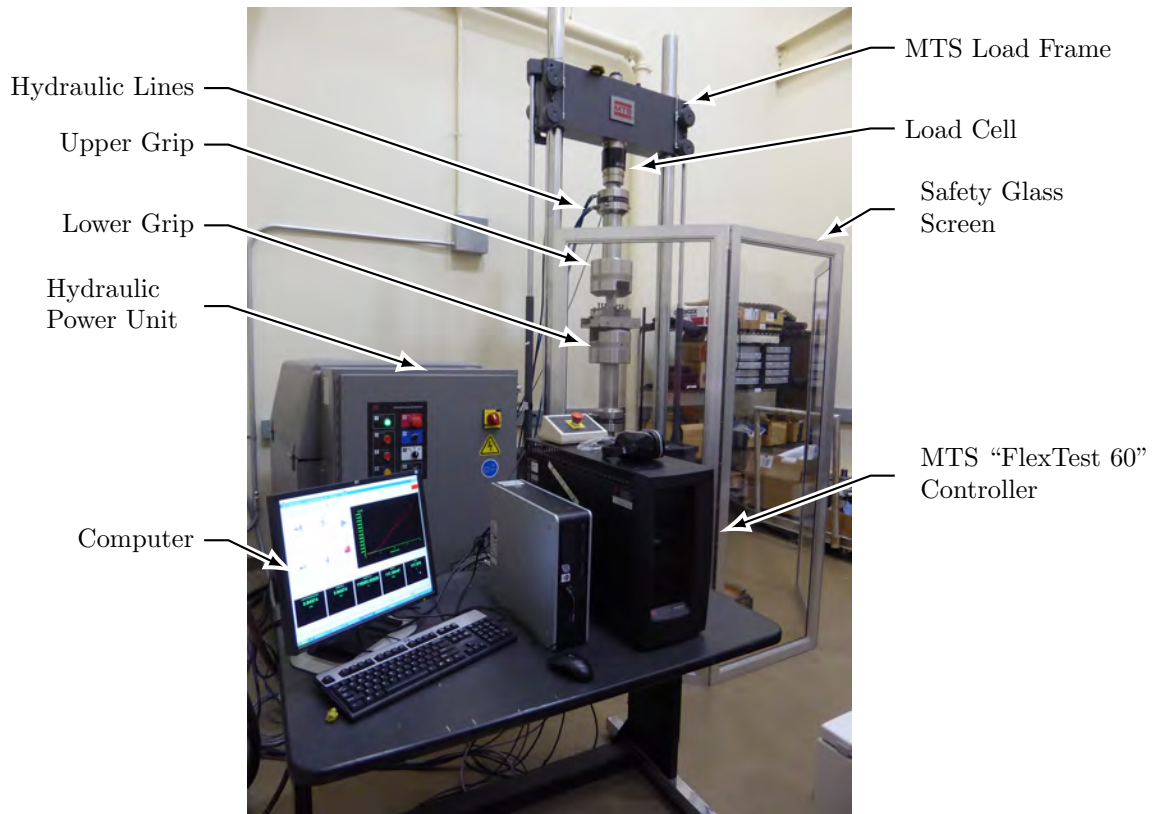


Figure 4.14: Load frame and laboratory setup for rebar strength tests

standing), model “370 Load Frame,” which was manufactured in 2009 and had a maximum capacity of 500 kN (126 000 lbs.). It had a vertical test space of 2002 mm (78.8 in.)<sup>6</sup>. The properly calibrated machine had a load measuring system (load cell) with a precision of  $\pm 1\%$  of the measured load. The hydraulic power unit was a detached system (to the left of the load frame) that provided the hydraulic pressure to drive the actuator (behind the computer) — which applied the load to the specimens — and the grips. Accordingly, several hydraulic lines were used to supply the hydraulic pressure from the power unit to the load frame components.

To sustain the high forces needed for tensile testing of GFRP rebars, the machine was equipped with heavy Model 647.50A grips, which were able to carry a static force of 550 kN (126 000 lbs.) and applied a clamping pressure of up to 69 MPa (10 ksi)<sup>7</sup>. The wedges inside the grip mechanism had a width of 4 in. (101.6 mm).

The load and/or displacement applications for the load system were controlled via a MTS “FlexTest 60” Controller, which was connected to all sensors, hydraulic, and electrical components, to properly drive the test and to collect the raw data. Furthermore, the controller was connected to the computer and to the MTS manual control panel to operate the machine and to monitor the test procedure. The manual control panel

<sup>6</sup> Information retrieved on April 3, 2017 from: [https://www.mts.com/cs/groups/public/documents/library/dev\\_004324.pdf](https://www.mts.com/cs/groups/public/documents/library/dev_004324.pdf)

<sup>7</sup> Information retrieved on April 3, 2017 from: [https://www.mts.com/cs/groups/public/documents/library/dev\\_003419.pdf](https://www.mts.com/cs/groups/public/documents/library/dev_003419.pdf)

shown in Figure 4.15 was used to adjust the position of the cross bar (depending on the specimen dimensions) and to open or close the grips with the desired pressure. Therefore, the panel had several switches to move



Figure 4.15: MTS load frame control panel

or lock the crossbar, and to control the grips. A handset (next to the control panel) was used for fine adjustments. It was equipped with a control wheel to adjust the position of the actuator cylinder and to control the load or displacement rate. The computer system illustrated in Figure 4.14 featured the “MTS TestWorks 4” software to control and operate the load and displacement settings from the workstation. The software interface allowed an accurate operation of the machine, including the definition of test parameters and live monitoring of test results as displayed in the following Figure 4.16. In addition, the program had an

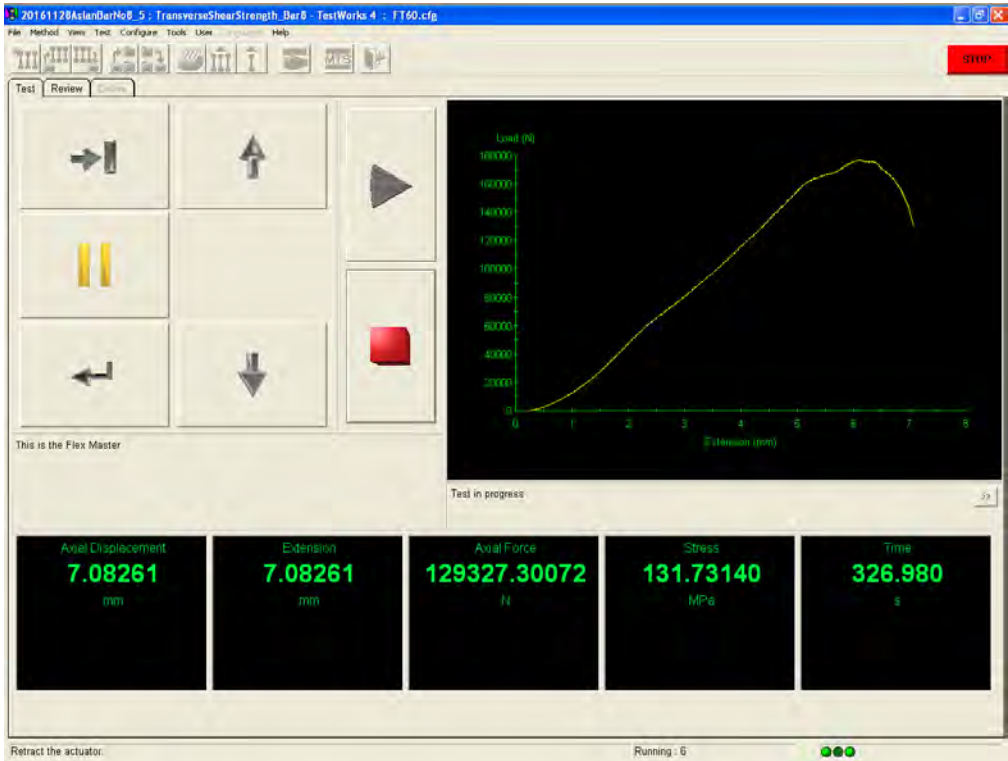


Figure 4.16: MTS test works interface — Used to control all strength test experiments

export function to retrieve the acquired raw test data and (if applicable) post-processed data.

At the University of Miami, a different test frame as part of the Structures and Materials Laboratory was used. Specifically, a Baldwin testing machine with a capacity of 890 kN (200 000 lbs.) was used for all strength experiments conducted in Miami. The load cell was calibrated prior to the testing process to reach a precision of  $\pm 1\%$ . This frame was screw driven and the test load was controlled through an MTS interface using the “MTS TestWorks 4” software (identical to the one used at the HPMI in Tallahassee, Florida), which operates the load and displacement settings from the workstation.

In both testing labs, an extensometer was used to measure localized displacement data for calculating strain values (for specimens tested in tension). Figure 4.17 shows the used MTS model 634.12-25 extensometer. This extensometer was properly calibrated to the machine by a certified service technician, one week



Figure 4.17: MTS extensometer for tensile tests

prior the first test runs.

#### 4.4.10 Test Fixture for Transverse Shear Tests

The fixture for the transverse shear test was built at the FAMU-FSU College of Engineering Machine Shop according to ASTM D 7617 (ASTM International, 2011c), to accommodate the test principle schematically explained in Figure 4.18. It can be seen that ASTM D7617 (ASTM International, 2011c) relies on the double shear principal and that the rebar is transversely separated at two surfaces. Accordingly, the maximum load measured in this experiment must be divided by two to determine the actual transverse shear strength. As this test directly cuts the rebar perpendicular to the longitudinal fibers, the measurement results are an indicator for the quality of the rebar fibers (whereas the horizontal shear strength test is an indicator for the quality of the resin).

The individual components of the transverse shear test fixture consisted of two V-form bar seats, two

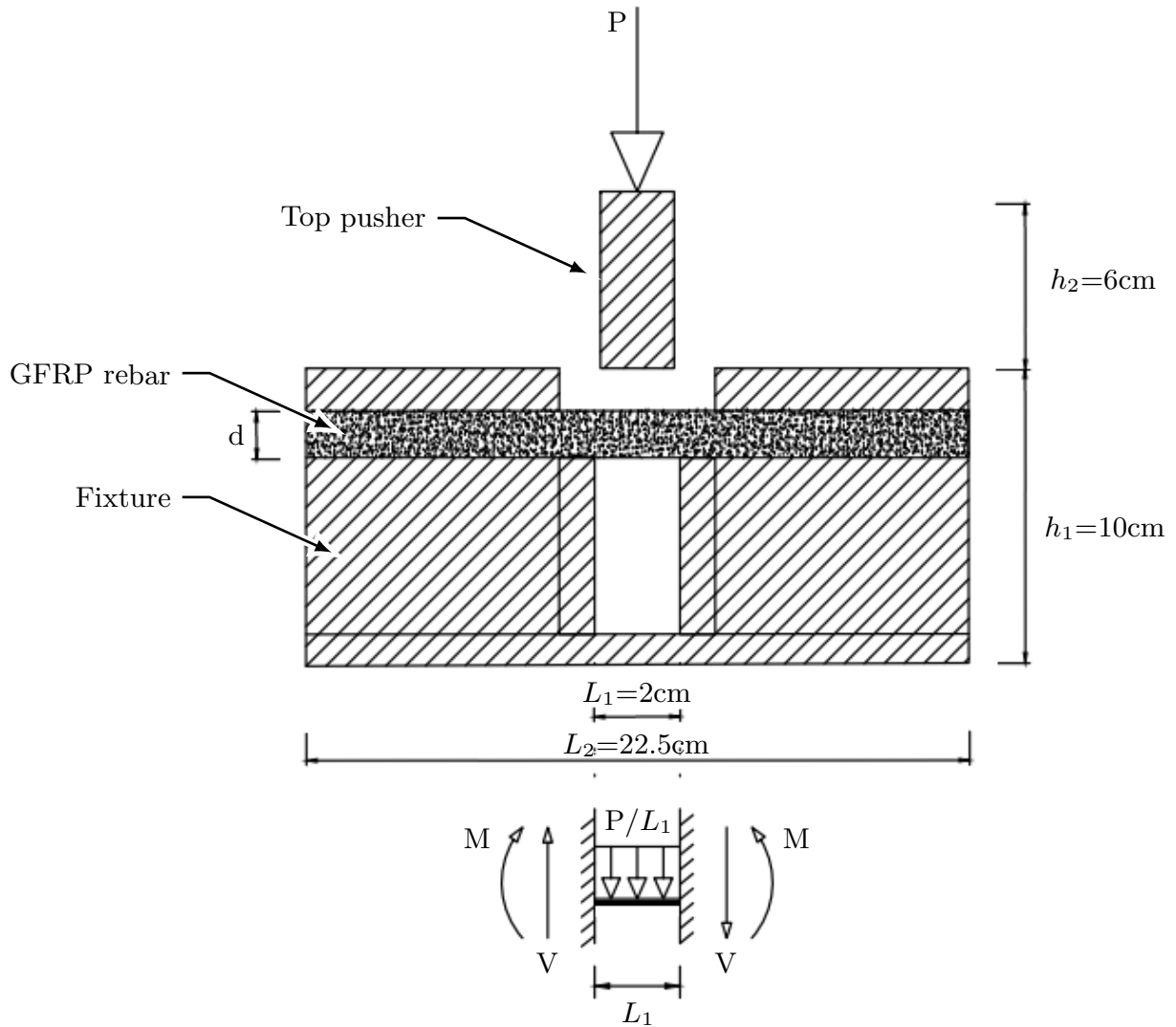


Figure 4.18: Transverse shear test concept

straps, two lower blades, an upper blade, and two guides machined from steel, as shown in Figure 4.19. The upper and lower blades were hardened to a 55 to 58 type C Rockwell hardness. This heat treatment increased the performance of the shear blades and avoided fast deterioration from mechanical aberrations, such that the fixture can be used for future applications. In total, four different sets of blades were produced to accommodate all four rebar diameters (#3, #5, #6 and #8) that were within the scope of this project. The bar seats, the two lower blades, and the two guides were transversely bolted together with two threaded rods, washers, and nuts. Between the lower blades and the guides, thin shims were placed to ensure that the upper blade fitted properly between the two lower blades. These shims were made of paper and fixed to the guides with tape to avoid having to hold the shims in place during disassemble of the fixture as the nuts and bolts had to be loosened after each test. The top two straps were also bolted to the bar seats using four bolts for each of them. Both straps held three alignment screws along the centerline (parallel to the rebar)

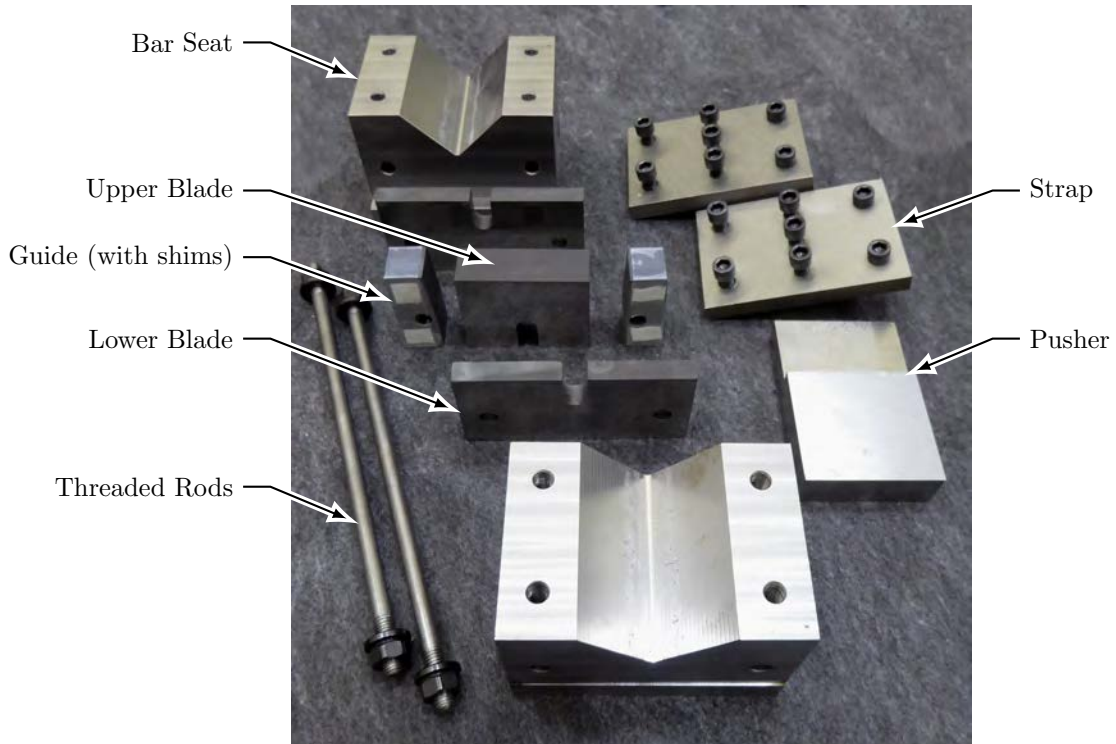


Figure 4.19: Transverse shear test fixture — Individual components

to clamp the specimen down and to hold it in place during testing. The fixture was mounted to the load frame via a stainless steel T-plate (shown in Figure 4.20a) that was clamped and supported by the bottom grip as seen in Figure 4.20b. After the T-plate was properly mounted, the test fixture was centered on top of base plate, so that the center/top shear blade was inline with the center of thrust of the load frame. The fixture was held in place via transverse screws to guarantee a proper and equal alignment for all tests. The upper blade was loosely placed on top of the bar before testing. The upper blade was not directly clamped to the top grip of the MTS machine; instead, it was pushed by an additional steel plate that was directly wedged between the MTS top grip. This pusher plate was minutely smaller than the upper shear blade (1 mm (0.04in.) all around), to ensure a perfect load transfer at the contact surfaces or at the compression interface. The following Figure 4.21 shows the assembled fixture in its final setup.

In Figure 4.21b, it can be seen that the top blade plate sat loosely on the rebar and that the top pusher was just about to make contact with the blade before the test was started. Then, the force was steadily increased until the rebar was “cut”, producing a transverse shear failure in the GFRP rebar, along both cutting planes. At the completion of the test, the blade was completely pushed through the specimen and the top pusher plate was lowered into the transverse shear test fixture, similar to Figure 4.21a. This setup was used to conduct all transverse shear strength tests for this project.



(a) Steel T-plate



(b) Mounted in load frame

Figure 4.20: Transverse shear test fixture — T-plate support

#### 4.4.11 Test Fixture for Horizontal Shear Tests

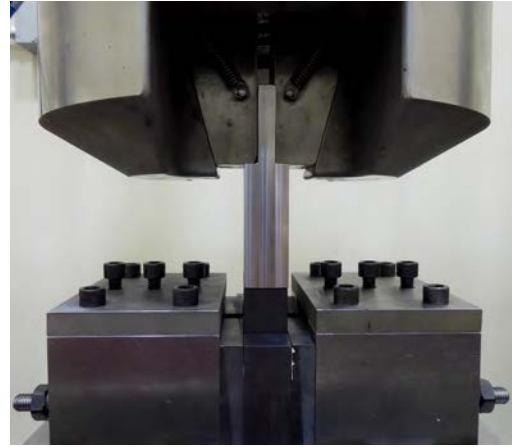
The fixture for the apparent horizontal shear test was built according to ASTM D 4475–02 (ASTM International, 2008a), to accommodate the test methodology schematically detailed in Figure 4.22. While the test setup resembles a three-point bending test, the objective was not to reach bending failure, but to produce horizontal shear to test the quality of the resin. To achieve this kind of failure, a small span-to-diameter ratio was selected; as proposed by ASTM D4475 (ASTM International, 2008a), the span-to-diameter ratio was chosen with 5 to 1. Accordingly, higher horizontal shear stresses than bending stresses were obtained, leading to inter laminar shear failure as detailed in Figure 4.23. As shown in the figure, these internal forces produce horizontal shear stresses parallel to the longitudinal axis of the tested rebar.

To accommodate ASTM D4475 (ASTM International, 2008a) requirements and to guarantee repeatable results, a horizontal shear test fixture was built with the components shown in Figure 4.24. The fixture itself, consisted of two bar supports and a loading nose built on a steel beam. Both the loading nose, as well as the two bottom supports, were suitable hardened steel rods with a groove in the middle to fit the individual rebar sizes. These steel rods were held in place, with the help of a spring on each side of the rod. According to ASTM guidelines, each rebar diameter requires specifically sized rollers with a defined groove for the rebar — at the bottom two supports and at the center load point. Therefore, four (4) sets of three (3) of these rollers were built, to accommodate the four (4) different bar diameters that were tested within the scope of this research project (see test matrix). The adjustable supports were slid onto the steel beam that





(a) Alignment of test fixture



(b) Test in progress

Figure 4.21: Transverse shear test fixture — Final test setup

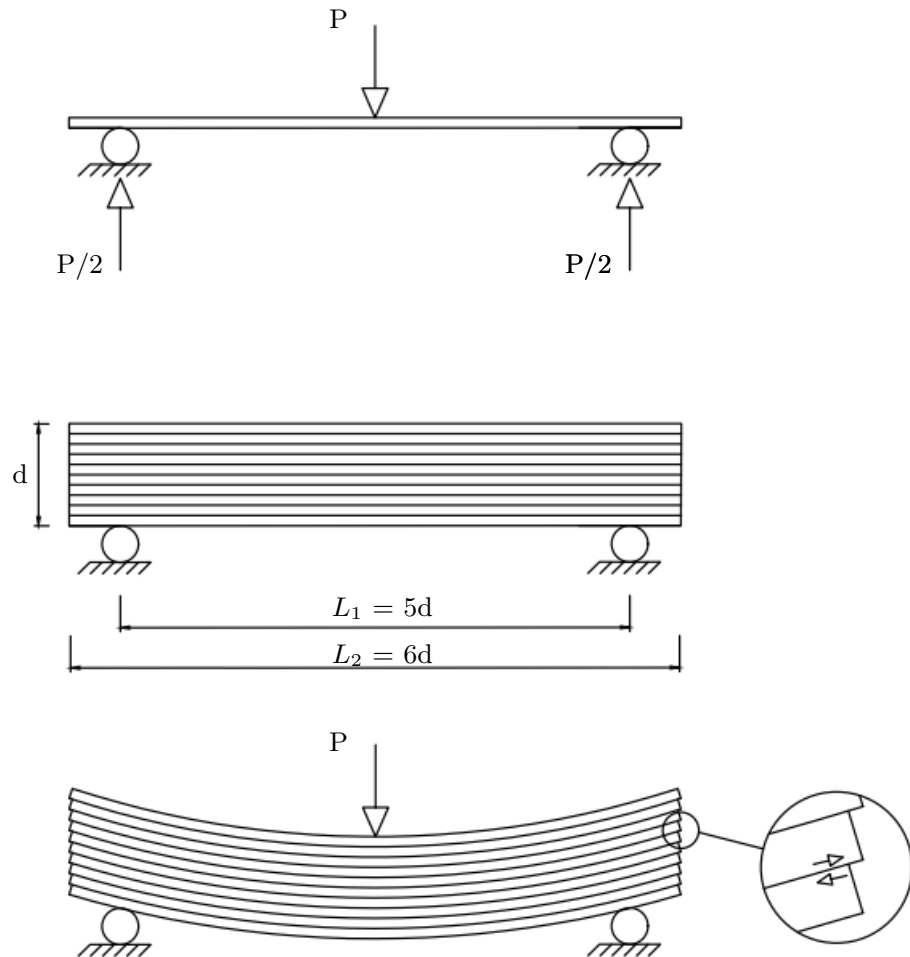


Figure 4.22: Horizontal shear test — Test methodology

was stiff enough to resist the test loads without significant displacement or bending. Each bottom support was adjustable along the steel beam to accommodate different span-to-diameter ratios. The two supports

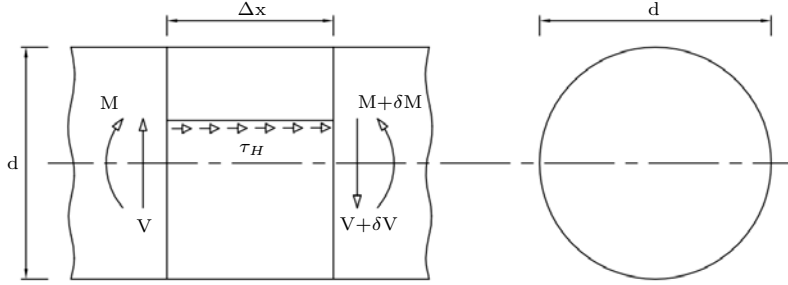


Figure 4.23: Horizontal shear test — Internal forces

and loading nose (for the center point loading) were made from stainless steel, but were also hardened to a Rockwell hardness of 55 to 58 type C, to improve the durability and life expectancy of the test setup. The completely assembled and mounted fixture is shown in Figure 4.25. This fixture aimed to test the horizontal shear stress, which is the shear stress produced between the different fibers in the longitudinal axis of the GFRP rebar. This fixture and the above described setup were used to conduct all horizontal shear strength tests according to ASTM D 4475 (ASTM International, 2008a).

#### 4.4.12 Test Fixture for Tensile Tests

As mentioned in Chapter 2, GFRP is an anisotropic material that is much weaker in the transverse direction than in the longitudinal one. For that reason, it was necessary to use anchors at both ends of the tensile stress specimens because proper anchors prevent fiber damage that otherwise would result from the grips of the tensile test machine (described Subsection 4.4.9), as standard grips usually impose a transverse force on the specimens (perpendicular to the longitudinal axis of the rebar). As mentioned above, the ASTM-recommended system includes thick-walled steel tubes filled with expansive grout for such anchors, as schematically shown in Figure 4.26. For the anchor preparation, the grout had to be filled into the upright standing steel tubes. To properly align the anchors with the GFRP rebars — which prevents eccentric loading during tensile strength testing — it was necessary to build a support frame according to ASTM D 7205 (ASTM International, 2011b). The frame that was designed for this research project is shown in Figure 4.27. The photo shows the frame as it was used for installing anchors at the first end (on the bottom) of nine (9) # 3 bars (front row) and nine (9) # 5 bars (back row). The frame was constructed from extruded aluminum profiles to guarantee high stiffness while maintaining its adjustability to adapt to different rebar sizes and lengths. Furthermore, these profiles provided a high precision assembly. The GFRP rebars were held in position by pipe clamps, which were mounted on the horizontal supports. Because the aluminum profiles — used for the supports — had T-slots for mounting screws, the position of the pipe clamps was easily adjustable. The horizontal supports were connected to the vertical elements by adjustable

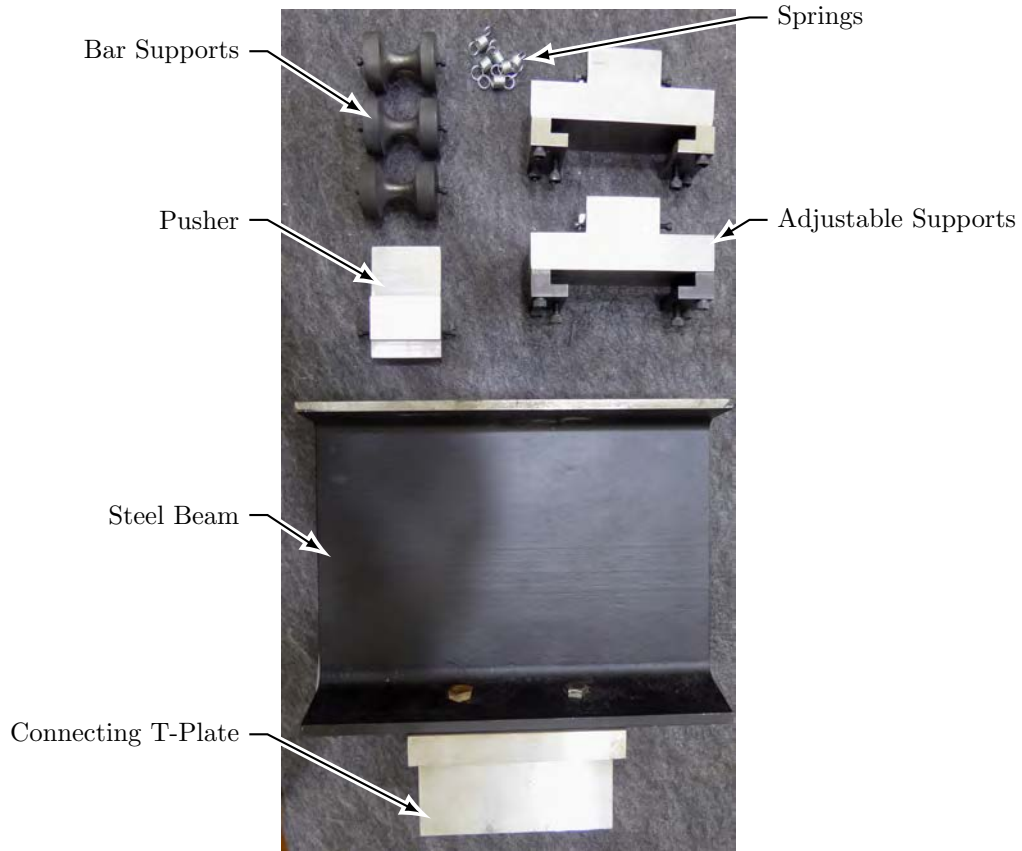
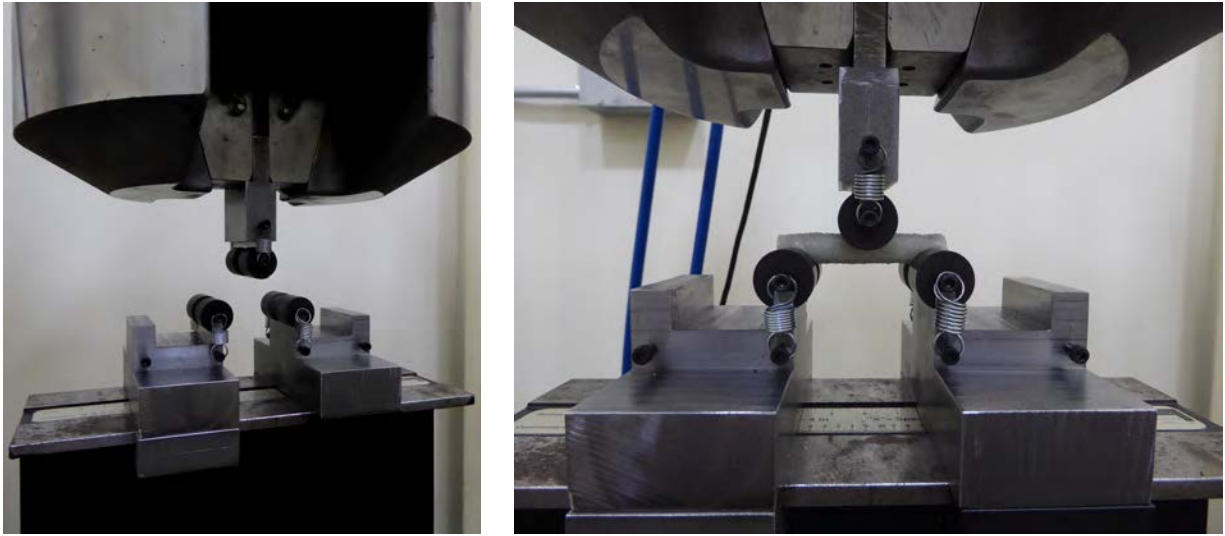


Figure 4.24: Horizontal shear test fixture — Components

corner brackets so that the horizontal bars were movable in the vertical direction. This flexible design was chosen to accommodate different positions of the horizontal bars for the preparation of tensile test rebar specimens with different dimensions. A melamine-covered particle board, which was fixed to the base frame, provided the base and support for the steel tube anchors; its surface coating allowed for easy cleaning and quick reuse of the system.

**Test Fixture for the Tensile Strength Test** This subsection describes the test fixture that was used to conduct the tensile tests. The fixture was needed in combination with the load frame described in Subsection 4.4.9 to test the FRP rebars in tension. This fixture was designed because the horizontal distance between the grips of the load frame was not wide enough to clamp the large rebar specimen anchors directly. The schematic drawing illustrated in Figure 4.28 shows that each fixture unit was an assembly of solid steel plates and threaded rods to provide sufficient space for the anchors between the bearing and T-plate on both specimen ends. The upper and the lower T-plates, which were made from two steel plates connected by a filled weld, were clamped by the upper and lower grips of the load frame, respectively. While the part of the T-Plate that was clamped by the load frame had a material thickness of 0.4 in. (10 mm), the lower horizontal



(a) Empty setup

(b) Specimen mounted

Figure 4.25: Horizontal shear test fixture — Mounted in load frame

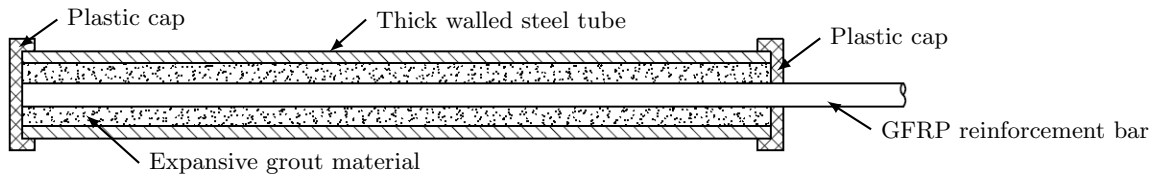


Figure 4.26: Schematic drawing of tensile test anchor according to ASTM D 7205-06

plate had the same thickness as the bearing plates with 1.0 in. (25.4 mm). The tensile forces applied by the load frame were transferred from the T-plate into the bearing plate via the threaded rods. These threaded rods had a length of 22 in. (559 mm) for adjustability and to provide space for a variety of anchor lengths. All components (bearing plate, threaded rods, T-plate) were held in place and connected to each other with flange nuts. An individual rod was secured on both sides of each plate via a nut and locknut. The bearing plate was designed (for bending and shear) to transfer the load from the anchors of the specimens to the threaded rods. Furthermore, for quick specimen exchange and for adaptability (universal use independent of specimen diameter), each bearing plate was slotted with a 1.5 in. (38.1 mm) gap and covered with two halves of a lock plate that were designed for a specific specimen diameter. Different lock plates — with different center hole openings — were designed and used to accommodate specific specimen diameters, because it was important to provide sufficient space for the GFRP rebar to move freely while guaranteeing adequate support for the anchors. These lock plates were secured to the bearing plates via  $\frac{1}{4}$  in. size cross recessed head screws. This setup allowed a fast and comfortable test process because only a few screws had to be removed when installing a new specimen after a test was completed. Furthermore, the setup ensured that all tensile forces were transferred into the specimens merely through the anchors. A photo of the completely assembled top

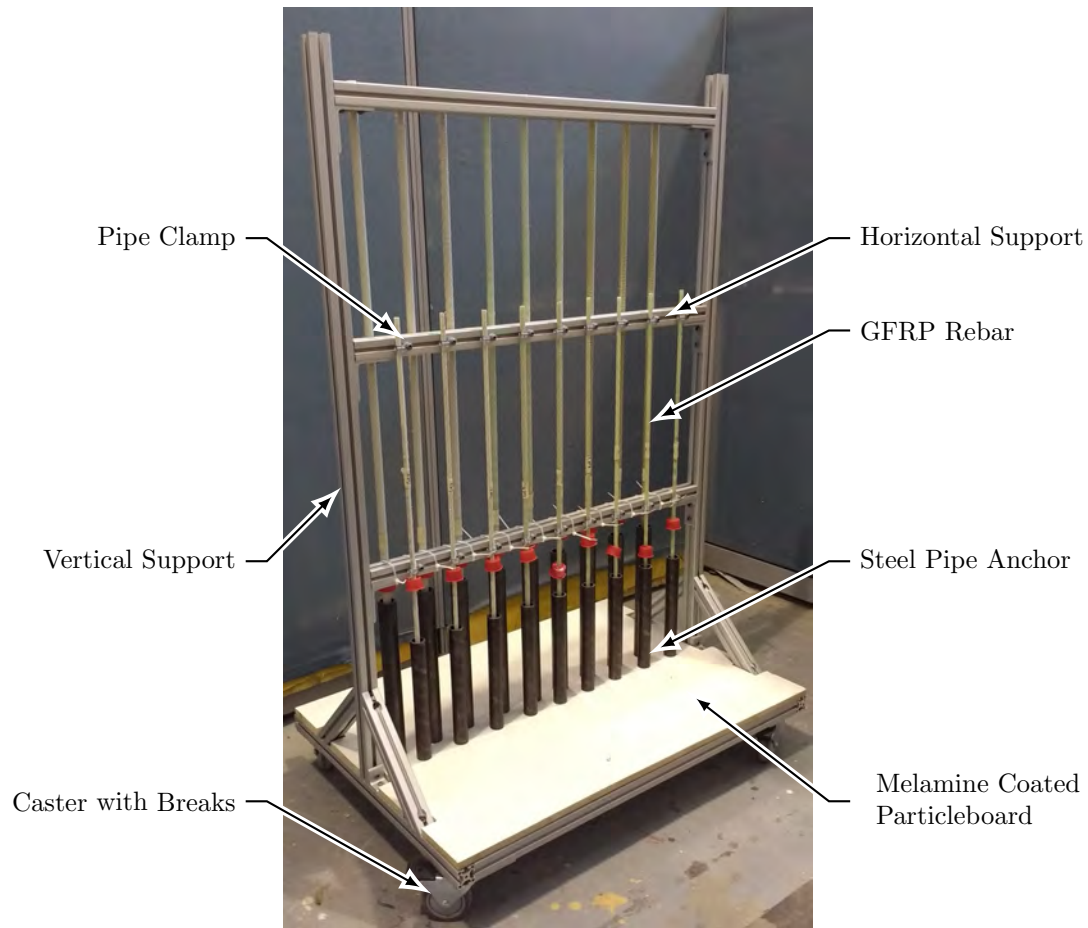


Figure 4.27: Support frame for anchor installation of tensile test specimens

unit of the fixture can be seen in Figure 4.29. The T-plate of the fixture was clamped by the upper grip of the load frame, which is described in the Subsection 4.4.9.

Both at Florida State University and University of Miami, standard test fixtures were used as defined in the respective ASTM standards. Moreover, inter-laboratory experiments were conducted to measure the reliability between the different instruments/fixtures at both laboratories (for each test procedure).

## 4.5 Test Procedures

For this research, the GFRP rebars were characterized via eight different test procedures, four were conducted to measure physical characteristics, and another four were used to define the strength properties. The physical properties that were tested focused on the cross-sectional dimensions, fiber contents, moisture absorption, and visual evaluations of the micro structure via SEM. The evaluated strength characteristics included transverse shear strength, horizontal shear strength, tensile strength, and bond-to-concrete strength. The following subsections detail how the glass FRP rebars were tested and which procedures were followed to obtain each

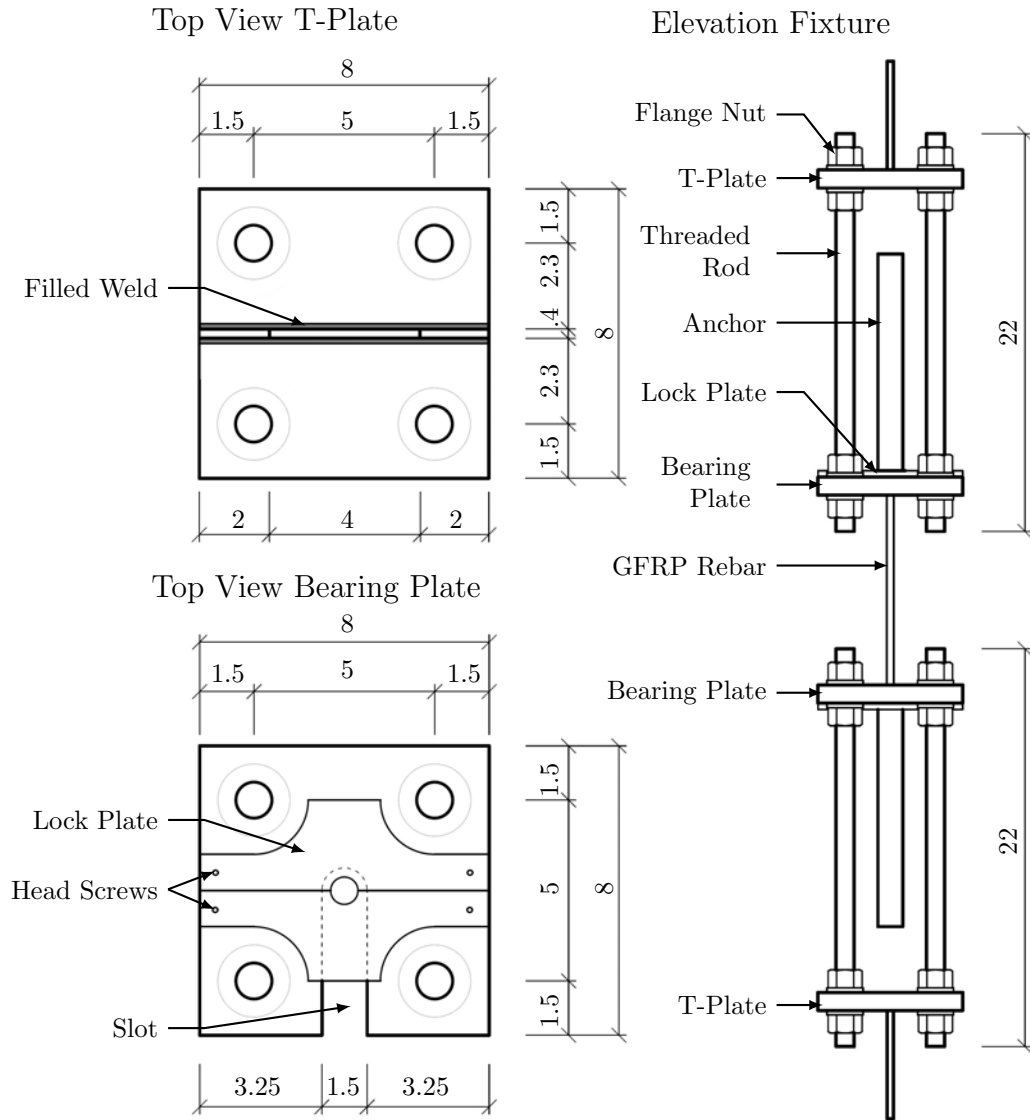


Figure 4.28: Tensile test fixture — Schematic drawing

individual material property.

#### 4.5.1 Measurements of Cross-Sectional Area

This subsection describes the methodology used to calculate the cross-sectional area per ASTM D792–13 (ASTM International, 2013).

#### Preparations and Specimen Production

The specimens for determination of the cross-sectional area were prepared at the University of Miami in the materials laboratory at the College of Engineering. As mentioned in Section 4.2.1, nine (9) specimens per

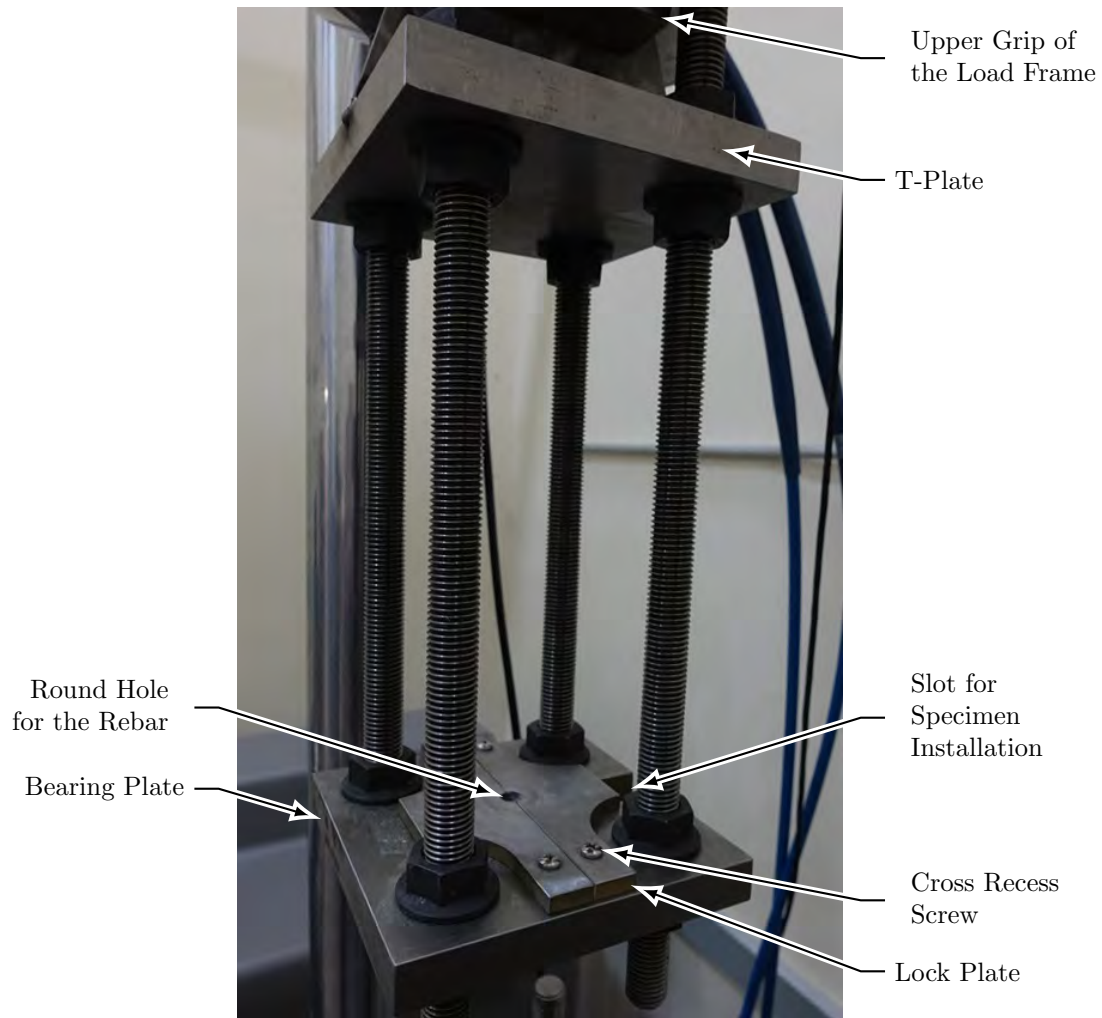
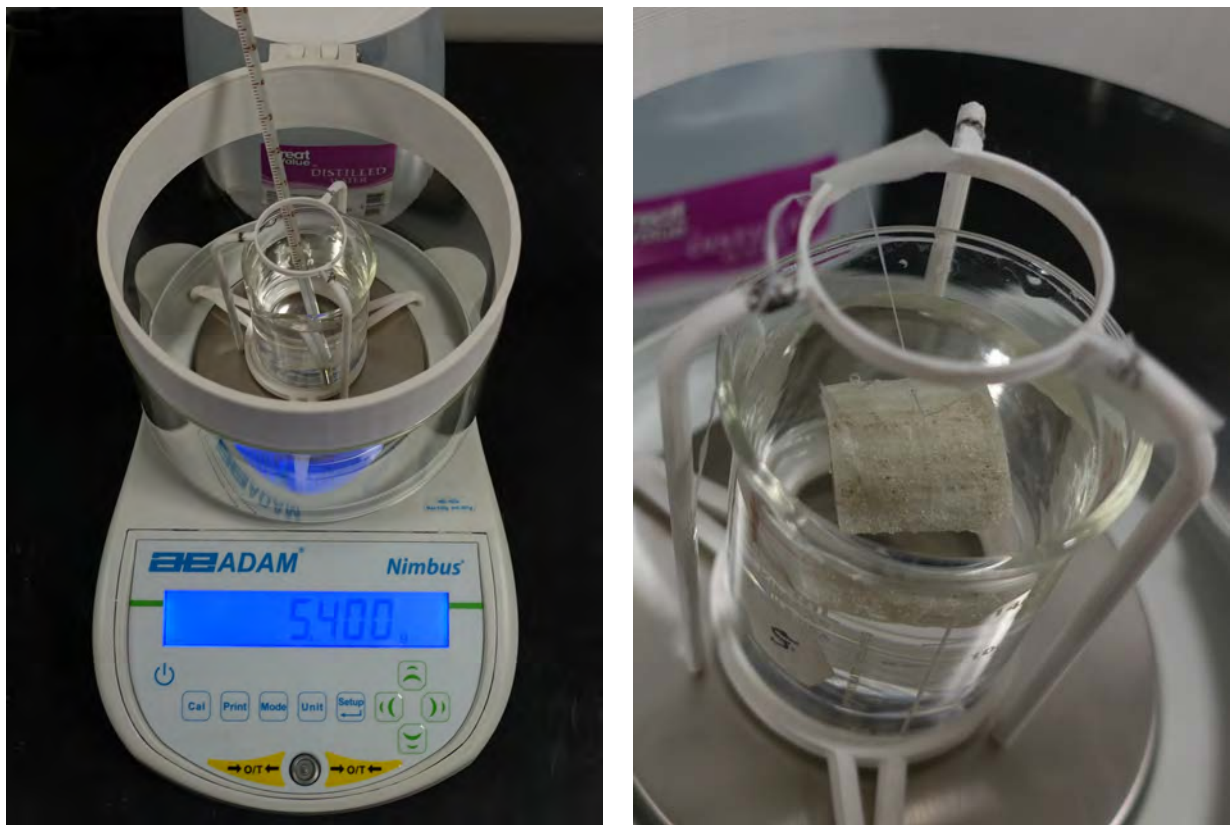


Figure 4.29: Tensile test fixture — Details

manufacturer and rebar size were chosen to preserve statistical significance. Therefore, a total of 81 specimens with a length of 1 in. (25.4mm) were prepared. The rebars were cut to length by using the precision saw described above. The saw was equipped with the diamond blade and the coolant tank was filled with water before cutting. The samples were clamped to the sample arm and adjusted through the black wheel on the left side of saw. Subsequently, the wheel speed of the saw blade was set to 250 rpm. After the safety cover was in place, the saw was started by using the control panel. The saw stopped automatically after a cut was completed. To avoid any corrosion damages to the blade, it was removed from the machine, thoroughly dried, and properly stored. Prior to testing, the samples were conditioned according to ASTM D 792-13 (ASTM International, 2013) for 40 h at  $(23 \pm 2)^\circ\text{C}$  within a  $(50 \pm 10)\%$  relative humidity. Then the specimens were tested according to the following test procedure.

## Test Procedure

The effective cross-sectional area was determined according to ASTM D792–13 (ASTM International, 2013). Actually, this standard described a method to determine the density and specific gravity (relative density) of plastics by displacement, but it was used to calculate the cross-sectional area and thus the diameter by using density, weight, and the known (and precision measured) length of each individual specimen. The test had to be conducted under standard laboratory conditions with a temperature of  $(23 \pm 2) ^\circ\text{C}$  and a relative humidity of  $(50 \pm 10) \%$ . The exact length of the specimens was measured three times per specimen from three angles ( $0^\circ$ ,  $120^\circ$ , and  $240^\circ$ ) with the caliper described in Subsection 4.4.3. After that, the temperature of the water was measured with the thermometer shown in Figure 4.30a, and the specimen was weighed in three different states: dry and without any suspension, the specimen together with the fixture, and the immersed specimen hanging from the fixture shown in Figure 4.30b. The 3D printed tripod under the water cup was designed



(a) Overview

(b) Immersed specimen

Figure 4.30: Test setup for measurement of cross-sectional properties

to uncouple the container from the measurement plate, so that only the weight of the immersed specimen (hanging from the fixture) was measured by the scale. Before weighing, the draft shield balance was closed and the balance was zeroed. At first, the specimen was measured dry, without any suspension. Then, the specimen was carefully placed on the strings of the suspension frame. Finally, the cup of water was placed



on the tripod and the specimen that was supported by the fixture was fully immersed in the water, as shown in Figure 4.30b. To avoid falsified test results, measurements were only taken, if no contact between the specimen and the wall or the bottom of the glass cup was guaranteed.

#### 4.5.2 Measurements of Fiber Content

The procedure for loss on ignition for cured reinforced resins is explained in this paragraph to describe how the fiber content for the tested FRP rebars was determined. ASTM D 2584–11 (ASTM International, 2011a) outlines this procedure and details the required conditions.

##### Preparations and Specimen Production

Similar to the specimen preparation for the cross-sectional dimension experiments, the specimens for this procedure were also conditioned in a temperature range from 21 °C to 25 °C (70 °F to 74 °F) at a relative humidity between 40 % and 60 %, for at least 40 hours prior to testing. The conditioned sample was then cut to the desired length of 25 mm (1 in.) with a precision of 0.05 mm (0.0019 in.).

##### Test Procedure

The weight of the conditioned sample ( $W_s$ ) was recorded to the nearest 0.05 g (0.0017 oz.) using an electronic balance. This weight was used as the 100 % reference value for calculating the fiber and resin contents (relative to the initial weight). Likewise, a clean and oven dried (heated at 500 °C to 0 °C for 10 minutes) crucible was weighed ( $W_c$ ) to the nearest 0.05 g (0.0017 oz.) to obtain the initial weight of the sample holder. The FRP rebar specimen was transferred to the crucible and the total weight of the specimen and the crucible ( $W_i$ ) was recorded to the nearest 0.05 g (0.0017 oz.). The crucibles and specimens of one specific size (e.g.; all # 8 rebar specimens) were placed in heat resistant metal rack as seen in Figure 4.31a. To burn off all resin, the crucible (of known mass) along with the specimen were exposed to a temperature of 542 °C to 593 °C (1000 °F to 1100 °F) in the muffle furnace described in Subsection 4.4.6 until the specimens reached a constant weight. Figure 4.31b shows an intermediate state and the specimen appearance half-way through the burning cycle after reaching approximately 300 °C (572 °F). It can be seen that the different product types (top row, Type-A; middle row, Type-B; and bottom row, Type-C rebars) showed a different response at this temperature level as the Type-A resin was mostly lost, while Type-B and Type-C rebars still contained resin. However, the structural integrity of all rebars was already lost at this temperature.

Nevertheless, the burning cycle was generally completed to the temperature required by ASTM. The crucible was then carefully removed from the muffle furnace and allowed to cool down to room temperature, before the cooled crucible including the fibers (and sand for rebars that used surface enhancement made



Figure 4.31: Specimens for fiber content test

from sand) was weighed using a precision electronic balance. This weight was recorded as final weight ( $W_f$ ). For the rebar products made with sand at the surface for bond enhancement, the weight of the sand ( $W_s$ ), was recorded and subtracted from the initial weight of the crucible and the specimen to obtain comparable and absolute fiber content percentages. Because fibers (and sand) are not susceptible to loss on ignition, the reduction in weight due to the burning process is equivalent to the weight of resin, and hence, the percentage of fibers was determined through the difference in weight before and after the burning process. As seen in Figure 4.31c, Type-A rebars included sand, which remained in the crucibles and was separated from the fibers. A detailed example of the glass fibers that remained in the crucibles after the burning process is shown in Figure 4.31d. For reliability of test results and to obtain representative values for the BFRP rebar product as a whole, the test was repeated five times for specimens taken from different sections of the production lot and the average value was assigned.

### 4.5.3 Measurements of Moisture Absorption

The test procedure described in ASTM D 5229 (ASTM-International, 1992) defines the standard method for determining the moisture absorption characteristics of FRP and it is explained here to detail how the porosity of the tested rebars was calculated. ASTM D 5229 offers seven different test procedures (A through E, Y, and Z) to assign moisture absorption properties for FRP in different environments. Procedure A is most commonly used, and was therefore followed as described for this research project as well.

#### Preparations and Specimen Production

Each specimen was first oven dried to eliminate potential moisture entrapped in the pores or at the surface. The dried and conditioned specimens were placed in storage bags to ensure that no moisture got in contact with the specimens.

#### Test Procedure

Three diameter measurements were taken at 120° intervals, perpendicular to the longitudinal axis of the FRP rebar, and those measurements were recorded to the nearest 0.001 mm ( $\frac{4}{10\,000}$  in.). Then, each specimen was weighed with a precision of 0.05 g (0.0017 oz.) in its dry state and recorded as  $W_i$ . The specimens were then submerged in distilled water as exemplified in Figure 4.32a. The submerged specimens were stored in a spec-



(a) Submerged in distilled water



(b) Overview of entire test group for Type-A rebars

Figure 4.32: Moisture absorption specimens

imen container (See Figure 4.32b) and placed inside the air circulated oven (described in Subsection 4.4.5) to maintain the temperature at 50 °C (122 °F) throughout the entire duration of the experiment. First weight measurements to record  $W_1$  after water conditioning were taken after two weeks. To obtain additional measurements, the specimens were removed from the water bath in two-week intervals (continuous conditioning) and surface dried with a fresh paper towel until no free water remained on the surface of the FRP rebar. The final weight of each specimen ( $W_f$ ) was measured and recorded to the nearest 0.05 g (0.0017 oz.). This

procedure was repeated and weight gains were monitored until three consecutive two-week measurements did not differ by more than 0.02% from one another. For reliability of test results and to obtain representative values for the BFRP rebar product as a whole, the test was repeated five times for specimens taken from different sections of the production lot and the average value was assigned.

#### 4.5.4 Measurements of Micro Defects (SEM)

The micro structure of the GFRP rebars was analyzed via scanning electron microscopy to evaluate the initial production quality and to monitor the degradation process throughout various temperatures and exposure durations.

#### Preparations and Specimen Production

The specimens were prepared and impregnated with epoxy, before the surface was polished and silver-coated with a sputter coater. A mixture of epoxy set resin, hardener, and conductive filler was prepared. The GFRP specimens were placed in a container and surrounded with epoxy. By leaving the top surface exposed to laboratory air in a storage container at room temperature, the epoxy resin cured within 24 hours. The cured specimens were released from the storage container and polished using a series of successively finer grit of abrasive paper and diamond paste to properly reveal the microstructure. A semi-automated polisher was used for surface smoothing and a sequence of successively finer silicon carbide paper of 240, 400, and 600 grit and diamond polishing pastes ranging from 6  $\mu\text{m}$  to 1  $\mu\text{m}$  were utilized. Each specimen was inspected under an ordinary microscope to monitor the polishing process. The last step in the preparation sequence required a sputter coater to cover the epoxy surface with a 10  $\mu\text{m}$  thin conductive layer by exposing the samples to silver particles for 110 s.

#### Test Procedure

To obtain high quality SEM images, a multi-technique dual beam field emission scanning electron microscope (Zeiss 1540EsB) was used. The samples were exposed to the beam with an acceleration voltage of 15 kV through an aperture of 30  $\mu\text{m}$ . By using the backscatter detector (BSD), the GFRP rebars were analyzed at a magnification of  $50\times$  with a working distance (WD) of 7 mm. Through the matrix feature, each individual SEM image was scanned with a resolution of 1024 pixel per row at a scan speed of 8 and with a 10% overlap to facilitate picture generation of the full cross section. The entire GFRP rebar cross section was generated using ImageJ by Fiji<sup>8</sup> to stitch the individual images together for a complete overview.

---

<sup>8</sup>Schindelin, J.; Arganda-Carreras, I. & Frise, E. et al. (2012), "Fiji: an open-source platform for biological-image analysis", Nature methods 9(7): 676-682, PMID 22743772, doi:10.1038/nmeth.2019

### 4.5.5 Measurements of Transverse Shear Strength

Transverse shear tests were conducted according to ASTM D 7617 (ASTM International, 2011c). Because this test procedure exposes FRP rods to direct shear stresses perpendicular to the longitudinal axis and the resin insignificantly contributes to shear resistance in this direction, this test characterizes the shear strength of the fibers (whereas the horizontal shear test explained in Subsection 4.5.5 characterizes the shear strength of the resin).

#### Preparations and Specimen Production

The specimens were cut from GFRP rods with a length of 60 in. (1.5 m), using the cutting saw described in Subsection 4.4.1 with a 12 in. (203 mm) diameter diamond saw blade shown in Figure 4.4a. Figure 4.33 exemplifies the specimens that were prepared for the transverse shear tests, all of which were cut to an equal length of 225 mm (8.85 in.), independent of the tested rebar diameter.



Figure 4.33: Specimens for transverse shear testing

After the specimens were cut to the required length, they were moved to the materials test laboratory and stored in standard laboratory conditions at  $(23 \pm 1) ^\circ\text{C}$  [ $(73.4 \pm 1.8) ^\circ\text{F}$ ] and  $(50 \pm 2) \%$  humidity without any prior conditioning process.

#### Test Procedure

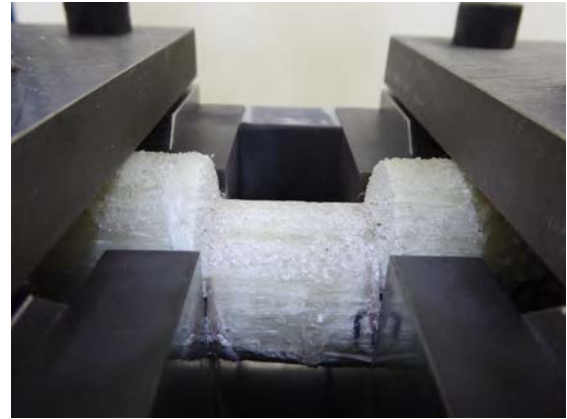
After the laboratory was cleaned and well prepared for testing, the MTS load frame described in the Subsection 4.4.9 was powered on. To move the crossbar into position prior to testing, the manual controls (shown in Figure 4.15) on the machine were adjusted. While the fixture was adjusted manually and the test specimen was carefully preloaded using the manual control dials, the actual test was controlled via the “TestWorks 4” software interface described in Subsection 4.4.9. The steel T-plate was mounted on the MTS machine as shown in Subsection 4.4.10 using the manual controls. The top pusher plate was installed in the top grip

of the load frame. Prior to placing the fixture on the already clamped steel T-plate and before testing, the diameter of each of the six specimens was measured at midpoint with a precisely calibrated micrometer. The specimens were grouped by diameter: #3, #5, #6 and #8. First, all 24 (six per diameter) specimens were measured and prepared for testing. After all measurements for the rebar groups were obtained, each of the six specimens was taken to failure using the transverse shear test fixture described in Subsection 4.4.10.

The GFRP rods were centered in the fixture, resting on the bar seats and the lower shear blades of the fixture, before the fixture was actually placed inside the load frame on the loading platform. After centering, the rod was clamped into place by using two sets of screws. At one end, the two outside holes/screws in the straps were used, and at the other side, the center hole/screw was used to press down the rebar. All screws were hand-tightened, per ASTM description. The fixture allowed three sets of screws on each end of the bar, so if the specimen appeared to move or not to be clamped properly, additional sets of screws were used. After the bar was clamped in place, the whole fixture with the fitted rod was placed on top of the already clamped steel T-plate. Before adjustment of the upper blade, the fixture was correctly centered and aligned with the top grip to ensure that the shear plate was centered underneath the center of thrust of the load frame. Accordingly, the top pusher, which had the same surface as the upper blade (already clamped to the top grip), was inserted between the bottom two shear plates (cf. Figure 4.21a). After the fixture was perfectly aligned, the top grip with the clamped pusher was elevated, leaving enough space to place the top blade between the GFRP rebar and the top pusher. Once the specimen was ready to be tested, the manual controls on the machine were locked, and from then on, the MTS load frame was computer-controlled. The tests were performed in displacement control mode with a displacement rate that lead to failure within 1 min to 10 min. After conducting the necessary pre-tests to study the behavior of the different rebar sizes and materials throughout transverse shear testing, the test rate was defined at 1.3 mm (0.05 in.)  $\frac{1}{\text{min}}$ , which was used to test specimens at test durations of around 220 s for rebars #3 and around 400 s for rebars #8, to consistently target a failure time between 60 s (1 min) and 600 s (10 min) as defined by ASTM D 7617M (ASTM International, 2011c). The force versus displacement behavior was continuously monitored with a 10 Hz frequency. A constant displacement rate was applied to obtain the data throughout all load increments and the post-failure to capture both, the ultimate strength (at maximum force) and the deformational behavior. Although sufficient test data was collected when the load dropped below 70% of the observed peak, all data was recorded until no more load was carried by the specimen to capture any unusual behavior that might be indicative of the material performance. Figure 4.34 shows the appearance of the transverse shear test fixture and how the specimen were deformed after the test was completed. It can be seen that the fibers were cut perfectly perpendicular to the longitudinal axis of the rebar and that the section under the top blade was lowered into the gap between the two bottom blades.



(a) Overview



(b) Detailed view

Figure 4.34: Specimen after completion of transverse shear test

#### 4.5.6 Measurements of Apparent Horizontal Shear Strength

The horizontal shear strength of FRP rebars is indicative of the resin quality because the test procedure described in ASTM D 4475 (ASTM International, 2008a) leads to inter-laminar shear failure. Due to the short span length in these tests, the created bending moment does not reach the failure capacity before the horizontal shear strength is attained. In rare cases (or for improper chosen span lengths), flexural failure might be noted. However, the results from such tests must be discarded as they do not characterize the horizontal shear strength of FRP rebars.

#### Preparations and Specimen Production

For the apparent horizontal shear strength test, the specimen length was defined by ASTM as one diameter greater than the span length between the two bottom supports, and that span length was based on the rebar diameter of the tested specimen. Or more precisely, it was defined via the span-to-diameter ratio from 1 to 3 up to 1 to 6 (ASTM International, 2008a) — dependent on the load rate or the total test duration. In this case, based on the laboratory experience at the FAMU-FSU College of Engineering and the University of Miami, a span-to-diameter ratio of 5 to 1 was selected to match the requirements of ASTM D 4475 and to prevent collision between the bottom and top rollers, should a GFRP rebar deflect significantly throughout the test. Therefore, to measure the apparent horizontal shear strength, specimens with a length of six times the diameter were prepared, as shown in Figure 4.35. This meant that the specimens for # 3 [diameter = 10 mm (3/8 in.)] had a length of 60 mm (2 1/4 in.), the specimens for # 5 [diameter = 16 mm (5/8 in.)] were 96 mm (3 3/4 in.) long, and the specimens for # 8 [diameter = 25 mm (1 in.)] were cut to a length of 150 mm (6 in.). After the specimens were cut to the required length, they were moved to the materials test laboratory and stored in standard laboratory conditions at  $(23 \pm 1) ^\circ\text{C}$  [ $(73.4 \pm 1.8) ^\circ\text{F}$ ] and  $(50 \pm 2) \%$  humidity without any



Figure 4.35: Specimens for apparent horizontal shear test

prior conditioning process.

### Test Procedure

After all materials and equipment were properly arranged in the laboratory, the MTS load system (see Subsection 4.4.9) was powered on, and the fixture for the apparent horizontal shear test (see Subsection 4.4.11) was mounted inside the load frame. Unlike the setup for the transverse shear test procedure, the fixture was mounted in the MTS load frame before the GFRP rebar was placed in/on the fixture. The first step was to place the beam with the T-plate shown in Figure 4.24 on top of the bottom grip of the load frame to guarantee that the center point of the three-point load test would be in line with the center of thrust of the load frame. Before clamping the beam in the bottom grip using the manual controls of the machine (cf. Figure 4.15), the beam was properly centered and aligned. To achieve proper alignment, the top grip holding the top roller (center point load) was lowered to a distance of about 2 cm to 3 cm (0.79 in. to 1.18 in.) above the beam for accurate reference. As soon as the beam was in the desired position, it was clamped by the bottom grip and the top grip was raised back up. Then, the bottom supports were slid onto the beam and into position to guarantee an equal distance from the center point, as shown in Figure 4.25a. The actual span length, or the distance between the two bottom supports, was determined based on the tested rebar size; five times the diameter of the tested rebar as described above in Subsection 4.4.11. With the fixture



correctly mounted, the GFRP rebar was placed on the two bottom roller supports. Afterwards, the rebar was aligned, such that its midpoint was centered for an equal unloaded overhang on both sides so that its longitudinal axis was perpendicular to the centered load point. Then, the manual controls on the machine were locked. The software was programmed to control the system via the “Exclusive Control” of the MTS TestWorks 4 software as explained in Subsection 4.4.9. The specimen was initially preloaded with a load that was less than 1% of the ultimate failure load. Tests were conducted using the test machine in displacement control mode, applying the load at a constant crosshead rate of 1.3 mm (0.05 in.)  $\frac{1}{\text{min}}$ . This rate was however reduced if the test took less than 20 s, and increased if it took more than 200 s, so that the duration of each test ranged between 20 s and 200 s to match the requirements of ASTM D 4475 (ASTM International, 2008a). As soon as the displacement of the crosshead was initiated, the horizontally supported GFRP rebar began to bend. In this type of test, it is likely for the fibers (and resin) of the FRP bars to slide horizontally past each other at the maximum failure load. Afterwards, the specimen may still carry loads and experience a similar sliding failure after a modest strength recovery — this may happen multiple times. Accordingly, the test data for the load and the displacement was recorded throughout the entire test at a 10 Hz data acquisition rate, to capture the load increments, the peak value, and the post failure behavior. Finally, the ultimate load was recorded, and the failure curve (load vs. displacement) was plotted. Because an incorrect selection of the span-to-length ratio could lead to a tensile or flexural failure, the failure type (shear or tension — due to bending) was documented. If a tensile failure occurred, the measurements and all values were discarded and additional tests were performed.

#### 4.5.7 Measurements of Tensile Properties

The tensile strength test and measurement of the elastic modulus for FRP rebars is described in ASTM D 7205 (ASTM International, 2012). Due to the low shear strength of FRP materials, these tests are complex and require extra care during specimen preparation because FRP rebars cannot simply be held in place or stressed like traditional black steel rebars because the fibers would be damaged. Accordingly, the following subsections detail the materials and supplies as well the preparation sequences that were needed to ready the specimens for tensile strength testing.

##### Materials and Supplies

**Steel Tubes** When testing FRP rebars in tension, proper anchors must be provided at both specimen ends to prevent transverse failure (perpendicular to the fibers) possibly induced by the clamping mechanism of load frame. These anchors were made from thick steel tubes filled with expansive grout. The measurements of these tubes were prescribed in ASTM D 7205 (ASTM International, 2012), and the precise dimensions were

dependent on the rebar size. For example, for a #3 rebar, a steel tubes with an outer diameter of 35 mm ( $1\frac{3}{8}$  in.) and a wall thickness of 4.8 mm (0.188 in.) were required. Tubes with an outer diameter of 41 mm ( $1\frac{5}{8}$  in.) and a wall thickness of 4.8 mm (0.188 in.) were used to meet the requirements for the #5 rebars. Dimensions for the other rebar diameters were chosen in similar fashions, according to the stipulations in ASTM D 7205 (ASTM International, 2011b). While ASTM prescribed the precise dimensions of the tubes, no requirements for the steel grade were defined. Therefore, tubes made from low carbon steel with a minimum yield strength of 207 MPa (300 psi) were used for economic reasons (low material costs, good machinability). These tubes provided the anchor material for all rebar specimens tested in tension. Accordingly, the anchor had to be connected to the rebar; this was done using expansive grout.

**Expansive Grout** The basic idea of the used anchor system was to allow an expansive grout material to expand within the thick-walled steel pipes to clamp the rebar into an anchor with a sufficient length for load development/transfer. Because of the high stiffness of the steel pipes, the grout exerts pressure on the rebar specimen, which maintains the specimen position inside the steel tube. The used expansive grout material was a proprietary product named Blue Bustar (shown in Figure 4.36a), and obtained through a distributor called Demolition Technologies Inc. (Greenville, Alabama). The powder material was batched in small portions and combined with water using a handheld electric mixer inside a 5 gal bucket as shown in Figure 4.36b. Two gallons (7.57 L) of water were needed to mix one 55 lbs. (24.95 kg) bag of grout material.



(a) 55 lbs. Bag



(b) Material preparation

Figure 4.36: Expansive grout

According to the manufacturer, this particular grout product can reach a peak pressure of approximately 69 MPa (10 ksi) within 7 days<sup>9</sup>. This material was chosen because it performed satisfactorily throughout

<sup>9</sup>As stated in the technical informations made available by Demolition Technologies Inc. Information retrieved on March 24, 2017 from: <http://www.demolitiontechnologies.com/expanding-grout-technical-info>

former GFRP research projects at the University of Miami (Kocaoz et al., 2005a; Schesser et al., 2014).

### Preparations and Specimen Production

This section details the specimen preparation and explains all steps that were required to ready the GFRP rebars for tensile strength testing. As mentioned above, three specimens per manufacturer and per lot and rebar size were prepared (note that for durability only # 3 rebars and a single lot were tested) to evaluate the repeatability of results under consideration of economical aspects. The total length of the specimens was the sum of the free length plus two times the anchor length. According to ASTM D 7205 (ASTM International, 2011b) the free test length should be not be less than 380 mm (15 in.) nor less than 40 times the rebar diameter. Accordingly, the measurements of the anchor tubes were dependent on the tested rebar size. For example, for a # 3 rebar, steel tubes with an outer diameter of 35 mm ( $1\frac{3}{8}$  in.) and a wall thickness of 4.8 mm (0.188 in.) were required. Pipes with an outer diameter of 41 mm ( $1\frac{5}{8}$  in.) and a wall thickness of 4.8 mm (0.188 in.) were used to meet the requirements for the # 5 rebars. These pipes were previously cut to a length of 300 mm (12 in.) for the # 3 rebars and to 380 mm (15 in.) for the # 5 according to Table A1.1. in ASTM D 7205–06 (ASTM International, 2011b). After cutting the anchors to the desired length, the insides of the pipes were cleaned with water, soap, and stainless steel scrubbing pads. As shown in Figure 4.37, plastic plugs were used to close the pipe segments on one side, to prevent leaking of the fluid grout material. Because

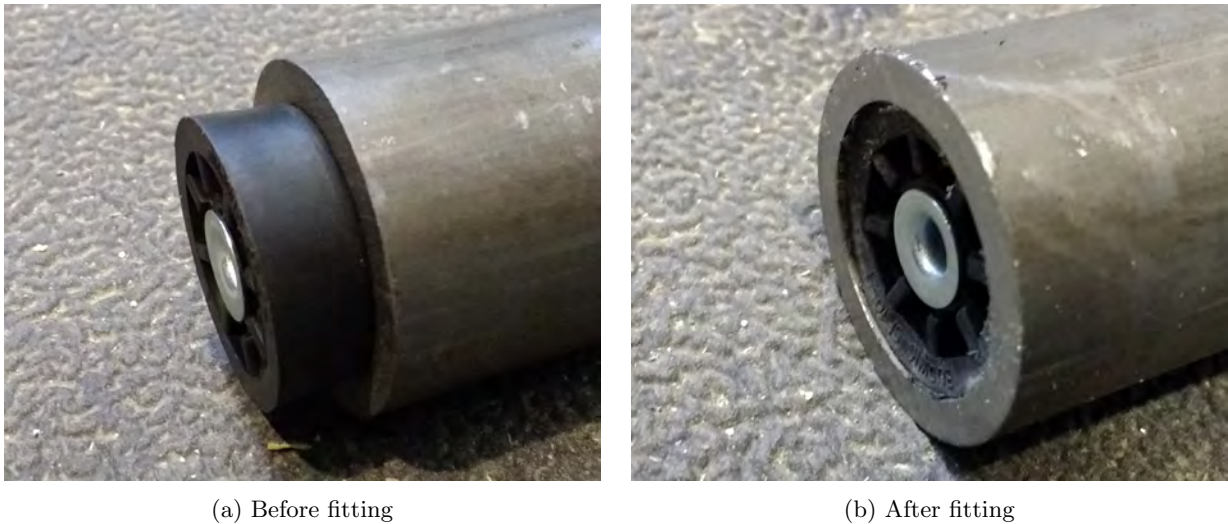


Figure 4.37: Fitting of plastic bumper

these plugs were conical and had a larger maximum outer diameter than the inside diameter of the pipes, a hammer was used to completely ram the plugs into the pipe for a tight fit. Upon completion of cutting the rebars to their desired length and fitting the steel tubes with plastic bumpers, the rebars were placed into the support frame (cf. Subsection 4.4.12, Figure 4.27) to mount the anchor construction. After placing the

rebars in the frame, a plastic cap with a center hole (shown in Figure 4.38) that matched the diameter of rebar was put over the lower end of the bars. The purpose of this cap was to close the top end of the anchor



Figure 4.38: Potting of the anchors for tensile test specimens

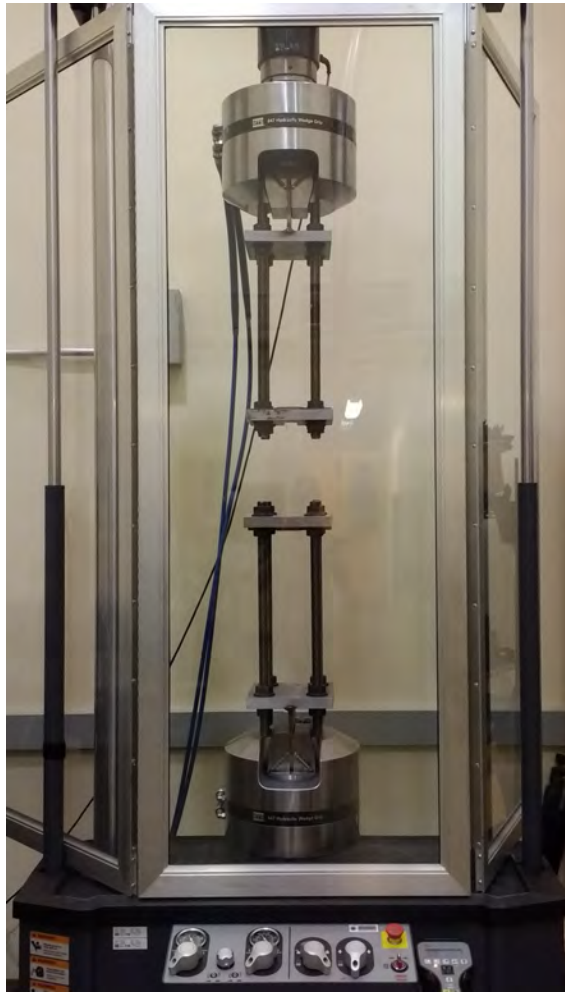
upon completion of the grout pour. Subsequently, the prepared steel pipes were placed on the melamine coated particleboard base (cf. Figure 4.27) and aligned with the aluminum frame. The alignment of the steel pipes was ensured by using masking tape as spacer. As shown in Figure 4.38, the rebars were also secured with cable ties before potting because a precise alignment of the rebars with the steel pipes was essential for a proper anchor system. A small bucket with a spout, shown in Figure 4.38, was used for potting. The space between the steel tubes and the rebars was completely filled with the grout material to ensure embedment throughout the full length of the anchor.

After a curing period of one day, the specimens were carefully removed from the alignment frame and were turned around to complete the grouting procedure at the opposite end. The specimens were removed from the frame after another day of curing to make room for additional rebar specimens. However, the specimens were stored for one week under laboratory conditions before any stresses were applied to the anchors or the rebars. The one-week curing period was maintained on account of the manufacturer specifications, which stated that the grout reaches the peak pressure after seven days.

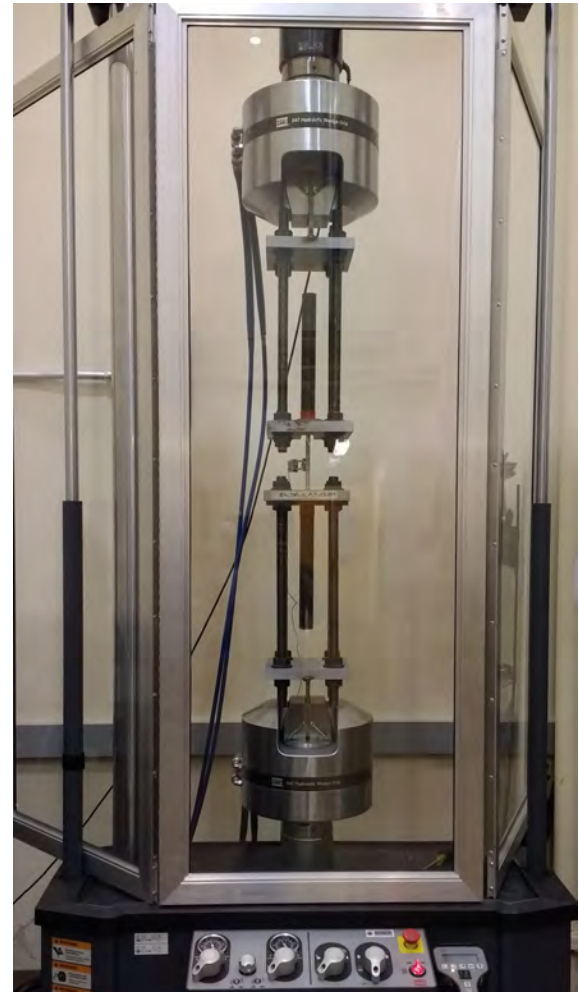
## Test Procedure

All tensile strength tests and elastic modulus experiments were conducted according to ASTM D 7205 (ASTM International, 2011b). The precise test sequence was dependent on the used load frame, as a fixture was needed for the “Model 370 Load Frame” at the HPMI in Tallahassee, whereas the load frame at the University of Miami was able to grip the rebars directly. Therefore, this subsection is divided in two paragraphs: The first one describes the procedure for the tensile test with the load frame in Tallahassee, while the second paragraph explains the procedure for the test machine in Miami.

**Tensile Tests in Tallahassee (“MTS Landmark Model 370 Load Frame”)** After preparing and cleaning the laboratory for testing, the MTS load frame, described in Subsection 4.4.9, was powered up and initialized according to the users manual. The crossbar position and the clamps were adjusted by using the manual controls on the test frame. At first, the lower T-plate of the fixture was clamped with a pressure of 30 MPa (4.35 ksi) into the lower grips of the testing machine by using a level to guarantee proper alignment. Subsequently, the upper T-plate was placed on the top of the lower one before clamping it with the upper grips of the machine. The aim of this procedure was to ensure that both plates had the same alignment and that the holes of both plates were positioned precisely above each other. After clamping the upper plate — also with a pressure of 30 MPa (4.35 ksi) — the crossbar was moved into a higher position to enable the installation of the threaded rods onto the upper T-plate. Once the rods were fixed with nuts onto the T-plate, the upper bearing plate was installed and also fixed by nuts. A level was used to achieve a horizontal alignment of the bearing plate. Afterwards, the cross bar of the test machine with the completed upper part of the fixture was moved into the highest possible position to achieve enough work space for the assembly of the lower part of the fixture. The four rods were fixed to the lower T-Plate by using nuts and locknuts, then the upper bearing plate was mounted by using a level to check the horizontal alignment. Depending on the diameter of the tested specimen, locking plates with the proper hole were used to hold the specimen in position. Figure 4.39a shows the test setup before the installation of a rebar. The safety glass was placed on the top of the table of the load frame to protect the laboratory staff from chipping fibers caused by the failure of the rebars. After the specimen was placed into the fixture and aligned properly by the locking plates, the crossbar of the machine was locked as shown in Figure 4.39b. Then, the cross bar lock switch was turned into the lock-position (cf. 4.4.9). Subsequently, the handset was used for fine adjustments (see Figure 4.15). An initial load of 1 kN (0.225 kip) was applied to the bar by using the setting wheel of the handset. Then, the extensometer was clamped onto the rebar in the middle of the free test length as it is shown in Figure 4.39b. From that moment on, the load frame was only controlled by the computer. All tests were performed in displacement control mode, the chosen displacement rate of 2.0 mm (0.08 in.) / min was



(a) Without specimen



(b) With mounted specimen

Figure 4.39: Test Setup

used to target a failure time between 60 s (1 min) and 600 s (10 min) as defined by ASTM D 7205 (ASTM International, 2011b). After starting the test program, the force versus displacement and the strain data were monitored continuously with a 10 Hz frequency. According to ASTM D 7205 (ASTM International, 2011b) the tensile chord modulus of elasticity should be calculated from the strain range of the lower half of the stress-strain curve, with the start point being a strain of 0.1% and the end point measuring 0.3% strain. Therefore, the extensometer was removed, when the strain exceeded 0.3%. The program stopped the load mechanism automatically when the force dropped by 70% or more. After the machine had stopped, the actuator cylinder returned to its starting position. The tested specimen was slid out of the test fixture after removing one locking plate from the top fixture and one locking plate from the bottom fixture. Afterwards, the next specimen was inserted into the fixture and the test procedure was repeated accordingly.

**Tensile Tests in Miami (“Baldwin 200k”)** The test process with the test machine in Miami differed from the process described above because no fixture was needed to conduct the tests. At first, the height of the cross bar was adjusted by using the manual controls of the machine so that the free test height between the upper and lower grips was slightly higher than the free length of specimen to be tested. Subsequently, the specimen was inserted from above into the testing machine by using a stepladder. In contrast to the above described test machine in Tallahassee, this machine did not make use of hydraulic grips. The wedge grips only held the specimen when tension was exerted. Therefore, a preload of about 1 kip (4.45 kN) was applied to the specimens to ensure a proper gripping. Then, the test process, which was similar to the machine described above, was started. The displacement rate was 2.0 mm/min (0.08 in./min) and the data was recorded with a frequency of 10 Hz. The extensometer was removed after the the strain exceeded 0.3%. The test was completed after the specimen failure was detected. Subsequently, the grips were manually loosened via a lever arm system to remove the tested specimen from the load frame. Afterwards, the same procedure was repeated to perform further tensile tests.

#### **4.5.8 Measurement of Bond-to-Concrete Strength**

In an effort to characterize the quality of the surface enhancement features of the various glass FRP rebars, concrete “pullout” tests according to ASTM D 7913 (ASTM International, 2014) were conducted. These tests measure the bond strength and test the interface between the concrete and the FRP rebar. The following subsections explain how the specimens were prepared for testing and which procedure was followed to test the specimens for this research project.

##### **Preparations and Specimen Production**

Bond test specimens were prepared as described in ASTM D 7913 (ASTM International, 2014). However, for economical testing, only #3 rebars were used to evaluate the bond performance of the GFRP rebars tested in this research project. Similar to the specimens for tensile testing, the rebar end that was to be gripped by the load frame was protected by a 300 mm-long grouted steel pipe to shield the rebar from destructive transverse stresses. The other end of the rebar was embedded in a 200 mm × 200 mm × 200 mm (7.9 in. × 7.9 in. × 7.9 in.) cube made from normal-weight concrete with a minimum nominal 28-day compressive strength of 31 MPa (4500 psi). To break the bond between the rebar and the concrete, 150 mm of the rebar (inside the cubes) were shielded to prevent stress concentration within the concrete cube and to guarantee a bond length of 5 times the diameter (50 mm (1.97 in.) for the tested #3 rebars). After the steel anchors were installed and cured, the cubes were casted using individual plywood molds, where fresh concrete was placed in two layers (each layer was equally compacted with an internal vibrator). The specimens were

demolded 2 days after the concrete was placed, and then left to cure at ambient conditions for 28 d before the specimens were tested or exposed to the aging environments.

**Test Procedure**

The specimens were tested following the method proposed in ASTM D 7913 (ASTM International, 2014). The tests were conducted in displacement control mode in a universal test frame with a capacity of 890 kN (200 kip). The load was applied with a displacement rate of  $0.5 \frac{\text{mm}}{\text{min}}$  and the load-displacement development throughout the entire test was monitored. In addition, the bond behavior after the maximum load was reached was recorded to evaluate the post-failure behavior. The applied load was recorded by the load cell integral to the test frame, while the displacement was recorded using three displacement transducers: two of them were placed on the loaded end of the rebar, while the third one was placed at the lower part of the concrete cube or the unloaded end of the rebar, as it can be seen in Figure 4.40. The data for both

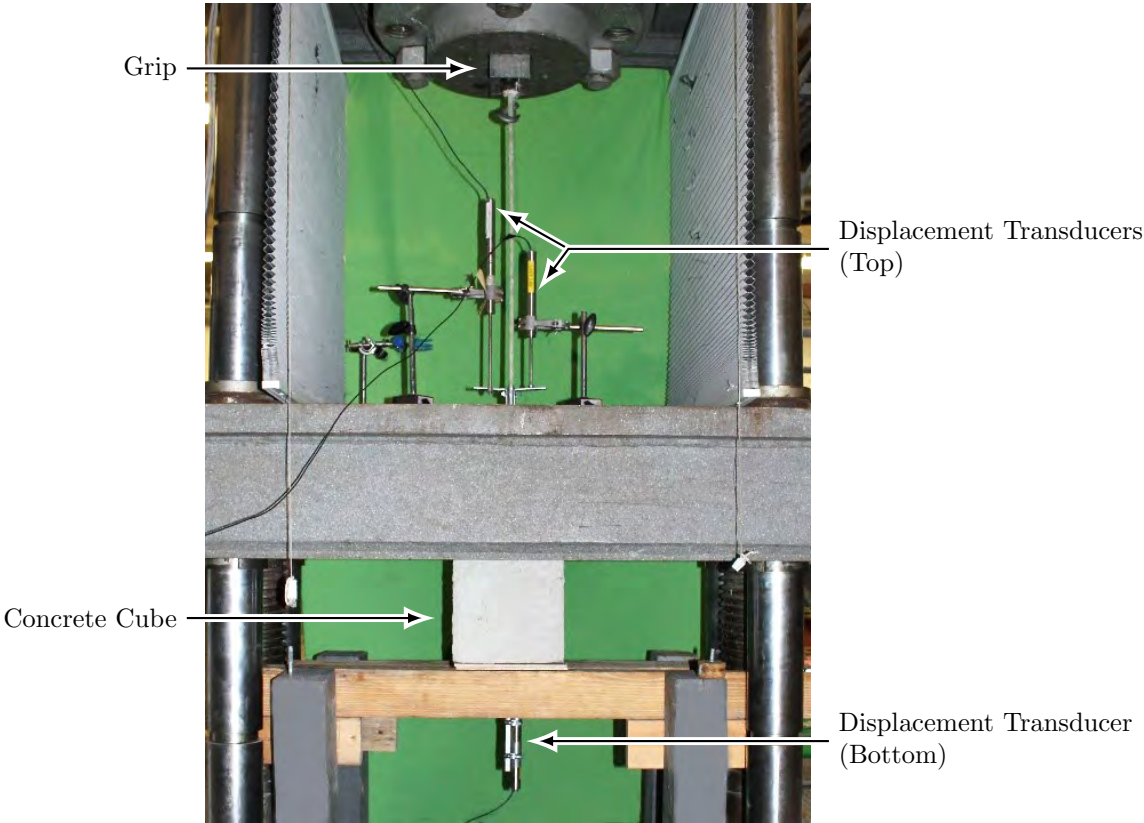


Figure 4.40: Bond-to-concrete strength experiment test setup

parameters (load and displacement) was recorded using an automatic data acquisition system with a data rate of 10 Hz. The results were filtered via Butterworth methods.



#### 4.5.9 Accelerated Conditioning Protocols — Specimen Aging

To accelerate the deterioration of GFRP rebars and to measure the long-term performance of GFRP rebars, specimens were exposed to seawater at different temperatures.

##### Equipment

All samples were submerged in seawater tanks located at the marine laboratory of the Rosenthal School of Marine and Atmospheric Science (RSMAS) at University of Miami (Miami, Florida). Six different FRP chambers were used to expose all the samples (two per temperature condition). The water was heated using conventional 4kW submersible heaters, and the temperature was constantly monitored using temperature data loggers.

##### Preparations and Specimen Production

Naked rebars were submerged in the tanks, in addition to already casted bond samples, and they were all exposed to seawater that was directly taken from the Biscayne Bay. The seawater was heated to different temperatures to accelerate the possible degradation process. In total, the Accelerated Conditioning Protocol (ACP) included three temperatures (23 °C, 40 °C, and 60 °C [74 °F, 104 °F, 140 °F]) and four different time periods (60 d, 120 d, 210 d, and 360 d). The conditioning of test samples is illustrated in Figure 4.41 and it can be seen that samples were stored in different water baths to expose individual specimen groups to different conditions. While Figure 4.41a provides an overview of the marine laboratory test setup, Figure 4.41b shows virgin material samples as they were placed in the storage tanks right before the seawater was allowed to enter the tanks. Figure 4.41c presents the specimens after six months of exposure to the ACP. In these tanks, the specimens were exposed to three different environments: Equal amounts of specimens were exposed to 23 °C, to 40 °C and to 60 °C. These temperatures were chosen because: i) 23 °C resembles laboratory conditions, ii) 60 °C is the most commonly used temperature for accelerated conditioning of FRP rebars (Chen et al., 2007; Benmokrane et al., 2017) and because it has been proposed by ASTM D 7705 (ASTM International, 2012) for aging of GFRP rebars in alkaline water, and iii) 40 °C provides reference values for cases in which extreme differences are observed between 23 °C and 60 °C.

##### Test Procedure

As stated in Chapter 4.2, the aging process was conducted only with #3 rebars because being the smallest rebar diameter inside the scope of the project, it is expected to experience the most severe effects. All the exposed rebars were submerged naked in the seawater tanks, except the samples prepared to evaluate the bond durability, which were submerged in water after the concrete cube was casted. In total, enough naked

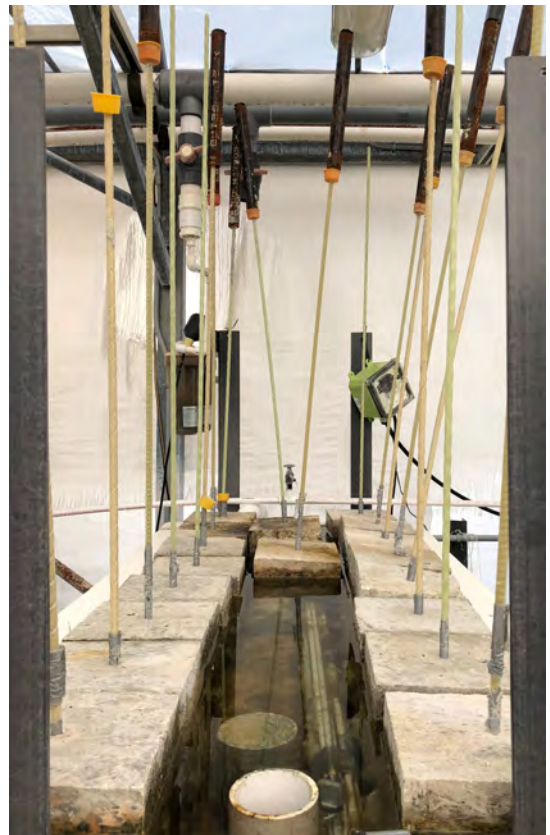
rebars and bond samples were exposed to conduct 36 test repetitions per test per rebar type, as tabulated in Table 4.2. In every case, once the defined exposure time was reached, the specimens were taken out from the water and transported to the laboratory of University of Miami. The testing plan once the rebars were taken out was consistent for every exposure period and temperature: i) the same day, the specimen preparation for all the test was done (cutting, potting, etc), ii) the day after the testing process began, testing each property per day in the following order: transverse shear, horizontal shear, moisture absorption, bond strength and tensile strength, and iii) the data was analyzed once the tests were finished.



(a) Storage tanks filled with specimens – overview



(b) Before exposure to temperature controlled seawater



(c) During exposure to temperature controlled seawater

Figure 4.41: Specimen conditioning according to accelerated conditioning protocol

# Chapter 5

## Experimental Results

### 5.1 Introduction

To concisely present all test results throughout this chapter, the acquired data from each test procedure were analyzed, filtered, and reduced, mainly to visualize the results graphically (if possible). While the following graphs present most of the test data, the most important test values (maximum stress, maximum displacement, etc.) for all specimens can be found in Appendix ???. Besides the individual specimen results, Appendix ??? also presents the most relevant statistical data for the individual test groups or samples, in which one sample groups all companion specimens of the same type.

### 5.2 Test Results from Measurements of Physical Properties

The physical properties that were tested according to the procedures described in the previous Chapter 4 included the cross-sectional dimensions, the fiber content, moisture absorption properties, and microstructure analysis via SEM imagery. The following subsections present the results accordingly, in the listed order.

#### 5.2.1 Cross-Sectional Dimensions Results

Table 5.1 provides an overview of the determined rebar properties. Because statistical evaluations revealed significant mean values, the table lists the average values (and omits standard deviation and coefficient of variation) for each characteristics. As shown in the table, the density values differed significantly between the manufacturers. The Type-B rebars had the lowest density with  $1845.3 \text{ kg/m}^3$  ( $115.20 \text{ lbs./ft}^3$ ) for the number # 3 specimens and  $1870.4 \text{ kg/m}^3$  ( $116.77 \text{ lbs./ft}^3$ ) for # 5 specimens, while the # 5 Type-C specimens measured the highest density with  $2155.3 \text{ kg/m}^3$  ( $134.55 \text{ lbs./ft}^3$ ). However, the density of the Type-C # 3

Table 5.1: Average cross-sectional properties results for all rebars

Rebar Type	Specific Gravity $\varphi/\varphi_w$	Density $\varphi$ kg/m <sup>3</sup>	Area A		Diameter d		
			mm <sup>2</sup>	in. <sup>2</sup>	mm	in.	
# 3	Type-A	2.05	2047	81.0	0.126	10.2	0.402
	Type-B	1.85	1845	86.1	0.133	10.5	0.413
	Type-C	2.01	2008	80.0	0.124	9.8	0.386
# 5	Type-A	2.06	2057	214.7	0.333	16.5	0.650
	Type-B	1.87	1870	219.1	0.340	16.7	0.657
	Type-C	2.16	2155	188.6	0.292	15.5	0.610
# 6	Type-C	2.06	2056	268.4	0.416	18.5	0.727
# 8	Type-A	2.08	2076	526.5	0.816	25.9	1.019
	Type-B	1.86	1861	541.3	0.839	26.3	1.033

rebar was significantly lower with 2008.1 kg/m<sup>3</sup> (125.36 lbs./ft<sup>3</sup>). The density of the two Type-A rebar sizes was almost identical with a density of about 2050 kg/m<sup>3</sup> (128.00 lbs./ft<sup>3</sup>), regardless of the bar size. While the measured diameter of the Type-A and Type-B rebars were larger than originally specified by the manufacturer, the Type-C #5 rebars measured a slightly smaller diameters than the values provided by the producer. This trend was also followed for the larger rebar diameters (#6 and #8 rebars). Type B #8 rebars showed the lowest density with 1861.0 kg/m<sup>3</sup> (116.18 lbs./ft<sup>3</sup>) while the density of Type-A rebars was 2076.0 kg/m<sup>3</sup> (129.60 lbs./ft<sup>3</sup>) for #8. Type C rebars (#6) however, had a density of 2056.0 kg/m<sup>3</sup> (128.35 lbs./ft<sup>3</sup>).

### 5.2.2 Fiber Content Results

The results for the fiber content measurements are visualized in Figure 5.1 to compare the individually tested specimens, the rebar sizes, and the rebar types. While each row in the figure represents a specific rebar type (manufacturer), each column shows a specific rebar size or diameter. One vertical bar in the charts shows the combined results for one tested specimen. The diagonally shaded (red) part of the bars are indicative of the fiber content, and the cross hatched (blue) parts symbolize the resin content. Because Type-A rebars were sand coated (for improved bond-to-concrete strength), the graphs in the top row also include material above 100%, represented by the solid black bars. It is emphasized that the 100% values for the Type-A rebars was not based on the total specimen weight, but on the total specimen weight minus the weight of the sand. Because the surface coating had a smaller percentage weight contribution as the rebar size increased, the solid black part of the bars reduced in size from left to right. When comparing the rebar types to one another,

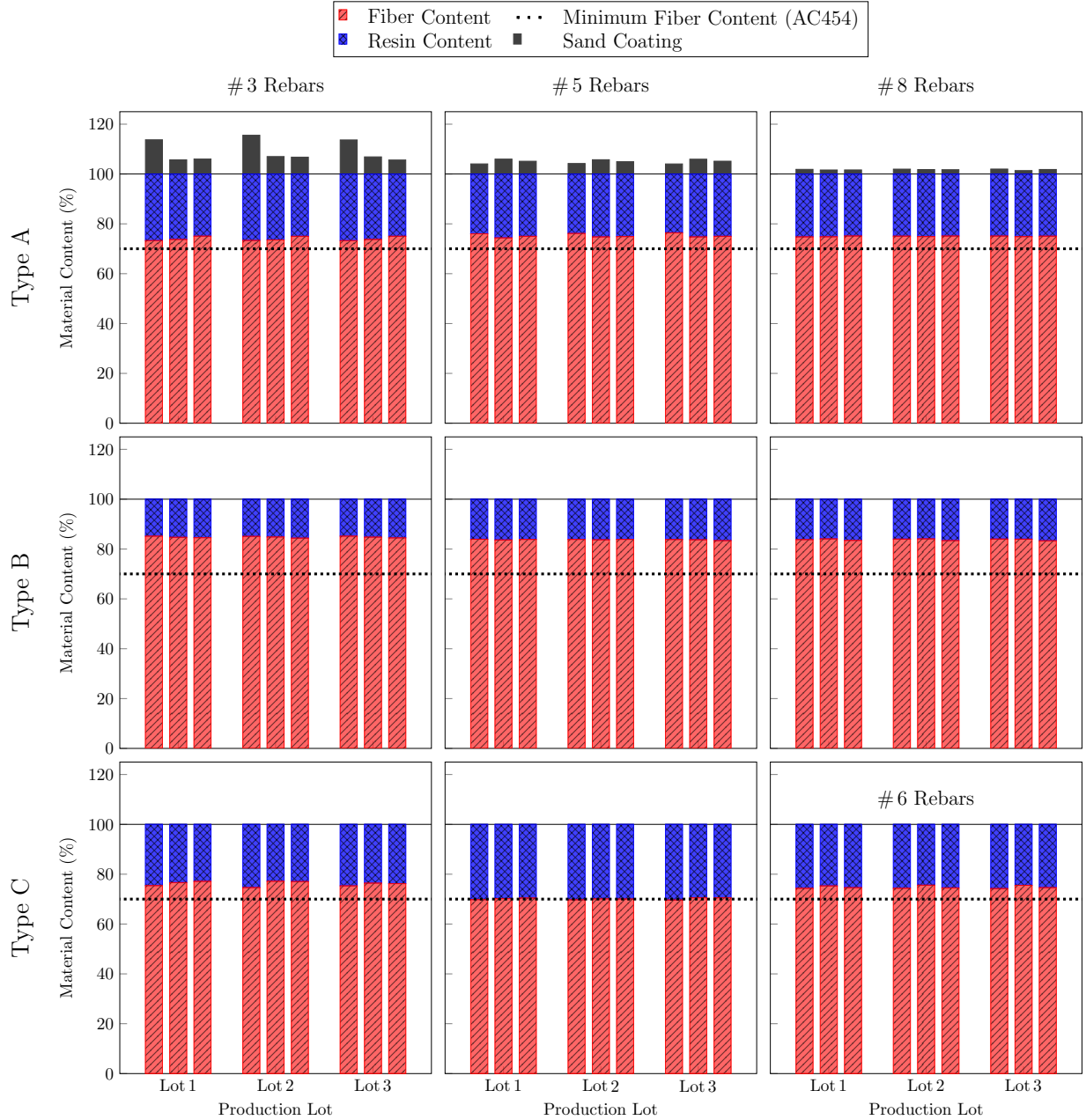


Figure 5.1: Fiber content results — relative material proportions

it can be seen that the fiber contents for the Type-A rebars were comparable to the one for the Type-C rebars, and that the Type-B rebars contained the highest percentage of fibers. However, all rebars meet the 70 % minimum fiber content requirement outlined in ICCE AC454 (ICC Evaluation Service, 2016). In general, it can be noted that the fiber and resin contents were considerably consistent for each manufacturer, independent of the rebar size or the tested lots. The only exception were the #5 Type-C rebars as their fiber content was lower than the ones for #3 and #5, but still the values were acceptable. Overall, the measurements showed proper production consistency for all rebar types and sizes.

### 5.2.3 Moisture Absorption Results

Figure 5.2 displays the weight change of the tested rebars in response to storage under deionized water for extended time periods. The graphs show a clear similarity in moisture absorption properties for Type-B and

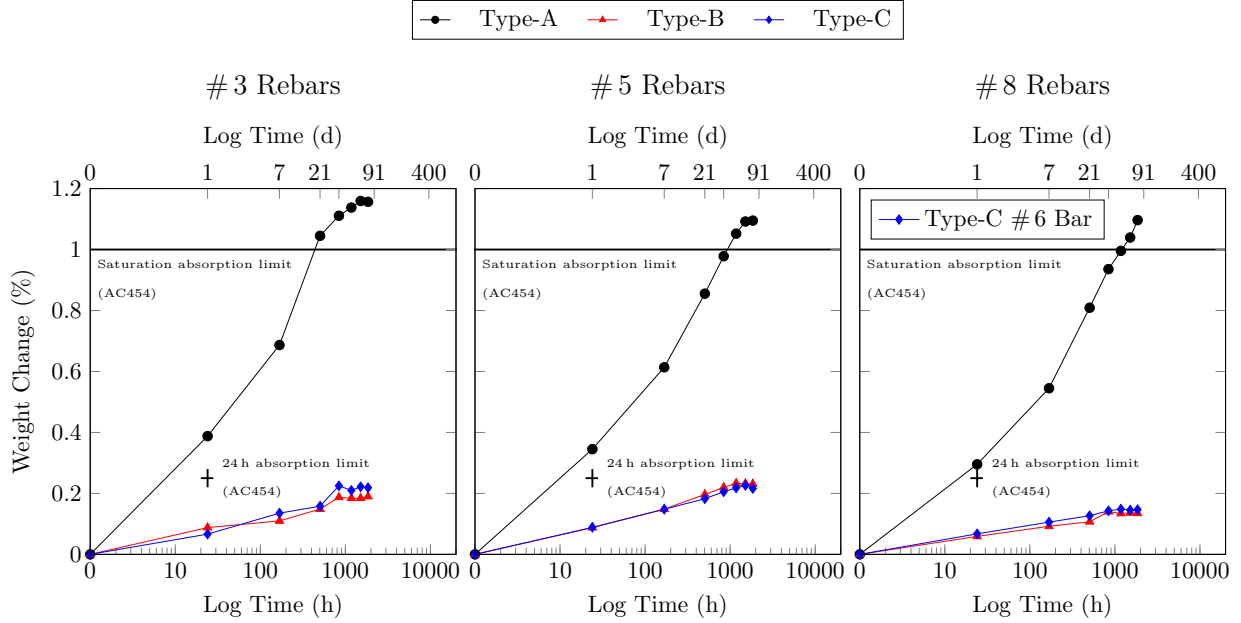


Figure 5.2: Moisture absorption results — relative weight gain (average values for all rebar types and sizes)

Type-C rebars, and a significantly different behavior for Type-A rebars. Independent of the tested rebar sizes, the absorption values for Type-B and Type-C rebars remained under 0.25% weight change until they reached a constant mass. However, all sizes from the Type-A rebars exceeded the initial 24 h 0.25% weight change limitation provided in ICCE AC454 (ICC Evaluation Service, 2016) and were saturated well above a weight change percentage of 1.0. Accordingly, no Type-A rebar met the absorption limitations outlined in ICCE AC454 (ICC Evaluation Service, 2016). Because the absorption properties are dependent on the porosity of the microstructure, each rebar type was also evaluated via SEM technology and the findings are presented in the next subsection.

### 5.2.4 Microstructure via SEM Imagery

The pictures in this subsection were taken to exemplify the microstructure of the cross section of representative GFRP rebar specimens. Figure 5.3 illustrates a subpart of the cross section, perpendicular to the fiber axis, of each rebar type. Each SEM picture that was chosen for the presented figure includes an example of the interface between the rebar and the surface enhancement feature, while showing a significant portion of the cross-sectional area. The pictures show that rebar Type-A was most porous while Type-B and Type-C

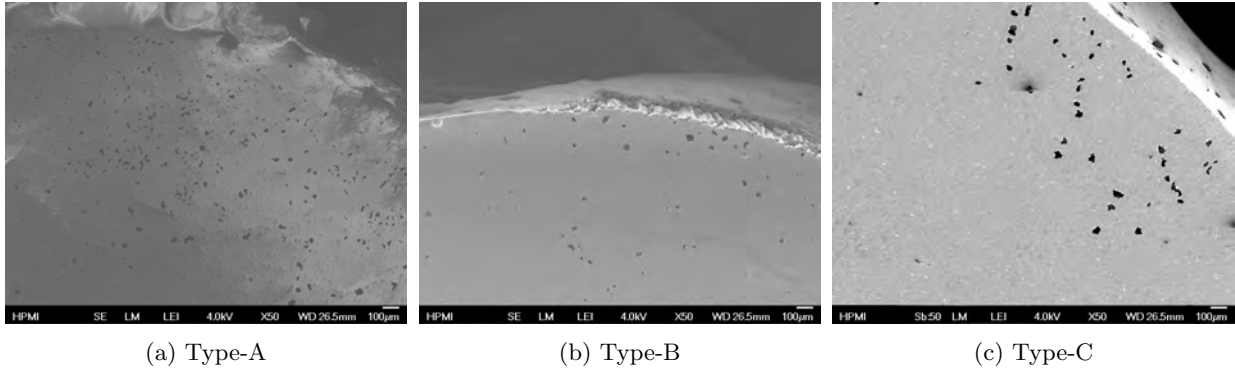


Figure 5.3: SEM pictures of virgin rebar materials — Rebar-surface enhancement interface

were comparable dense. The micro-structural voids were most concentrated around the perimeter; while possibly circumstantial for these pictures, Figure 5.4 further emphasizes this finding as it displays combined SEM pictures that were taken to capture the micro structure of each rebar type and size. While each row represents a specific rebar type, each column indicates a particular rebar size. Because every SEM picture was taken with the same resolution — to produce pictures similar to the ones found in Figure 5.3 — the pictures in the last column (for the larger rebars) were assembled from more than 144 individual SEM images. Again, it can be seen that Type-B rebars were as dense as Type-C rebars, while Type-A rebars had a significant void volume. For all rebar types, more pores were found in areas closer to the perimeter than in areas closer to the rebar core.

In addition to the SEM pictures of representative cross sections, images of the surface enhancements were captured to further study the concrete-rebar interface. The images in Figure 5.5 show the outer surface of the rebar parallel to the longitudinal axis. As seen in Figure 5.5c, the resin that bound the sand coating to rebar Type-A did not fully cover the longitudinal fibers and numerous holes in the outer resin layer were observed. Presumably, the majority of the air voids in the outer resin resulted from sand grains that were not properly adhered. For rebar Type-B, some of the outermost fibers were also exposed and not fully covered with resin. A thick parallel layer of resin surrounded the helical wrapping fibers, which were diagonally oriented from the bottom center of the picture to the top right (c.f. Figure 5.5b). Finally, Figure 5.5c shows that the outer surface for Type-C rebars was most densely covered and had minor defects with minimal exposure of longitudinal fibers. The figure clearly shows that the lugs (to improve the bond-to-concrete properties of the rebar) were made completely from resin.

### 5.3 Test Results from Measurements of Strength Properties

To fully characterize the GFRP rebars for strength properties, individual specimens were tested for transverse shear, horizontal shear, tensile, and bond-to-concrete performance. The following subsections concisely



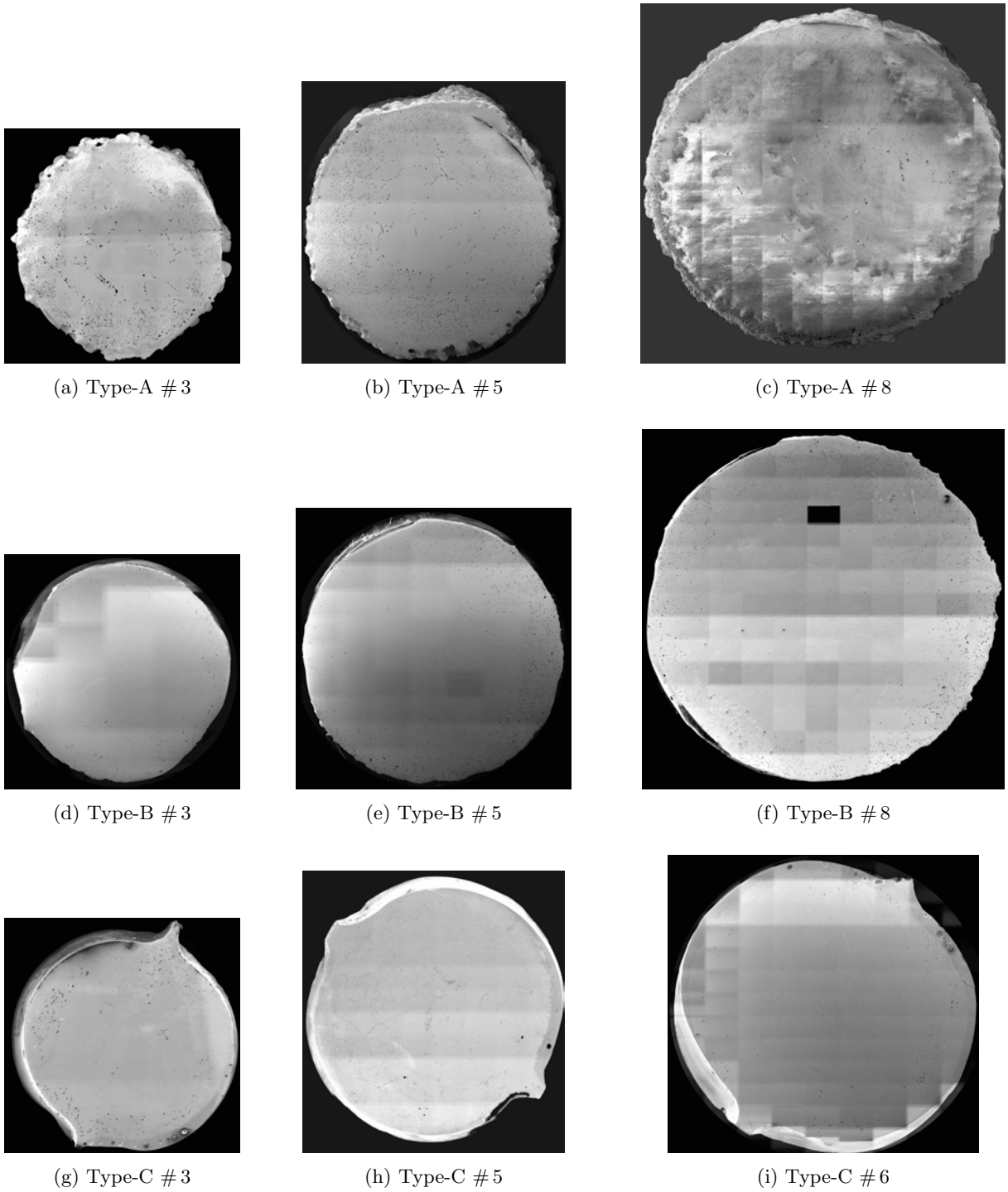
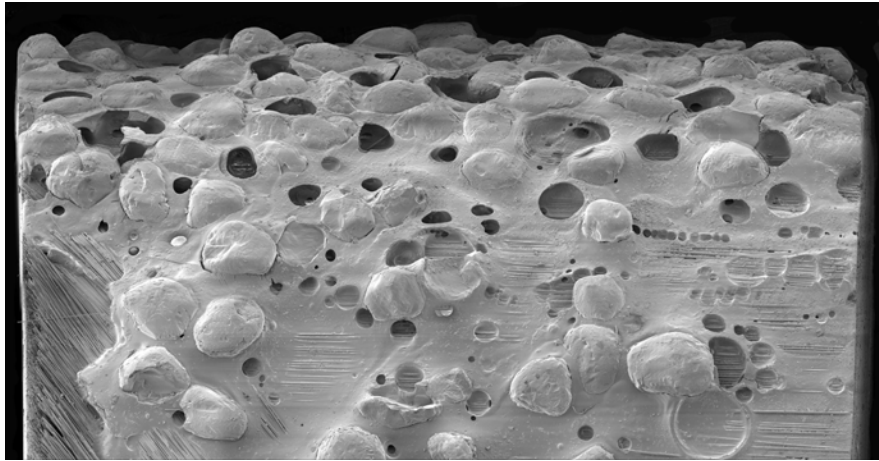
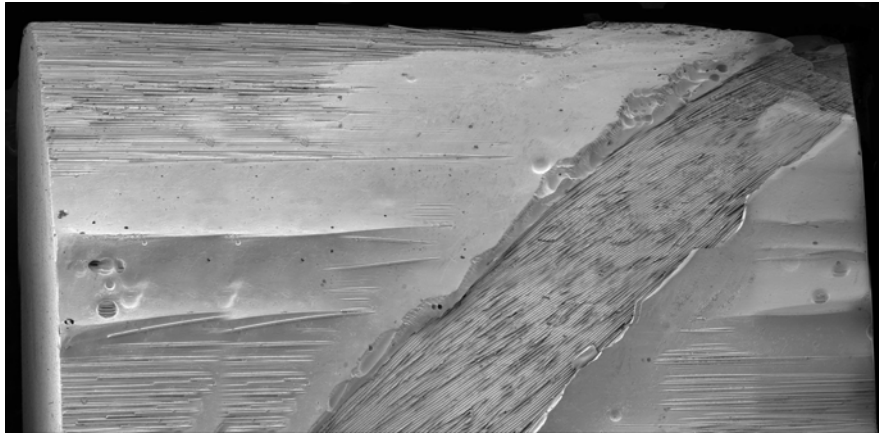


Figure 5.4: SEM pictures of virgin rebar materials — Cross section

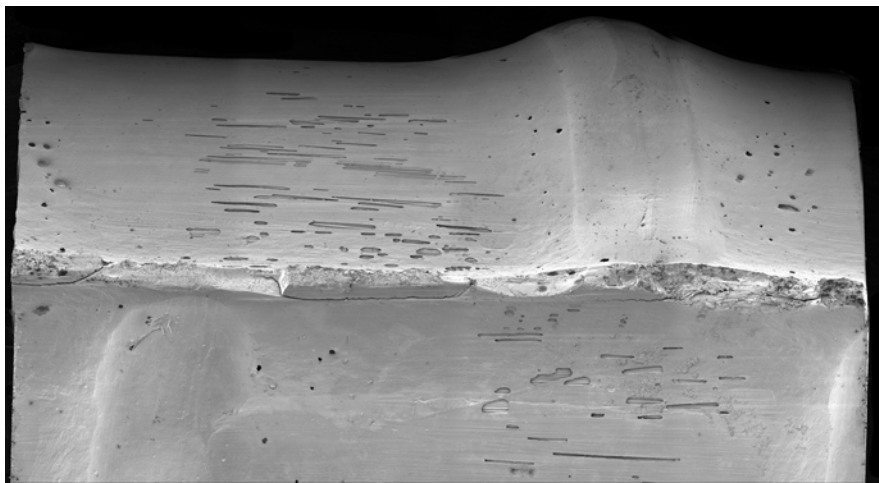
present the generalized rebar behavior for all types and sizes. While the data is mostly presented in graphical format, the individual maximum values for each individual specimen can be found in Appendix ??.



(a) Type-A



(b) Type-B



(c) Type-C

Figure 5.5: SEM pictures of virgin rebar materials — Surface enhancement

### 5.3.1 Transverse Shear Strength Results

Figure 5.6 provides a visual comparison of the transverse shear behavior throughout all tested specimens. While the values on the y-axis describe the load development, the x-axis is indicative of the displacement

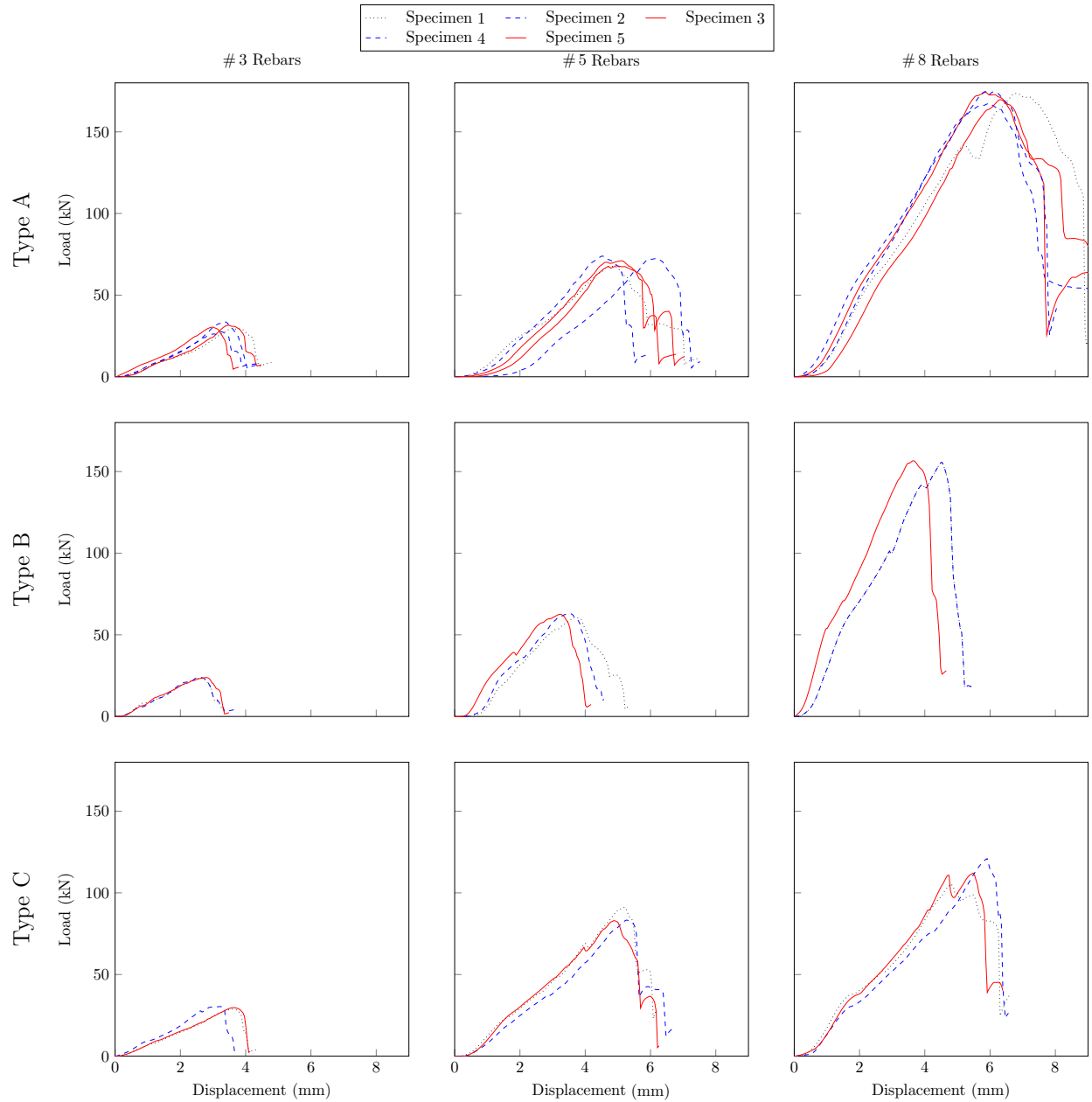


Figure 5.6: Transverse shear behavior of virgin material

of the top fiber (or the shear blade). Accordingly, it can be seen that the larger rebar diameters sustained higher loads at higher displacements. Each rebar size sustained the maximum test load between a fiber displacement of  $\frac{1}{4}$  and  $\frac{1}{3}$  of the rebar diameter. However, when calculating the stress values, by dividing the measured loads by two time (double shear) the corresponding cross-sectional areas, the transverse shear

stiffness increased with increasing rebar diameter.

**Mode of Failure**

The failure mode was identical for all tested rebars, independent of manufacturer and rebar size. The test fixture according to ASTM was designed to produce a “scissor-like” cut at the center, applying direct shear stresses perpendicular to the longitudinal axis of the rebar. Accordingly, all GFRP rebars were cut along two planes, separated by the distance equivalent to the width of the upper shear blade. Figure 5.7 shows the failed specimens. To study the failure process, the broken GFRP rebars were analyzed in detail. To exemplify

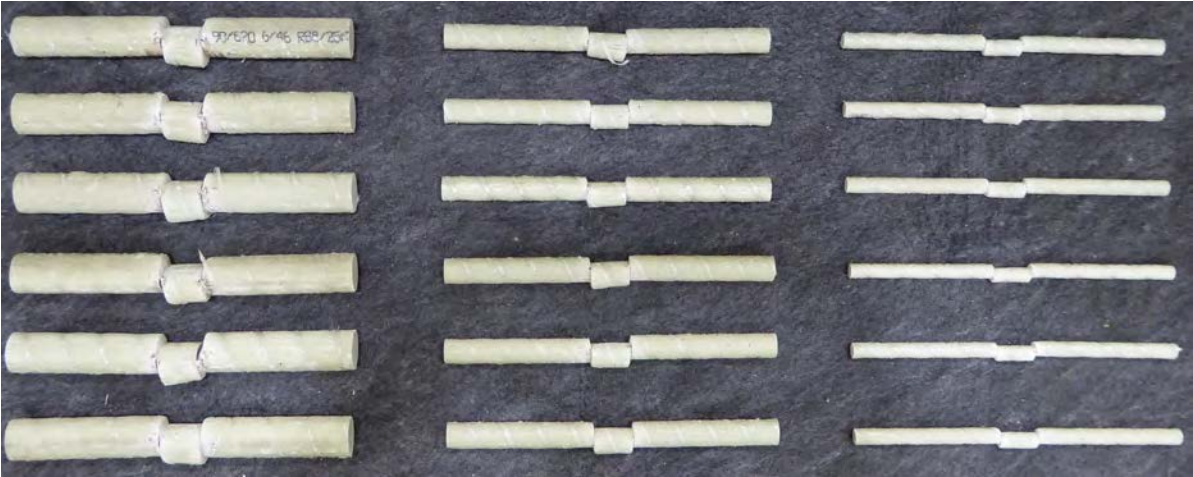


Figure 5.7: Transverse shear test — failure mode of all tested rebar sizes

the observed shear failure, Figure 5.8 shows a close-up of the failure pattern for Type-A #8 rebars. It can be seen that the fibers were initially aligned with the longitudinal direction, but throughout the test they tend to bend, as the upper blade goes through the two lower blades. In Figure 5.8c, it can be seen how the outer fibers were cut perpendicular to the longitudinal axis, but the fibers closer to the center were bent downwards (at the top) or upwards (at the bottom) until the final failure was reached.

**5.3.2 Horizontal Shear Strength Results**

The response of the tested GFRP rebars to a short-span three point load is visualized in Figure 5.9 to illustrate the apparent horizontal shear behavior. Similar to the graphs shown for the transverse shear tests, the y-axis displays the load that was sustained by the specimen throughout the test, while the x-axis is indicative of the displacement of the top fiber of the bend rebar. As seen in the graphs, after initial seating the specimens displayed a fairly linear behavior until 85 % of the maximum load was reached. Then the curves flattened and after a maximum displacement of 2 mm, the peak load was reached and a load drop occurred promptly. However, some load was recovered until the next sudden load drop.



(a) Longitudinal view



(b) Isometric view



(c) Close-up of cutting facet

Figure 5.8: Transverse shear test — failure mode in detail

### Mode of Failure

The failure mode was similar for all specimens, as shown in Figure 5.10. The test consisted of a three point load test with a short span length to produce shear stresses along the horizontal plane parallel to the GFRP rebar axis. If an improper span-to-diameter ratio is chosen for this test, flexural stresses, instead of apparent horizontal shear stresses, may dominate the failure pattern ASTM D4475 (ASTM International, 2008a). However, in this research project, that was not the case, and all specimens suffered the apparent horizontal shear failure, forming a horizontal failure plane, as shown in Figure 5.10. It can be seen, that failure occurred in a horizontal plane on the longitudinal axis of the GFRP rebar. Most of the specimens, showed more than one failure plane. This happened because the test was continued after the first load peak was reached to study the post failure behavior. However, the tests were stopped when three or four additional failure planes appeared. Each of these planes, developed at each of the load peaks. Figure 5.11 exemplifies a detailed view of the horizontal shear failure for Type-A #8 specimen. It can be seen how the horizontal plane was generated along the longitudinal axis of the specimen, forming a continuous plane of failure throughout the

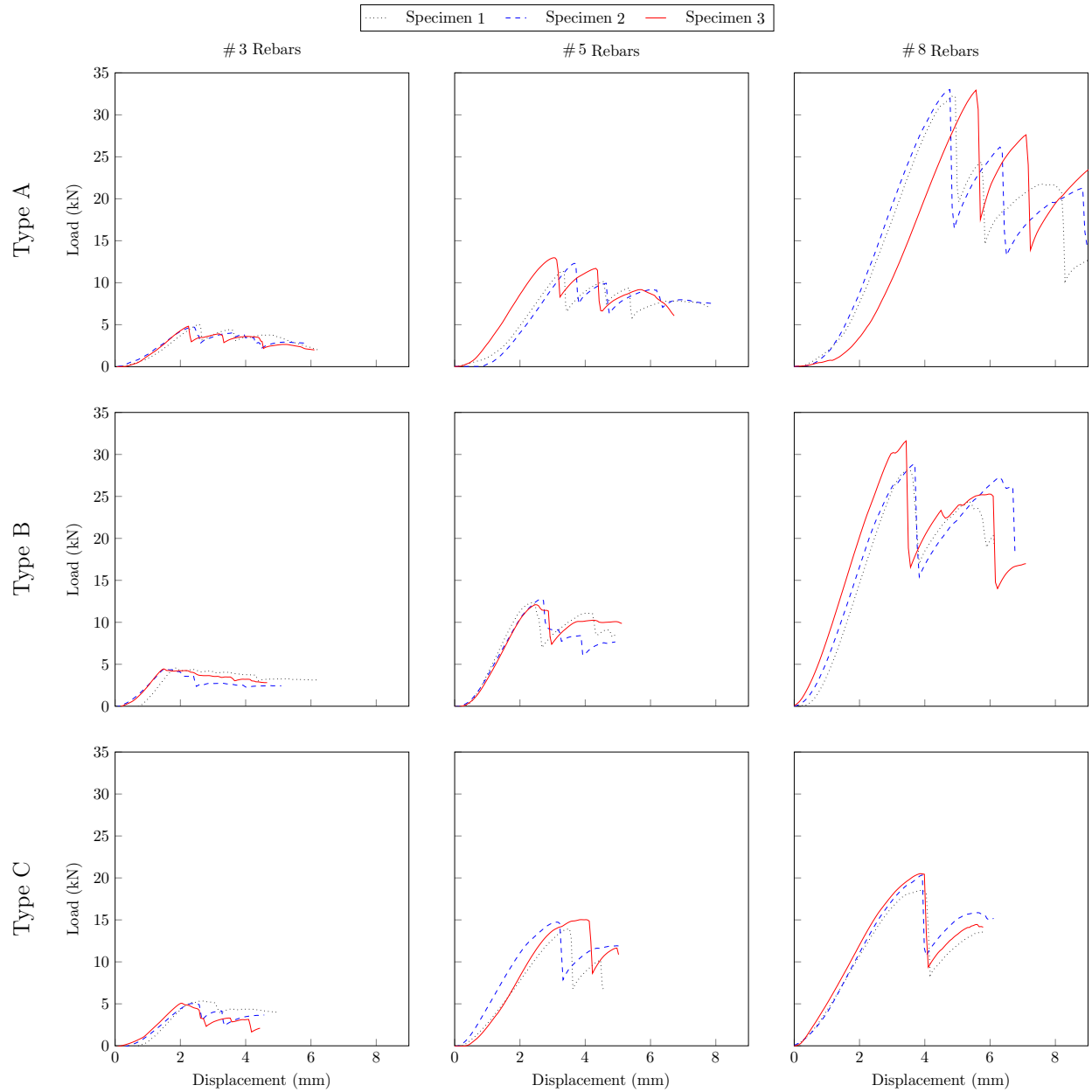


Figure 5.9: Horizontal shear behavior of virgin material

rebar specimen.

### 5.3.3 Tensile Properties Results

The tensile behavior was measured via a load cell, extensometers, and the extension of the load frame cross-head. The following Figure 5.12 shows complete tensile load behavior of the three different rebar types and sizes and therefore, includes measurements from the extensometer *and* the cross-head displacement. The graphs display the longitudinal strain along the x-axis and the measured load on the vertical y-axis. At a value of 0.5%, the extensometer was removed (to protect the equipment) and the data afterwards was taken



(a) Type-A #3



(b) Type-A #5

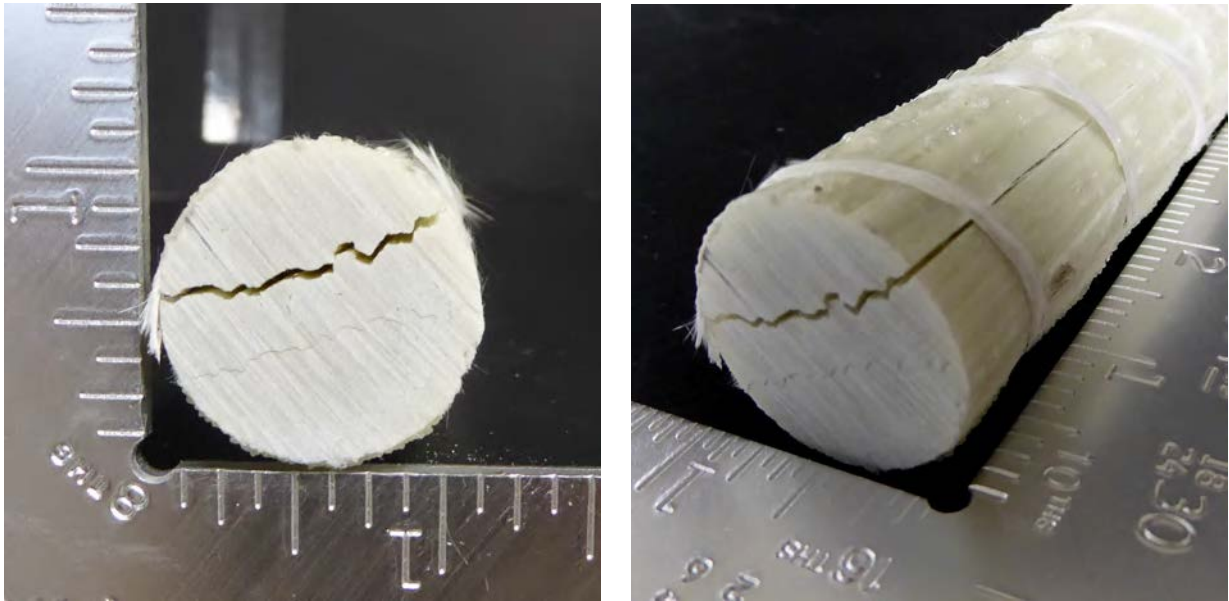


(c) Type-A #8

Figure 5.10: Horizontal shear test — failure mode

from the cross-head extension. To determine the strain values for the latter part, the cross-head extension was divided by the distance between the grips, which was not as precisely determined as the extensometer opening. Therefore, a kink appears in the curves shown in Figure 5.12 at a 0.5% strain value. However, the data shows that the tensile behavior of all bars, independent of bar type or size, was similar because the shapes of the curves are comparable. The maximum recorded loads increase from the left column to the right column, because larger rebars provide more room for more load carrying fibers. Due to the increased free specimen length for larger rebar sizes, the strain values also grew from left to right, which lead to the similarity of the different data curves. The graphs show that the load capacity of the GFRP rebars was dependent on the cross-sectional dimensions and that larger rebars withstand more load before failure.

To quantify and compare the elastic moduli of the tested GFRP rebars, the stress-strain behavior shown in Figure 5.13 was evaluated. Because ASTM D7205 (ASTM International, 2011b) suggests determining the elastic modulus throughout the initial 3% and because the extensometer (for exact measurement of the strain of the outermost fibers) was removed at a strain value of 5%, the graphs show a limited strain range along



(a) Front view

(b) Isometric view

Figure 5.11: Horizontal shear test — failure mode in detail

the x-axis and a maximum corresponding stress of 400 MPa (5.8 ksi). Despite the different load capacities shown in Figure 5.12, the slopes of the stress-strain curves in Figure 5.13 are comparable and nearly identical (per row) for each rebar type. The numeric values for the elastic moduli can be found in Appendix D for each individual specimen, while the average results are listed in the following summary subsection ??.

### Mode of Failure

According to ASTM D7205 (ASTM International, 2011b) three different failure modes may occur when testing GFRP rebars in tension: (1) tensile rupture, (2) rebar slippage (bar slips out of anchor), and (3) anchor slippage (anchor slips out of fixture/grips). Failure modes (2) rebar slippage and (3) anchor slippage are caused by insufficient specimen preparation or improper test procedure. Because failure would not be due to material performance in those cases, the test results from specimens that failed in failure mode (2) or (3) are not useful. However, in this research project, no specimen failed due to rebar or anchor slippage, and all tensile specimens failed similarly due to material failure (failure mode 1) of the GFRP rebar within the free specimen length. Hence, tensile rupture of the GFRP rebar was the recorded failure mode for each bar that was tested.

After each rebar group was taken to ultimate failure and removed from the test frame, the specimens were arranged on the laboratory floor to observe and record the failure modes; these failure modes are displayed in the following Figures 5.14 through 5.16. Figure 5.14 shows the characteristic failure patterns for the Type-A rebars. For these specimens, a clear brush-like failure pattern was noted and the fibers delaminated along the



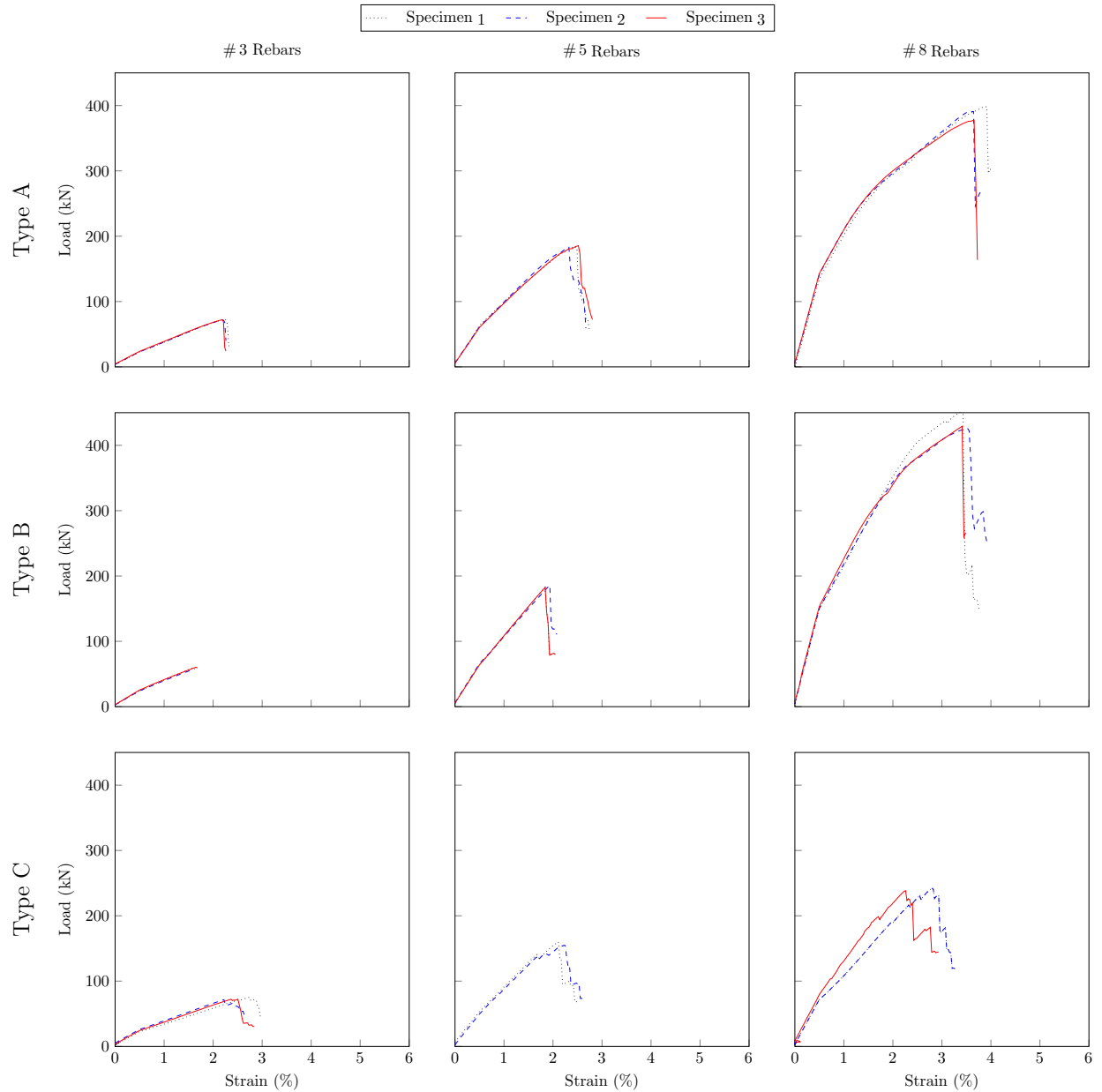


Figure 5.12: Tensile behavior of virgin material

free length of the specimen. Throughout testing, it was noted that the fibers that provided the helical wraps on the rebar surface delaminated at approximately 70% of the ultimate load, significantly before failure in the longitudinal fibers occurred. However, this premature failure did not have an influence on the load-displacement development of the rebars (cf. Figure 5.12). The failed helical wrap fibers can be distinguished from the longitudinal fibers in Figure 5.14 by the lighter color.

Similar to the previous photos, Figure 5.15 illustrates the post-failure pattern for the Type-B rebar specimens. All specimens, regardless of their dimensions, displayed similar failure patterns. The failure mode differed slightly from the one observed for Type-A rebar specimens because the fibers did not form

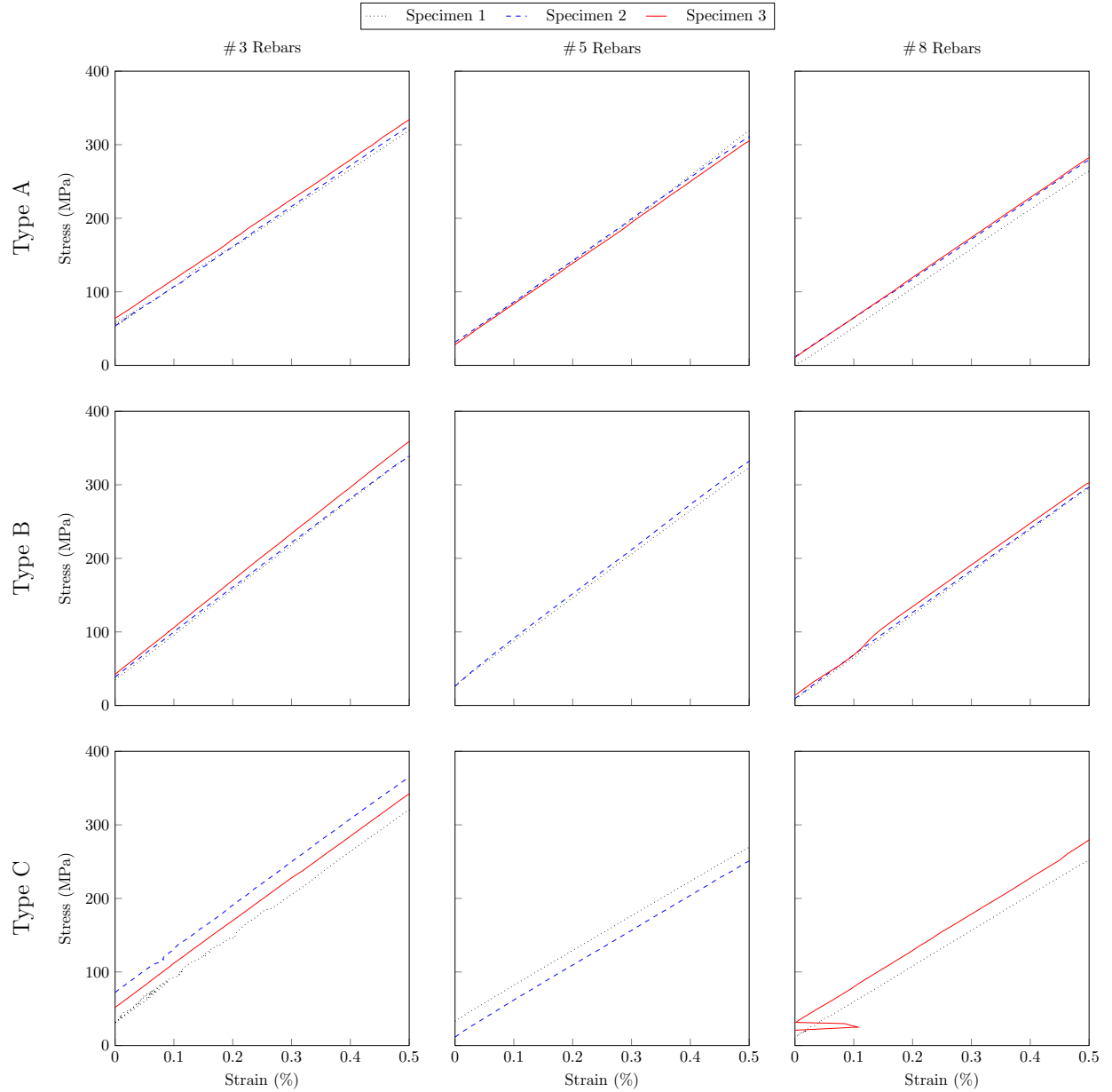


Figure 5.13: Stress-strain behavior of virgin material (elastic modulus)

such a distinct brush-like failure pattern. However, all specimens suffered fiber delamination throughout the entire free specimen length similar to the failure pattern of the following type-C rebars described below (cf. Figure 5.16). Furthermore, similar to Type-A rebars, delamination of the helical wraps occurred before the longitudinal fibers failed, at approximately 70% of the ultimate load. For these specimens, delamination was clearly visible because the color of the resin matrix turned from pale green to white as soon as a crack occurred (must distinctly be seen in Figure 5.15a).

The ultimate failure patterns for the tested Type-C rebars are shown in Figure 5.16. The failure pattern of all specimens was similar, regardless of specimen dimensions. All specimens showed a delamination of the



(a) Type-A #3



(b) Type-A #5



(c) Type-A #8

Figure 5.14: Tensile failure of tensile tested rebars — Type-A

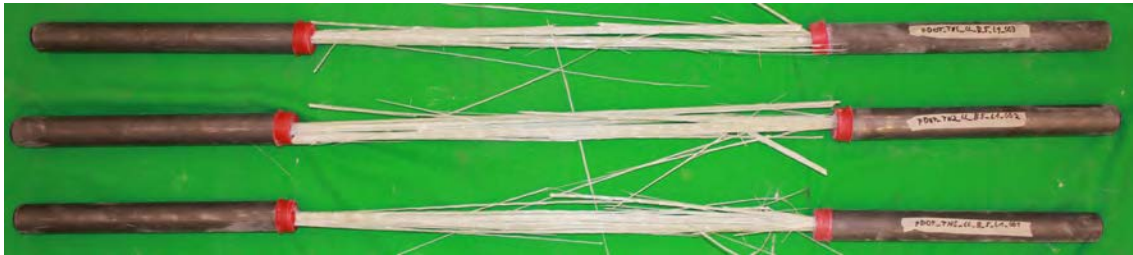
fibers over the entire free specimen length, which led to the shown feathered out, brush-like failure pattern. Accordingly, no explicit localized failure point was identified. In fact, every single individual fiber had a different failure point (along the axis of the rebar), which was most likely to occur within close proximity of the anchors.

In summary, the failure mode of all specimens was very comparable. Rebar failure occurred progressively from the outside toward the inside (the outer fibers failed before the inner ones)<sup>1</sup>. All tested specimens showed a delamination of the fibers over the entire free specimen length, as shown in the figures above. It was not possible to localize an explicit failure point of the specimen because every single fiber had a different fracture point. After breakage, the fibers immediately delaminated from the rest of the rebar. The broken

<sup>1</sup> This behavior was captured and noted because the specimens were also filmed with high-speed video technology. No further discussion is offered here because the high-speed video analysis was outside of the scope of this research project.



(a) Type-B #3



(b) Type-B #5



(c) Type-B #8

Figure 5.15: Tensile failure of tensile tested rebars — Type-B

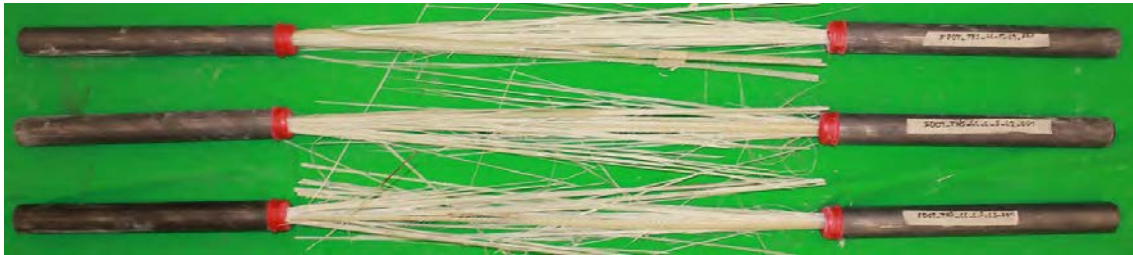
and delaminated fibers feathered out, forming a brush-like failure pattern. While the broken fibers of Type-A and Type-C rebars were widely spread out, the Type-B rebar fibers were more contained. Furthermore, a premature delamination — of the fibers that provided the helical wraps (Type-A and Type-B) — was noted for all specimens. The delamination of these helical wraps occurred at approximately 70% of the ultimate load. This, however, did not have an influence on the load-displacement development of the rebars.

### 5.3.4 Bond-to-Concrete Strength Results

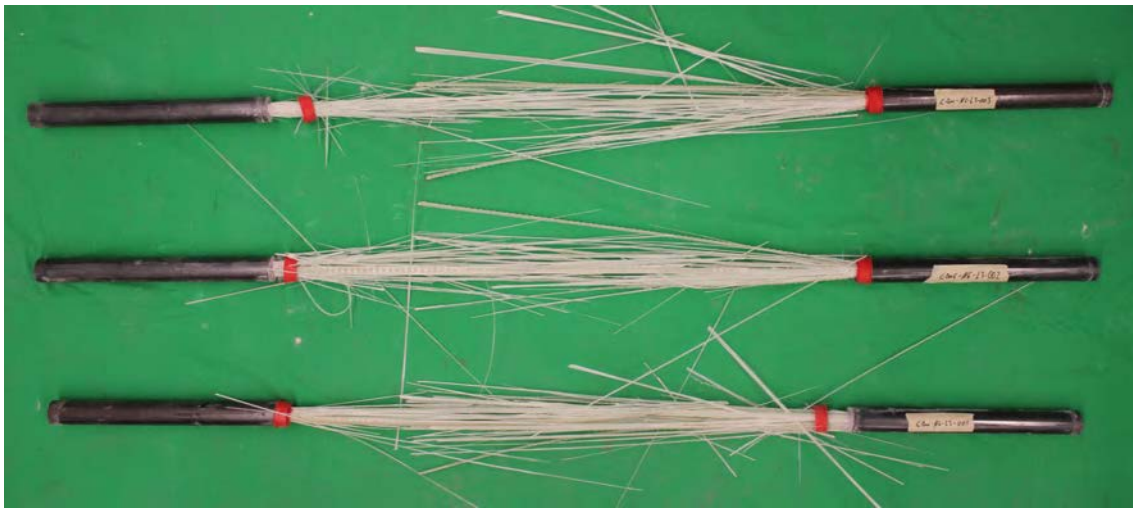
The bond-to-concrete behavior was observed to measure the rebar slip at the load and free end of each cube as described in Chapter 4. Figure 5.17 illustrates the failure envelopes for the three tested rebar types based on three specimens per envelope. It can be seen that Type-A rebars measured the highest bond stiffness, followed by Type-C rebars, and that Type-B rebars showed the least stiff bond behavior in this research project. The observed slip behavior at the free specimen end was significantly different for the three tested surface enhancements. The combination of sand coating and helical wraps (Type-A) lead to the strongest bond, which appeared linear for initial 80% of the bond load capacity, and the highest average bond strength.



(a) Type-C #3



(b) Type-C #5



(c) Type-C #8

Figure 5.16: Tensile failure of tensile tested rebars — Type-C

After the bond capacity was reached, the rebars continued to slip but without a noticeable increase or decrease in the applied load. The linear bond-to-concrete behavior for surface lugs (Type-C) became nonlinear after the initial 30% of the bond load capacity. The load continued to increase thereafter, but with notable slip at the free end. Rebars with helical groove (without sand on the surface) showed the weakest bond-to-concrete performance. But more importantly, those rebars slipped significantly as they continued to accept additional load.

### Mode of Failure

The failure appearance of the tested FRP rebars and the concrete cubes were documented for each specimen. After the pullout test, a picture of the rebar portion that used to be embedded in the concrete was taken, and

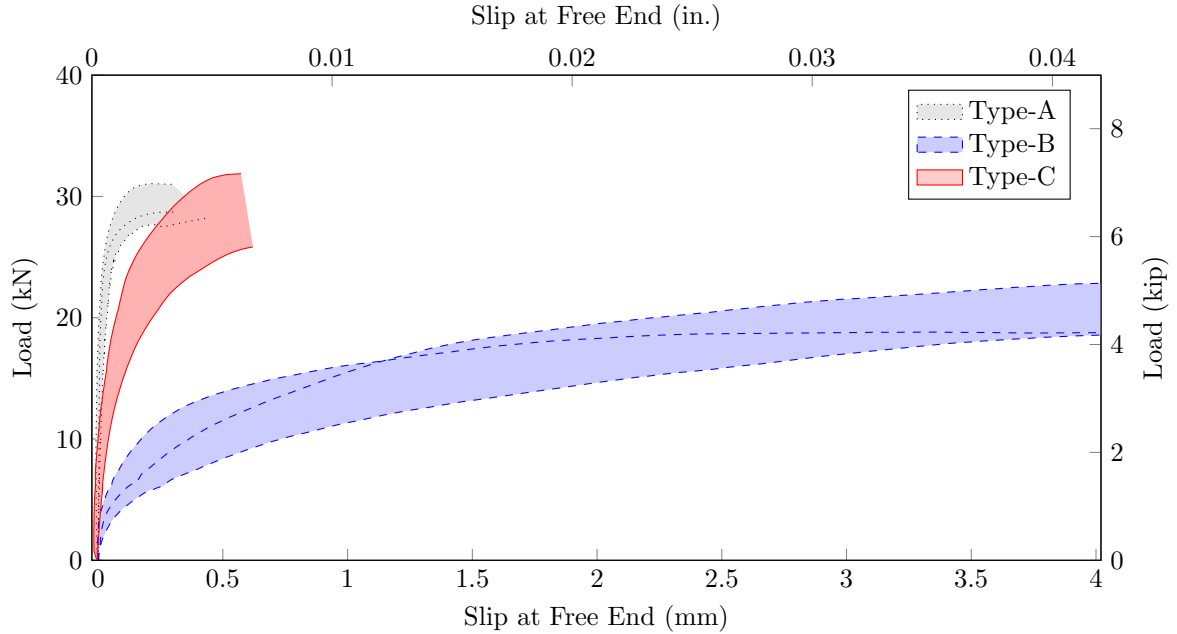
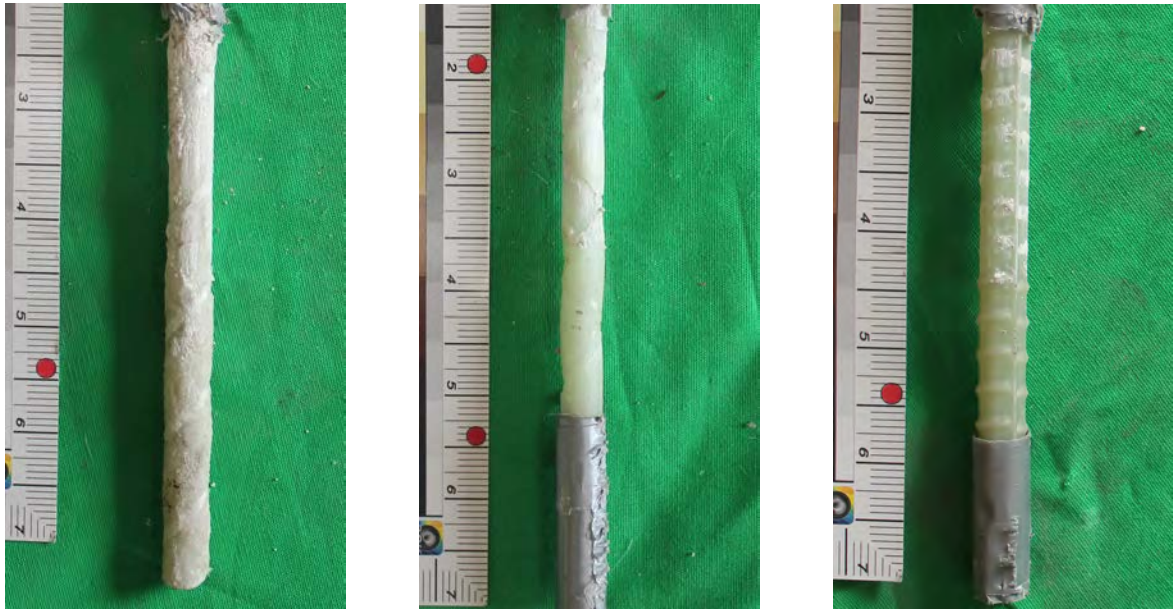


Figure 5.17: Bond-to-concrete behavior of virgin material

a picture of the concrete at the former interface was captured. For the latter, it was necessary to manually split the concrete cube after each specimen test was completed because none of the pullout tests produced a concrete split failure<sup>2</sup>. In other words, all specimens slipped out due to failure at the rebar-concrete interface, more specifically due to rupture of the GFRP rebar surface enhancement. Representative pictures of the failed surface enhancement for each rebar type are illustrated in Figure 5.18 for clarification of the surface enhancement dependent failure. The rebars in these pictures are arranged such that the cube would have been on the bottom and the rebar were pulled out of the cube toward the top of the picture. The photos show that the rebar core remained intact and that each surface was abraded. In Figure 5.18a the sand coat failed throughout the bonded length and on the right side of the rebar it can be seen that virtually no sand grain remained on the surface. For Type-B rebars in Figure 5.18b, the rebar held on to some cement paste in and close to the helical groves but the majority of the rebar appeared clean after pullout. The lugs of rebar Type-C were completely sheared off during pullout testing, and the final failure appeared as shown in Figure 5.18c. The lugs were evidently made from resin only and it can be assumed that bond strength of Type-C rebars was mainly affected by the shear strength of the resin.

While the numeric durability results are presented in the following section, the appearance of pulled out rebars after material degradation are shown here for direct comparison. Based on the SEM pictures shown above, it was clear that the GFRP rebars suffered highest degradation for longer duration in the 60 °C

<sup>2</sup> It is noted that the concrete cubes in this research project did not split because of the chosen limited rebar size (#3 only). Companion tests with larger rebar diameter specimens were also conducted — outside of the scope of this research project — and it was found that splitting of the concrete cubes becomes more likely as the rebar diameter increases.



(a) Type-A (b) Type-B (c) Type-C

Figure 5.18: Bond failure at rebar interface of all rebar types in virgin state

saltwater environment. Accordingly, Figure 5.19 illustrates the three different rebar types as they appeared after 365 days at the highest exposure temperature only. Similar to Figure 5.18, Figure 5.19 shows that the



(a) Type-A (b) Type-B (c) Type-C

Figure 5.19: Bond failure at rebar interface of all rebar types after 365 day of exposure to 60 °C saltwater

bond failure was driven by failure of the GFRP rebar surface enhancement. However, Figures 5.19a and 5.19b show that the outermost fibers of the rebar, beneath the surface enhancement, were also affected and some of them fractured and were exposed (best seen in Figure 5.19a). While Figure 5.19c shows that the lugs

of rebar Type-C were sheared off (just as they were in the virgin state), it also shows that the accelerated conditioning had a degrading effect and lead to a more random bond failure that was not as clean as it was in the virgin state.

As mentioned above, the cubes were split open after the pullout tests were completed to evaluate the internal concrete failure surface. The appearance of the concrete after virgin pullout testing is documented in Figure 5.20 and the photos were oriented to show the pullout direction toward the top of each picture.

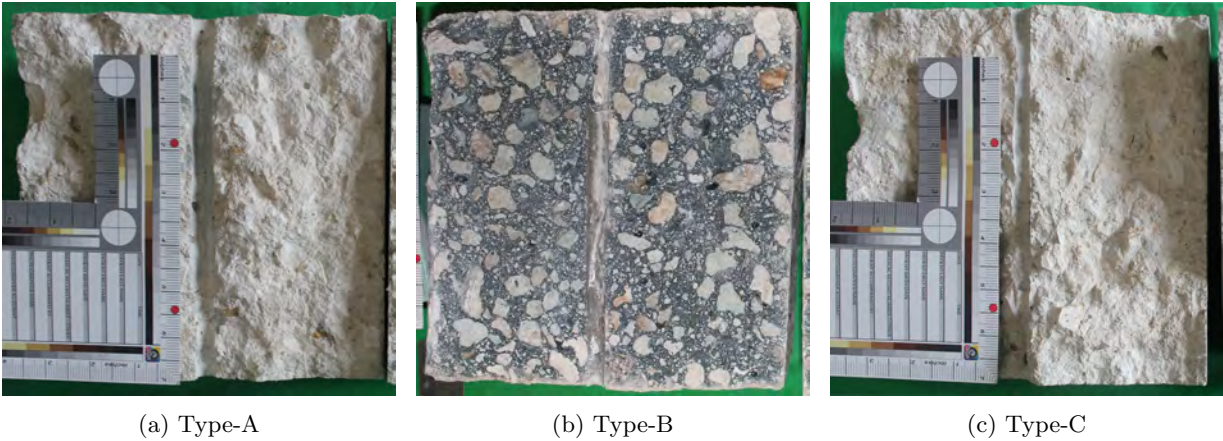


Figure 5.20: Bond failure at concrete interface of all rebar types in virgin state

While the color of the concrete appeared different for the concrete cube in Figure 5.20b (because the picture was taken directly after the concrete cube was split open and the other ones were taken much later), no significant difference at the concrete side was noted for the various rebar types. In some cubes the imprint of the rebar was more noticeable than for others, but an initially expected clear difference (for example grooves due to lugs) was not always found.

To complement the photos in Figure 5.19, Figure 5.21 shows the corresponding concrete cube halves that were documented for specimens exposed to 60 °C saltwater for 365 days. Similar to Figure 5.20, no significant

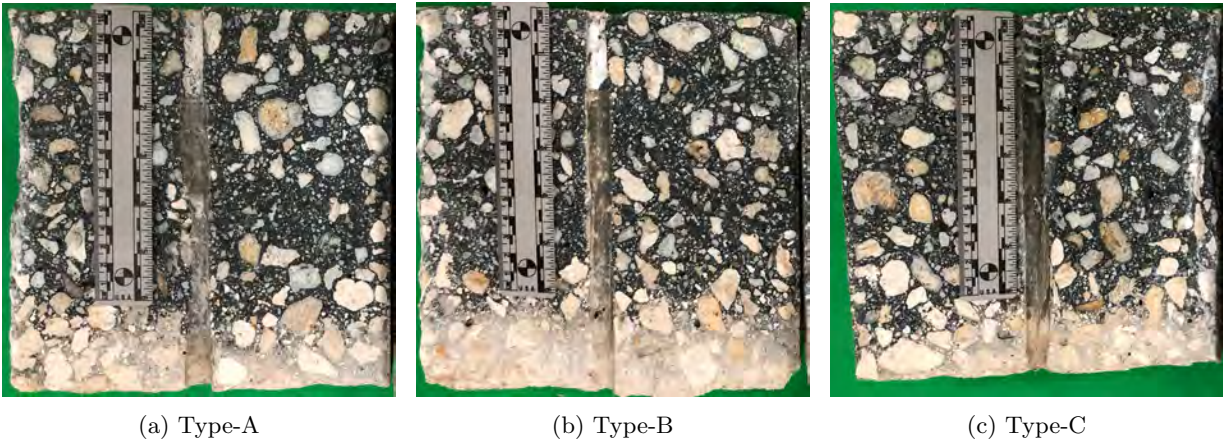


Figure 5.21: Bond failure at concrete interface of all rebar types after 365 day of exposure to 60 °C saltwater



differences for the split open concrete cubes were found.

## 5.4 Summary of Material Characterization Tests

To conclude the material characterization, the following Tables 5.2 through 5.4: Acceptance criteria evaluation for Type-C 6 rebars summarize all experimental findings for each rebar type and size. Each table is representative for one of the nine tested rebars and it lists the conducted test methods, the respective measurement, three different acceptance criteria (FDOT Section 932, AC454, and ASTM D7957), and symbols to indicate if the criteria was met (✓) or if the rebar failed to meet the particular acceptance test (✗).

Tables 5.2 through 5.4 list the acceptance matrix for the Type-A rebars. The tables show that a

Table 5.2: Acceptance criteria evaluation for Type-A #3 rebars

Test Method	Test Description	Unit	Per diameter		FDOT 932-7/2017		AC454		ASTM D7957	
			Nom.	Exp.	Criteria	✓/✗	Criteria	✓/✗	Criteria	✓/✗
ASTM D 792	Measured Cross Sectional Area	in. <sup>2</sup>	0.110	0.126	0.104 – 0.161	✓	0.104 – 0.161	✓	0.104 – 0.161	✓
ASTM D 2584	Fiber Content	% wt.	76	76	≥ 70	✓	≥ 70	✓	≥ 70	✓
ASTM D 570	Moist. Absorption short term @50 °C	%	0.39	0.39	≤ 0.25	✗	≤ 0.25	✗	≤ 0.25	✗
ASTM D 570	Moist. Absorption long term @50 °C	%	1.11	1.11	≤ 1.0	✗	n/a	n/a	≤ 1.0	✗
ASTM D 7205	Min. Guaranteed Tensile Load	kip	12.8	12.8	≥ 13.2	✗	≥ 13.2	✗	≥ 13.2	✗
ASTM D 7205	Min. Guaranteed Tensile Strength	ksi	115.4	101.5	n/a	n/a	n/a	n/a	n/a	n/a
ASTM D 7205	Modulus	ksi	7,480	6,580	≥ 6,500	✓	≥ 6,500	✓	≥ 6,500	✓
ASTM D 7205	Max. Strain	%	1.85	1.85	n/a	n/a	n/a	n/a	n/a	n/a
ASTM D 7617	Min. Guaranteed Transverse Shear	ksi	38.09	33.48	≥ 22	✓	≥ 22	✓	≥ 19	✓
ASTM D 4475	Horizontal Shear Stress	ksi	6.23	5.43	n/a	n/a	≥ 5.5	✓	n/a	n/a
ACI440. 3R,B.3	Bond-to-concrete strength	ksi	1.64	1.53	≥ 1.1	✓	≥ 1.1	✓	≥ 1.1	✓

significant amount of acceptance criteria were not met and that the performance increased with increasing rebar size. However, the moisture absorption limitation of 1% was exceeded for all rebar sizes.

Tables 5.5, 5.6, and 5.7 show the measured performance of Type-B rebars for bar sizes #3, #5, and #8, respectively. While the Type-B rebars performed better than the Type-A rebars, the minimum guaranteed tensile load and the minimum guaranteed transverse shear stress were not attained by the #3 rebars and the #5 rebars, respectively. The #8 rebars, however, passed all acceptance criteria.

Tables 5.8 through 5.10 show the performance evaluation of Type-C rebars. In these tables, it can be seen that the Type C rebars met all acceptance criteria, independent of the evaluated rebar sizes. While all three rebar sizes passed, it is noted that the largest rebar in Type-C was a #6 rebar, and that this one can not be compared to the #8 rebars of Type-A and Type-B.

Table 5.3: Acceptance criteria evaluation for Type-A # 5 rebars

Test Method	Test Description	Unit	Per diameter		FDOT 932-7/2017		AC454		ASTM D 7957	
			Nom.	Exp.	Criteria	✓/✗	Criteria	✓/✗	Criteria	✓/✗
ASTM D 792	Measured Cross Sectional Area	in. <sup>2</sup>	0.307	0.333	0.288 – 0.388	✓	0.288 – 0.388	✓	0.288 – 0.388	✓
ASTM D 2584	Fiber Content	% wt.	76	76	≥ 70	✓	≥ 70	✓	≥ 70	✓
ASTM D 570	Moist. Absorption short term @50 °C	%	0.35	0.35	≤ 0.25	✗	≤ 0.25	✗	≤ 0.25	✗
ASTM D 570	Moist. Absorption long term @50 °C	%	1.17	1.17	≤ 1.0	✗	n/a	n/a	≤ 1.0	✗
ASTM D 7205	Min. Guaranteed Tensile Load	kip	34.6	34.6	≥ 29.1	✓	≥ 32.2	✓	≥ 29.1	✓
ASTM D 7205	Min. Guaranteed Tensile Strength	ksi	112.9	104.1	n/a	n/a	n/a	n/a	n/a	n/a
ASTM D 7205	Modulus	ksi	7,810	7,200	≥ 6,500	✓	≥ 6,500	✓	≥ 6,500	✓
ASTM D 7205	Max. Strain	%	1.67	1.67	n/a	n/a	n/a	n/a	n/a	n/a
ASTM D 7617	Min. Guaranteed Transverse Shear	ksi	24.44	26.52	≥ 22	✓	≥ 22	✓	≥ 19	✓
ASTM D 4475	Horizontal Shear Stress	ksi	6.07	5.62	n/a	n/a	≥ 5.5	✓	n/a	n/a
ACI440. 3R,B.3	Bond-to-concrete strength	ksi	1.81	1.74	≥ 1.1	✓	≥ 1.1	✓	≥ 1.1	✓

Table 5.4: Acceptance criteria evaluation for Type-A # 8 rebars

Test Method	Test Description	Unit	Per diameter		FDOT 932-7/2017		AC454		ASTM D 7957	
			Nom.	Exp.	Criteria	✓/✗	Criteria	✓/✗	Criteria	✓/✗
ASTM D 792	Measured Cross Sectional Area	in. <sup>2</sup>	0.785	0.816	0.738 – 0.913	✓	0.738 – 0.913	✓	0.738 – 0.913	✓
ASTM D 2584	Fiber Content	% wt.	75	75	≥ 70	✓	≥ 70	✓	≥ 70	✓
ASTM D 570	Moist. Absorption short term @50 °C	%	0.30	0.30	≤ 0.25	✗	≤ 0.25	✗	≤ 0.25	✗
ASTM D 570	Moist. Absorption long term @50 °C	%	0.94	0.94	≤ 1.0	✓	n/a	n/a	≤ 1.0	✓
ASTM D 7205	Min. Guaranteed Tensile Load	kip	71.7	71.7	≥ 66.8	✓	≥ 70.6	✓	≥ 66.8	✓
ASTM D 7205	Min. Guaranteed Tensile Strength	ksi	91.3	87.8	n/a	n/a	n/a	n/a	n/a	n/a
ASTM D 7205	Modulus	ksi	7,610	7,320	≥ 6,500	✓	≥ 6,500	✓	≥ 6,500	✓
ASTM D 7205	Max. Strain	%	1.46	1.46	n/a	n/a	n/a	n/a	n/a	n/a
ASTM D 7617	Min. Guaranteed Transverse Shear	ksi	23.70	24.64	≥ 22	✓	≥ 22	✓	≥ 19	✓
ASTM D 4475	Horizontal Shear Stress	ksi	5.95	5.72	n/a	n/a	≥ 7.7	✗	n/a	n/a
ACI440. 3R,B.3	Bond-to-concrete strength	ksi	1.29	1.26	≥ 1.1	✓	≥ 1.1	✓	≥ 1.1	✓

## 5.5 Test Results from Measurements of Durability Properties

In this section, the findings from the durability experiments are presented. First, the micro-structure and the effects of prolonged exposure at different temperatures are presented, and then the retention of the various strength characteristics are displayed via the determined average values.

Table 5.5: Acceptance criteria evaluation for Type-B #3 rebars

Test Method	Test Description	Unit	Per diameter		FDOT 932-7/2017		AC454		ASTM D 7957	
			Nom.	Exp.	Criteria	✓/✗	Criteria	✓/✗	Criteria	✓/✗
ASTM D 792	Measured Cross Sectional Area	in. <sup>2</sup>	0.110	0.133	0.104 – 0.161	✓	0.104 – 0.161	✓	0.104 – 0.161	✓
ASTM D 2584	Fiber Content	% wt.	84	84	≥ 70	✓	≥ 70	✓	≥ 70	✓
ASTM D 570	Moist. Absorption short term @50 °C	%	0.09	0.09	≤ 0.25	✓	≤ 0.25	✓	≤ 0.25	✓
ASTM D 570	Moist. Absorption long term @50 °C	%	0.19	0.19	≤ 1.0	✓	n/a	n/a	≤ 1.0	✓
ASTM D 7205	Min. Guaranteed Tensile Load	kip	10.7	10.7	≥ 13.2	✗	≥ 13.2	✗	≥ 13.2	✗
ASTM D 7205	Min. Guaranteed Tensile Strength	ksi	96.5	79.8	n/a	n/a	n/a	n/a	n/a	n/a
ASTM D 7205	Modulus	ksi	8,880	7,350	≥ 6,500	✓	≥ 6,500	✓	≥ 6,500	✓
ASTM D 7205	Max. Strain	%	1.36	1.36	n/a	n/a	n/a	n/a	n/a	n/a
ASTM D 7617	Min. Guaranteed Transverse Shear	ksi	32.16	26.60	≥ 22	✓	≥ 22	✓	≥ 19	✓
ASTM D 4475	Horizontal Shear Stress	ksi	6.34	5.22	n/a	n/a	≥ 5.5	✓	n/a	n/a
ACI440. 3R,B.3	Bond-to-concrete strength	ksi	3.37	3.06	≥ 1.1	✓	≥ 1.1	✓	≥ 1.1	✓

Table 5.6: Acceptance criteria evaluation for Type-B #5 rebars

Test Method	Test Description	Unit	Per diameter		FDOT 932-7/2017		AC454		ASTM D 7957	
			Nom.	Exp.	Criteria	✓/✗	Criteria	✓/✗	Criteria	✓/✗
ASTM D 792	Measured Cross Sectional Area	in. <sup>2</sup>	0.307	0.340	0.288 – 0.388	✓	0.288 – 0.388	✓	0.288 – 0.388	✓
ASTM D 2584	Fiber Content	% wt.	83	83	≥ 70	✓	≥ 70	✓	≥ 70	✓
ASTM D 570	Moist. Absorption short term @50 °C	%	0.09	0.09	≤ 0.25	✓	≤ 0.25	✓	≤ 0.25	✓
ASTM D 570	Moist. Absorption long term @50 °C	%	0.22	0.22	≤ 1.0	✓	n/a	n/a	≤ 1.0	✓
ASTM D 7205	Min. Guaranteed Tensile Load	kip	36.6	36.6	≥ 29.1	✓	≥ 32.2	✓	≥ 29.1	✓
ASTM D 7205	Min. Guaranteed Tensile Strength	ksi	119.5	107.9	n/a	n/a	n/a	n/a	n/a	n/a
ASTM D 7205	Modulus	ksi	8,390	7,580	≥ 6,500	✓	≥ 6,500	✓	≥ 6,500	✓
ASTM D 7205	Max. Strain	%	1.67	1.67	n/a	n/a	n/a	n/a	n/a	n/a
ASTM D 7617	Min. Guaranteed Transverse Shear	ksi	21.96	19.83	≥ 22	✗	≥ 22	✗	≥ 19	✗
ASTM D 4475	Horizontal Shear Stress	ksi	5.95	5.38	n/a	n/a	≥ 5.5	✓	n/a	n/a
ACI440. 3R,B.3	Bond-to-concrete strength	ksi	1.89	1.80	≥ 1.1	✓	≥ 1.1	✓	≥ 1.1	✓

### 5.5.1 Durability of Microstructure via SEM Imagery

Figures 5.22 through 5.24 illustrate one distinct subpart of the cross section — the interface between the fiber body of the rebar and the surface enhancement — for a detailed representation of the microstructure after exposure to the saline environments, while Figures 5.25 through 5.27 show the entire cross-sectional surface. The pictures in the latter figures were created from up to 49 individual SEM images to provide an overview of the entire rebar after saltwater exposure. Each row in the following figures represents an exposure duration with the longest duration at the bottom, and each column is representative of a specific exposure temperature, where the highest conditioning temperature is to be found in the right column. Of

Table 5.7: Acceptance criteria evaluation for Type-B # 8 rebars

Test Method	Test Description	Unit	Per diameter		FDOT 932-7/2017		AC454		ASTM D 7957	
			Nom.	Exp.	Criteria	✓/✗	Criteria	✓/✗	Criteria	✓/✗
ASTM D 792	Measured Cross Sectional Area	in. <sup>2</sup>	0.785	0.839	0.738 – 0.913	✓	0.738 – 0.913	✓	0.738 – 0.913	✓
ASTM D 2584	Fiber Content	% wt.	84	84	≥ 70	✓	≥ 70	✓	≥ 70	✓
ASTM D 570	Moist. Absorption short term @50 °C	%	0.06	0.06	≤ 0.25	✓	≤ 0.25	✓	≤ 0.25	✓
ASTM D 570	Moist. Absorption long term @50 °C	%	0.14	0.14	≤ 1.0	✓	n/a	n/a	≤ 1.0	✓
ASTM D 7205	Min. Guaranteed Tensile Load	kip	87.4	87.4	≥ 66.8	✓	≥ 70.6	✓	≥ 66.8	✓
ASTM D 7205	Min. Guaranteed Tensile Strength	ksi	111.4	104.2	n/a	n/a	n/a	n/a	n/a	n/a
ASTM D 7205	Modulus	ksi	8,240	7,710	≥ 6,500	✓	≥ 6,500	✓	≥ 6,500	✓
ASTM D 7205	Max. Strain	%	1.51	1.51	n/a	n/a	n/a	n/a	n/a	n/a
ASTM D 7617	Min. Guaranteed Transverse Shear	ksi	22.71	24.28	≥ 22	✓	≥ 22	✓	≥ 19	✓
ASTM D 4475	Horizontal Shear Stress	ksi	5.86	5.47	n/a	n/a	≥ 7.7	✗	n/a	n/a
ACI440. 3R,B.3	Bond-to-concrete strength	ksi	1.42	1.37	≥ 1.1	✓	≥ 1.1	✓	≥ 1.1	✓

Table 5.8: Acceptance criteria evaluation for Type-C # 3 rebars

Test Method	Test Description	Unit	Per diameter		FDOT 932-7/2017		AC454		ASTM D 7957	
			Nom.	Exp.	Criteria	✓/✗	Criteria	✓/✗	Criteria	✓/✗
ASTM D 792	Measured Cross Sectional Area	in. <sup>2</sup>	0.110	0.118	0.104 – 0.161	✓	0.104 – 0.161	✓	0.104 – 0.161	✓
ASTM D 2584	Fiber Content	% wt.	76	76	≥ 70	✓	≥ 70	✓	≥ 70	✓
ASTM D 570	Moist. Absorption short term @50 °C	%	0.07	0.07	≤ 0.25	✓	≤ 0.25	✓	≤ 0.25	✓
ASTM D 570	Moist. Absorption long term @50 °C	%	0.23	0.23	≤ 1.0	✓	n/a	n/a	≤ 1.0	✓
ASTM D 7205	Min. Guaranteed Tensile Load	kip	13.7	13.7	≥ 13.2	✓	≥ 13.2	✓	≥ 13.2	✓
ASTM D 7205	Min. Guaranteed Tensile Strength	ksi	124.2	116.7	n/a	n/a	n/a	n/a	n/a	n/a
ASTM D 7205	Modulus	ksi	7,950	7,450	≥ 6,500	✓	≥ 6,500	✓	≥ 6,500	✓
ASTM D 7205	Max. Strain	%	1.80	1.80	n/a	n/a	n/a	n/a	n/a	n/a
ASTM D 7617	Min. Guaranteed Transverse Shear	ksi	38.95	36.58	≥ 22	✓	≥ 22	✓	≥ 19	✓
ASTM D 4475	Horizontal Shear Stress	ksi	7.30	6.89	n/a	n/a	≥ 5.5	✓	n/a	n/a
ACI440. 3R,B.3	Bond-to-concrete strength	ksi	2.20	2.14	≥ 1.1	✓	≥ 1.1	✓	≥ 1.1	✓

specific interest for these pictures is the visualized porosity because the pores space can be related to the moisture absorption properties, and affects the material degradation. Accordingly, the pores are available for chloride or other contaminates/deposits and the (sized) fibers adjacent to the pores are more susceptible to microstructure deterioration because of the missing protective resin matrix. For more clarity, this is further discussed in Chapter 7.

A representation of the detailed microstructure for the Type-A rebars is given in Figure 5.22, and it can be seen that the surface enhancement (sand coated) adhered considerably well to the main body of the rebar, with minimal voids at the interface. However, this rebar type was noticeably porous with significant voids.

Table 5.9: Acceptance criteria evaluation for Type-C # 5 rebars

Test Method	Test Description	Unit	Per diameter		FDOT 932-7/2017		AC454		ASTM D 7957	
			Nom.	Exp.	Criteria	✓/✗	Criteria	✓/✗	Criteria	✓/✗
ASTM D 792	Measured Cross Sectional Area	in. <sup>2</sup>	0.307	0.292	0.288 – 0.388	✓	0.288 – 0.388	✓	0.288 – 0.388	✓
ASTM D 2584	Fiber Content	% wt.	70	70	≥ 70	✓	≥ 70	✓	≥ 70	✓
ASTM D 570	Moist. Absorption short term @50 °C	%	0.09	0.09	≤ 0.25	✓	≤ 0.25	✓	≤ 0.25	✓
ASTM D 570	Moist. Absorption long term @50 °C	%	0.21	0.21	≤ 1.0	✓	n/a	n/a	≤ 1.0	✓
ASTM D 7205	Min. Guaranteed Tensile Load	kip	30.1	30.1	≥ 29.1	✓	≥ 32.2	✗	≥ 29.1	✓
ASTM D 7205	Min. Guaranteed Tensile Strength	ksi	99.5	104.4	n/a	n/a	n/a	n/a	n/a	n/a
ASTM D 7205	Modulus	ksi	6,840	7,180	≥ 6,500	✓	≥ 6,500	✓	≥ 6,500	✓
ASTM D 7205	Max. Strain	%	1.67	1.67	n/a	n/a	n/a	n/a	n/a	n/a
ASTM D 7617	Min. Guaranteed Transverse Shear	ksi	33.10	31.56	≥ 22	✓	≥ 22	✓	≥ 19	✓
ASTM D 4475	Horizontal Shear Stress	ksi	7.27	7.63	n/a	n/a	≥ 5.5	✓	n/a	n/a
ACI440. 3R,B.3	Bond-to-concrete strength	ksi	1.18	1.21	≥ 1.1	✓	≥ 1.1	✓	≥ 1.1	✓

Table 5.10: Acceptance criteria evaluation for Type-C # 6 rebars

Test Method	Test Description	Unit	Per diameter		FDOT 932-7/2017		AC454		ASTM D 7957	
			Nom.	Exp.	Criteria	✓/✗	Criteria	✓/✗	Criteria	✓/✗
ASTM D 792	Measured Cross Sectional Area	in. <sup>2</sup>	0.442	0.416	0.415 – 0.539	✓	0.415 – 0.539	✓	0.415 – 0.539	✓
ASTM D 2584	Fiber Content	% wt.	75	75	≥ 70	✓	≥ 70	✓	≥ 70	✓
ASTM D 570	Moist. Absorption short term @50 °C	%	0.07	0.07	≤ 0.25	✓	≤ 0.25	✓	≤ 0.25	✓
ASTM D 570	Moist. Absorption long term @50 °C	%	0.14	0.14	≤ 1.0	✓	n/a	n/a	≤ 1.0	✓
ASTM D 7205	Min. Guaranteed Tensile Load	kip	45.5	45.5	≥ 40.9	✓	≥ 44.2	✓	≥ 40.9	✓
ASTM D 7205	Min. Guaranteed Tensile Strength	ksi	103.0	109.4	n/a	n/a	n/a	n/a	n/a	n/a
ASTM D 7205	Modulus	ksi	7,070	7,510	≥ 6,500	✓	≥ 6,500	✓	≥ 6,500	✓
ASTM D 7205	Max. Strain	%	1.68	1.68	n/a	n/a	n/a	n/a	n/a	n/a
ASTM D 7617	Min. Guaranteed Transverse Shear	ksi	29.76	28.02	≥ 22	✓	≥ 22	✓	≥ 19	✓
ASTM D 4475	Horizontal Shear Stress	ksi	6.37	6.75	n/a	n/a	≥ 7.7	✗	n/a	n/a
ACI440. 3R,B.3	Bond-to-concrete strength	ksi	1.56	2.14	≥ 1.1	✓	≥ 1.1	✓	≥ 1.1	✓

The voids were mostly located along the perimeter of the cross section, but some minor voids were also found toward the center of the rebar (bottom right corner). In addition, it can be noted that the amount of pores increased from left to right; in other words, the elevated temperatures lead to more destructive effects.

Figure 5.23 illustrates the representative microstructure of the Type-B rebars. Because the surface enhancement consisted of helical wrapping and each SEM image is an individual slice at a specific location, no statement about the microstructure of the surface enhancement can be made. Compared to the previous Figure 5.22, the cross-section appeared more dense with reduced pores. Most spaces between the fibers were properly filled with resin. Again, the effect of the accelerated aging can be seen, because more voids were

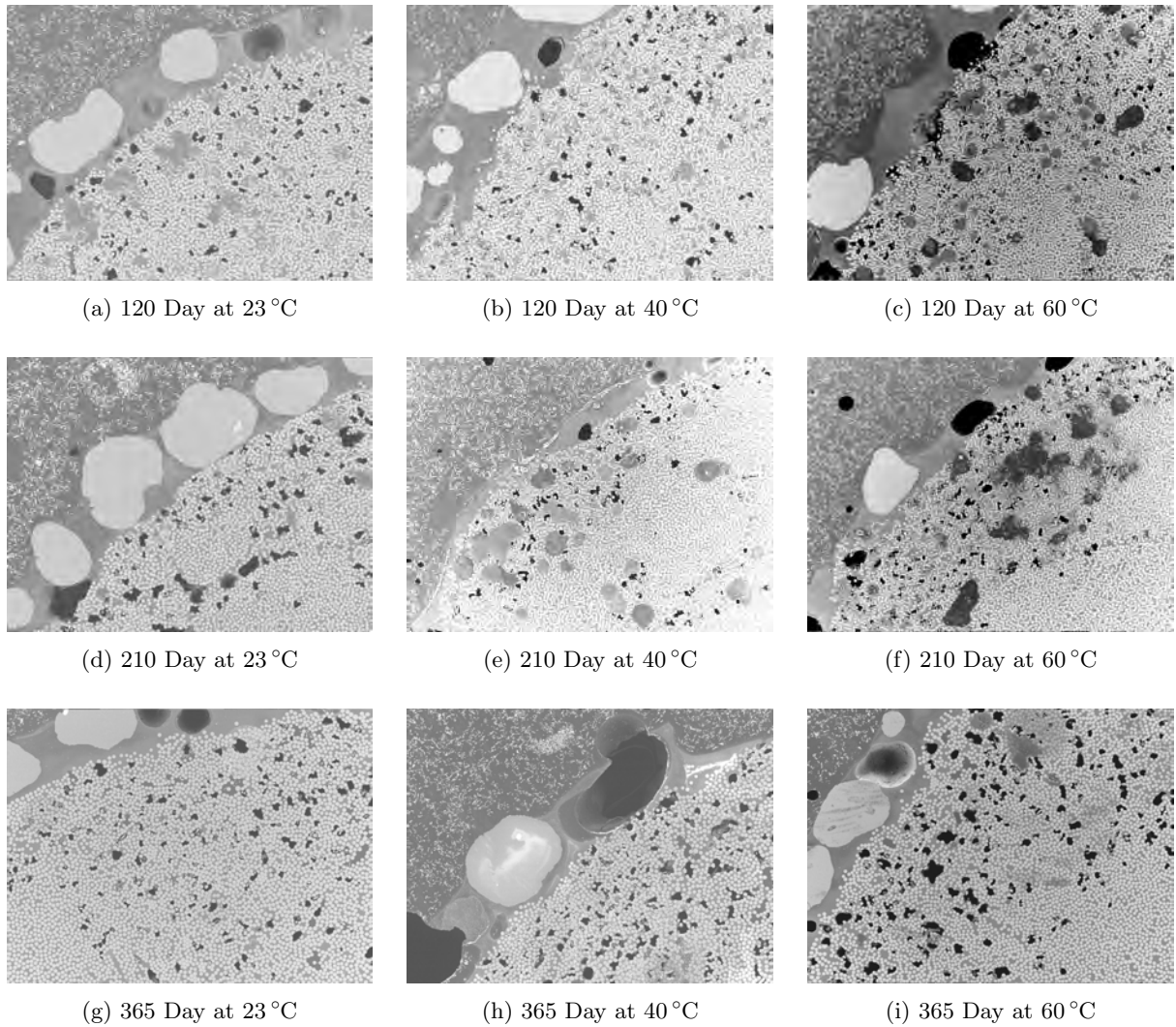


Figure 5.22: Individual SEM pictures for Type-A rebars after saltwater exposure

observed for the pictures on the right side (at 60 °C). This effect was not as pronounced as it was for the Type-A rebars, but it was still noticeable.

Type-C rebars are shown in Figure 5.24 to illustrate the effect of accelerated aging on the GFRP rods with lugs. While it had the same height as the lugs, it must be noted that the embossment (best seen in Figures 5.24a and 5.24b) does not represent the lugs (to enhancement the bond-to-concrete properties) but instead a production seam that ran along the entire length of the bar, parallel to the axis. Accordingly, this production seam was completely filled with fibers. The lugs however, were made only from resin and not filled with fibers (but this could not be captured through the SEM images). Similar to the previous Figure 5.23 but opposite to Figure 5.22, the amount of voids was considerably low. Nevertheless, it is noted that the fiber distribution was not as dense for these Type-C rebars as it was recorded for the Type-B rebars. It can be seen that some areas (in dark gray but not black) did not contain fibers and were completely filled with

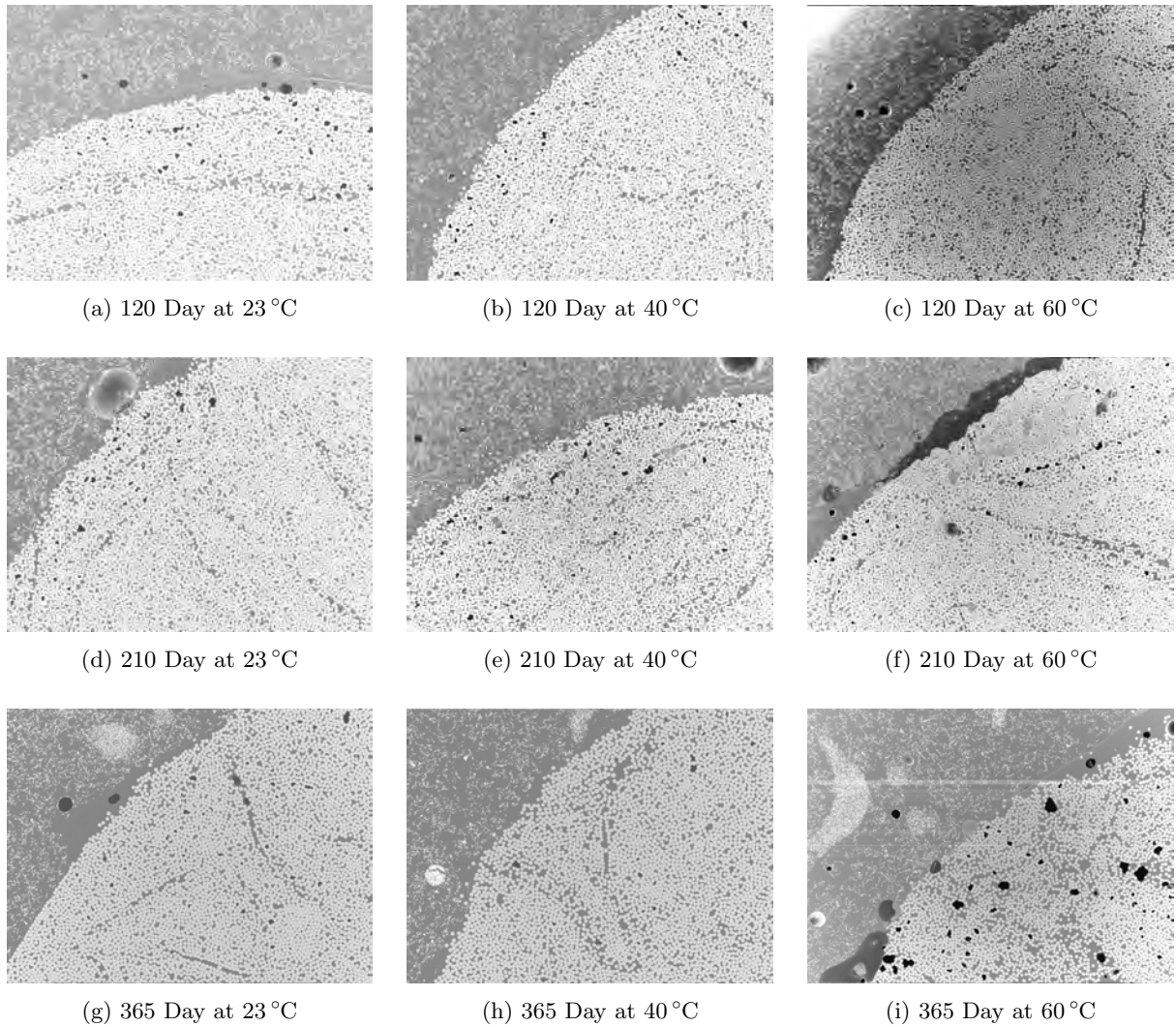


Figure 5.23: Individual SEM pictures for Type-B rebars after saltwater exposure

resin, which lead to a cross section with minimal voids.

The following Figure 5.25 shows the representative microstructure of the entire cross section for Type-A rebars. These images show that the porosity for the Type-A rebars was more significant towards the circumference and that the voids occurred mostly on one side (ranging from  $180^{\circ}$  to  $270^{\circ}$ ). It is assumed that this must be related to the proprietary production method or the specific pultrusion process in which one side of the bar receives either better impregnated fibers or more pressure. This is most likely the result of an open mold pultrusion process. However, while reasonable based on the images, no definitive statement can be made because the authors are unaware of the actual production sequence. Figure 5.25 further emphasizes the findings reported for Figure 5.22 because the effect of increased temperatures can be clearly and better seen as the pore amount and sizes increased from left to right (from  $23^{\circ}\text{C}$  to  $60^{\circ}\text{C}$ ). The interface to the surface enhancement appeared most affected.

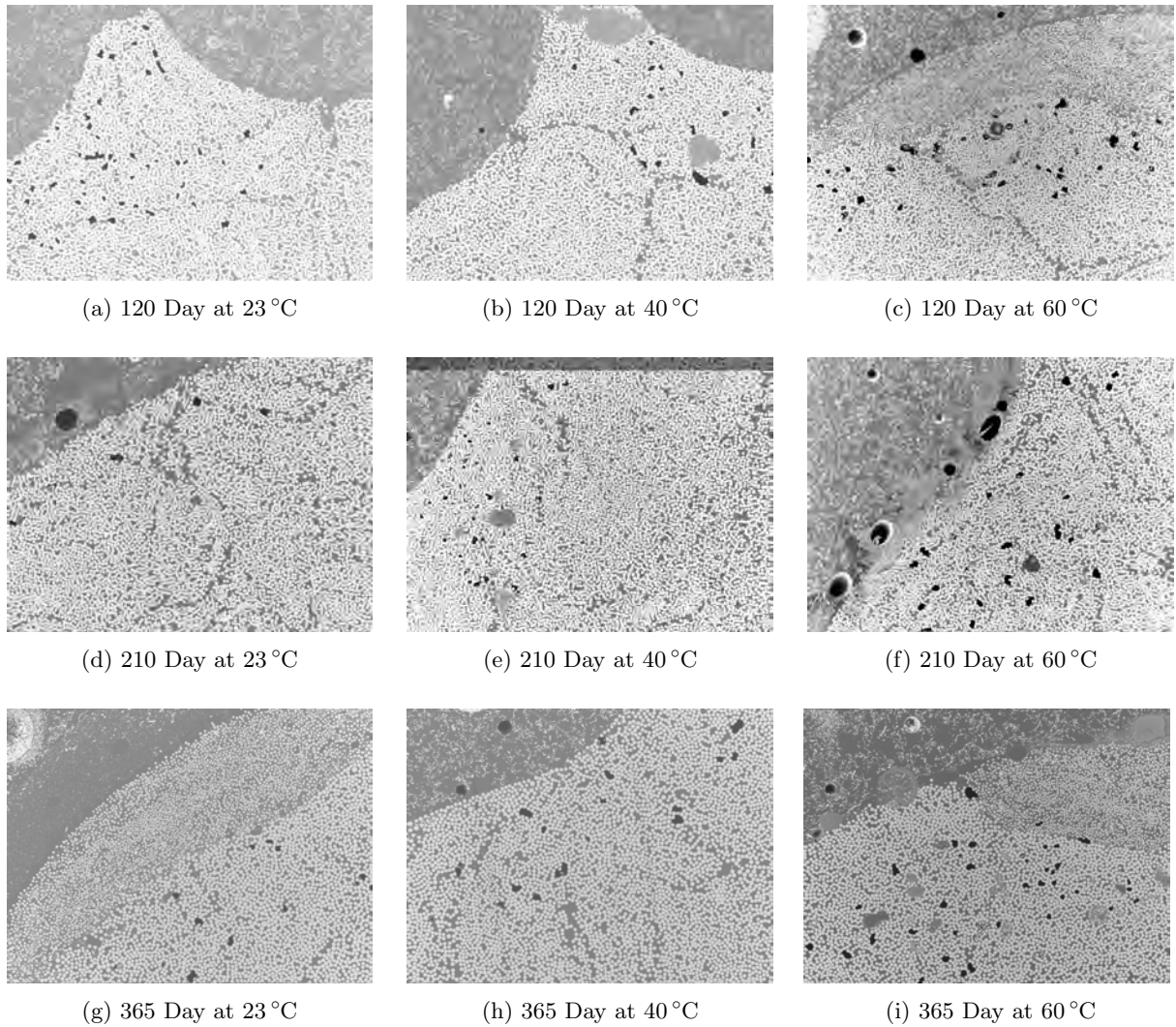


Figure 5.24: Individual SEM pictures for Type-C rebars after saltwater exposure

The images in Figure 5.26 show that the Type-B rebars had the most uniform distribution of fibers throughout the entire cross section. The random patterns of dark streaks were not voids but resin-filled spaces between the light gray fibers. With increasing temperatures, voids started to occur but insignificantly when compared to Type-A rebars. In fact, based on Figures 5.25, 5.26, and 5.27, Type-B rebars identified as the most dense and least porous rebars in this research project.

Finally, Figure 5.27 visualizes the entire cross section of Type-C rebars throughout the various exposure conditions. These images clarify the location of the production seam that occurred twice (separated by 180°) along the perimeter of the rebar. The image in Figure 5.27i appears unclear and partially blurry because the SEM detector was not properly aligned nor cleaned when some of the detail images (need to produce the full cross section) were captured. It is emphasized that only the black (and not the gray) areas are representative of voids or microstructure defects. Accordingly, Type-C rebars were well produced with proper fiber and



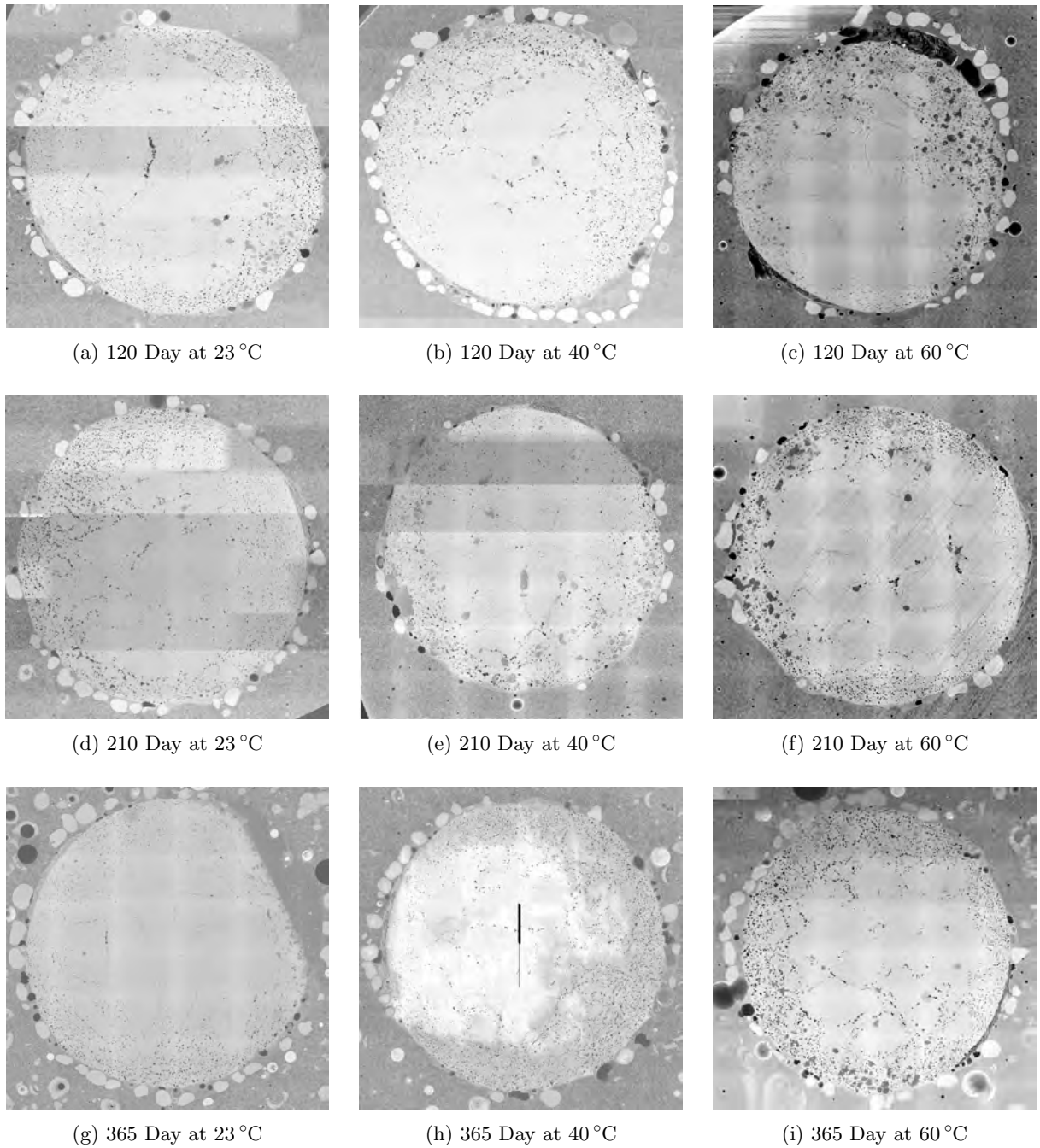


Figure 5.25: Combined SEM pictures for Type-A rebars after saltwater exposure

resin distribution, in which the small spaces between the fibers were mostly filled with resin. While not as significant as for Type-A rebars, the Type-C rebars represented in Figure 5.27 suffered more microstructure damage due to the accelerated aging protocol than the Type-B rebars.

Based on the SEM pictures obtained for the purpose of this research project and based on a relative comparison, Type-A rebars appeared to be most susceptible to micro-damages because of its high initial porosity. These microstructure findings are directly reflected in the moisture absorption properties that are

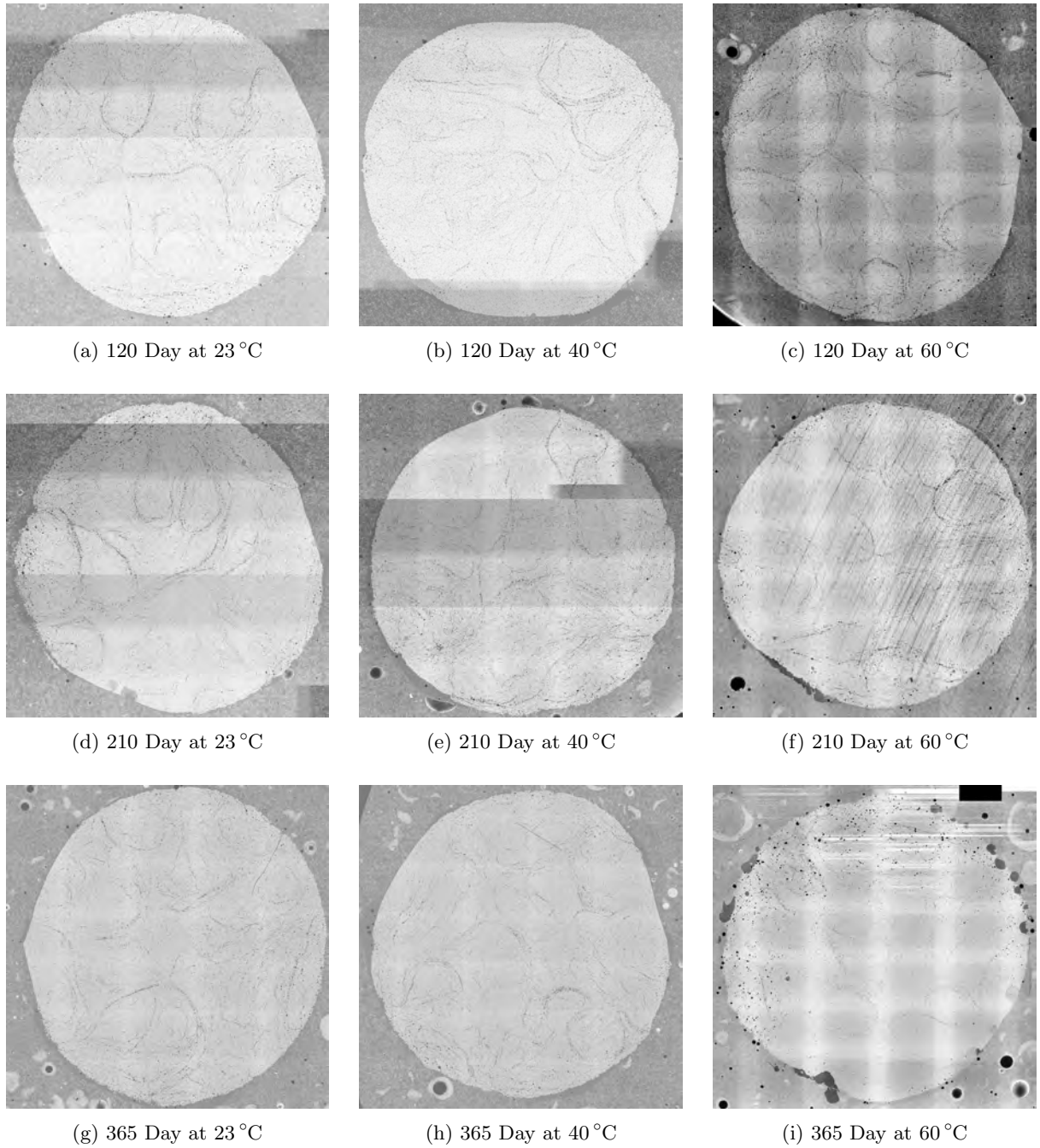


Figure 5.26: Combined SEM pictures for Type-B rebars after saltwater exposure

presented in the previous subsection. While Type-C rebars showed a high quality microstructure, Type-B rebars seemed to be the most durable ones.

### 5.5.2 Durability of Strength Properties

While the graphs in Section 5.3 describe all measured virgin material characteristics, the graphs below illustrate the material performance after exposure to the aging environments in reference to the benchmark

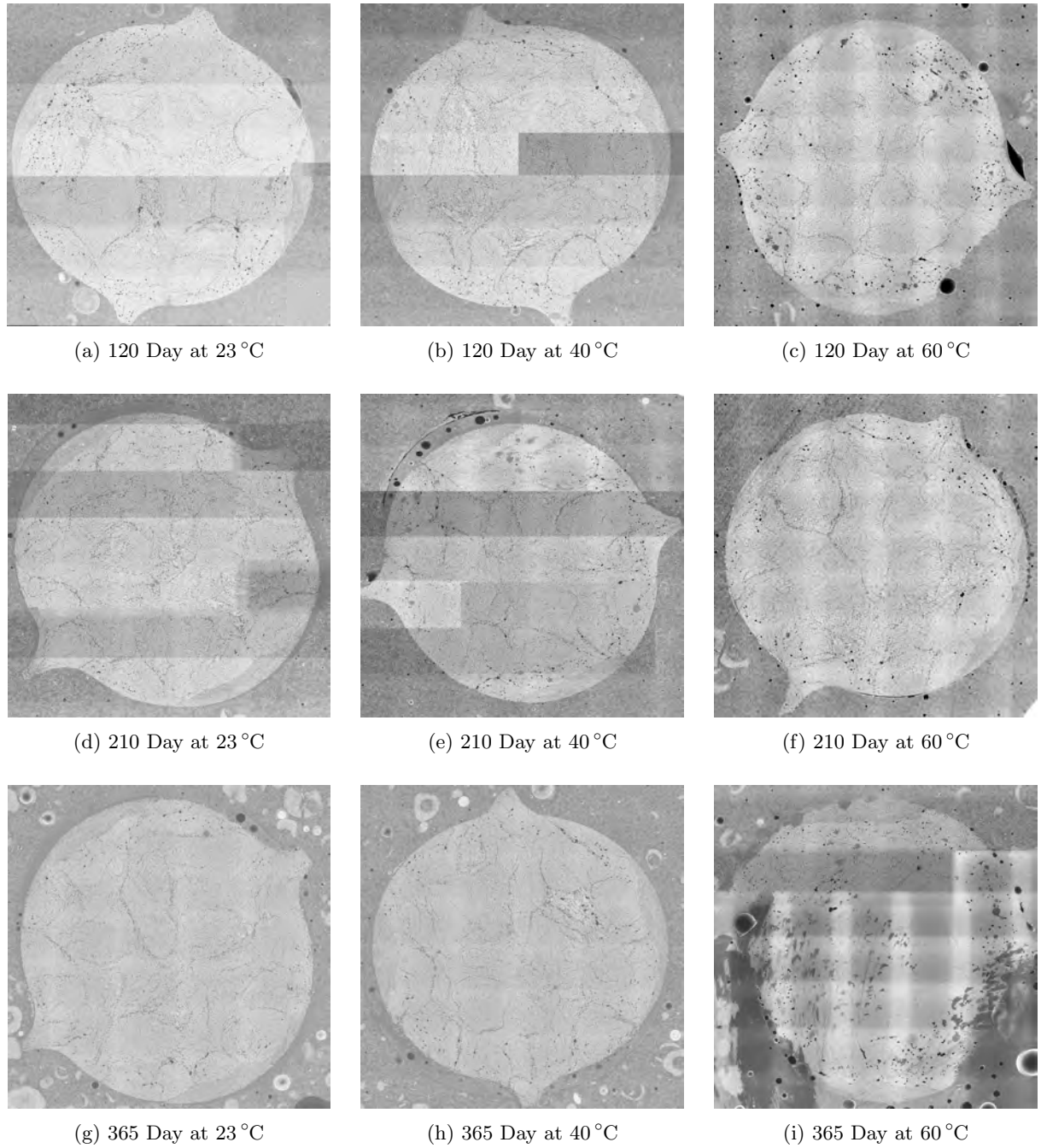


Figure 5.27: Combined SEM pictures for Type-C rebars after saltwater exposure

values presented above. As mentioned in Chapter 4, specimens were exposed to saltwater solutions at three different temperatures (23 °C, 40 °C, and 60 °C) for a one-year duration, in which specimens were removed and tested after four different time periods (60 d, 120 d, 210 d, and 365 d). Accordingly, the following graphs capture these conditions and plot the exposure duration on x-axis (in linear form) and the retention of the individual property along the y-axis. The three different temperature conditions are represented by three different data sets; in each of the following graphs, 23 °C is identified through round markers, 40 °C through

diamond shape markers, and 60 °C through triangular markers. The average values indicated by each marker were calculated by averaging at least three individual specimen results, for which the individual specimen results can be found in Appendix D.

Figure 5.28 displays the relative strength retention of the fiber-driven transverse shear characteristics. While the data fluctuated initially (throughout the early test periods), it can be seen that the strength values

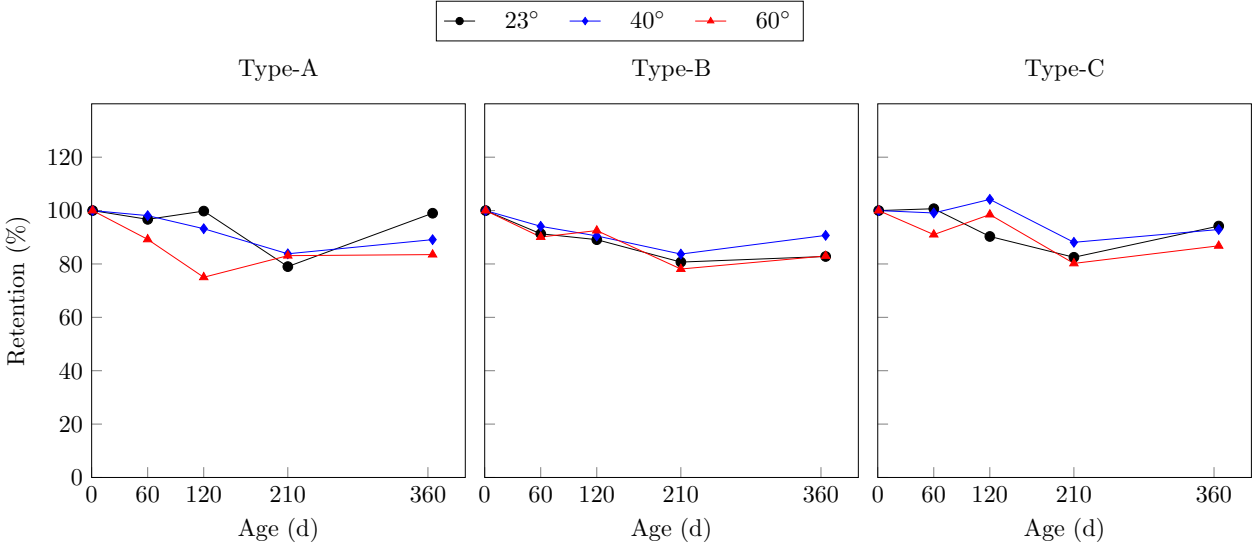


Figure 5.28: Retention of transverse shear strength

decreased with time. The majority of retention values remained above 80 %, but all of them remained above 70 %. Similar to the SEM pictures shown above, the graphs show that higher temperatures lead to more severe impacts, or in this case caused higher strength degradation.

The retention performance of the more resin-driven apparent horizontal shear strength characteristics is shown in Figure 5.29. Compared to Figure 5.28, the degradation of the horizontal shear strength appeared insignificant, and remained almost constant (c.f. Type-A). Some data points even suggested a strength improvement, which may indicate post-curing of the resin, but could also result from the general distribution and standard deviation of the measured results. Due to the limited amount of specimens tested for each of the displayed data points, definitive statements about the apparent strength improvement could not be made. However, it must be emphasized that the measurements from this test procedure depend much more on the resin than any other property reported in this project.

The degradation of the tensile strength based on the various aging conditions is plotted in Figure 5.30. Notably for this test procedure, the higher temperature environment of 60 °C led to significantly more strength reduction than the two lower conditioning temperatures. While 23 °C and 40 °C lead to strength reductions of no more than 80 %, the higher temperature environment degraded the material down to as low as 60 %.

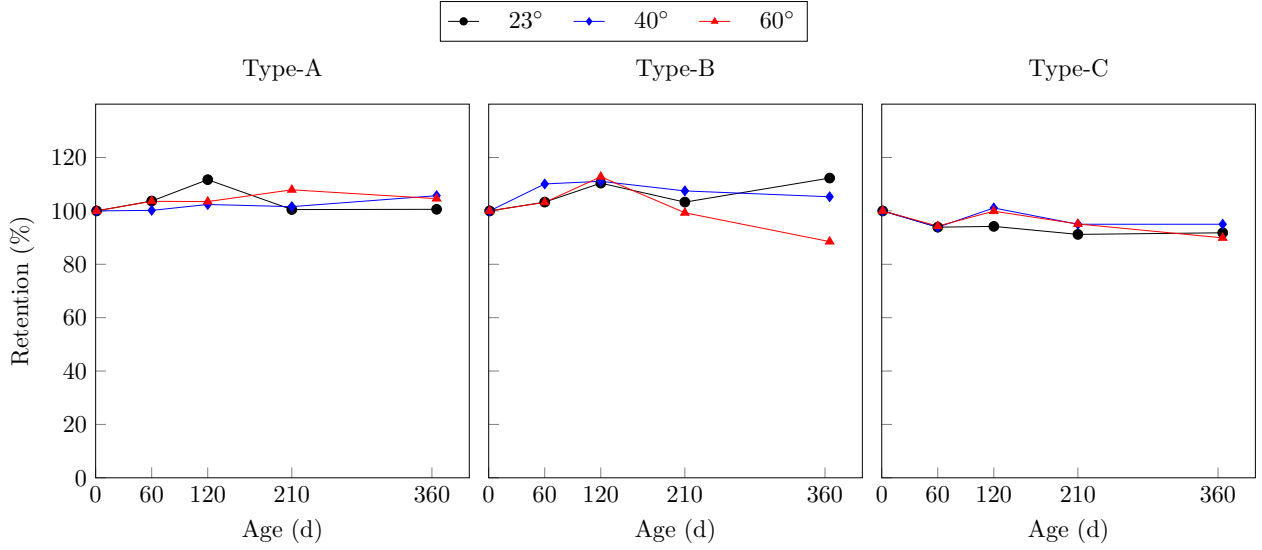


Figure 5.29: Retention of horizontal shear strength

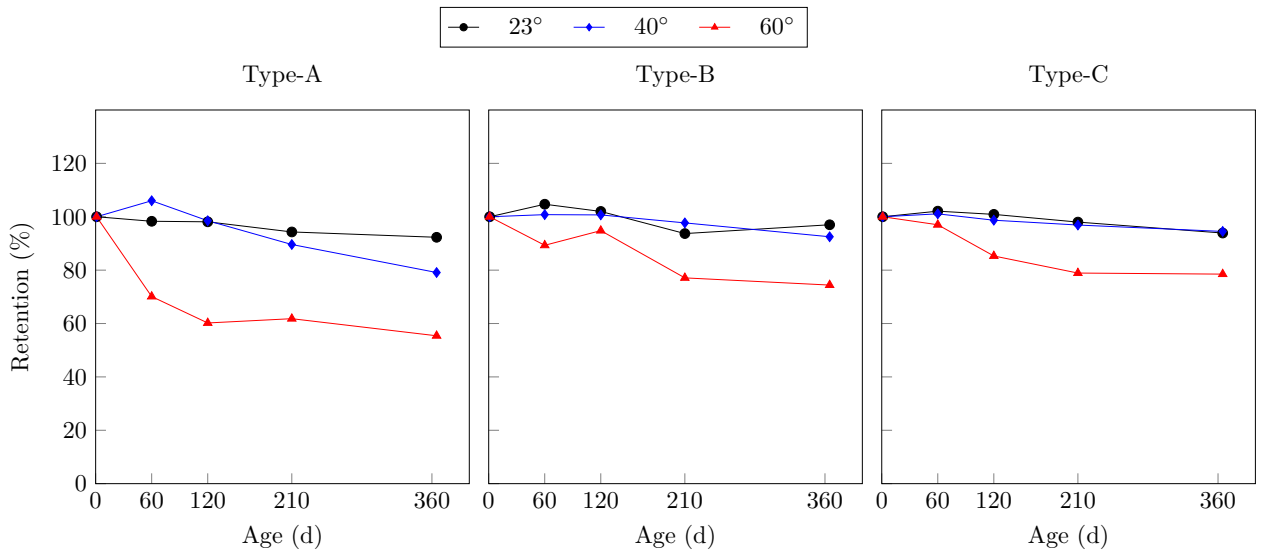


Figure 5.30: Retention of tensile strength

However, this extreme retention was only exhibited by Type-A rebars, and Type-B and Type-C rebars showed minor degradation for the low temperature environments and ranged around 80% for the highest aging temperature.

While the elastic modulus and the tensile strength were determined through the same test procedure, the property retention of these two characteristics may differ because the tensile strength depends on the performance of all fibers, while the strain measured for the elastic properties is generally only measured at the outermost fiber. Accordingly, it was expected to see a different retention behavior in Figure 5.30 for the elastic modulus than for the retention of the tensile strength. The elastic moduli remained nearly

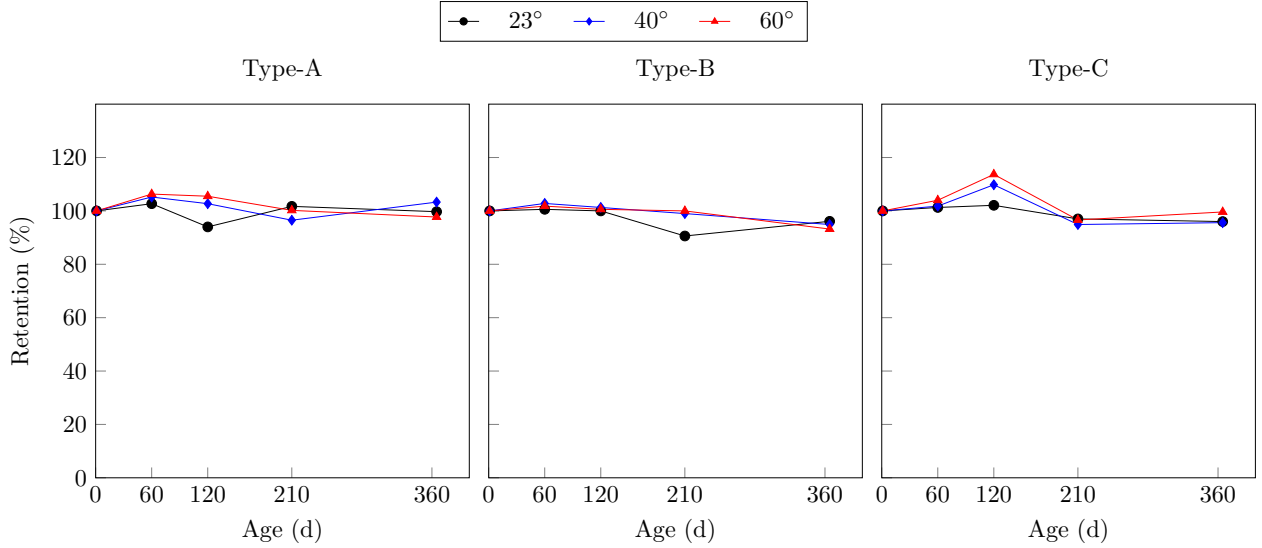


Figure 5.31: Retention of elastic modulus

constant throughout the duration of this project or were at least not significantly affected. Even the different temperature environments did not lead to an appreciable difference in retention characteristics. It must be emphasized that this does not indicate that no degradation occurred. Rather, the authors believe that this indicates that the strength properties and the strain properties of the outermost fibers degraded similarly such that the stress-strain relationship remained nearly constant.

The bond-to-concrete retention was measured for GFRP rebars embedded in concrete cubes that were partially submerged in the conditioning solutions to age the concrete-rebar interface and to simulate splash-zone conditions. The determined retention properties based on these tested specimens is graphed in Figure 5.32. Due to the inherent variability of this test procedure, the averaged results (based on three individual data points) fluctuated. Nevertheless, the data showed deterioration of the bond-to-concrete property. While the retention of Type-A and Type-B rebars was comparable, Type-B rebars showed the least bond-to-concrete degradation.

To further evaluate the bond behavior, specific rebar slip values were compared (throughout the test periods) according to the guidelines provided in ACI Committee 440 (2012). Therefore, the slippage behavior through the bond stress measurements at 0.05 mm, 0.10 mm, and 0.25 mm ( $\frac{2}{1000}$  in.,  $\frac{4}{1000}$  in., and  $\frac{1}{100}$  in.) as well as the slip measurement at the maximum measured bond stress were plotted in Figure 5.33 with an emphasis on the different exposure conditions and durations. Other than for the graphs presented above, the benchmark values and the reduction values are graphed on an absolute (not relative) scale along the y-axis. Accordingly, the short horizontal solid bars represent the benchmark values at each ACI 440.3R relevant slip value. These graphs emphasize the degradation behavior in general but also underline the possibility of resin

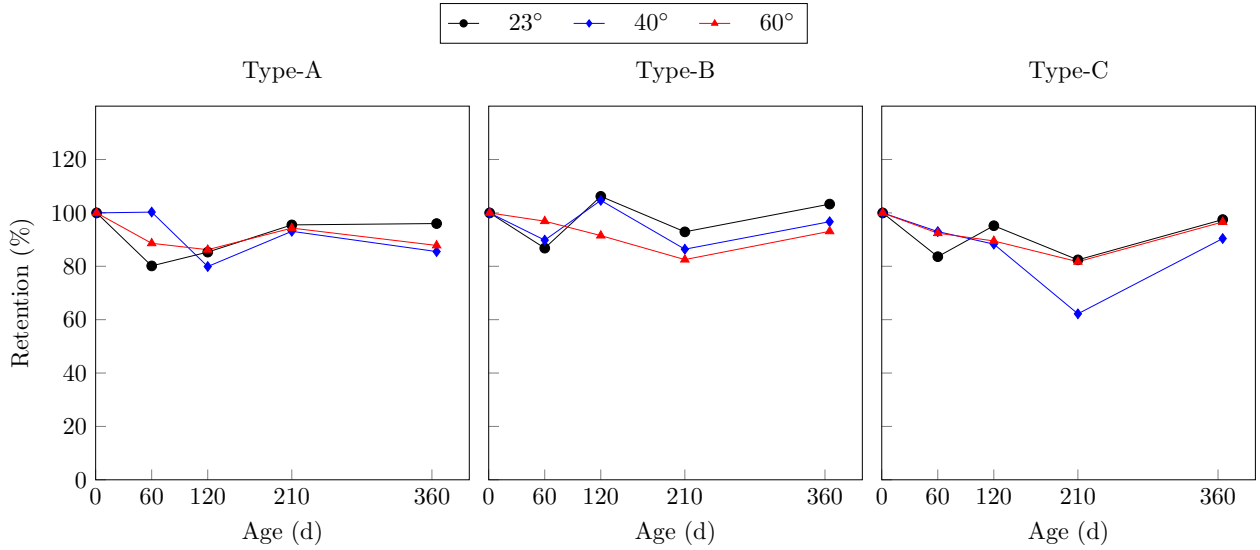


Figure 5.32: Retention of bond-to-concrete strength

post-curing contemplated in the context of Figure 5.29 because all slip values (except at the maximum stress) for the Type-B rebars (middle row) in Figure 5.33 show absolute values *above* the values measured for the virgin Type-B rebars.

For a final summary of all relative strength retention values, Figure 5.34 visualizes the results from all experiments (based on average measurements) for all rebar types, temperature conditions, and exposure durations. It is once again emphasized that the property retention presented in the graphs above is a relative property retention. While each rebar type showed a similar retention trend throughout the individually graphed properties, the absolute benchmark values presented in Section 5.3 should be considered. For example, a 20% percent reduction in tensile strength in a real structural application may be much more severe for rebars that measured higher initial (benchmark) strengths.

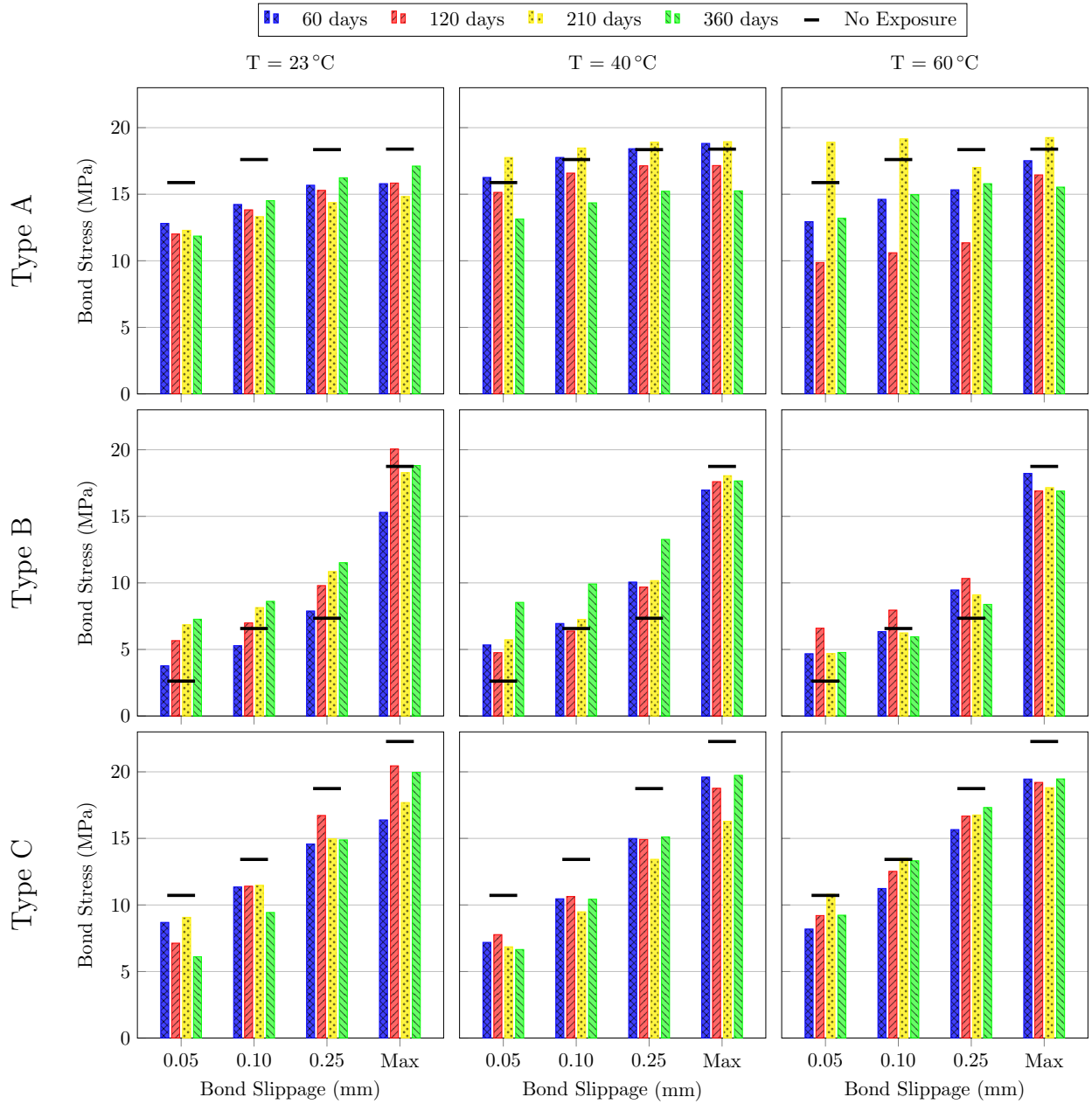


Figure 5.33: Bond strength slippage



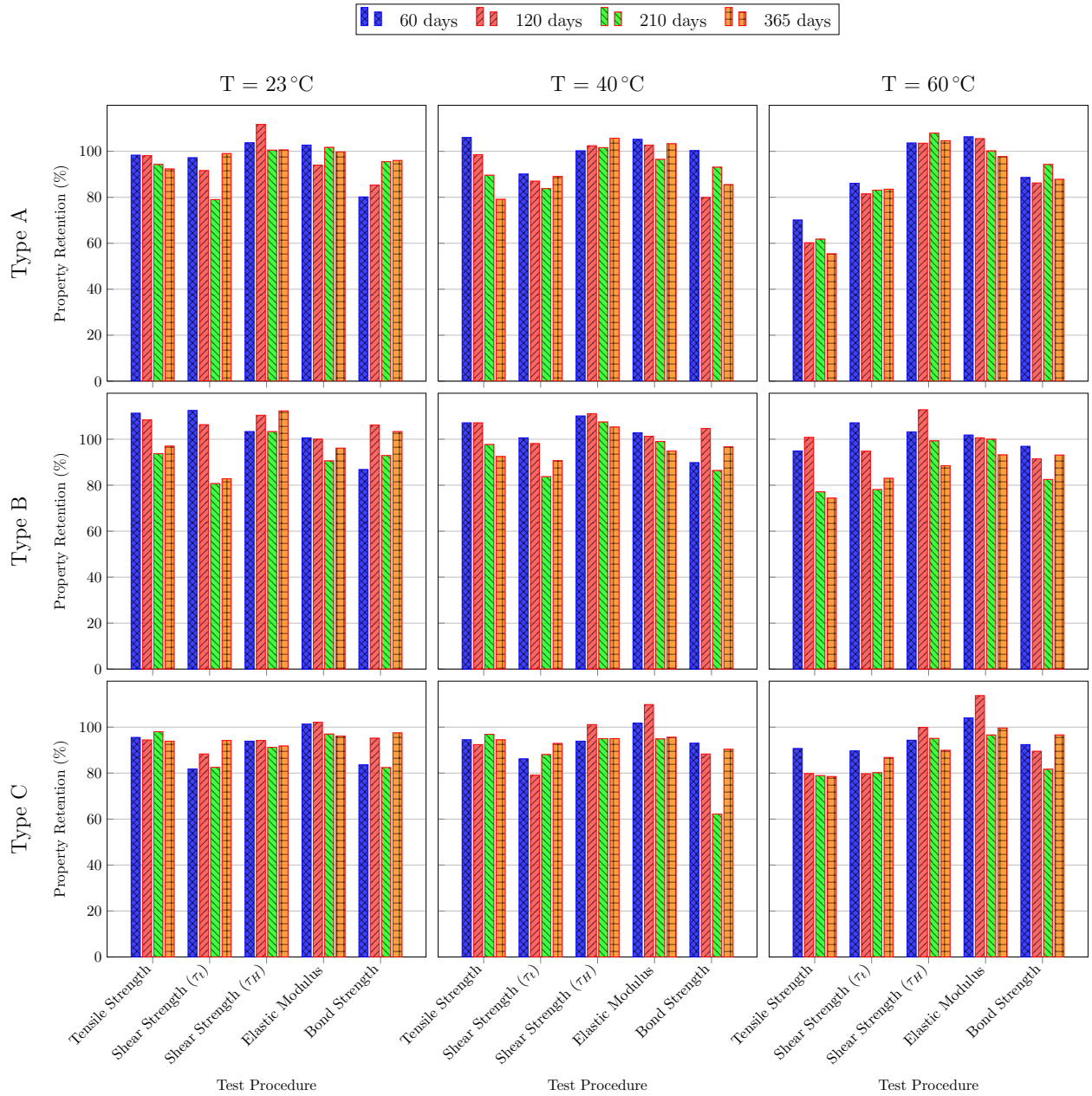


Figure 5.34: Summary of strength retention of GFRP rebars throughout exposure to accelerated conditioning

# Chapter 6

## Durability Modeling

### 6.1 Introduction

The use of GFRP reinforcement is gaining importance as internal reinforcement for reinforced concrete (RC) structures, primarily due to the corrosion-resistant properties. One of the most important applications for this alternative reinforcement is its use in coastal RC structures where corrosion of traditional steel rebars is critical (Nolan et al., 2018) and poses significant issues for the longevity of infrastructure. Because the driving force for such alternative reinforcement bars is the lifespan extension of RC structures, the durability and the prediction of the service life of GFRP rebars must be carefully and systematically evaluated, as these aspects are fundamental and important for the expansion and extended application of this technology. Experiments (and analysis models) that simulate, for example, GFRP rebars in heavily cracked concrete structures in coastal regions are missing from the literature, but are needed to fully embrace the new material. For the purpose of this study, service life predictions were determined via durability models based on mathematical and physics principles.

### 6.2 Durability Model

The goal of the durability model and its application presented in this section was to predict the long-term behavior of GFRP rebars to properly anticipate the service life of such rebars in harsh saltwater environments. Accordingly, chemical reaction/degradation models were merged with experimentally acquired information obtained through destructive testing of distinct rebar products after various time periods in accelerated aging conditions. It was the goal to develop a multi-parametric, long-term behavior prediction for GFRP rebars via the Arrhenius model based on measured strength values (tensile strength, elastic moduli, transverse and horizontal shear strengths, and bond-to-concrete strength) for three different rebar products (Type-A,

Type-B, and Type-C).

The Arrhenius equation is a formula proposed by Svante Arrhenius in 1889, which he developed to model the temperature dependent reaction rates of chemical processes. This equation supports the historically proven generalization that the rate of reaction at room temperature doubles every 10 °C for many chemical reactions (Pauling, 1988). The Arrhenius relationship is expressed as follows:

$$k = A_0 e^{\frac{-E_a}{RT}} \quad (6.1)$$

where:

$k$  Rate coefficient

$T$  Absolute temperature

$A_0$  Pre-exponential or Arrhenius factor (constant for every chemical reaction)

$R$  Universal gas constant

$E_a$  Activation energy for the reaction to happen

To remove the negative exponential, both sides of the equation can be set to  $-1$  and the remaining expression can be inverted to obtain the following form:

$$\frac{1}{k} = \frac{1}{A_0} e^{\frac{E_a}{RT}} \quad (6.2)$$

In this form, the rate coefficient,  $k$ , is expressed as the inverse of the time that is needed for a material property to reach a given value (Chen et al., 2006). By applying natural logarithms to both sides of the equation, the general Arrhenius equation can be transformed into the following linear expressions (intensity of slope, slope and interception with the  $y$ -axis) , which clarifies the relationship for improved interpretation:

$$\ln \left( \frac{1}{k} \right) = \frac{E_a}{R} \frac{1}{T} - \ln A \quad (6.3)$$

It can be seen that the logarithm of the time needed for a material property to reach a certain value is a linear function of  $\frac{1}{T}$  with the slope  $\frac{E_a}{R}$ . Hence,  $E_a$  and  $A$  can be calculated from the slope of the regression together with the point of intersection between the regression and the  $y$ -axis.

The Arrhenius model in the form presented above can be supplied with input data obtained from accelerated aging protocols (ACP) to calculate and predict the long-term behavior of FRP rebars. Accelerated aging protocols are designed to intensify the chemical reactions that cause the degradation process

by aggravating conditions such as heat, humidity, etc. To evaluate material deterioration via the Arrhenius model, a single predominant deterioration mechanism must be assumed, because if more than one chemical reaction (with different properties) or even other degradation mechanisms (mechanical or defect related) will be undergone at the same time (instead of a principal mechanism), it will be impossible to differentiate the various reactions, and therefore, the calculated rate constant would not be representative. In other words, to apply this model appropriately, the single dominant degradation mechanism should not change with time or temperature throughout exposure, while the rate of degradation should be accelerated through increased temperatures.

Many researchers have used accelerated aging protocols for Arrhenius models to predict the durability and resilience of FRP rebars (Chen et al., 2006; Dejke and Tepfers, 2001; Dong et al., 2016; Robert et al., 2009; Robert and Benmokrane, 2013; Wang et al., 2017; Yan and Lin, 2017; Wu et al., 2014). In each of these research projects, the durability of a single (and not combined) mechanical property (tensile, horizontal shear, or bond-to-concrete strength) was evaluated. The researchers exposed rebars to accelerated conditions in different solutions, such as alkaline solutions or regular tap water, combined with a variety of temperatures, mainly ranging from 23 °C to 60 °C. However, previous studies have not studied the effect of multi-parametric data, and to the best knowledge of the authors, the novelty of this study is related to the following three aspects:

- (i) No study exists that evaluates the durability of “naked” GFRP rebars exposed to seawater.
- (ii) The resilience of the bond between GFRP rebars and plain concrete exposed to seawater has not been addressed before. One other study that uses saline rich environments is known; however, it was under the condition of fibre reinforced concrete.
- (iii) No service life prediction study has been conducted using a multi-parametric approach; only individual, single mechanical properties have been used in the published literature.

For this study, five different physio-mechanical properties (tensile strength, elastic modulus, transverse and horizontal shear strength, and most importantly, bond-to-concrete strength) were taken into account and addressed throughout the service life prediction.

Based on the work done by other researchers (Chen et al., 2006; Dong et al., 2016; Robert and Benmokrane, 2013), the following initial assumptions were proposed: (i) the primary assumption for this model is that only one dominant material degradation mechanism is active during the reaction and that this mechanism will not change with time or temperature throughout exposure; only the rate of degradation accelerates with increased temperature. (ii) No post curing or little effect of the post curing of the resin is assumed due to the temperature of the accelerated conditioning protocols with 24 °C, 40 °C, and 60 °C. Therefore, it was

assumed that exposure to increased temperatures does not affect the curing properties of the resins.

### 6.2.1 Degradation Laws

With the experimental data based on the Accelerated Aging Protocols, the relationship between the retention of a mechanical property over time, or degradation rate coefficient,  $k$ , needs to be evaluated. For that, different mathematical models have been used in the literature by various researchers. Tannous and Saadatmanesh (1998) proposed a model based on moisture absorption, assuming that the affected area is completely degraded and thus could not be considered as load carrying, which may be too conservative.

Other mathematical models exist in addition to the moisture absorption one, such as the one developed by Litherland et al. (1981), shown in Equation 6.4.

$$Y = a \log(t) + b \quad (6.4)$$

Through this model the researchers were able to successfully predict the long-term behavior of glass fiber concrete (GRC). After this model was widely used by other researchers (Robert and Benmokrane, 2013; Dong et al., 2016; Dejke and Tepfers, 2001), some used a modified version (Dejke and Tepfers, 2001) with a logarithmic scale, as suggested by Litherland et al. (1981) through the following Equation 6.5.

$$\log(Y) = a \log(t) + b \quad (6.5)$$

Dejke and Tepfers (2001) showed that the results were very comparable, or slightly improved for a double logarithmic scale proposed by Litherland et al. (1981). This model is generically applied using the following scheme:

- The retention values over time are plotted on a double logarithmic scale (log-log graph) or single logarithmic scale, depending on the chosen model.
- The linear regression (in a log-log environment) for each group of retention values is calculated for each individual temperature exposure.
- For the Arrhenius model to be valid, the linear regressions for different comparable data sets should be parallel. In other words, if they are not parallel, the model does not apply because the material would not respond equally to the temperature, and therefore, it is not the reaction rate that changes.
- If applicable, the numerical horizontal distance between individual regression lines (see  $m$  value in Figure 6.1), which defines the reaction differences due to varying temperatures, can be used to predict the equivalent time shift (in years) between the different exposure temperatures. This is called the “time

shift factor method” and the factor defines the effect on the degradation based on time, relative to the difference in temperature. Accordingly, this method facilitates an interpolation approach such that it applies to any desired temperature other than the ones used for the tested accelerated conditioning protocols.

- A predictive service life is then evaluated for a chosen temperature by calculating the time needed to reach a certain degradation retention percentage.

The following Figure 6.1 represents an example of this model that was created by Yan and Lin (2017), who evaluated the long-term bond degradation of GFRP rebars in fiber-reinforced concrete exposed to saline-rich conditions. In total, 105 bond specimens were submerged in a saline solution at 50 °C and 70 °C for up

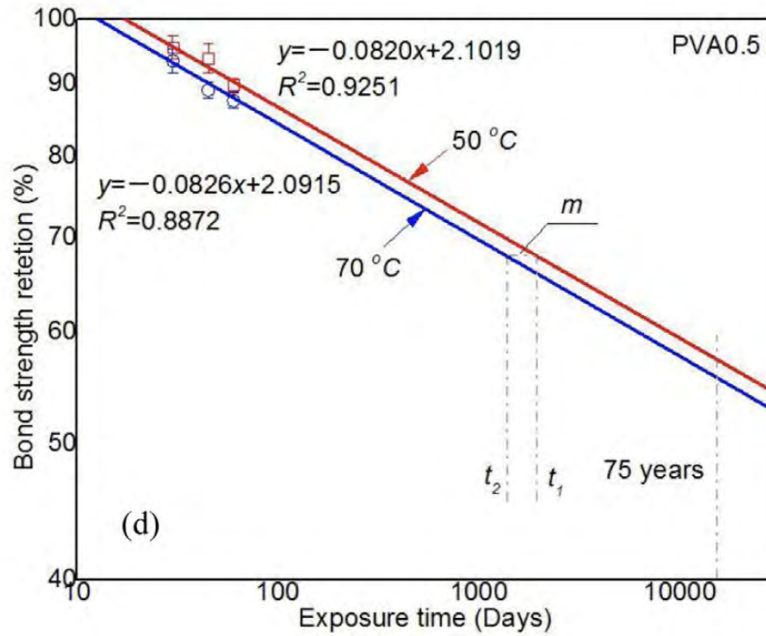


Figure 6.1: Bond retention over time in a double logarithmic scale according to (Yan and Lin, 2017)

to 60 days. It can be seen that the retention values were plotted on a double logarithmic scale and the linear regression lines for each of the data sets were calculated. Since a double logarithmic scale was used, an exponential trend line was determined so that the regression appeared to be linear (visually). From this trend line, the time shift factor ( $m$ ) was calculated as  $t_1 - t_2$ . Moreover, the predicted bond strength retention for a service life of 75 years was marked.

In the following sections, the degradation over time in a double logarithmic scale for the different mechanical properties tested for this research project are shown: transverse shear strength, horizontal shear strength, tensile strength, elastic modulus, and bond-to-concrete strength. All data points were based on the results obtained throughout the experimental program. For every individual mechanical property, two main aspects

were evaluated to determine the validity of the Arrhenius model: (i) First, the coefficient of determination, or  $R^2$  value, was checked. This value generally ranges from 0 to 1 and numerically evaluates how well the linear trend-line (on a log-log graph) fits the data set; a value closer to 1 indicates a better fit. (ii) Then, the parallelism of the trend lines within each graph was evaluated: for each rebar type and mechanical property, the three trend lines corresponding to the three different temperatures should be parallel and the increase of temperature should lead to intensified degradation (negative slope) if the Arrhenius model applies. Finally, the obtained values were compared to the ones found in the literature, summarized in Table 6.1. This ta-

Table 6.1: Existing durability modeling research projects

Research Study	FRP Type	Analyzed Mechanical Property	Accelerated Aging			$R^2$
			Solution	Duration d	Temperature °C	
Wang et al. (2017)	B, C, & G FRP	Horizontal shear	Simulated seawater & sea sand concrete	< 84	25, 40, 55	0.71-0.99
Yan et al. (2017)	G FRP	Bond	Saline solutions	< 60	50, 70	0.88-0.95
Dong et al. (2016)	B, & G FRP	Bond	Seawater	< 240	25, 40, 55	0.88-0.99
Wang et al. (2017)	B, & G FRP	Tensile	Simulated seawater & sea sand concrete	< 63	23, 40, 48, 55	0.96
Wu et al. (2014)	B FRP	Tensile	Alkaline, salt, acid & de-ionized water	< 63	25, 40, 55	0.85-0.99
Robert et al. (2013)	G FRP	Tensile	Concrete + saline solution	< 365	23, 40, 50, 70	0.96-0.99
Robert et al. (2009)	G FRP	Tensile	Concrete + tap water	< 240	23, 40, 50	0.94-0.99
Chen et al. (2006)	G FRP	Tensile	Alkaline	< 240	20, 40, 60	0.92-0.99
Dejke et al. (2001)	G FRP	Tensile	Alkaline, concrete, and tap water	< 365	23, 40, 60	NA

ble compiles some of the most significant FRP rebar (Glass, Basalt, and Carbon FRP) durability modeling projects based on the Arrhenius relationship. It can be inferred that the deterioration of the tensile strength was the main focus of past studies, though a few projects studied the degradation of the horizontal shear strength and the bond-to-concrete strength. The exposure solutions, as well as the exposure durations and temperatures, vary significantly. However, no study extended a 1 year duration. The  $R^2$  values reported in the literature are relatively consistent with average values above 0.9 and not less than 0.71.

### Transverse Shear Strength

The degradation plots for the durability of the transverse shear strength in this research are shown in Figure 6.2. For each of the rebar types (A, B, and C), the average retention values after 60 d, 120 d, 210 d, and 365 d are plotted as individual data points on double logarithmic scales and the calculated linear trend lines (on a log-log graph) are shown for each conditioning temperature. In addition, the  $R^2$  values were calculated as shown in each plot. It is noted that the  $R^2$  values vary significantly, ranging from 0.040 to 0.750, showing a clear inconsistent material response to the temperature exposure. Compared to the literature, other researchers showed more consistent results that reached  $R^2$  values above 0.70 (Chen et al., 2006; Dejke and Tepfers, 2001; Dong et al., 2016; Robert et al., 2009; Robert and Benmokrane, 2013; Wang

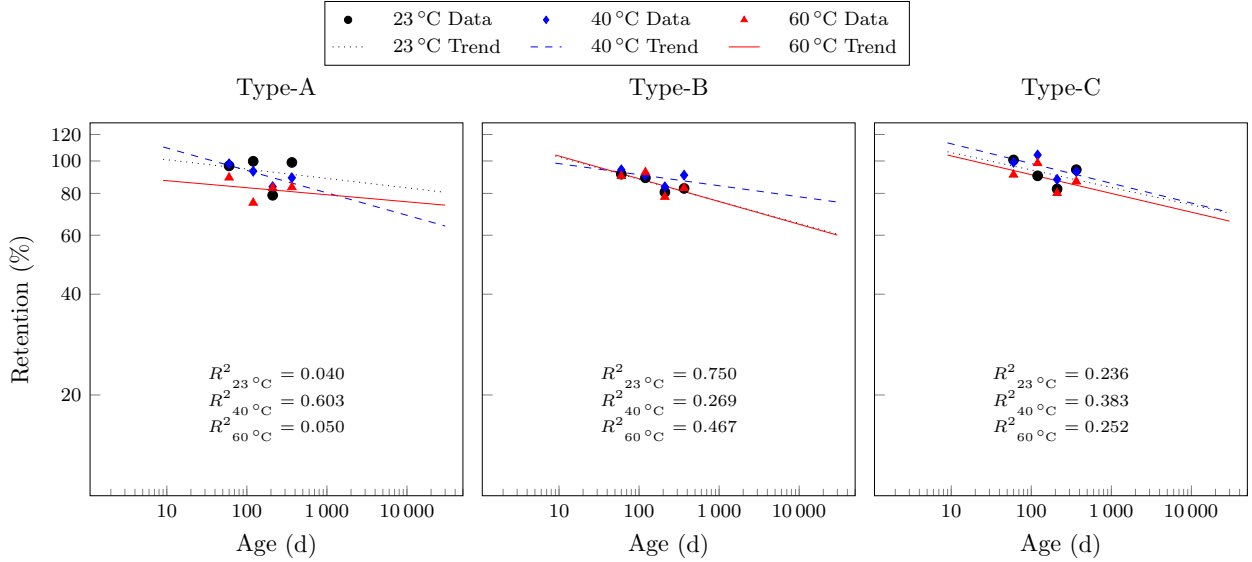


Figure 6.2: Transverse shear strength retention over time in a double logarithmic scale

et al., 2017; Yan and Lin, 2017; Wu et al., 2014) for durability assessment of tensile, horizontal, and bond strength (see Table 6.1). Thus, it can be concluded that the linear fit is not reflective for the data determined in this research. Moreover, the trend lines are not parallel to each other (for each rebar type), which indicates that the Arrhenius model might not apply for the tested materials and conditions. The trend lines for Type-C rebars show best parallelism among the three tested products, but the 23 °C data breaks the rule because it is located between 40 °C and 60 °C, while it should be situated above. Because the data does not support the use of the Arrhenius model, no further evaluation was possible. To the best knowledge of the authors, no study currently exists that focused on the long-term behavior of the transverse shear strength or applied durability modeling to this particular mechanical property. No comparison to existing research can be offered here.

### Horizontal Shear Strength

For the evaluation of the long-term deterioration of the horizontal shear strength (which is mostly affected by the quality of the resin), similar graphs as for the transverse shear strength were plotted in Figure 6.3. As seen before, the  $R^2$  values were very inconsistent and attained very low values, ranging from 0.003 to 0.749, signifying an inconsistent material response to the aging process. The parallelism was not maintained either: Type-C rebars trend lines were closest to be parallel, but not sufficient to consider the Arrhenius model as applicable. It is also noticeable that in some cases, such as for 40 °C and 60 °C for Type-A and 23 °C for Type-B, the trend appeared to be positive, which contradicts the assumptions of Arrhenius and the degradation process. In the literature, a similar research study can be found relative to the long-term-performance



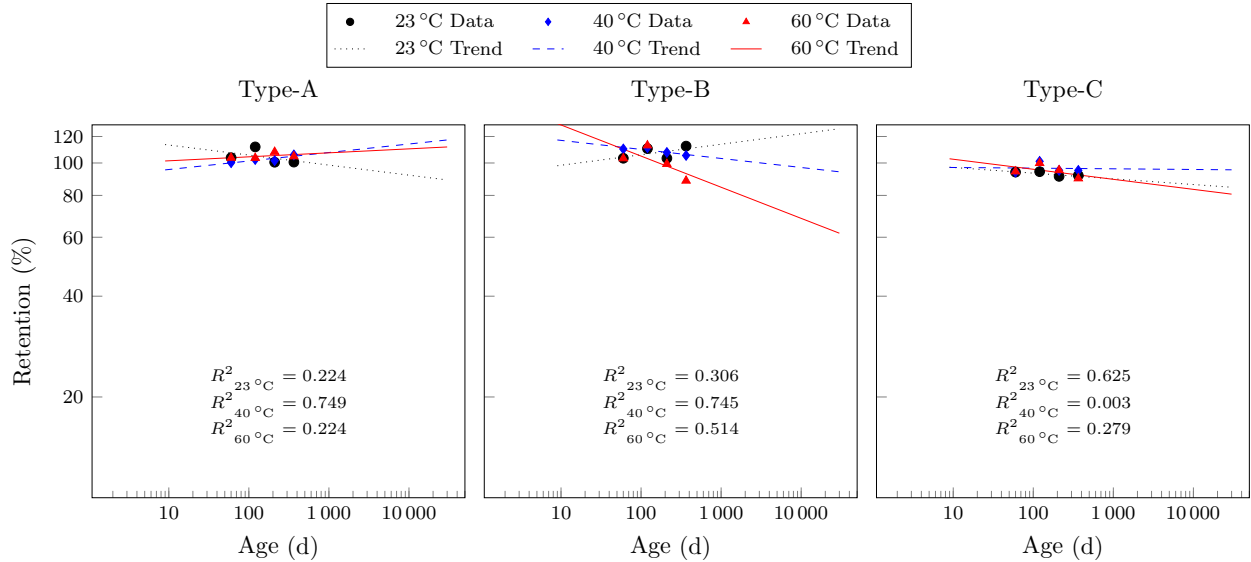


Figure 6.3: Horizontal shear strength retention over time in a double logarithmic scale

modeling of the horizontal shear strength using the Arrhenius model: Wang et al. (2017) evaluated the degradation of the horizontal shear strength properties for Glass, Basalt, and Carbon FRP rebars in seawater and sea sand concrete. In that study, degradation values based on accelerated aging of up to 84 d were used to feed the Arrhenius model, and the researchers were able to show parallel trend lines. This was not reproducible here: the difference in exposure solution and the short exposure time used by Wang et al. (2017), as compared to the exposure durations used in this research project, were considered as potential reasons.

### Tensile Strength

Among all evaluated mechanical properties in this study, the tensile strength values throughout different exposure conditions and at different ages lead to the highest and most consistent coefficient of determination, ranging from 0.666 to 0.995. These values are closer to the ones determined by others (Chen et al., 2006; Dejke and Tepfers, 2001; Dong et al., 2016; Robert et al., 2009; Robert and Benmokrane, 2013; Wang et al., 2017; Yan and Lin, 2017). However, as seen in Figure 6.4, the parallelism between the various prediction lines of the individual rebar types was rather poor, which negates the time shift factor or made it impossible to apply this method. Tensile strength and its degradation over time is among the most evaluated mechanical property in the literature (Robert et al., 2009; Chen et al., 2006; Dejke and Tepfers, 2001; Wang et al., 2017; Robert and Benmokrane, 2013; Wu et al., 2014), and broader knowledge for the degradation behavior of this property is available (see Table 6.1). Though the research projects available in the literature reported parallelism between the trend lines for different temperatures, this finding could not be reproduced for material tested after saltwater exposure in this project. The various aging solutions (no seawater was used in any previous

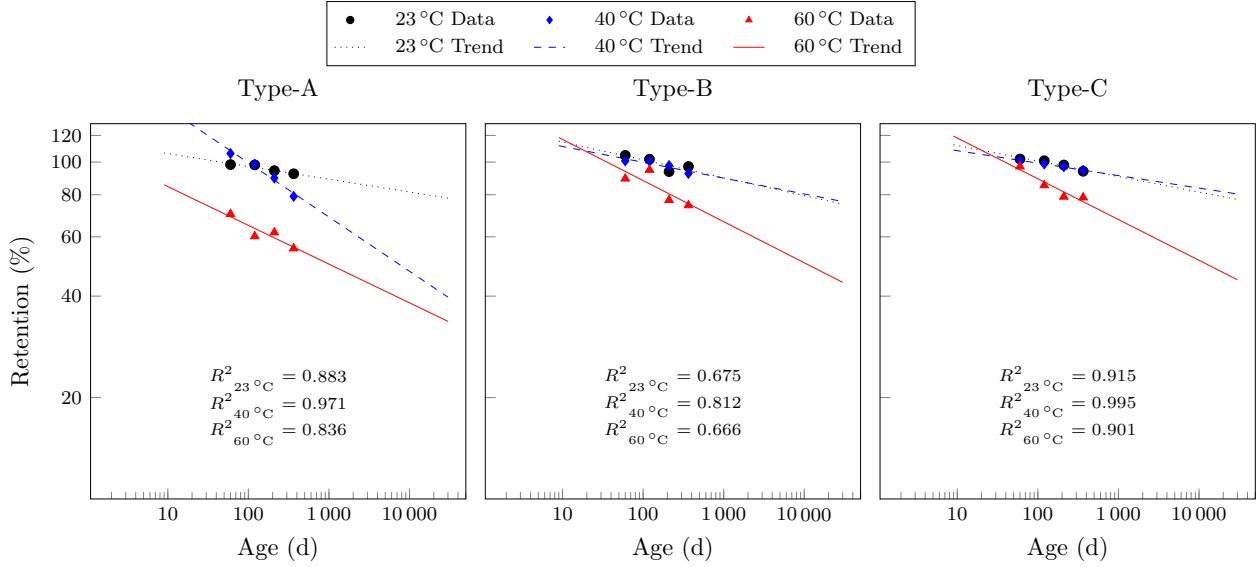


Figure 6.4: Tensile strength retention over time in a double logarithmic scale

study) and the dissimilar exposure conditions/durations are the potential reasons for these differences.

### Elastic Modulus

The  $R^2$  values for the linear trend lines reflecting the data set for the elastic modulus retention showed high variability ranging from 0.006 to 0.910. But among the five tested mechanical properties, the elastic modulus is the one that initially appeared to fit the degradation model best, with mostly parallel trend lines, specifically for Type-B rebars. However, as seen in Figure 6.5 where the degradation plots for the retention of E-modulus are shown, the degradation of the elastic modulus appeared to be not accelerated by the increased temperatures, at least not for Type-B and Type-C, because the trend lines relative to 23 °C and 40 °C were almost equivalent and below the one for 60 °C. Accordingly, the authors disregard the applicability of the Arrhenius model to predict the long-term behavior of this mechanical property as well.

### Bond-to-Concrete Strength

Finally, Figure 6.6 shows the plots for the bond strength deterioration for the three evaluated GFRP rebar products. Among all tested properties in this study, the bond-to-concrete strength is the one with the lowest  $R^2$  values, ranging from 0.005 to 0.918, signifying how scattered the obtained data was. Unlike the findings reported by Yan and Lin (2017) and Dong et al. (2016), the trend lines calculated from the data in this study did not show any parallelism for any of the evaluated rebar types. In fact, the graphs show how scattered the data and how different the calculated prediction trends were. Similar to the data for the horizontal shear strength, some trend lines had a positive slope, which would indicate that the material performance improved

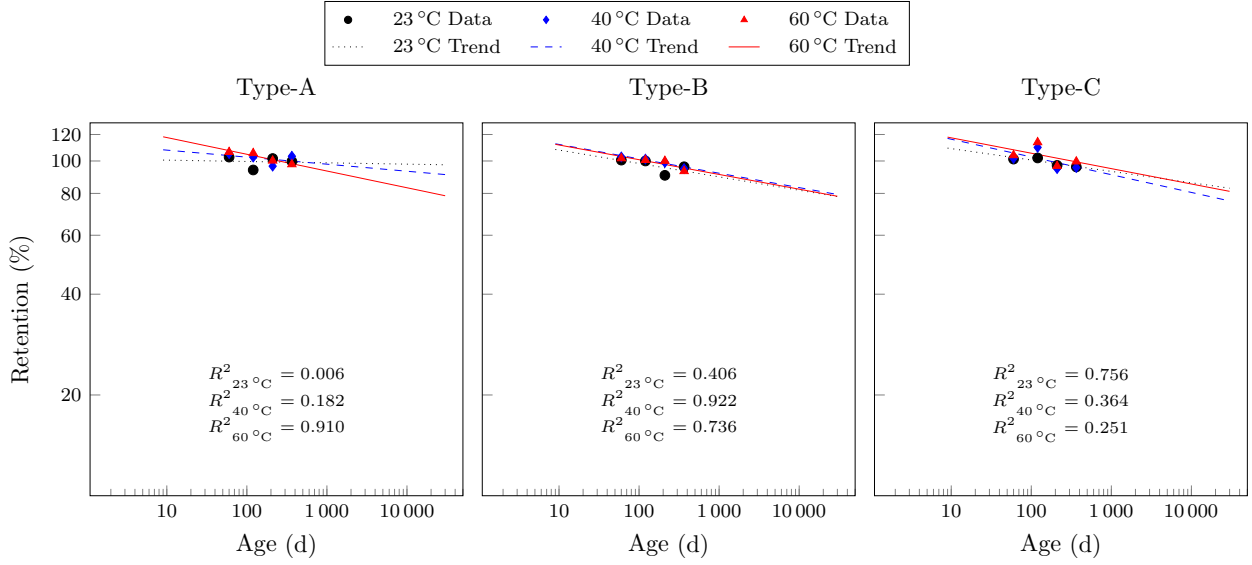


Figure 6.5: Elastic modulus retention over time in a double logarithmic scale

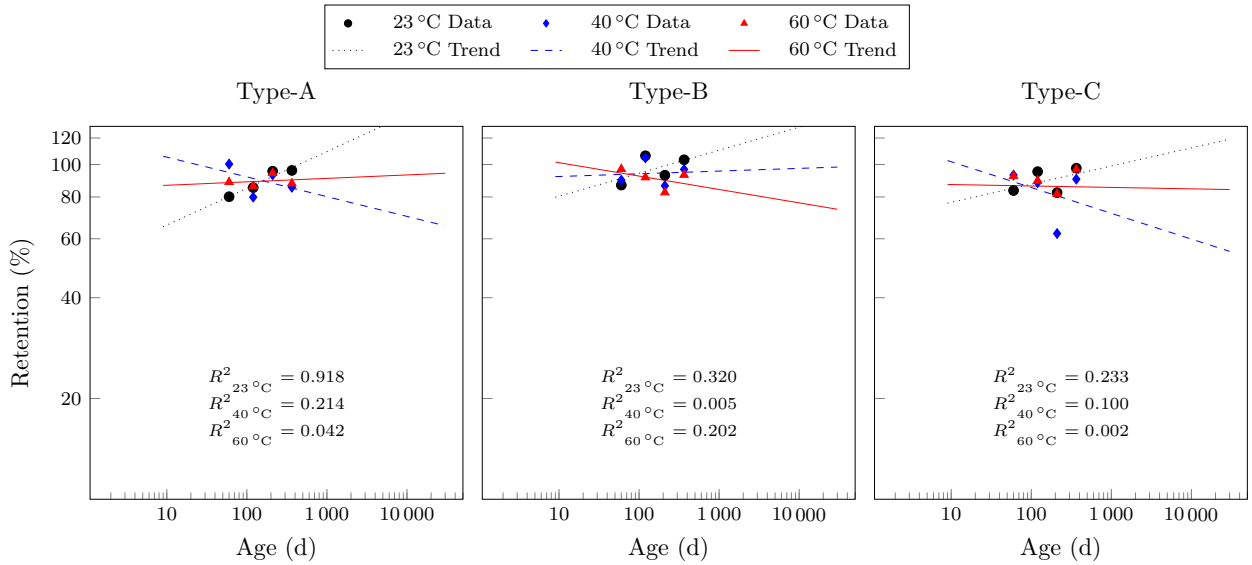


Figure 6.6: Bond-to-Concrete strength retention over time in a double logarithmic scale

with exposure to elevated temperatures for extended time periods. However, this is unlikely or unrealistic and it has to be assumed that the Arrhenius model is not applicable or that more than one strength-affecting process contributes to the long-term behavior.

## 6.2.2 Degradation Rate Alternative

Besides the approach developed by Litherland et al. (1981), other models exist to determine the rate coefficient for FRP rebars. The Arrhenius model considers the degradation to be purely chemical. Based on the kinetics

of chemical reactions, the rate of change of the concentration of a reactant over time for a single reactant 'A', or rate of reaction, can be expressed as follows:

$$r_A = \frac{dC_A}{dt} \quad (6.6)$$

In addition, rate of reaction can also be expressed as seen in Equation 6.7, where 'k' is the rate coefficient and accounts for temperature effects, while 'α' is defined as the reaction order, which is equal to the stoichiometric ratio of reactants to products for elementary reactions.

$$r_A = kC_A^\alpha \quad (6.7)$$

The rate coefficient 'k' follows the Arrhenius law and rises exponentially with temperature.

Combining and integrating Equations 6.6 and 6.7, the concentration of a reactant as a function of time, can be obtained:

$$-\frac{dC_A}{dt} = -r_A = kC_A^\alpha \quad (6.8)$$

$$\int_0^t -k dt = \int_{C_A}^{C_{A0}} \frac{dC_A}{-r_A} \quad (6.9)$$

$$kt = - \int_{C_A}^{C_{A0}} \frac{dC_A}{C_A^\alpha} \quad (6.10)$$

$k$  Rate coefficient for order 'n' reaction ( $\frac{\text{mol}}{\text{L}} \frac{1-n}{s}$ )

$\alpha$  Order of reaction

$C$  Concentration ( $\text{lbs.} \frac{\text{mol}}{\text{L}^3}$ )

$r$  Rate of reaction ( $\frac{\text{mol}}{\text{Ls}}$ )

Table 6.2 lists the solutions for these integrals for different orders of reaction. The time-dependent perfor-

Table 6.2: Integrated Rate Equations

reaction order	reaction	rate equation	integrated form
0	A - R	$-r_A = kt$	$kt = C_{A0} - C_A$
1	A - R	$-r_A = kC_A$	$kt = \ln \frac{C_{A0}}{C_A}$
2	2A - R	$-r_A = kC_A^2$	$kt = \frac{1}{C_A} - \frac{1}{C_{A0}}$
3	3A - R	$-r_A = kC_A^3$	$kt = \frac{1}{2} \left( \frac{1}{C_A^2} - \frac{1}{C_{A0}^2} \right)$

mance equations for each order can be plotted to evaluate which form generates a straight line and defines the order of reaction based on the experimental data.

Based on the findings for the simple Arrhenius model presented above, only the degradation of the tensile properties were further evaluated using the alternative models. The degradation rates were calculated as the slope of the linear regression fitting the data points equivalent to the integrated forms listed in Table 6.2. Figure 6.7 plots the integrated forms for the four different reaction orders over time as they were recorded for the three evaluated rebar types. In addition, the linear regressions for each data set are shown. The slope of these linear regressions represent the rate coefficient 'k' relative to each reaction order, and the numerical values for those rate coefficients for all rebars and exposure conditions are listed in Table 6.3. Moreover, the  $R^2$  values for the linear fit were also calculated to assess the statistical validity for each case. As seen from Table 6.3, except for Type-A at 60 °C and Type-B at 23 °C, the  $R^2$  values increased to over 0.80, which is considered to be relevant. However, between the different reaction orders, the  $R^2$  values did not vary significantly, though trend produced a better fit with an increased reaction order. Accordingly, the four orders were evaluated further.

After the rate coefficient 'k' was calculated, the Arrhenius expression based on natural logarithms on both sides of the equation (c.f. Equation 6.3) was plotted. In this so-called Arrhenius plot, the logarithm of the inverse of the rate coefficient is plotted against the inverse of the temperature. The slope of these plots is directly related to the activation energy,  $E_a$  (activation energy divided by the universal gas constant). In addition, the intercept of the plot with the Y-axis is equivalent to the logarithm of the pre-exponential or Arrhenius factor, 'A'. Table 6.4 summarizes the results obtained for the different cases, and shows that all  $R^2$  values were determined to exceed 0.8. Type-A rebars showed the best fit, followed by Type-B and Type-C rebars.

After all required parameters are calculated, the model can be extrapolated for any desired temperature. For the purpose of this report, the service life at three different temperatures was predicted: (i) 25 °C as the annual mean temperature in South Florida, (ii) 20 °C as the average temperature in North Florida, and (iii) 10 °C for the mean temperature in Northern United States. Figure 6.9 shows the service life models for the different rebar types, different reaction orders, and different predictive temperatures. It can be inferred that predictions based on different reaction orders vary significantly. Therefore, to evaluate the fit of each model, the Sum of Squares of Error, or  $SSE$ , for each case was calculated, which corresponds to the sum of the squared differences between the prediction for each observation and the corresponding experimental value. Table 6.5 summarizes the obtained  $SSE$  values for each order of reaction, temperature and type of rebar. It can be seen, that the model predicting the service life for Type-A rebars had a five to ten times higher total error than Type-B or Type-C rebars. Comparatively, the zeroth order lead to the highest error and the second order to the lowest one, for almost every evaluated case. Therefore, the second order was considered most appropriate in view of the obtained experimental data.

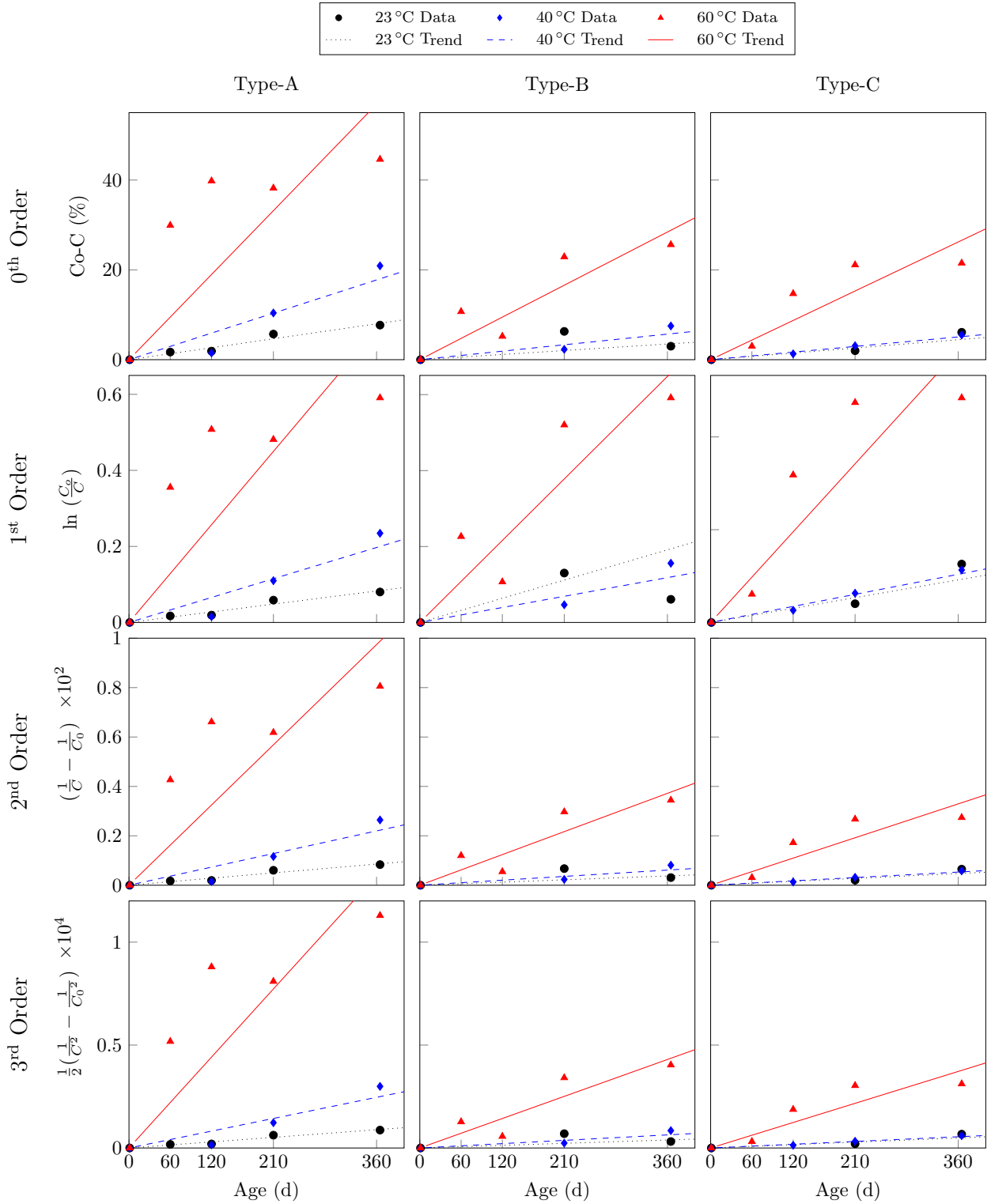


Figure 6.7: Graphical representation of the degradation rate, 'k'

Table 6.3: Calculation of degradation rate,  $k$ 

Manufacturer	Temperature	Order	$k$	$R^2$
Type-A	23 °C	0	$2.221 \times 10^{-2}$	0.952
		1	$2.299 \times 10^{-4}$	0.954
		2	$2.381 \times 10^{-6}$	0.955
		3	$2.467 \times 10^{-8}$	0.956
	40 °C	0	$4.932 \times 10^{-2}$	0.873
		1	$5.476 \times 10^{-4}$	0.885
		2	$6.105 \times 10^{-6}$	0.894
		3	$6.835 \times 10^{-8}$	0.899
	60 °C	0	$1.580 \times 10^{-1}$	0.593
		1	$2.042 \times 10^{-3}$	0.650
		2	$2.706 \times 10^{-5}$	0.707
		3	$3.679 \times 10^{-7}$	0.762
Type-B	23 °C	0	$9.707 \times 10^{-3}$	0.379
		1	$1.006 \times 10^{-4}$	0.377
		2	$1.042 \times 10^{-6}$	0.375
		3	$1.080 \times 10^{-8}$	0.373
	40 °C	0	$1.581 \times 10^{-2}$	0.847
		1	$1.640 \times 10^{-4}$	0.857
		2	$1.701 \times 10^{-6}$	0.846
		3	$1.766 \times 10^{-8}$	0.845
	60 °C	0	$7.894 \times 10^{-2}$	0.811
		1	$8.998 \times 10^{-4}$	0.823
		2	$1.033 \times 10^{-5}$	0.835
		3	$1.194 \times 10^{-7}$	0.845
Type-C	23 °C	0	$1.235 \times 10^{-2}$	0.805
		1	$1.274 \times 10^{-4}$	0.808
		2	$1.315 \times 10^{-6}$	0.811
		3	$1.358 \times 10^{-8}$	0.814
	40 °C	0	$1.407 \times 10^{-2}$	0.909
		1	$1.442 \times 10^{-4}$	0.912
		2	$1.479 \times 10^{-6}$	0.915
		3	$1.517 \times 10^{-8}$	0.918
	60 °C	0	$7.281 \times 10^{-2}$	0.794
		1	$8.142 \times 10^{-4}$	0.804
		2	$9.147 \times 10^{-6}$	0.814
		3	$1.033 \times 10^{-7}$	0.822

### 6.3 Summary and Conclusions

In this chapter, the Arrhenius model was evaluated using two different degradation laws: (i) the one developed by Litherland et al. (1981) where the retentions were plotted against time on a double logarithmic scale, and (ii) the model used for kinetics of reactions. To facilitate the multi-parametric study, the first model was applied to the data and model predictions for all five physio-mechanical properties and the findings for all three rebar types are summarized in the following Figure 6.10. This figure facilitates a complete and concise

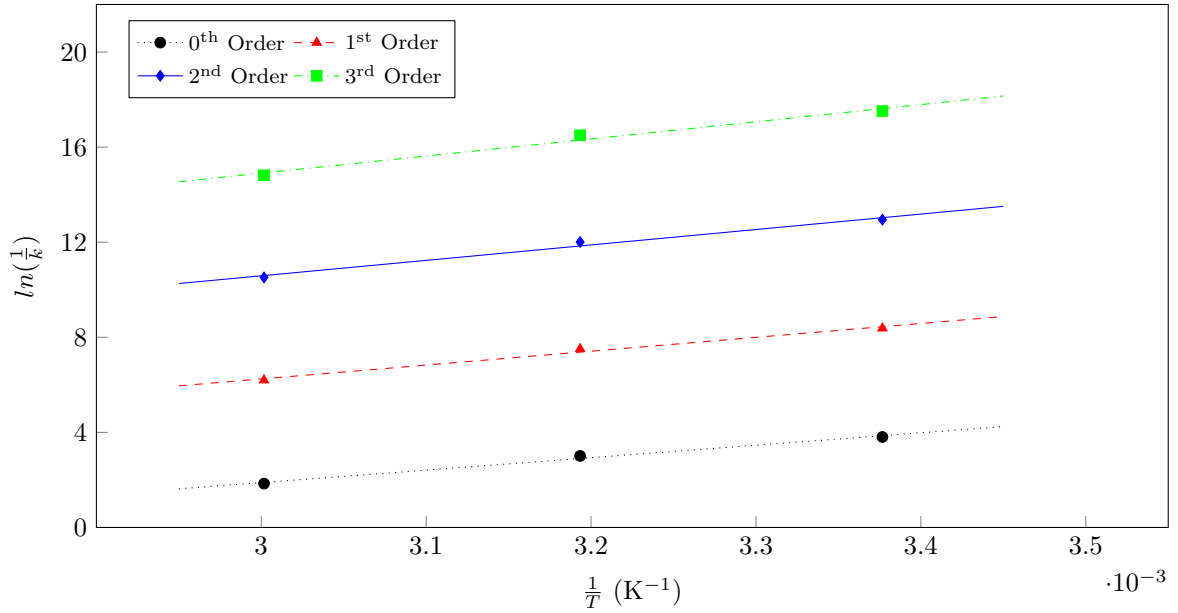


Figure 6.8: Arrhenius plots for different reaction orders

Table 6.4: Calculation of the activation energy

Manufacturer	Order	$E_a$	A	$R^2$
Type-A	0	43 561.9	1 014 542.1	0.991
	1	48 487.1	76 624.0	0.989
	2	53 967.9	7234.8	0.987
	3	60 007.6	855.1	0.984
Type-B	0	46 642.0	1 363 485.4	0.920
	1	48 765.2	32 952.9	0.915
	2	51 050.7	849.6	0.909
	3	53 498.8	23.4	0.904
Type-C	0	39 576.5	91 913.5	0.815
	1	41 372.5	1936.0	0.810
	2	43 268.5	42.5	0.806
	3	45 264.9	1.0	0.801

overview of all degradation plots: each column represents a rebar type, while an individual mechanical property can be found in each row. Moreover, to compare the quality of the predicted performance, a summary of all  $R^2$  values is presented in Table 6.6. The table summarizes the  $R^2$  values, but also signifies the slopes (negative or positive) for all temperatures, rebar types, and mechanical properties; if a deterioration behavior was predicted, a negative sign was given. This was indicative of the fit for the Arrhenius model to evaluate which physio-mechanical property can be modeled best through this approach.

After analyzing extensive data sets and performing prediction calculation for numerous physical FRP rebars characteristics, the authors conclude that the approach developed by Litherland et al. (1981) is not



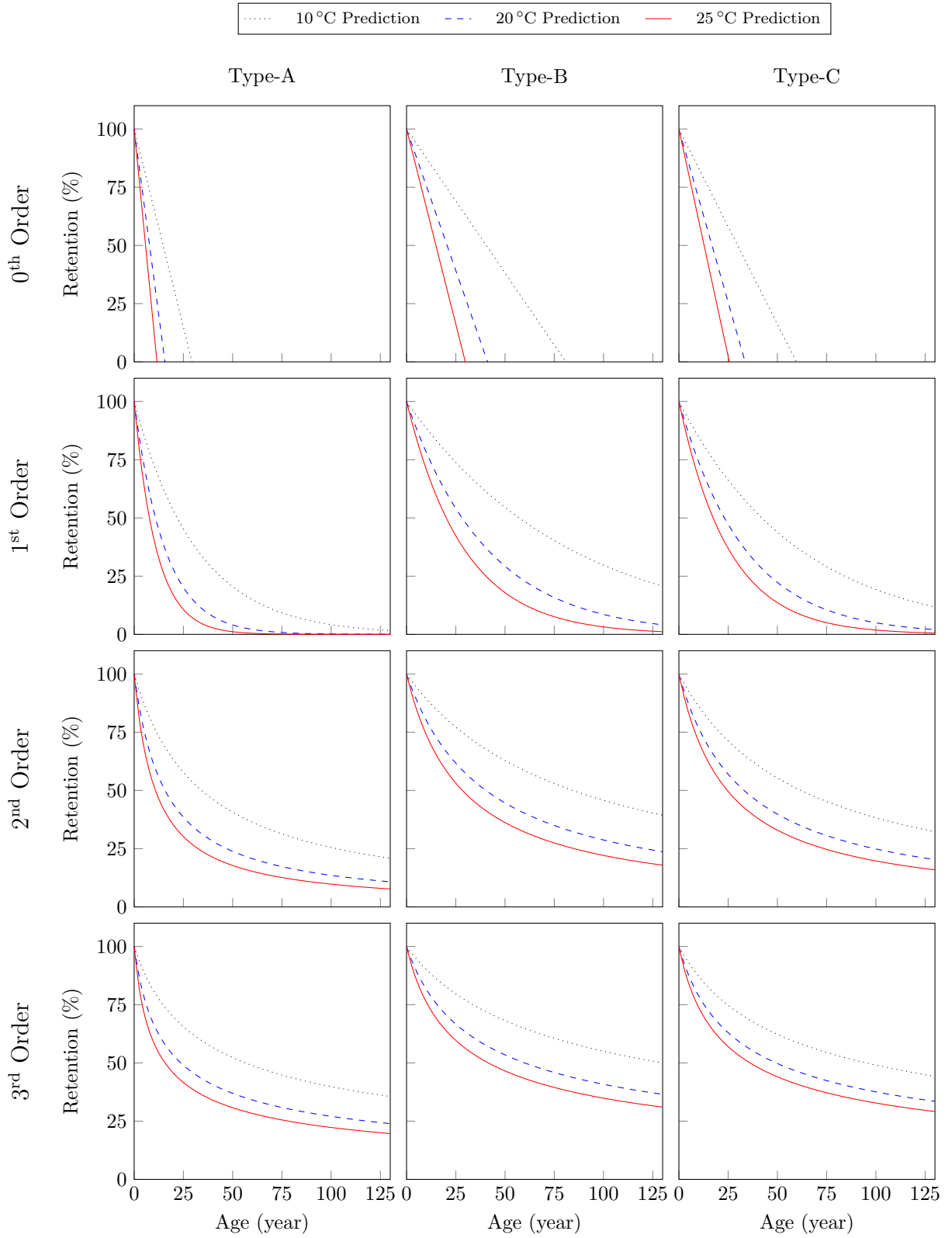


Figure 6.9: Service life prediction for different temperatures

Table 6.5: Sum of Squares of Errors (SSE) for all the reaction orders and rebar types

Rebar type	Temperature	Reaction order			
		0 <sup>th</sup>	1 <sup>st</sup>	2 <sup>nd</sup>	3 <sup>rd</sup>
Type-A	23	2.0	1.9	1.8	1.8
	40	108.2	116.8	127.4	341.8
	60	1047.3	738.0	517.3	346.3
	$\Sigma$	1157.5	856.7	646.4	690.0
Type-B	23	56.4	56.4	56.5	56.6
	40	13.8	14.2	14.6	46.2
	60	104.1	93.0	86.6	83.9
	$\Sigma$	174.3	163.7	157.7	186.8
Type-C	23	16.6	16.9	17.1	17.4
	40	4.1	4.2	4.3	12.0
	60	96.9	78.9	65.3	55.2
	$\Sigma$	117.7	99.9	86.7	84.6

Table 6.6: Coefficients of determination ‘ $R^2$ ’ and slopes of trend lines for all rebar types, temperatures, and mechanical properties

Mechanical property	Manufacturer	$R^2$			Slope		
		23°C	40°C	60°C	23°C	40°C	60°C
Tensile strength	Type-A	0.883	0.971	0.836	-	-	-
	Type-B	0.675	0.812	0.666	-	-	-
	Type-C	0.915	0.995	0.901	-	-	-
E-Modulus	Type-A	0.006	0.603	0.050	-	-	-
	Type-B	0.269	0.406	0.467	-	-	-
	Type-C	0.760	0.383	0.252	-	-	-
Transverse shear	Type-A	0.039	0.603	0.050	-	-	-
	Type-B	0.750	0.269	0.467	-	-	-
	Type-C	0.236	0.383	0.252	-	-	-
Horizontal shear	Type-A	0.224	0.749	0.224	-	+	+
	Type-B	0.306	0.514	0.745	+	-	-
	Type-C	0.279	0.625	0.003	-	-	-
Bond	Type-A	0.918	0.214	0.042	+	-	+
	Type-B	0.320	0.005	0.202	+	+	-
	Type-C	0.233	0.100	0.002	+	-	-

applicable for durability modeling of GFRP rebars exposed to seawater. Except for the tensile strength results, which generated  $R^2$  values close to 1, the findings varied significantly with distinctively low coefficient

of determination. In addition, most trend lines determined for this research project (within each mechanical property and rebar type) diverted from being parallel. This leads to the conclusion that GFRP rebars directly exposed to seawater might not be predominantly affected by a chemical deterioration process, as it is assumed by the Arrhenius model. It has to be assumed that other degradation mechanisms (besides chemical reactions) affect the rebar, and that mechanical- or defect-related factors (or a combination of those) contribute to the long-term behavior of GFRP rebars in saltwater.

However, the authors also applied the principles of kinetics of reactions as an alternative approach to the afore mentioned model. Four different reaction orders were evaluated (from zero to three). After evaluating each order in detail by calculating the Sum of Squares of Error, or *SSE*, it was concluded that the second order fitted the experimental data best. Even if the results look more appropriate than the ones obtained from the first model, the high values of *SSE* (above one thousand with 4 data points and an average retention value of 70 %) show that other models should be considered for future studies to improve the prediction accuracy. In fact, the reported *SSE* values emphasize that the degradation mechanisms is driven or at least affected by other processes and not just chemical reactions/degradations.

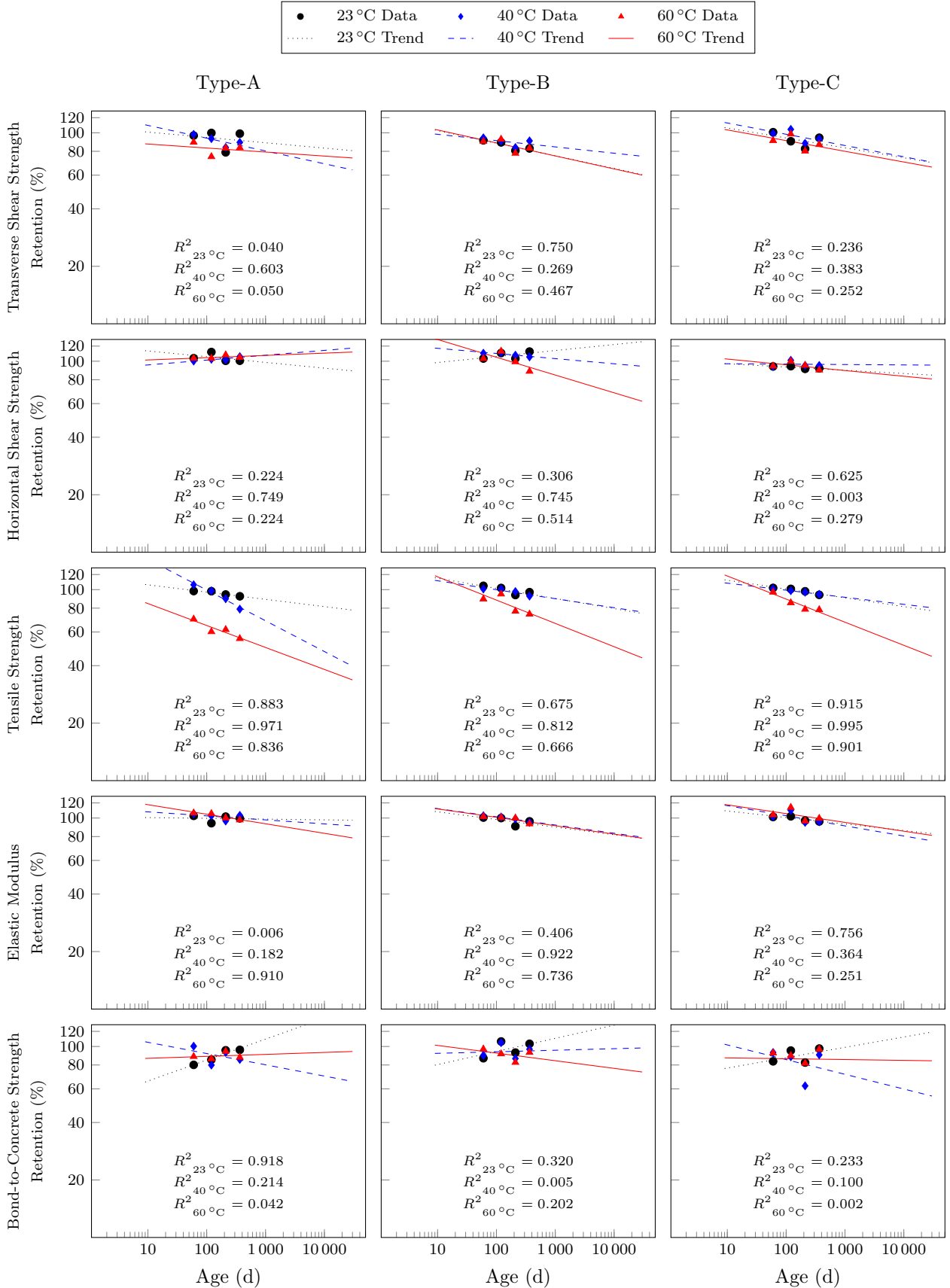


Figure 6.10: Long-term prediction based on Arrhenius relationship — Summary

# Chapter 7

## Discussion

### 7.1 Research Significance

The Florida Department of Transportation continues to implement innovative materials to enhance the sustainability and durability of taxpayer-funded infrastructure. Technologies developed over the last two decades have facilitated the use of glass fiber reinforced polymer composites as internal reinforcement bars for concrete structures, which have proven to be an alternative to traditional steel reinforcement due to significant advantages such as high tensile strength, lightness, magnetic transparency, and most importantly, corrosion resistance, which equates to improved durability and structural life extension. Hence, a key initiative for the Department is the implementation of GFRP bars for reinforcement of concrete structures because its implementation will lead to prolonged service life of FDOT owned and maintained infrastructure in the future.

In recent years, the number of reinforced concrete structures specifying GFRP rebars to enhance durability has increased significantly, and in response numerous GFRP rebar manufacturers have emerged. These manufacturers have developed different GFRP rebar types, which are produced via various proprietary concepts that lead to different products with a multitude of shapes, properties, and surface enhancement to create the bond with concrete. Hence, prior to implementing GFRP rebar technology in state infrastructure projects, it is imperative for the Department to evaluate the performance (mechanical and bond to concrete properties) and durability (material degradation) properties of commonly available GFRP rebars, with a special focus on the rebar compatibility in aggressive environments such as those experienced in Florida. The state of Florida is characterized by a terrestrial humid subtropical climate in the northern and central parts; while the south has a tropical savanna climate as defined by the Koppen-Geiger climate zones (Chen and Chen, 2013; Hittle and Zucker, 2004; Stabenau and Kotun, 2012). In addition, the salinity of much of

the water bodies in Florida has undergone dramatic changes over the past century. The overwhelming trend emerging from numerous studies and surveys is an increased salinity (Wingard et al., 2018). The increased demand on the infrastructure as well as environmental challenges due to the unique climate and location of the State of Florida result in an accelerated degradation of the infrastructure, which needs to be addressed by making progress toward safe and long-term infrastructure solutions.

For this project, these aggressive environmental factors were reflected and studied; the tested rebar specimens were exposed to accelerated aging conditions and evaluated for property retention to quantify the suitability of GFRP rebar technology for the use and applicability in Florida. This project aimed to provide data-driven information about commonly available GFRP rebar products with a wide array of physical characteristics to assist the Florida Department of Transportation in the current implementation efforts. Thereby, this project directly benefits the State by establishing the use of reliable GFRP rebar technologies for concrete reinforcement as a resilient solution for infrastructure. This report specifically provides material performance data, documents how durability concerns were experimentally addressed, and offers recommendations for the integration of this emerging technology with a focus on existing FDOT guidelines.

## 7.2 Critical Analysis of Major Findings

The results summarized in Chapter 5 showed performance differences between the manufactured rebar types but also size specific differences; some products did not meet the minimum specifications currently defined in FDOT Section 932 (Florida Department of Transportation, 2018). All three tested Type-A rebar sizes failed to meet the maximum moisture absorption criteria for both short-term and long-term (saturation). Moreover, Type-A # 3 rebars failed to meet the minimum guaranteed tensile load. Similarly, Type-B # 3 rebars failed to meet the minimum guaranteed tensile strength requirements, and # 5 rebars failed in transverse shear; # 8 rebars, however, met all specification requirements. Finally, Type-C was the only rebar type that met all specification requirements listed in FDOT Section 932 (Florida Department of Transportation, 2018).

The long-term performance of the three different GFRP rebar types was assessed by exposing # 3 rebars to seawater at different temperatures. Additional rebar sizes were not considered because maximum deterioration effects were expected for the smallest rebar size evaluated in this study; this approach was also taken by others, such as Wang et al. (2017). After 365 d at temperatures of 24 °C, 40 °C, and 60 °C, the maximum relative loss in properties were observed at the highest temperature.

Among the evaluated strength properties (transverse shear strength, horizontal shear strength, tensile strength and elastic modulus, and bond-to-concrete strength), the tensile strength was notably the most affected property for all three manufacturers; minimum retention values ranged around 67 % for Type-A, 74 %

for Type-B, and 78 % for Type-C. These values were slightly higher than the ones obtained in comparable studies: Robert and Benmokrane (2013) immersed GFRP rebars in saline solution to determine a maximum tensile strength retention of approximately 85 % after 365 d at 50 °C, while Al-Salloum et al. (2013) found a retention of about 87 % after 540 d. Reasons for the differences are assumed to be related to the different rebar types that were tested, but most importantly, the temperature used to accelerate aging was significantly lower (50 °C instead of 60 °C).

The durability results showed that the tensile strength decreased throughout the aging process, while the elastic modulus remain constant. In fact, the elastic modulus did not decrease by more than 5 % for any of the tested products, matching the findings by other researchers (Robert and Benmokrane, 2013; Al-Salloum et al., 2013). This was attributed to the utilized test method and the nature of this property. First, in this test method, the strain of the rebar is only measured at the surface or for the outermost fibers, while the tensile force is distributed across the entire cross-sectional area, but has to be transferred from the rebar anchors to the outer fibers toward the core. Second, the elastic modulus is described by the change in strain (of the outer fiber) over the change in stress. If both properties, the stretchability of the outer fiber, and the load capacity of the entire rebar decrease similarly, the slope of the stress-strain curve remains potentially unaffected while the load/stress capacity decreases due to aging.

After 365 d of exposure, the degradation of the transverse shear strength over time was the highest for the rebars aged at 60 °C. Rebar Type-A had a strength reduction of about 16.5 %, rebar Type-B of 17 %, and rebar Type-C of 13 %. Compared to other similar research projects, Benmokrane et al. (2017) saw comparable transverse shear strength reduction after exposing GFRP rebars (made of vinyl-ester and epoxy resin) to alkaline solution at 60 °C but after only 60 % of exposure time (208 d compared to 365 d). Therefore, it has to be concluded that alkaline environments are more critical than saline-rich environments for this mechanical fiber-driven material property.

The decrease in horizontal shear strength was less than 8 % for Type-B, around 10 % for Type-C, and Type-A measured an approximate strength increase of 5 %. The horizontal shear strength retention values were higher than those found in the literature. Chen et al. (2007) recorded a degradation of 10 % after exposing rebars to saline solution at 60 °C for no more than 45 d. While the retention or degradation values were comparable, the numbers presented in this study were obtained after significantly longer exposure durations (eight times as long). The differences may be attributed to a variation in constituent materials and to recent advancements in material developments.

The bond-to-concrete strength deterioration average at around 20 % for all tested products. Dong et al. (2016) exposed GFRP rebars to seawater at 40 °C for 60 d and found a degradation of approximately 7 %. In this study, fiber reinforced concrete instead of plain concrete was evaluated. However, the results were very

comparable to the ones obtained for the study presented in this report at similar temperature and age: 7% for Type-C rebars, 10% for Type-B, and no apparent degradation for Type-A.

Five different physio-mechanical properties were evaluated for durability purposes to provide a deeper insight on the possible degradation mechanism of GFRP rebars exposed to seawater. In general, it was found that the degradation of the tested material characteristics was more strongly related to the fiber-affected material tests (tensile strength and transverse shear strength) than the ones associated with the resin-driven properties (horizontal shear). For every rebar type, the highest reduction was recorded for the tensile strength (up to approximately 30% of reduction), while the transverse shear strength was the second most affected property (with a maximum strength decrease of about 20%). However, the reduction in horizontal shear strength was significantly lower (no more than 10%) for every rebar type. This led to the conclusion that in saltwater solutions, the resin properties do not suffer degrading effects as significantly as the glass fibers do. Moreover, the visual evidence of the micro-structural integrity captured by SEM imagery showed that the fibers and the interface between the fibers and resin were the most affected regions throughout the cross section of the rebars. However, the exact deterioration mechanism remains not fully understood.

The prediction model for the service life of each GFRP rebar type used in this research project was the Arrhenius model, with different variations to calculate the degradation rate. One of the main assumptions for the applicability of this model was the existence of a single predominant degradation mechanism. But after evaluating the experimental data via the model, it was found that the simple Arrhenius approach may not be applicable because a combination of different degradation mechanisms seems to exist, which cannot be dissociated by this model. Therefore, it was concluded that multiple degradation processes take place for GFRP rebars in high-temperature saline solutions, which affect the durability of rebars differently; based on the combined observations it was reasoned that the glass fibers and the bond between the resin and the fibers were more affected than the resin itself.

The moisture absorption and the porosity visualized through SEM imagery were directly related, and at the same time associated with the degradation of the rebars. The relation between moisture absorption and durability has been recognized by other researchers as well (Benmokrane et al., 2017) and it was stated that a higher moisture absorption leads to decreased rebar durability. Therefore, SEM imagery is an indispensable tool to detect void patterns, which indicates the performance of GFRP rebars over time.

### **7.3 Supplementary Findings**

While clear performance differences and specific rebar behavior were observed and recorded for the purpose of the research project and the major findings were in line with the initial objectives of this study, supplementary findings were documented throughout the various project phases. This section lists additional lessons learned



from the performed research and provides further guidance, which appeared relevant for the consideration and implementation of GFRP rebar technology.

Through the market analysis survey, which was conveyed to numerous GFRP manufacturers around the world, it was found that different GFRP rebar producers manufacture rebar sizes that differ significantly from the nominal dimensions; some produce rebars under the nominal dimensions and others produce rebars that exceed the nominal dimensions. This leads to different strength characteristics, which differs from the actual (nominal dimension related) strength (or the manufacturer reported strengths). For many construction companies and design firms this can be misleading, and it potentially creates controversial understanding of the true mechanical GFRP rebar properties and the actual dimensions (which can be critical when determining spacing requirements between rebars).

In addition, the survey revealed that quicker quality control tests for GFRP rebars for manufacturing companies are needed. To date, the tensile test is the most commonly used test to determine production batch quality. Though this test provides the direct tensile behavior of the rebars (the most critical parameter for design), it requires significant time investment (up to one week) to complete the tests due to long specimen preparation needs. In other words, production errors would not be detected in a timely matter and a significant material amount might be wasted if the tensile test results reveal that the material does not meet the threshold values defined by the applicable acceptance criteria. Therefore, while the current approach is not economical, it is also environmentally disastrous. To further improve material testing for GFRP rebars, side studies<sup>1</sup> were performed to evaluate the flexural strength of GFRP rebars and to determine correlation to the tensile strength. This approach appears valuable because flexural testing of FRP rebars are fast, economical, and relate to the stiffness and capacity of the evaluated product.

The failure mode observed during tensile testing (c.f. Subsection 5.3.3) via high-speed video technology<sup>1</sup> revealed that the outer fibers (and the helical wrapping fibers) failed first, before the inner ones did. The failure progressed from the outside toward the rebar core. This was attributed to the nature of the currently standardized test procedure. Because GFRP rebars have a low transverse capacity compared to the longitudinal strength, the rebars must be protected by grout or epoxy filled steel pipes to guarantee a smooth stress transfer from the grips of the load frame to the rebar. Since the outermost fibers are stressed — by the grout fiber interface — before the stress is transmitted to the inner fibers, and because the activation of the cross section is not uniform due to the shear lag effect (Kocaoz et al., 2005b), the outer fibers are the ones that stretch the most, and therefore, fail first. Moreover, for Type-A rebars, which were wrapped with external helical fibers, it was observed that the helical wrapping fibers failed before any of the longitudinal fibers fractured. This was contributed to the confinement that these helical fibers provide and produce; with increasing tensile stretch, the helical fibers tighten up around the rebar and for geometric reasons they

---

<sup>1</sup> These studies were outside the scope of this research project.

further restrain the rebar to reduce the eccentricity between the thrust of the tensile force and the helix. In consequence, the helical fibers experience the highest amount of stretch, and forces, which are not inline with the axis of the helical fibers. The effect of the helical fibers for the tensile performance of FRP rebars has not been quantified in this project and should be further examined.

## 7.4 Limitations

The market analysis has proven that many different rebar types exist, some with unique properties and features. Accordingly, the reported behavior of GFRP rebars is not universally applicable and must be limited because three specific products from three manufacturers were tested and compared against each another. While some features were compared on an absolute scale, some properties were compared relative to one another. However, the authors believe that some general feature-related characteristics can provide valuable insight for other FRP rebar products with similar features. For example, the bond-to-concrete performance showed clear differences for the various surface enhancement types and it appears reasonable to assume that other rebars with similar surface enhancement will show similar behavior. Likewise, the material performance after saltwater exposure showed that high temperature environments lead to the most severe material degradation and that some properties (fiber driven) were more affected than others (resin driven). These findings provide insight and guidance for future studies, although the authors explicitly advice using caution when extrapolating the conclusions from this project to other or future FRP rebar materials.

An extended exposure time for the rebar samples would result in a more accurate prediction of service life. The chosen exposure duration of 365 d for this project was the same as the duration evaluated by Deijke and Tepfers (2001) and Robert and Benmokrane (2013) but longer than mentioned by others (Chen et al., 2006; Dong et al., 2016; Robert et al., 2009; Wang et al., 2017; Yan and Lin, 2017; Wu et al., 2014) who evaluate GFRP rebar durability (c.f. Table6.1). However researchers such as Khatibmasjedi (2018) exposed GFRP rebars for two years and showed that degradation of the bond-to-concrete performance was significantly affected within the first year but remained considerably constant thereafter. Therefore, it appears that different material characteristics are differently affected by prolonged exposure. More research is needed to quantify the effects on distinct GFRP rebar engineering properties.

This research project evaluated the durability of naked rebars exposed directly to seawater, which was done to simulate heavily cracked reinforced concrete structures. However, rebars in regular structures are not directly exposed to seawater and mostly surrounded by a high alkaline environment due to concrete embedment. Other researchers (Chen et al., 2006; Deijke and Tepfers, 2001; Wu et al., 2014) have assessed the durability of GFRP rebars exposed to alkaline solution, which simulates pore solution of concrete; however, to the best knowledge of the authors, no research project exists in which naked rebars were exposed to both

high pH and seawater. While some have used saline solutions, no research based on actual ocean saltwater appears to be available.

For this project, the material characteristics and durability properties of three different commercially available GFRP rebar types exposed to high temperature seawater were evaluated. For economical reasons and to cover a wide array of test procedures and material characteristics, the test repetitions (per rebar type, size, and test procedure) were limited. While average values and some statistical numbers were determined, a full statistical evaluation of the obtained results was not feasible, and the reliability of the reported averaged values must be carefully considered. Specifically for the bond-to-concrete experiments, the variability was a significant issues as these results are generally scattered due to the nature of the test. Similar variabilities were seen by others (Khatibmasjedi, 2018), but this could be addressed through a larger test array in future studies.

## 7.5 Future Directions and Follow-up Research

Based on the major and secondary findings, and the acknowledged limitations of this research project, the authors are of the opinion that further research is crucial for quality control and durability assessment of GFRP rebars. The authors propose to further evaluate the durability of GFRP rebars in marine environments to validate the obtained results and to provide more substantial data for this critical aspect. Because the FDOT considers FRP material specifically for the application in marine concrete structures, it is important to further study the degradation mechanisms of FRP rebars in combined conditions. Thus, the authors recommend to expose rebars to conditioning solutions that — in addition to the effect of saltwater — also account for the high pH concentration in concrete. This can be achieved by adding hydroxides to seawater, instead of adding it to tap water — as it was done by others (Chen et al., 2006; Dejke and Tepfers, 2001) — similar to the research approach reported by Wang et al. (2017); Robert and Benmokrane (2013). Such a study will complement the simulated heavily cracked marine structure (rebars exposed directly to seawater) and add valuable information about uncracked structure in seawater (salinity and alkalinity).

A more thorough research toward the bending properties of GFRP rebars is needed to develop a quick test procedure that leads to a reduction of test efforts when characterizing GFRP rebars. This research should experimentally address the relationship between the bending and tensile performances of various rebar types. A standardized quick strength test is needed to improve quality control of GFRP rebars and to provide a faster, cheaper, and more environmentally friendly test procedure for FRP rebar manufacturers and certifying laboratories.

The confinement and potential strengthening or weakening effects of external wrapping fibers on the tensile behavior of FRP rebars should be further evaluated because FRP rebar specific aspects can be ad-

dressed. Findings from such studies will lead to more economical and strength improved FRP rebar products and quantification of the confinement effects can help the department to select better materials for FDOT construction projects.

As stated in Chapter 6, one of the assumptions for the applicability of the Arrhenius model was that no post curing of the resin occurs. To proof this numerically, differential scanning calorimetry (DSC) technology can be utilized: with it, the thermal behavior and characteristics such as the glass transition temperature ( $T_g$ ) and curing process of the rebar materials can be defined. Benmokrane et al. (2017) has also recommended such tests to relate the results to rebar durability. For example, after conditioning the samples at 60 °C for 206 d, a reduction of  $T_g$  was seen in GFRP rebars made from epoxy resin, which was related to the moisture uptake over the aging process or plasticizing effect. In a future research project, the glass transition temperature ( $T_g$ ) values should be evaluated via differential scanning calorimetry (DSC) for various rebars or material types. Such test procedures can be conducted to classify resin curing rates and it will help to determine if post curing of a specific rebar type occurred, or not.

Finally, the conventional test method to evaluate the bond properties between GFRP rebars and concrete is based on a pullout test in which the rebar is pulled out from a concrete cube. Due to the methodology of this test, the concrete cube is compressed as the rebar is pulled out. Because reinforcement bars are mostly used to compensate for the lack of tensile capacity in the concrete, rebars are mostly placed in structural part that are subjected to tension. In other words, a rebar in tension in a real structure is surrounded by concrete in tension, and not in compression as it is the case for the traditional pullout method. The difference in strength between the concrete in real structures and the one of the pullout test and the opposite direction of the Poisson's effect make it difficult to infer the real bond behavior through this test. Therefore, the authors suggest that further research should be conducted to characterize the bond performance of FRP rebars via test methods that simulate a more realistic situation in which both the concrete and the rebar are in tension.

# Chapter 8

## Conclusions

### 8.1 Summary

This project was conducted to characterize and evaluate the performance of three commercially available GFRP rebars based on the acceptance criteria described in FDOT Standard Specifications for Road and Bridge Construction Section 932 — Nonmetallic Accessory Materials for Concrete Pavement and Concrete Structures (Florida Department of Transportation, 2018). Specifically, three dissimilar rebar types were tested for this research study to evaluate the effects of different constituent material combinations and various surface enhancements. From each rebar type, three different rebar diameters (# 3, # 5 and # 6 or # 8) were chosen to test and analyze a wide spectrum of commonly used rebar sizes in construction projects. In total, eight different physio-mechanical properties were evaluated for the purpose of this study: cross-sectional area, fiber content, moisture absorption, micro-structural properties (SEM), transverse shear strength, horizontal shear strength, tensile properties, and the bond-to-concrete strength. While all material properties were determined in the virgin material state for characterization purposes, strength properties were also assessed for rebar specimens that were exposed to accelerated aging conditions at 23 °C, 40 °C, and 60 °C for 60 days, 120 days, 210 days, and 365 days to evaluate the rebar durability. The data from the accelerated aging experiments were used for durability modeling via Arrhenius relationships in an effort to predict the service life of the evaluated GFRP rebars.

The material characterization results showed performance differences between the manufactured rebar types but also size specific differences; some products did not meet the minimum specifications defined in FDOT Section 932 (Florida Department of Transportation, 2018). While some rebar types of a specific size failed to meet a single performance criteria, a different rebar size from the same manufacturer passed all acceptance criteria. Rebar Type-C was the only one that met all specification requirements requested in

FDOT Section 932 (Florida Department of Transportation, 2018) for all evaluated sizes (# 3, # 5, and # 6).

Through the experimental evaluation of the long-term strength performances, it was noted that the maximum relative loss in strength capacity occurred for the specimens exposed to the highest temperature and that the reduction increased with extended exposure durations. Among the evaluated strength properties (transverse shear strength, horizontal shear strength, tensile strength and elastic modulus, and bond-to-concrete strength), the tensile strength was by far the most affected property for all rebar types. However, the elastic modulus, which was also assessed through tensile strength tests, did not show significant decreases for any of the tested rebar types. All rebars retained more horizontal shear strength than transverse shear strength throughout the accelerated conditioning process, and the bond-to-concrete strength deterioration was found to average at around 20% for all tested products.

Through the obtained data from strength experiments conducted on aged GFRP rebars, the service life for each rebar type was predicted via analytical methods. The Arrhenius model was utilized, because it facilitates long-term predictions based on data from relatively short time periods (365 d). Accordingly, the performance in harsh environments was theoretically predicted based on multiple strength parameters to evaluate the suitability of the Arrhenius approach for FRP rebar degradation. The degradation rate is one of the main parameters needed for the model, and in this study it was determined for each material property individually for a multi-parametric approach. In this project, two different methods for the service life prediction were considered: (i) plotting the degradation over time on a double logarithmic scale, and (ii) basic kinetics of reactions.

## 8.2 Conclusions

Based on the presented research findings, which were obtained through a comprehensive literature review, a GFRP rebar market analysis, material characterization, durability testing, service life modeling, and discussions offered throughout this report, the following conclusions were drawn:

- A vast variety of GFRP rebar products with dissimilar features and strength capacities exist in the current market. No two GFRP rebar types are alike and specific performance differences occur for materials from dissimilar manufacturers.
- The most common and most important acceptance test (tensile test) for FRP rebars is cumbersome and not efficient. Additional quick test procedures, potentially based on bending tests, could improve GFRP rebar implementation and quality control efforts.
- The micro-structure of GFRP rebars, detected via scanning electron microscopy, is directly related to the moisture absorption characteristics.

- Size-specific performance differences exist such that a particular rebar size from one manufacturer may pass the current acceptance criteria, while another size from the same product line may not be acceptable. Individual size specific acceptance tests should be performed for implementation of other/new/additional products.
- Tensile failure due to fiber rupture occurs from the outer fiber toward the rebar core because the external fibers are stretched the most when using the currently standardize test method (grouted steel anchors). This failure mechanism is the reason for the size effect observed in large diameter rebars or the so-called shear lag.
- Helical wrapping fibers may affect the tensile strength and fail first, before the longitudinal fibers fracture.
- The bond-to-concrete performance is dependent on the surface enhancement. Sand-coated rebars provide a very high “bond stiffness” with minimal slippage before reaching the bond capacity, followed closely by ribbed rebars, while helical wrapping without additional coating may lead to significant slippage (based on the materials tested for this research).
- High temperatures during accelerated conditioning have a more significant impact on the material degradation. Future tests should be conducted at the 60 °C level, or at least above 40 °C.
- Out of the commonly tested four GFRP rebar strength characteristics, the tensile capacity of GFRP rebars suffers the most degradation (in this research a 30 % reduction was recorded) due to accelerated conditioning.
- The elastic modulus of GFRP rebars remains virtually unaffected throughout aging.
- Accelerated aging in saltwater solutions degrades both shear strength properties. However, the transverse shear strength is much more affected than the horizontal shear strength.
- Fiber-driven material characteristics such as the tensile strength or the transverse shear strength suffer more severely from aging in saline-rich environments than resin-driven strength properties (i.e. horizontal shear strength).
- The Arrhenius approach may not be applicable to the degradation process of the tested materials because a combination of different degradation mechanisms for GFRP rebars in high-temperature saltwater seems to exist. This cannot be dissociated through the standard Arrhenius model.

- Scanning electron microscopy is an indispensable tool to detect voids in GFRP rebars. These voids are directly related to the moisture absorption properties and are indicative of the GFRP rebar performance over time.
- Materials with a high void ratio suffer more severe effects when exposed to harsh environments than GFRP rebar products that were produced to form a denser micro-structure. Accordingly, moisture absorption and scanning electron microscopy should be considered for “quick testing” and initial evaluation of new products.

### 8.3 Recommendations

This study was conducted to support FDOT efforts to fully embrace and implement GFRP rebar technology for safe and reliable use in concrete structures. Based on the activities completed as part of this study and the findings presented above, FDOT Specifications Section 932 (Florida Department of Transportation, 2018) updates may be considered based on the following recommendations:

#### 1. **New Test Standards:**

**Horizontal Shear:** Horizontal shear tests are recommended as an additional test requirement. This test evaluates the quality of the resin and provides a quantitative parameter related to the load transfer between individual resin and fiber planes. Throughout the state-of-the-art review for this study, it was found that horizontal shear tests are currently a commonly used quality-control test procedure, mostly due to its simplicity. Adding this test to the specification requirements, especially for project material acceptance, will increase the reliability and control of FRP rebars. Moreover, it can also be used at a laboratory level for long term monitoring and to study possible delamination mechanics due to resin degradation. The suggested standard test method for the horizontal shear test is described in ASTM D 4475 (ASTM International, 2008a). Currently, neither FDOT Section 932 (Florida Department of Transportation, 2018) nor ASTM D 7957 (ASTM International, 2017) provide any limiting criteria for this property. However, AC454 (ICC Evaluation Service, 2016) suggests a rebar size dependent minimum value that appears reasonable for the use in Florida.

**Flexural Properties:** Flexural tests on rebars were not part of this project, but were also found to be a quality control test used by manufacturers. Results obtained through such tests have low variability and provide reliable data<sup>1</sup>. Similar to the horizontal shear test, the flexural test can be promptly

---

<sup>1</sup> As determined in companion studies, outside of the scope of this work.



conducted to obtain quantitative results. This test can be included as part of project acceptance tests, and potentially replace tensile tests in the future, because it is theoretically possible to correlate the tensile strength to the flexural elastic modulus. If implemented correctly, flexural tests can reduce the turnaround time for rebar evaluations and lower the costs for quality control measures.

## **2. Scanning Electron Microscopy (SEM) Imaging:**

Representative scanning electron microscopy images of the rebar cross-section are recommended as an additional specification. In this study, it was found that the SEM images for each manufacturer were distinctive, hence producing a characteristic “finger print” identification image of the rebar cross section, which serves as a qualitative reference for each manufacturer and rebar size. This provides a unique reference for FDOT, where changes in manufacturing, which may not lead to changes in benchmark properties but possibly affect long term properties, can be detected. SEM images can therefore be used to verify the micro-structural integrity after a manufacturer changes material suppliers or alters other aspects related to the manufacturing process.

## **3. Bond Properties:**

It has been observed that different surface enhancements may meet the minimum bond strength specification, however the pseudo “bond stiffness” (bond strength vs. relative slip) may significantly differ and affect the performance of RC structures in various ways. When reporting the ultimate bond strength, the measurement of the relative slip and the magnitude of the pseudo “bond stiffness” should be included. At this time, a value for this pseudo “bond stiffness” cannot be recommended based on the limited experimental results. However, the bond stiffness is considered a dependent parameter that affects serviceability requirements, and thus needs to be further evaluated, because the maximum bond strength alone is not reflective of the bond performance of a specific GFRP rebar.

It has been demonstrated that excessive bond strength with limited bond slip due to strong mechanical interlocking of sand-coated FRP rebars or bars with lugs may lead to excessive tensile stresses in the surrounding concrete. As a result of these tensile stresses, the concrete may split and cause an undesired structural failure in members reinforced with FRP rebars. Accordingly, an upper limit for the bond strength and possibly bond stiffness may need to be considered for the full implementation of GFRP rebars.

Although bond degradation for the evaluated rebars may have been within a reasonable range, it has been found in previous studies that Type-B rebars suffer significant degradation under exposure conditions identical to the ones used for this study, resulting in a loss of up to 50% of the ultimate

bond strength (Khatibmasjedi and Nanni, 2017)<sup>2</sup>. Accordingly, testing the bond durability may be needed to properly characterize GFRP rebars and additional specification criteria for FDOT Section 932 (Florida Department of Transportation, 2018) should be considered, either in general or for rebars that do not use well established surface enhancements. These test should be based on the test procedure described in ACI 440.3R,B3 (ACI Committee 440, 2012) after exposing concrete embedded GFRP rebars in applicable harsh environments via accelerated conditioning (as it was used for this study). Numerical values for acceptance criteria cannot be recommended at this time, because the specific “bond stiffness findings” were merely qualitative and outside of the scope of this study.

#### 4. **Exposure Environments for Accelerated Conditioning**

This project focused on saltwater as an aging solution to determine the long-term performance of GFRP rebars in harsh environments and to evaluate its applicability for marine structures in Florida where GFRP rebars are expected to reduce corrosion and the corresponding maintenance costs. Additional and different conditioning solutions may affect FRP rebars differently and potentially yield different findings — possibly leading to less favorable property retention. To better predict the behavior and conditions of FRP reinforced concrete structures exposed to seawater, future projects should consider exposure conditions that combine high pH values with saltwater exposure.

#### 5. **Service Life Modeling:**

The long-term durability performance results of GFRP rebars using different temperatures was purposely selected to apply and test for Arrhenius relationships in an effort to predict the service life of the evaluated GFRP rebars. Based on the property retention values and the durability results, the findings through an Arrhenius model have been inconclusive. The Authors believe that underlying assumptions for the Arrhenius model (simple one component chemical reaction) do not apply to GFRP rebars exposed to temperatures up to 60 °C immersed in saltwater. Hence, non-Arrhenius relationships such as Fick’s diffusion law should be considered for future research projects that target the service life predictions for GFRP rebars. Moreover, the same underlying assumptions applied to the use of Arrhenius model to GFRP rebars in other aging environments should be revisited.

#### 6. **Glass Transition Temperature, $T_g$**

The glass transition temperatures were traditionally evaluated using Dynamic Mechanical Analysis (DMA). This method has been substituted in the ASTM GFRP specification (ASTM International, 2017) by Differential Scanning Calorimetry (DSC). This change is also recommended for FDOT Specification Section 932, for two reasons: 1) it is considered pragmatic because the degree of cure can be

---

<sup>2</sup> The manufacturer has since modified the surface deformation to improve this behavior.

obtained in the same test program, and 2) it provides synergy between other specifications. Additionally, it restricts the different definitions that  $T_g$  can obtain, providing more conservative  $T_g$  magnitudes.

# Bibliography

ACI Committee 440 (2012). *ACI 440. 3R - Guide Test Methods for Fiber- Reinforced Polymer (FRP) Composites for Reinforcing or Strengthening Concrete and Masonry Structures*.

Ahmed, E. A., El-Sayed, A. K., El-Salakawy, E., and Benmokrane, B. (2010). “Bend Strength of FRP Stirrups: Comparison and Evaluation of Testing Methods.” *Journal of Composites for Construction*, 14(1), 3–10.

Al-Salloum, Y. A., El-Gamal, S., Almusallam, T. H., Alsayed, S. H., and Aqel, M. (2013). “Effect of harsh environmental conditions on the tensile properties of GFRP bars.” *Composites Part B: Engineering*, 45(1).

American Society of Civil Engineers (2016). “Infrastructure report card.” *ASCE News*, 53, 1–36.

ASTM-International (1992). *Standard test method for moisture absorption properties and equilibrium conditioning of polymer matrix composite materials*, (D5229). ASTM International, West Conshohocken, PA.

ASTM International (2008a). *Standard Test Method for Apparent Horizontal Shear Strength of Pultruded Reinforced Plastic Rods By the Short-Beam Method*, (D4475). ASTM International, West Conshohocken, PA.

ASTM International (2008b). *Standard Test Methods for Density and Specific Gravity (Relative Density) of Plastics by Displacement*, (D729). ASTM International, West Conshohocken, PA.

ASTM International (2011a). *Standard Test Method for Ignition Loss of Glass Strands and Fabrics*, (D2584). ASTM International, West Conshohocken, PA.

ASTM International (2011b). *Standard Test Method for Tensile Properties of Fiber Reinforced Polymer Matrix Composite Bars*, (D7205). ASTM International, West Conshohocken, PA.

ASTM International (2011c). *Standard Test Method for Transverse Shear Strength of Fiber-reinforced Polymer Matrix Composite Bars*, (D7617). ASTM International, West Conshohocken, PA.

- ASTM International (2012). *Standard Test Method for Alkali Resistance of Fiber Reinforced Polymer (FRP) Matrix Composite Bars used in Concrete Construction*, (D7705). ASTM International, West Conshohocken, PA.
- ASTM International (2013). *Standard Test Methods for Density and Specific Gravity ( Relative Density ) of Plastics by Displacement*, (D792). ASTM International, West Conshohocken, PA.
- ASTM International (2014). *Standard Test Method for Bond Strength of Fiber-Reinforced Polymer Matrix Composite Bars to Concrete by Pullout Testing*, (D7913). ASTM International, West Conshohocken, PA.
- ASTM International (2017). *Standard Specification for Solid Round Glass Fiber Reinforced Polymer Bars for Concrete Reinforcement*, (D7957). ASTM International, West Conshohocken, PA.
- Bagherpour, S. (2012). *Polyester*, chapter Fibre Reinforced Polyester Composites, 135–166. InTech.
- Balázs, G. L. and Borosnyói, A. (2001). *Composites in Construction: A Reality*, Vol. 264, chapter Long-term, 84–91. American Society of Civil Engineers.
- Benmokrane, B., Ali, A. H., Mohamed, H. M., ElSafty, A., and Manalo, A. (2017). “Laboratory assessment and durability performance of vinyl-ester, polyester, and epoxy glass-FRP bars for concrete structures.” *Composites Part B: Engineering*, 114, 163–174.
- Benmokrane, B., Wang, P., Ton-That, T. M., Rahman, H., and Robert, J.-F. (2002). “Durability of Glass Fiber-Reinforced Polymer Reinforcing Bars in Concrete Environment.” *Journal of Composites for Construction*, 6(3), 143–153.
- Busel, J. P. (2012). “Fiber reinforced polymer {(FRP)} composites rebar. Presentation, American Composites Manufacturers Association.
- Chen, D. and Chen, H. W. (2013). “Using the köppen classification to quantify climate variation and change: An example for 1901–2010.” *Environmental Development*, 6, 69–79.
- Chen, Y., Davalos, J. F., and Ray, I. (2006). “Durability prediction for GFRP reinforcing bars using short-term data of accelerated aging tests.” *Journal of Composites for Construction*, 10(4), 279–286.
- Chen, Y., Davalos, J. F., Ray, I., and Kim, H. Y. (2007). “Accelerated aging tests for evaluations of durability performance of FRP reinforcing bars for concrete structures.” *Composite Structures*, 78(1), 101–111.
- Claire, G. G. (2015). “Non-Traditional shape GFRP Rebars for Concrete Reinforcement. Dissertation, University of Miami.

- Dejke, V. and Tepfers, R. (2001). “Durability and service life prediction of GFRP for concrete reinforcement.” *Proc., 5th Int. Conf. on Fiber-Reinforced Plastics for Reinforced Concrete Structures (FRPRCS-5)*, Vol. 1. Thomas Telford London, 505–516.
- Dong, Z., Wu, G., Xu, B., Wang, X., and Taerwe, L. (2016). “Bond durability of BFRP bars embedded in concrete under seawater conditions and the long-term bond strength prediction.” *Materials and Design*, 92, 552–562.
- Fava, G., Carvelli, V., and Pisani, M. A. (2016). “Remarks on bond of {GFRP} rebars and concrete.” *Elsevier*, 93, 210–220.
- Florida Department of Transportation (2017). *Standard Specifications for Road and Bridge Construction*.
- Florida Department of Transportation (2018). “*Standard Specifications for Road and Bridge Construction — Section 932.*” Standard specifications, Florida Department of Transportation.
- Florida Department of Transportation Forecasting and Trends Office (2018). “*The FDOT source book.*” Mobility performance report, Florida Department of Transportation.
- High, C., M, H., Seliem, Safty, A. E., and Rizkalla, S. H. (2015). “Use of basalt fibers for concrete structures.” *Construction and Building Materials*, 37.
- Hittle, C. and Zucker, M. (2004). “*Northeastern florida bay estuarine creek data, water years 1996-2000.*” Data series report 105, U.S. Geological Survey, Miami, Florida.
- ICC Evaluation Service (2016). *AC454 - Acceptance Criteria for Fiber-Reinforced Polymer (FRP) Bars for Internal Reinforcement of Concrete Members*.
- Inmana, M., Thorhallssonb, E. R., and Azrague, K. (2017). “A mechanical and environmental assessment and comparison of basalt fibre reinforced polymer (bfrp) rebar and steel rebar in concrete beams.” *Energy Procedia*, 111, 31–40.
- Joshi, S. C., Lam, Y. C., and Tun, U. W. (2003). “Improved cure optimization in pultrusion with pre-heating and die-cooler temperature.” *Elsevier*, 34, 1151–1159.
- Khatibmasjedi, M. (2018). “*Sustainable Concrete Using Seawater and Glass Fiber Reinforced Polymer Bars.*” Dissertation, University of Miami, Coral Gables, FL 33146.
- Khatibmasjedi, S. and Nanni, A. (2017). “Durability of GFRP reinforcement in SEACON.” *CDCC 2017 — The Fifth International Conference on Durability of Fiber Reinforced Polymer (FRP) Composites for Construction and Rehabilitation of Structures, At Sherbrooke, Quebec, CANADA.*

- Kocaoz, S., Samaranayake, V., and Nanni, A. (2005a). “Tensile characterization of glass frp bars.” *Composites Part B: Engineering*, 36(2), 127 – 134.
- Kocaoz, S., Samaranayake, V. A., and Nanni, A. (2005b). “Tensile characterization of glass frp bars.” *Composites Part B: Engineering*, 36(2), 127–134.
- Litherland, K. L., Oakley, D. R., and Proctor, B. A. (1981). “The use of accelerated ageing procedures to predict the long term strength of grc composites.” *Cement and Concrete Research*, 11(3), 455–466.
- Markets and Markets (2016). “FRP Rebar Market by Resin Type, by Fiber Type, by Application - Global Forecasts to 2021.” *PR Newswire Association LLC*.
- Micelli, F. and Nanni, A. (2004). “Durability of FRP rods for concrete structures.” *Construction and Building Materials*, 18(7), 491–503.
- Nanni, A., Luca, A. D., and Zadeh, H. J. (2014). *Reinforced Concrete with FRP Bars: Mechanics and Design*, chapter Materials, 23–33. 978-0-415-77882-4. CRC Press.
- Nolan, S., Rossini, M., and Nanni, A. (2018). “Seawalls, SEACON and Sustainability in the Sunshine State.” *Transportation Research Board 97th Annual Meeting. Washington, DC*. 123–129.
- Okelo, R. and Yuan, R. L. (2005). “Bond Strength of Fiber Reinforced Polymer Rebars in Normal Strength Concrete.” *Journal of Composites for Construction*, 9(3), 203–213.
- Pauling, L. (1988). (*General Chemistry*). Dover Publications.
- Portland Cement Association (2002). “*Type and causes of concrete deterioration*.” techreport IS536.01, Portland Cement Association (PCA).
- Purdue ECT Team (2007). “{FRP} Rebar {(AFRP, CFRP, GFRP)}”. Factsheet, Purdue University.
- Robert, M. and Benmokrane, B. (2013). “Combined effects of saline solution and moist concrete on long-term durability of GFRP reinforcing bars.” *Construction and Building Materials*, 38.
- Robert, M., Cousin, P., and Benmokrane, B. (2009). “Durability of GFRP reinforcing bars embedded in moist concrete.” *Journal of Composites for Construction*, 13(2), 66–73.
- Schesser, D., Yang, Q. D., Nanni, A., and Giancaspro, J. W. (2014). “Expansive grout-based gripping systems for tensile testing of large-diameter composite bars.” *Journal of Materials in Civil Engineering*, 26(2), 250–258.

- Stabenau, E. and Kotun, K. (2012). “*Salinity and hydrology of florida bar status and trends 1990-2009.*” Status and Trends Report. SFNRC Technical Series, National Park Service, South Florida Natural Resources Center, Everglades National Park, 950 N. Krome Avenue, Homestead, FL 33030-4443.
- Tannous, F. E. and Saadatmanesh, H. (1998). “Environmental effects on the mechanical properties of e-glass frp rebars.” *ACI Materials Journal*, 95(2), 87-100.
- Wang, H. and Belarbi, A. (2012). “Bond Durability of {FRP} Bars Embedded in Fiber Reinforced Concrete.” *Journal of Composites for Construction*, 16, 371-380.
- Wang, Z., Zhao, X.-L., Xian, G., Wu, G., Raman, R. K. S., Al-Saadi, S., and Haque, A. (2017). “Long-term durability of basalt-and glass-fibre reinforced polymer (BFRP/GFRP) bars in seawater and sea sand concrete environment.” *Construction and Building Materials*, 139, 467-489.
- Wang, Z., Zhao, X. L., Xian, G., Wu, G., Singh Raman, R. K., and Al-Saadi, S. (2017). “Durability study on interlaminar shear behaviour of basalt-, glass- and carbon-fibre reinforced polymer (B/G/CFRP) bars in seawater sea sand concrete environment.” *Construction and Building Materials*, 156, 985-1004.
- Wingard, G., Cronin, T., Holmes, C., Willard, D., Dwyer, G., Ishman, S., Orem, W., P Williams, C., Albietz, J., Bernhardt, C., A Budet, C., Landacre, B., Lerch, T., Marot, M., and E Ortiz, R. (2018). “*Ecosystem history of southern and central biscayne bay: Summary report on sediment core analyses – year two.*” Open-file report, U.S. Geological Survey.
- Wu, G., Dong, Z., Wang, X., Zhu, Y., and Wu, Z. (2014). “Prediction of Long-Term Performance and Durability of BFRP Bars under the Combined Effect of Sustained Load and Corrosive Solutions.” *Journal of Composites for Construction*, 19(3), 4014058.
- Yan, F. and Lin, Z. (2017). “Bond durability assessment and long-term degradation prediction for GFRP bars to fiber-reinforced concrete under saline solutions.” *Composite Structures*, 161, 393-406.



# Appendices

# Appendix A

## Manufacturer Survey

The contact to the manufacturers around the world was done via E-mail, Skype or Telephone. However, the most effective way to collect the necessary data was a survey based questionnaire that was distributed via E-mail. After contacting the manufacturers briefly via telephone or E-mail, the survey was sent to gather the most important and applicable facts about the production details and product specific properties. The survey was created using the online research software Qualtrics, a service offered to the Florida State University. The survey included 13 different questions; The first six, were general questions about the manufacturer and their production. The last seven however, were specific questions about the three bar sizes which were part of the scope of this research project: bar number # 3 (diameter = 10 mm (3/8 in.)), # 5 (diameter = 16 mm(5/8 in.)), # 8 (diameter = 25 mm (1 in.)). For the company Marshall (C-bar), a slightly modified survey was prepared to include the number # 6 bar (diameter = 20 mm(6/8 in.)) instead of the number # 8 bar, because Marshall currently does not produce a C-bar with a diameter of 25 mm (1 in.).



**GFRP Research Project**

Q1.- Please provide your company name: \_\_\_\_\_

Q2.- Production planning.

- We produce GFRP rebars on demand
- We stock GFRP bars in large quantities (multiple bar sizes with more than 500m (1640ft))
- We stock GFRP bars in small quantities (any bar sizes with less than 500m (1640ft))

Q3.- What is your production capacity?

	Production per day	Unit	
	Value	m/day	ft/day
Production capacity		<input type="radio"/>	<input type="radio"/>

Q4.- What is/are the cross-sectional shape(s) that you produce?

- Round solid
- Round hollow
- Oval solid
- Oval hollow
- Y-shape
- Quadratic
- Other (please specify which other shapes you produce) \_\_\_\_\_

Q5.- Which surface enhancement methods do you use to improve the bond to concrete?

- Sand coating
- Helical wrap
- Helical rib
- Other (please specify which) \_\_\_\_\_

Q6.- Which diameters do you produce? (please provide all diameters that are produced by your company)

- < #3 Bar: Diameter = 10mm (3/8 inch); please, specify: \_\_\_\_\_
- #3 Bar: Diameter = 10mm (3/8 inch)
- #4 Bar: Diameter = 13mm (4/8 inch)
- #5 Bar: Diameter = 16mm (5/8 inch)
- #6 Bar: Diameter = 19mm (6/8 inch)
- #7 Bar: Diameter = 22mm (7/8 inch)
- #8 Bar: Diameter = 25mm (1 inch)
- #9 Bar: Diameter = 29mm (1 1/8 inch)
- #10 Bar: Diameter = 32mm (1 2/8 inch)
- #11 Bar: Diameter = 36mm (1 3/8 inch)
- > #11 Bar: Diameter = 36mm (1 3/8 inch) ; please, specify: \_\_\_\_\_

Q7.- Please provide the measured diameter of the following bars:

	Measured diameter	Unit	
	Value	mm	inch
#3 Bar: Diameter = 10mm (3/8 inch)		<input type="radio"/>	<input type="radio"/>
#5 Bar: Diameter = 16mm (5/8 inch)		<input type="radio"/>	<input type="radio"/>
#8 Bar: Diameter = 25mm (1 inch)		<input type="radio"/>	<input type="radio"/>

Q8.- Please provide the nominal area for the following bars.

	Nominal area	Unit	
	Value	mm <sup>2</sup>	inch <sup>2</sup>
#3 Bar: Diameter = 10mm (3/8 inch)		<input type="radio"/>	<input type="radio"/>
#5 Bar: Diameter = 16mm (5/8 inch)		<input type="radio"/>	<input type="radio"/>
#8 Bar: Diameter = 25mm (1 inch)		<input type="radio"/>	<input type="radio"/>

Q9.- Please enter the tensile load capacity for the following bars.

	Tensile load capacity	Unit	
	Value	kN	kips
#3 Bar: Diameter = 10mm (3/8 inch)		<input type="radio"/>	<input type="radio"/>
#5 Bar: Diameter = 16mm (5/8 inch)		<input type="radio"/>	<input type="radio"/>
#8 Bar: Diameter = 25mm (1 inch)		<input type="radio"/>	<input type="radio"/>

Q10.- What is the ultimate tensile strength of the following bars?

	Maximum tensile stress	Unit	
	Value	MPa	ksi
#3 Bar: Diameter = 10mm (3/8 inch)		<input type="radio"/>	<input type="radio"/>
#5 Bar: Diameter = 16mm (5/8 inch)		<input type="radio"/>	<input type="radio"/>
#8 Bar: Diameter = 25mm (1 inch)		<input type="radio"/>	<input type="radio"/>

Q11.- What is the modulus of elasticity for the following bars?

	Modulus of elasticity	Unit	
	Value	GPa	ksi
#3 Bar: Diameter = 10mm (3/8 inch)		<input type="radio"/>	<input type="radio"/>
#5 Bar: Diameter = 16mm (5/8 inch)		<input type="radio"/>	<input type="radio"/>
#8 Bar: Diameter = 25mm (1 inch)		<input type="radio"/>	<input type="radio"/>

Q12.- Please provide the maximum strain/elongation under tensile stress.

	Maximum strain/elongation
	Value (in %)
#3 Bar: Diameter = 10mm (3/8 inch)	
#5 Bar: Diameter = 16mm (5/8 inch)	
#8 Bar: Diameter = 25mm (1 inch)	

Q13.- Please provide the weight per unit length for each of the following bars.

	Weight per length	Unit	
	Value	kg/m	lb/ft
#3 Bar: Diameter = 10mm (3/8 inch)		<input type="radio"/>	<input type="radio"/>
#5 Bar: Diameter = 16mm (5/8 inch)		<input type="radio"/>	<input type="radio"/>
#8 Bar: Diameter = 25mm (1 inch)		<input type="radio"/>	<input type="radio"/>

## Appendix B

# Visual Rebar Documentation

### B.1 Introduction

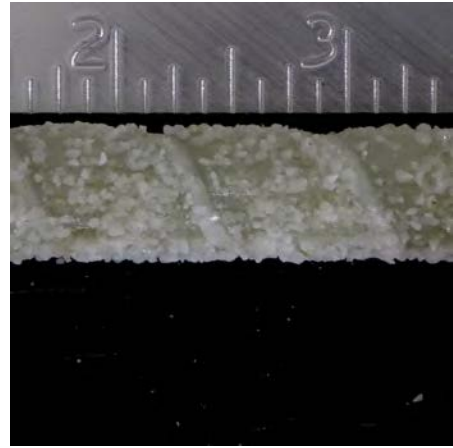
The GFRP rebars are currently not standardized — like traditional steel rebars — and therefore, products may differ significantly from one another, such that each rebar manufacturer may produce entirely different rebars. For example, due to the different surface enhancement features, the true outer measured diameter within a nominal bar size type is not consistent throughout different manufacturers. This visual documentation aims to provide an overview of some of the most commonly available GFRP rebars for concrete elements. The following pictures were captured in the laboratories at the FAMU-FSU College of Engineering and critical attention was paid to consistent view angles and perspectives, to facilitate a comparison between different products and similar or different sizes. Four (4) pictures per individual GFRP bar provide easy access to all rebar specific features, to exemplify how the products of different companies look like and/or compare to each other. Both straight and bent bars were included and also both glass and basalt FRP rebars were taken into account.

## B.2 GFRP straight bars

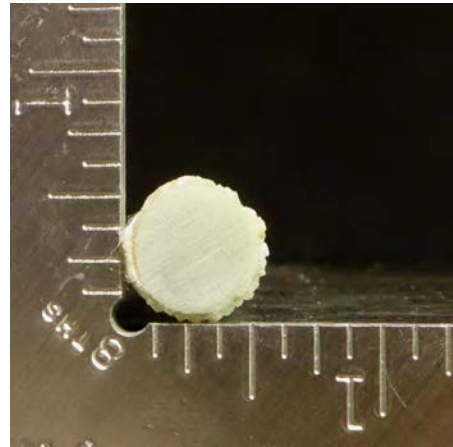
For the straight bars, four different angle views per individual GFRP bar are provided to capture the principal features, which include: i) the longitudinal plan view; ii) the close up of surface enhancement detailed typology; iii) the cross section after rebar was cut perpendicular to the longitudinal axis; and iv) an isometric view.



Longitudinal overview



Surface enhancement closeup



Cross section



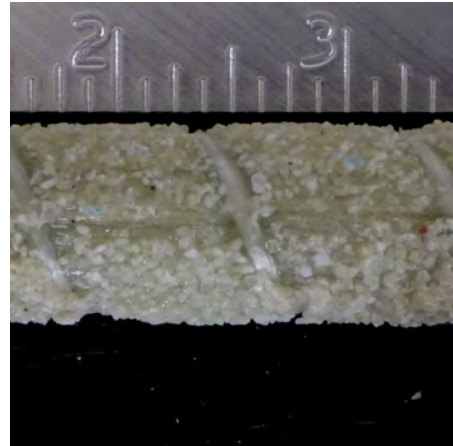
Isometric view

Figure B.1: AFR #4 Bar

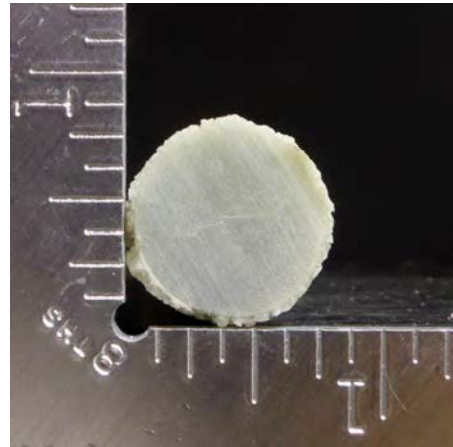




Longitudinal overview



Surface enhancement closeup



Cross section

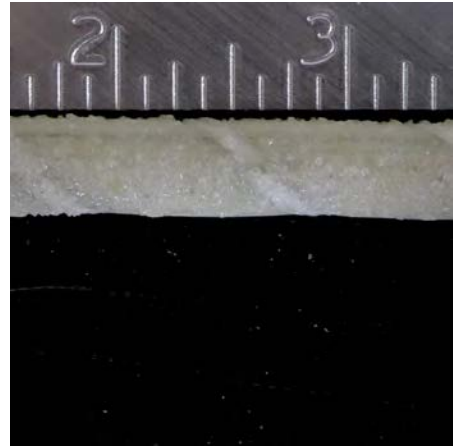


Isometric view

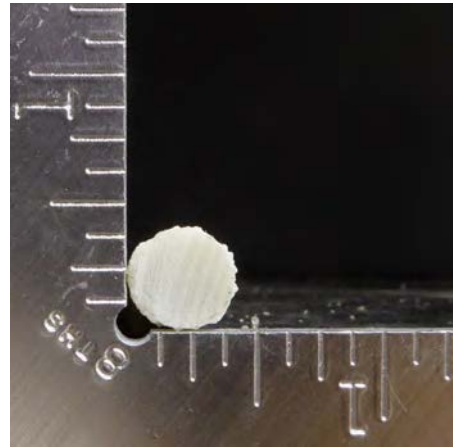
Figure B.2: AFR #6 Bar



Longitudinal overview



Surface enhancement closeup



Cross section

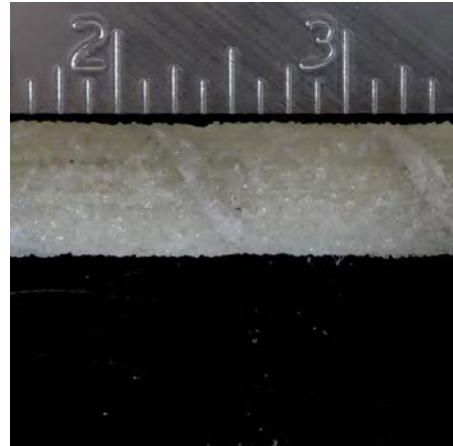


Isometric view

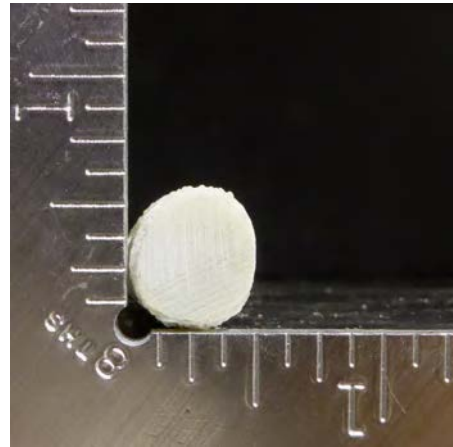
Figure B.3: ASL # 3 Bar



Longitudinal overview



Surface enhancement closeup



Cross section

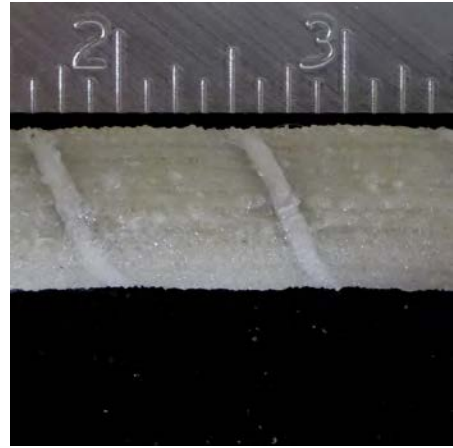


Isometric view

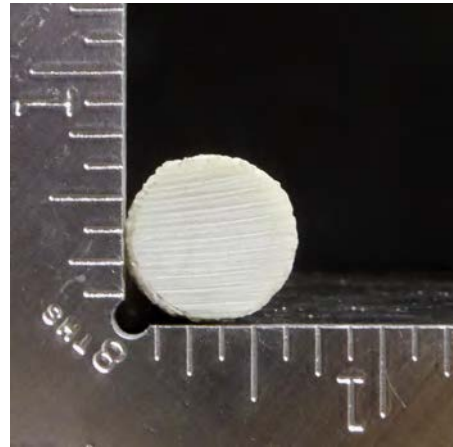
Figure B.4: ASL # 4 Bar



Longitudinal overview



Surface enhancement closeup



Cross section



Isometric view

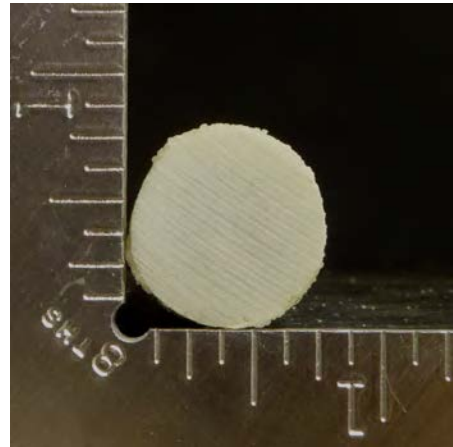
Figure B.5: ASL # 5 Bar



Longitudinal overview



Surface enhancement closeup



Cross section

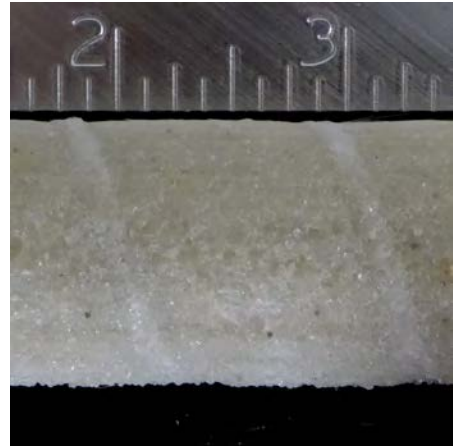


Isometric view

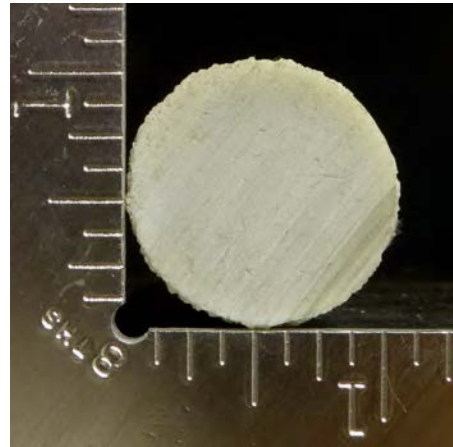
Figure B.6: ASL #6 Bar



Longitudinal overview



Surface enhancement closeup



Cross section



Isometric view

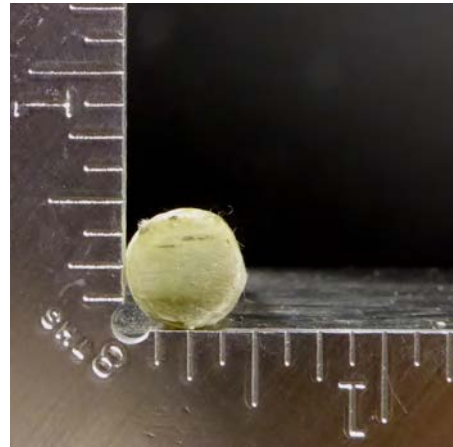
Figure B.7: ASL #8 Bar



Longitudinal overview



Surface enhancement closeup



Cross section



Isometric view

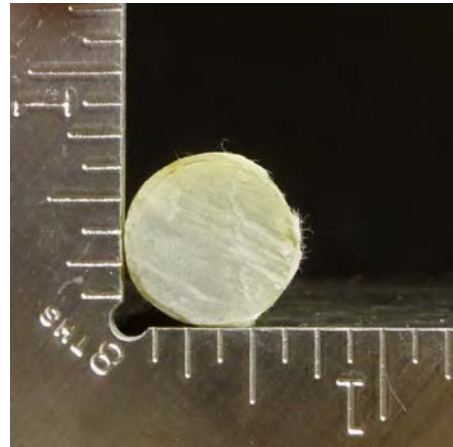
Figure B.8: ATP #3 Bar



Longitudinal overview



Surface enhancement closeup



Cross section



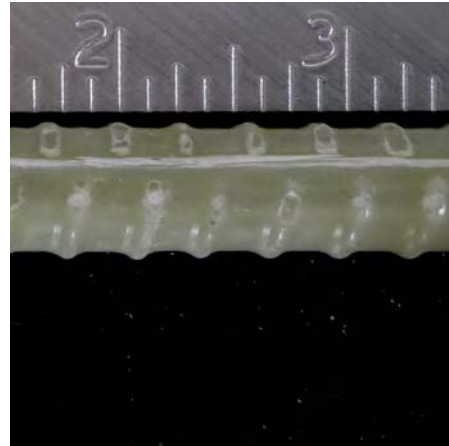
Isometric view

Figure B.9: ATP # 5 Bar





Longitudinal overview



Surface enhancement closeup



Cross section

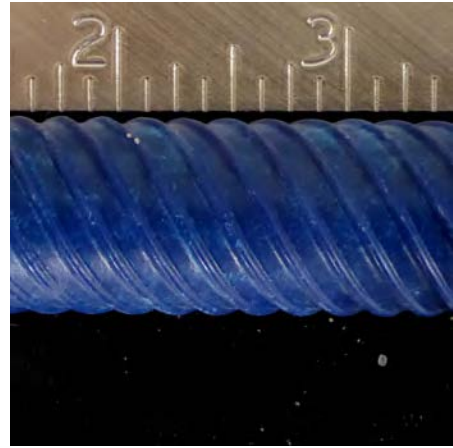


Isometric view

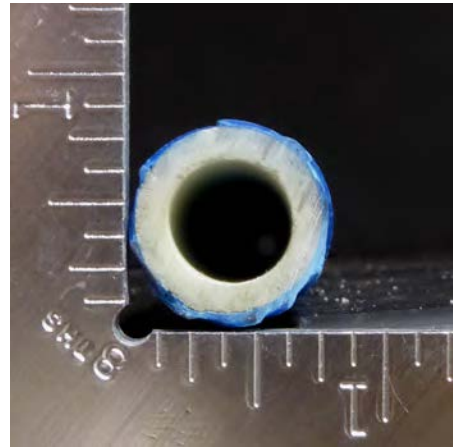
Figure B.10: MAR # 4 Bar



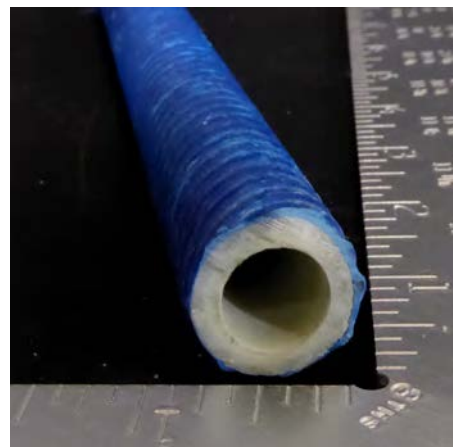
Longitudinal overview



Surface enhancement closeup



Cross section

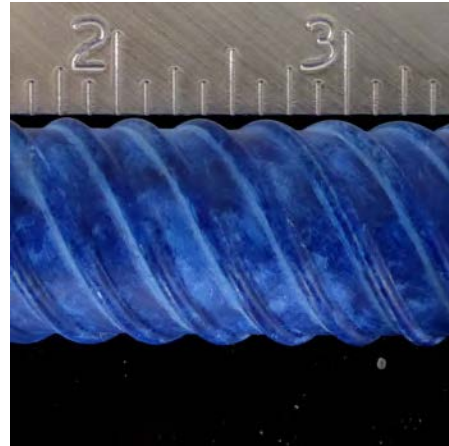


Isometric view

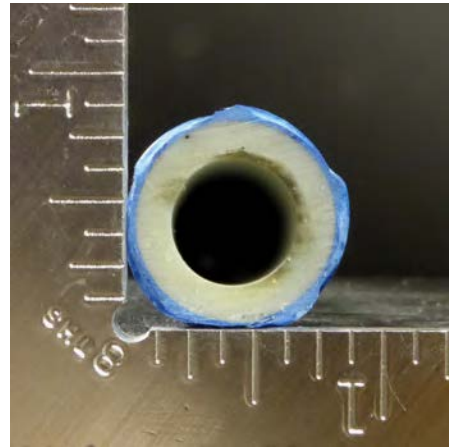
Figure B.11: CRT #6 Bar



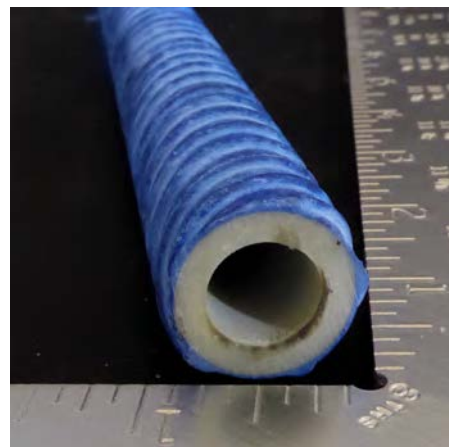
Longitudinal overview



Surface enhancement closeup



Cross section

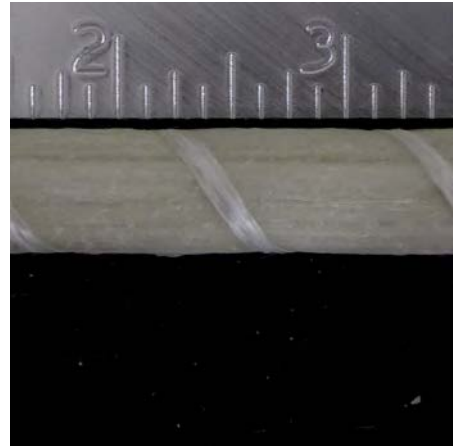


Isometric view

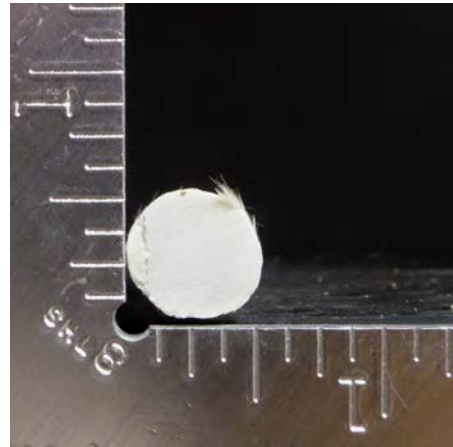
Figure B.12: CRT #7 Bar



Longitudinal overview



Surface enhancement closeup



Cross section

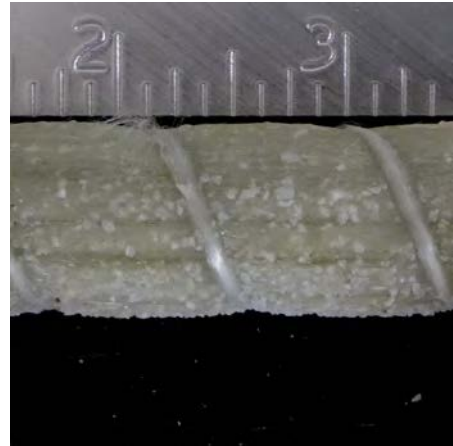


Isometric view

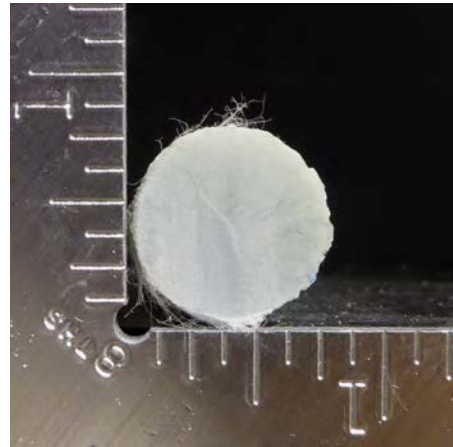
Figure B.13: RAW # 4 Bar



Longitudinal overview



Surface enhancement closeup



Cross section

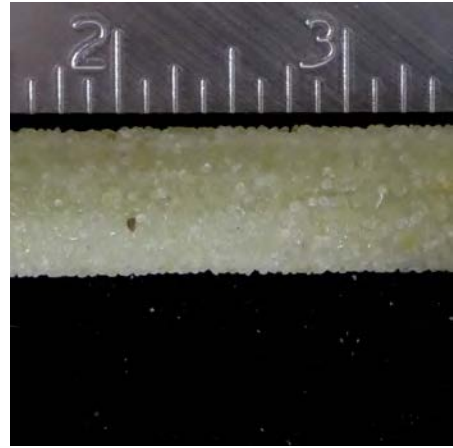


Isometric view

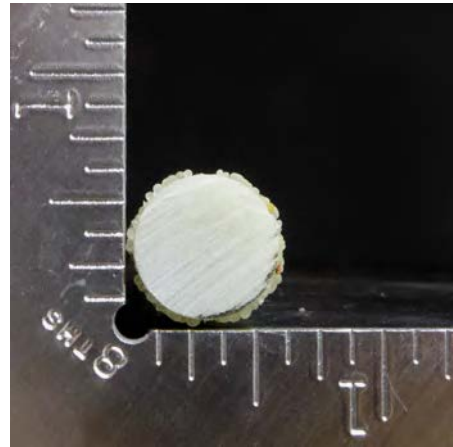
Figure B.14: RAW #6 Bar



Longitudinal overview



Surface enhancement closeup



Cross section

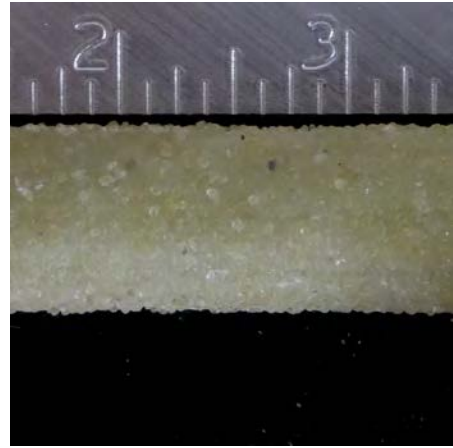


Isometric view

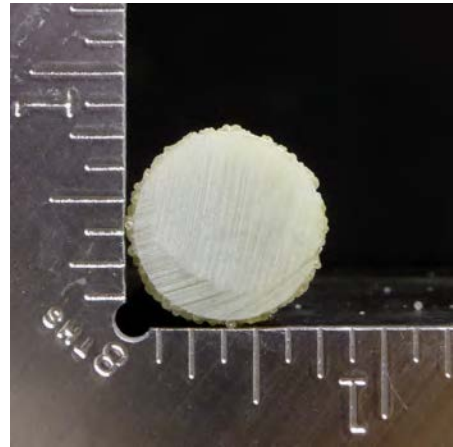
Figure B.15: PAL #5 Bar



Longitudinal overview



Surface enhancement closeup



Cross section

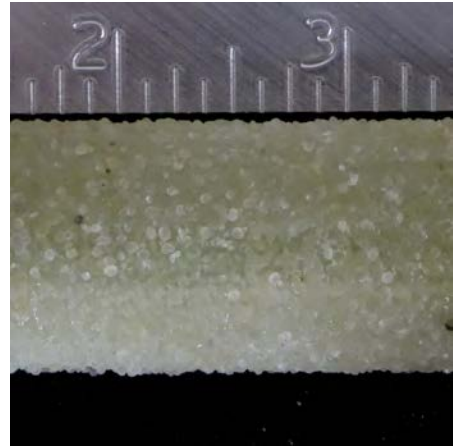


Isometric view

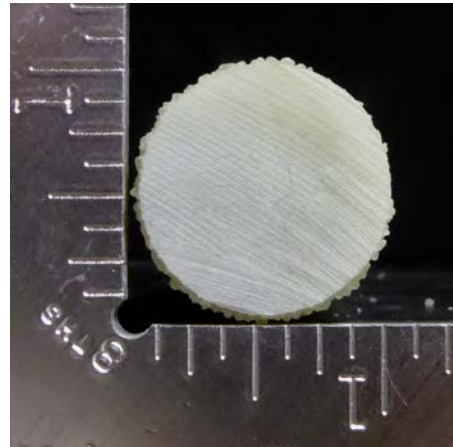
Figure B.16: PAL #6 Bar



Longitudinal overview



Surface enhancement closeup



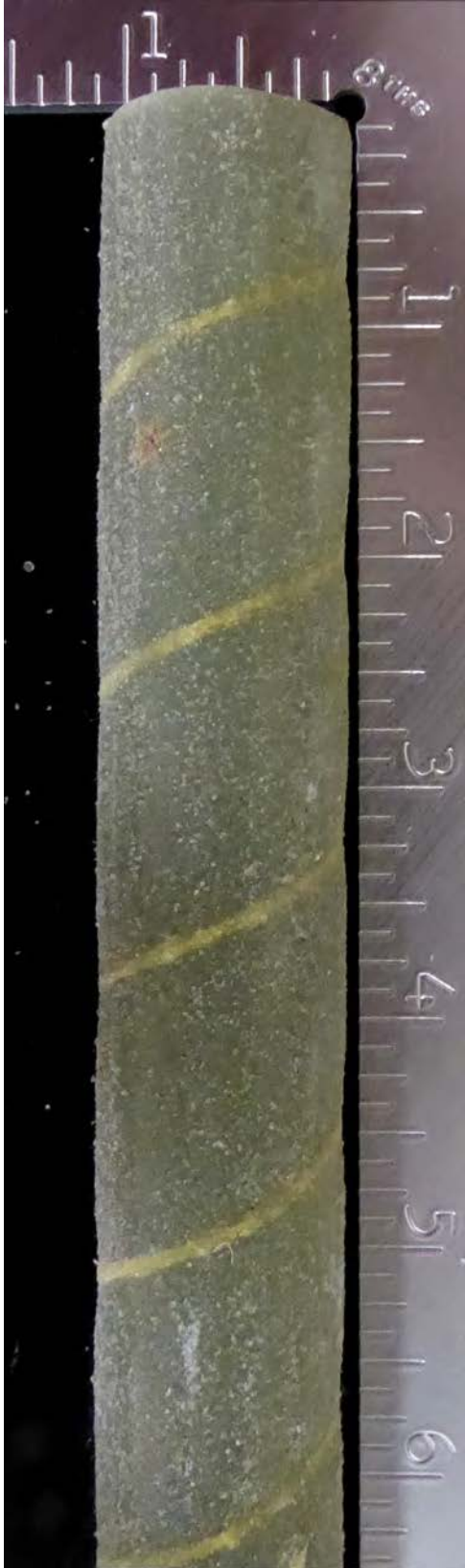
Cross section



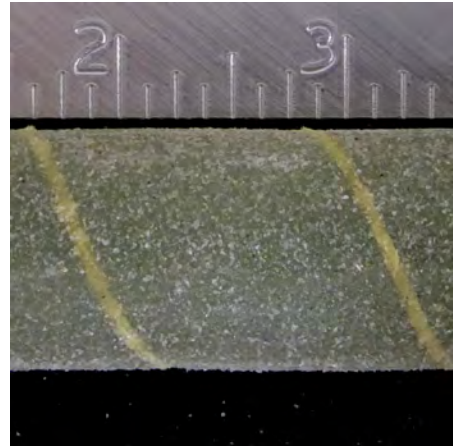
Isometric view

Figure B.17: PAL #8 Bar

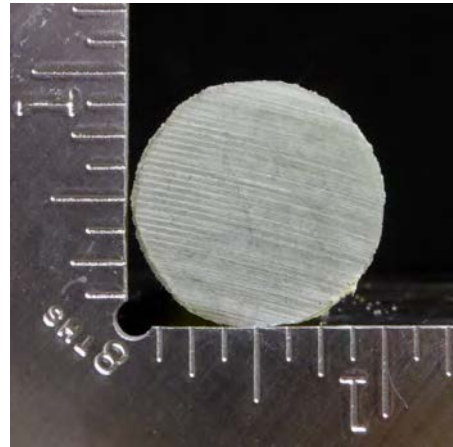




Longitudinal overview



Surface enhancement closeup



Cross section

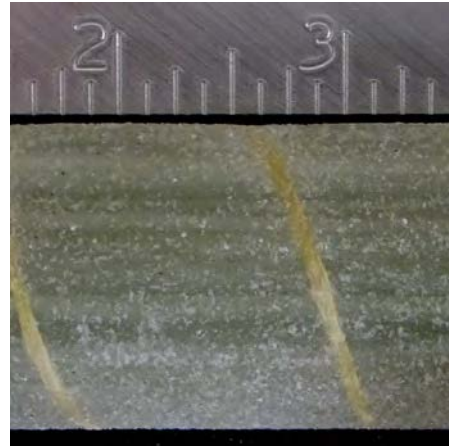


Isometric view

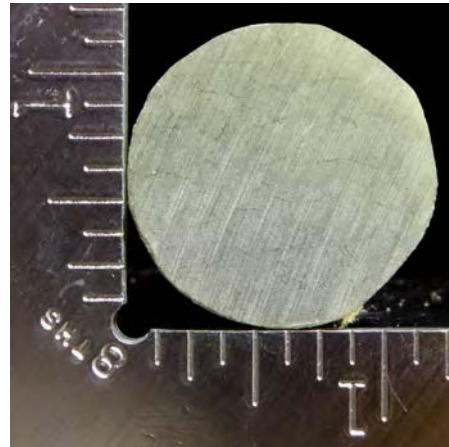
Figure B.18: SIR # 8 Bar



Longitudinal overview



Surface enhancement closeup



Cross section



Isometric view

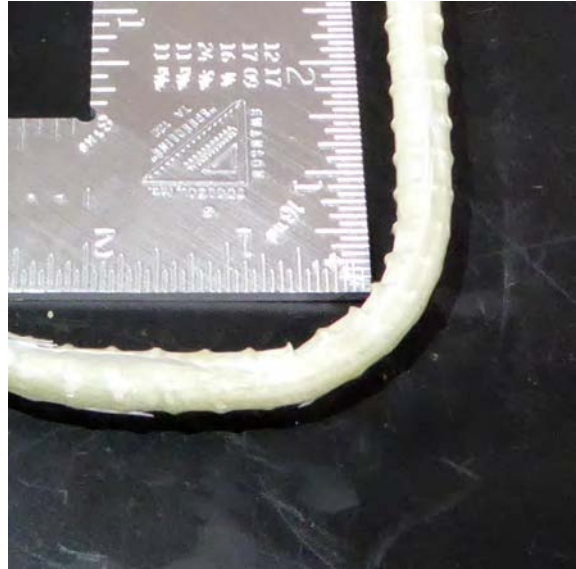
Figure B.19: SIR # 10 Bar

### **B.3 GFRP bent bars**

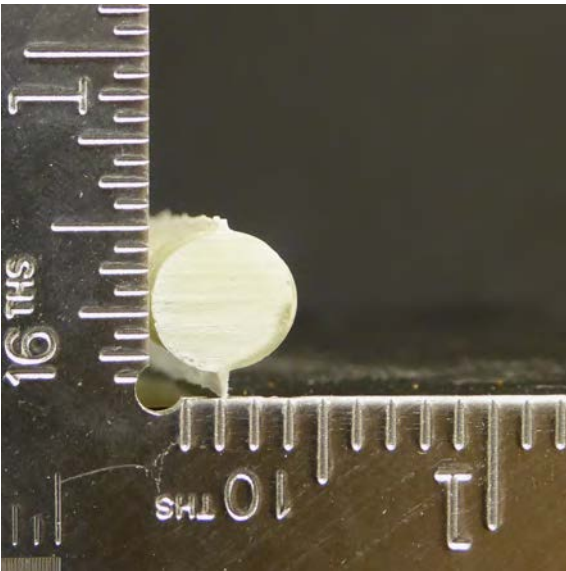
For the bent bars, four different angle views per rebar were also provided: i) the outer radio in isometric view; ii) the inner radio in isometric view; iii) the cross section after rebar was cut perpendicular to the longitudinal axis; and iv) the close up of surface enhancement detailed typology.



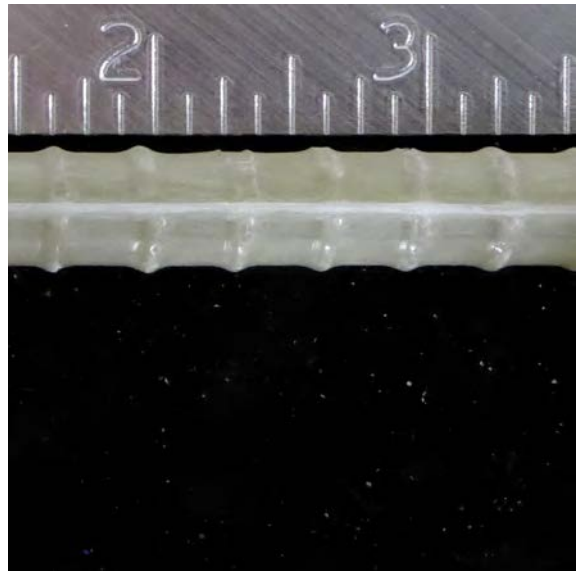
Outer radio in isometric view



Inner radio in isometric view

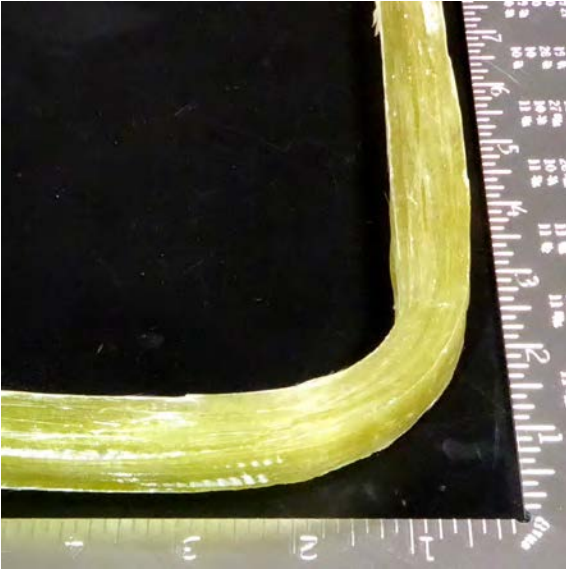


Cross section

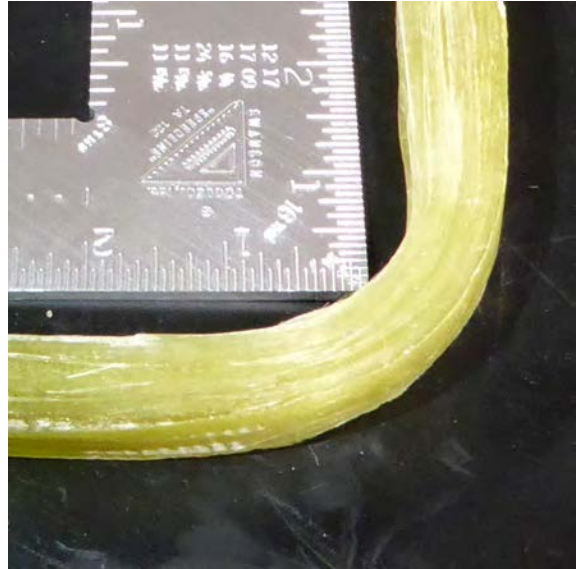


Surface enhancement closeup

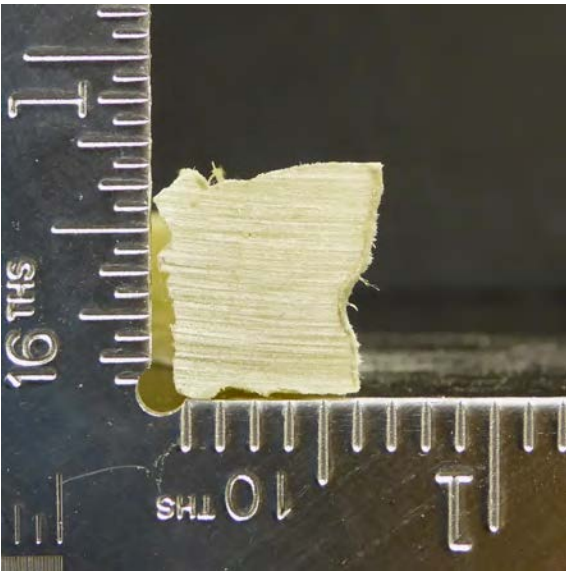
Figure B.20: MAR #3 Bar



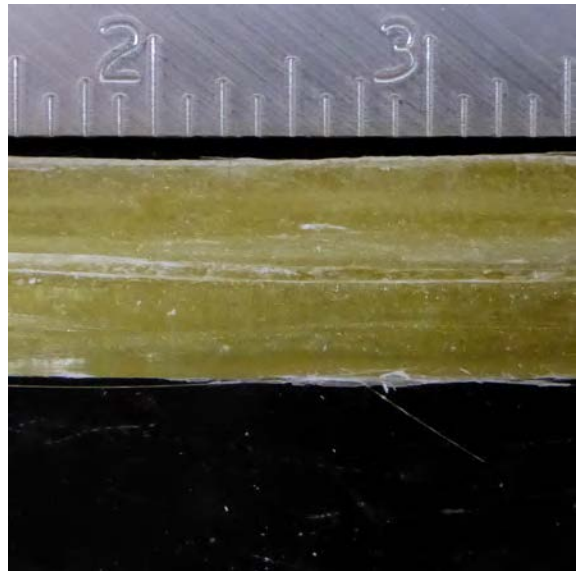
Outer radio in isometric view



Inner radio in isometric view



Cross section



Surface enhancement closeup

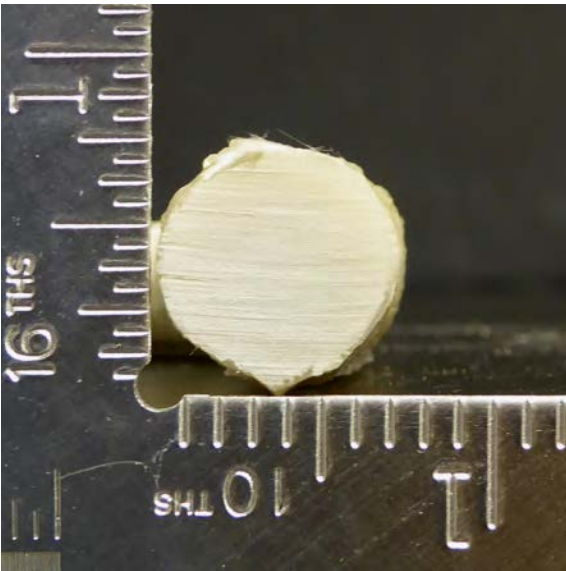
Figure B.21: ATP #5 Bar



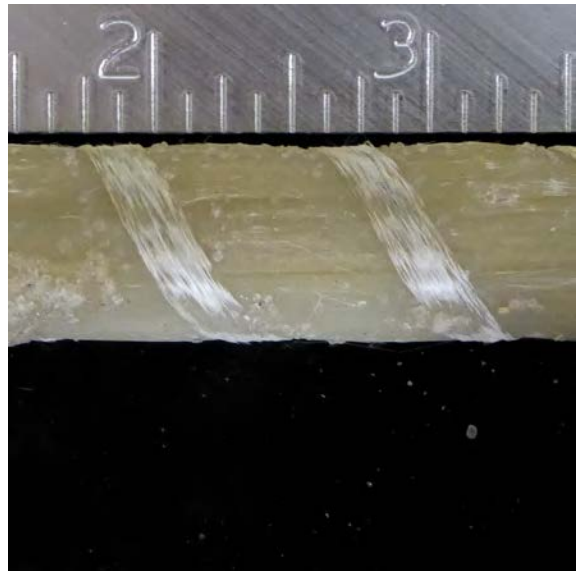
Outer radio in isometric view



Inner radio in isometric view



Cross section



Surface enhancement closeup

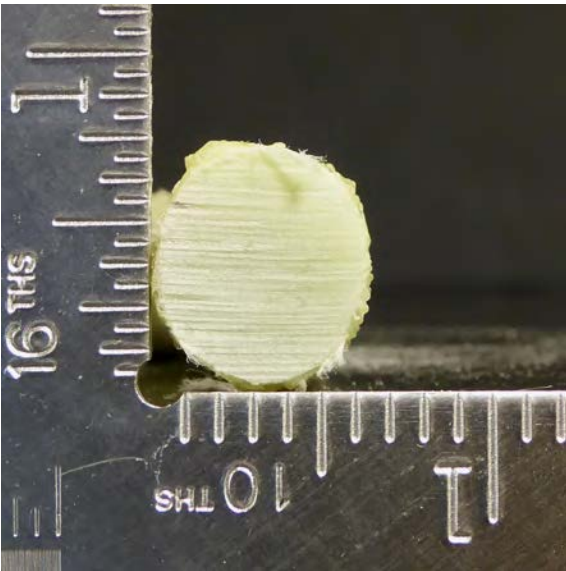
Figure B.22: ASL #5 Bar



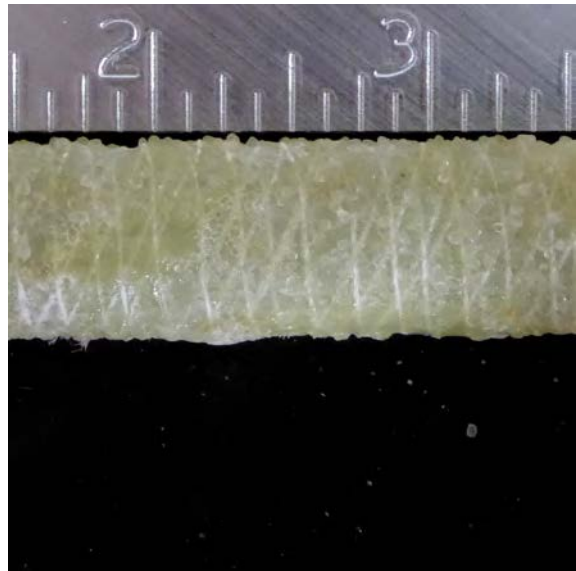
Outer radius in isometric view



Inner radius in isometric view



Cross section



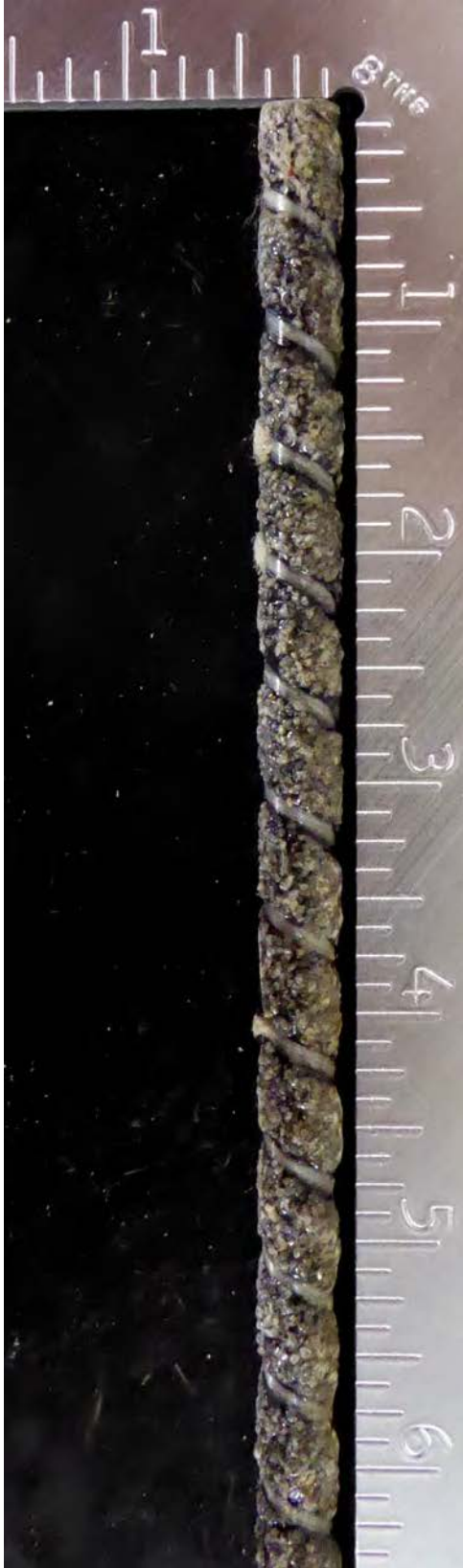
Surface enhancement closeup

Figure B.23: PAL #5 Bar

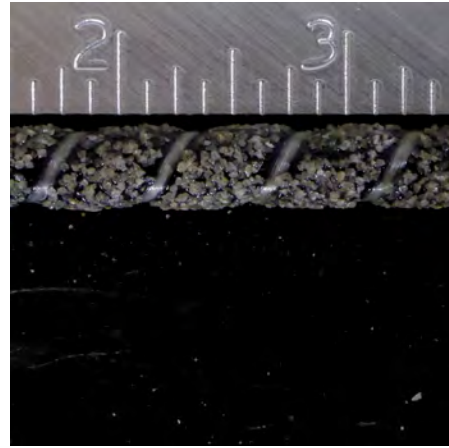
## **B.4 Basalt FRP straight bars**

Additionally, basalt fiber rebars were documented, as these are comparable products and (if applicable) currently most commonly used to replace GFRP rebars. The following visual documentation shows straight basalt FRP rebars made by "Raw Energy Materials Corp. manufacturer, in Florida (USA). For proper comparison, each rebar was photographed four times with the same viewing angles and distances as the straight GFRP rebars shown above.

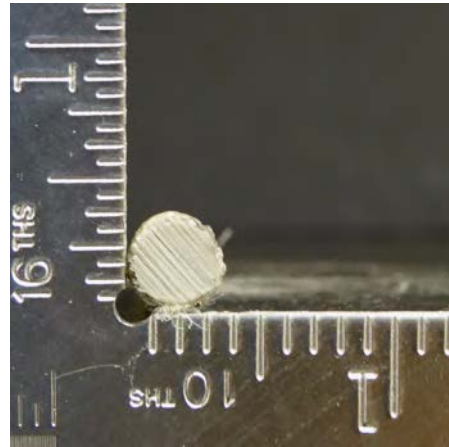




Longitudinal overview



Surface enhancement closeup

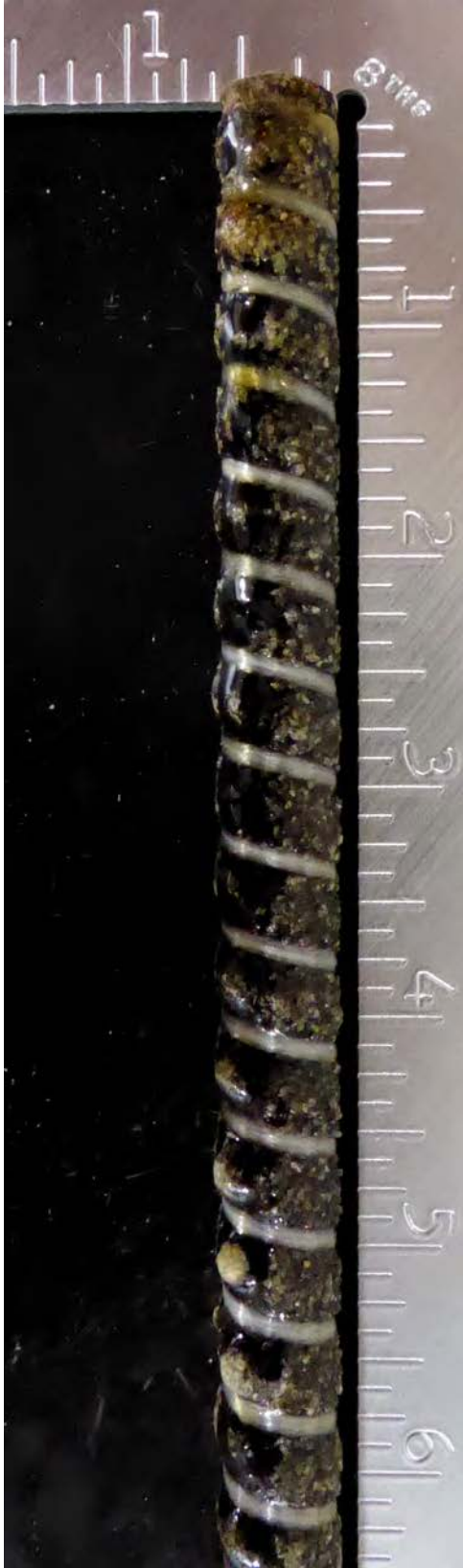


Cross section

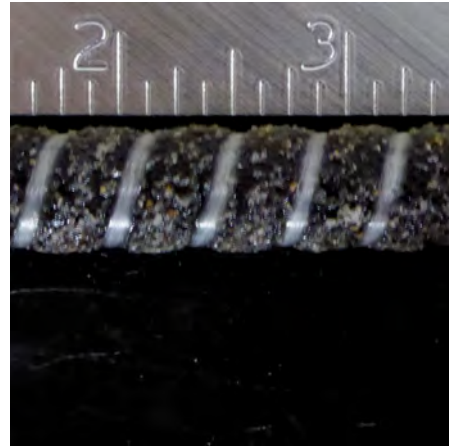


Isometric view

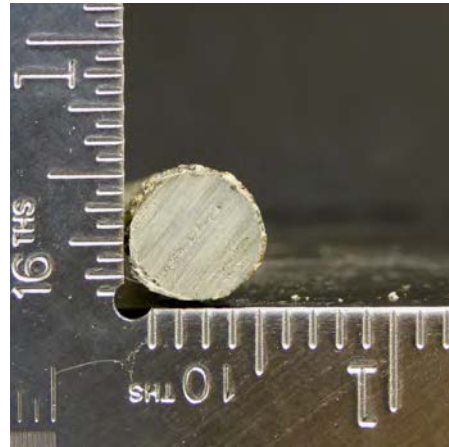
Figure B.24: RAWBas # 3 Bar



Longitudinal overview



Surface enhancement closeup

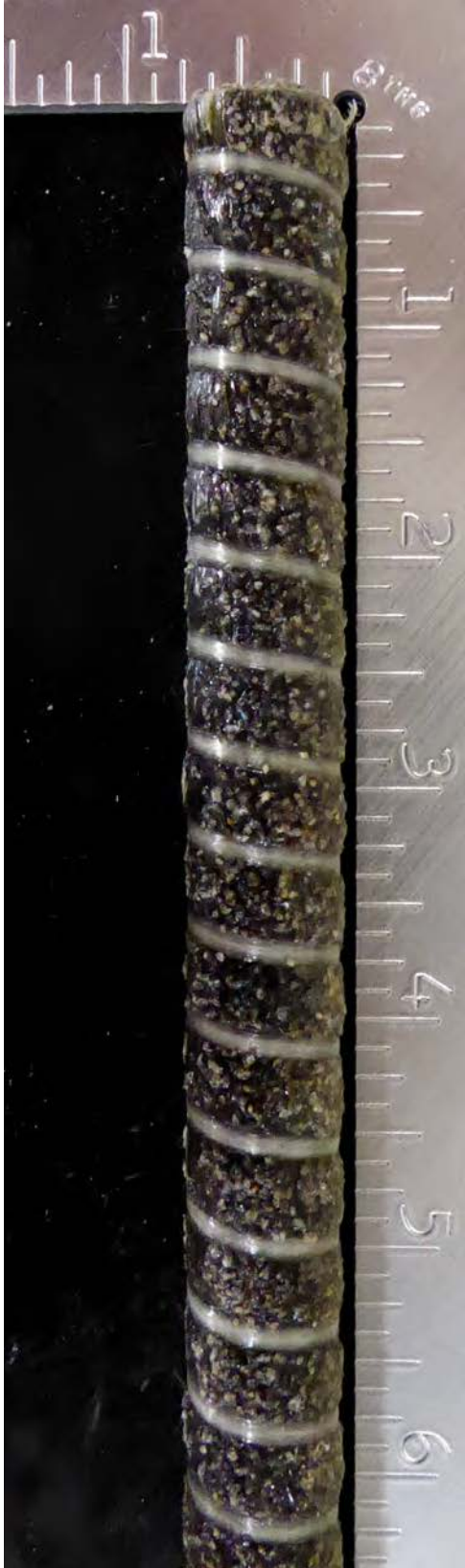


Cross section

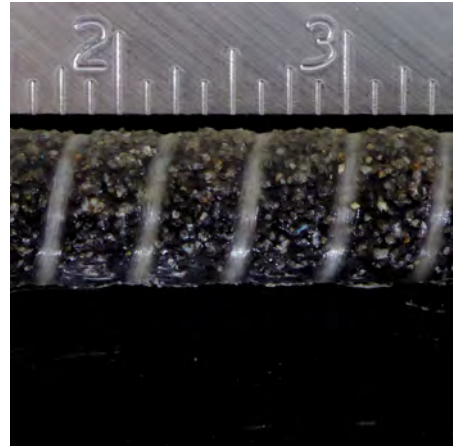


Isometric view

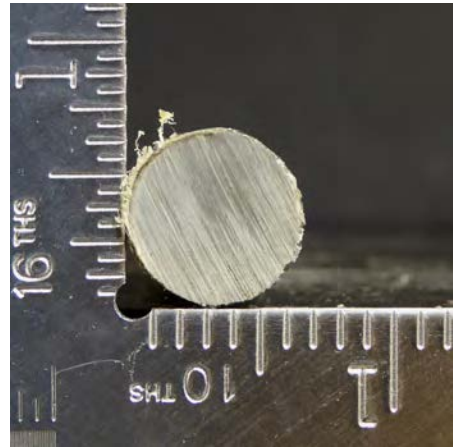
Figure B.25: RAWBas # 4 Bar



Longitudinal overview



Surface enhancement closeup



Cross section



Isometric view

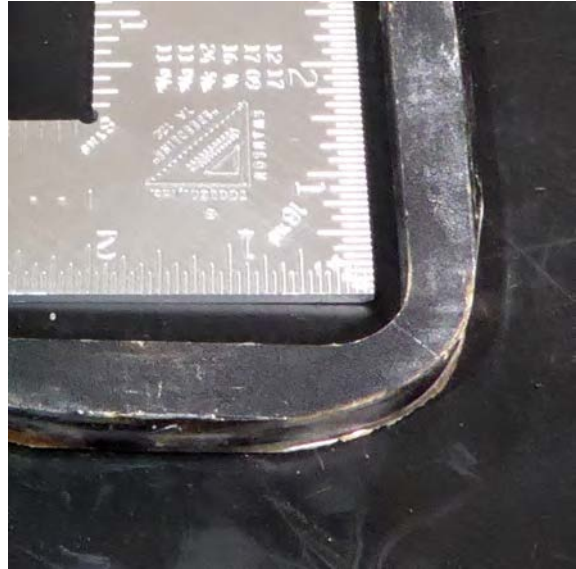
Figure B.26: RAWBas #6 Bar

## **B.5 Basalt FRP bent bars**

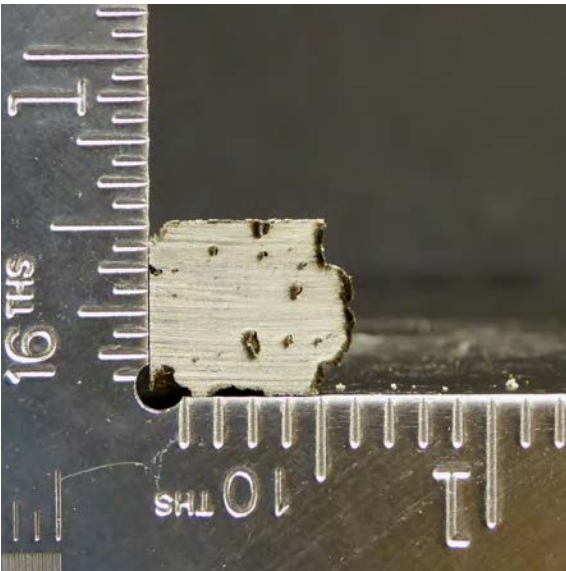
Finally, bent bars made from basalt FRP are shown below. The pictures are arranged analogous to the photos shown above for the GFRP bent bars.



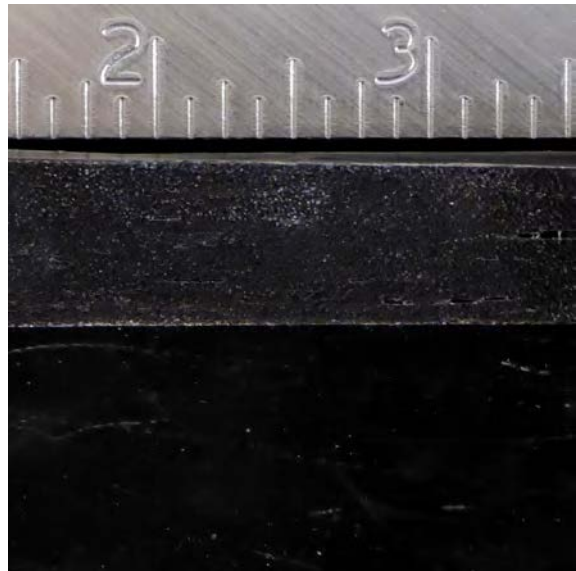
Outer radius in isometric view



Inner radius in isometric view



Cross section



Surface enhancement closeup

Figure B.27: RAWBas #4 Bar

## Appendix C

# Quality Control Plans

Control plan n° PRD02-PC006 prototype / pre-production / production		Contact name/tel.	Date of creation 7 avril 2008	Date of update 7 avril 2008							
Part n°/rev.		Team X. Seynave	Approved by Engineering/date								
Part name <b>V-Rod</b>		Approved by Quality/date									
Supplier Pultrall Inc.		Approved by other/date									
N°	Operation	Tool/ location	Method		Records	Corr. Action					
			Characteristics	Spec. car.			Instrument	Sample Size Freq.	Method of ctrl.		
0	<b>raw material inspection</b>	lab.	Product	Process	Spec./tol.	Size	Freq.	Instrument	Method of ctrl.	Records	Corr. Action
			viscosity of resin		LAB02-F01	1	1/resin lot number	LAB02-IT02	VI-001	LAB02-F01	LAB02-F01
			reactivity of resin			1		BT-001 TH-007	LAB02-IT03		
			linear weight of roving		LAB02-F03	1	1/roving lot number	LAB02-IT04	B-004	LAB02-F03	LAB02-F03
1.2	<b>die/infeed installation</b>	pul.		die ID		n/a	1/setup	n/a	n/a	PRD02-F87	change die
1.3	<b>reinforcement</b>	pul.		roving count		n/a	1/setup	n/a	n/a	PRD02-F87	adjust count
1.4	<b>heating of die</b>	pul.		temperature		n/a	1/setup	n/a	n/a	PRD02-F87	adjust controller
2	<b>resin mix</b>	pul.		scales check		PRD02-F76	1/shift	P-001 P-002	PRD02-F76	PRD02-F76	calibrate scales
		mix.		mix ratios		PRD02-FRxx	1	1/mix	B-005 B-009	PRD02-IT09	PRD02-F02 V-Soft
3.1	<b>start of production</b>	pul.	length		+5/-10mm		1/cav.	tape	n/a	PRD02-F92	adjust controller of saw
			wicking		0 spot		1/cav.	basic fuchsin	LAB03-IT02		adjust process parameters
			flexural strength		PRD02-T62		1/cav.	1/setup	TO-001 CC-001	LAB03-IT25	
	cure ratio		≥98%		DSC	1	1/setup		LAB03-IT09		
	Tg		≥100°C			1	1/setup				

N°	Operation	Tool/ location	Characteristics		Spec. car.	Method					Records	Corr. Action		
			N°	Product		Process	Spec./tol.	Instrument	Sample Size	Sample Freq.			Method of ctrl.	
3.2	<b>production</b>	pul.					n/a	n/a	2/shift	visual	PRD02-F01	adjust count		
					roving count	±5%	n/a	n/a	2/shift				adjust controller	
					temperature	±3°F	n/a	n/a	2/shift					
								n/a	n/a	2/shift				
								n/a	n/a	2/shift				
					length		+5/-10mm	tape	100%	2/shift	n/a	PRD02-F51	adjust controller of saw	
					wicking		0 spot	basic fuchsin	1/cav.	2/shift	LAB03-IT02		adjust process parameters	
					cure ratio		≥98%	DSC	1	1/shift	LAB03-IT09	server	adjust process parameters	
				lab.					1	1/shift				
				coating					1	1/cav.			n/a	adjust process parameters
13	<b>final inspection</b>	pul.					n/a	n/a	100%	visual	PRD02-F05 PRD02-F126 V-Soft	adjust quantity		
					bar count	PRD02-F05 V-Soft	n/a	n/a	100%	visual				
					tensile properties (except dowels)	see customer's req.	TO-004	5	1/lot	LAB03-IT34		LAB03-F02	discard bars	
													n/a	
					effective cross-sectional area			graduated cylinder	5	1/lot	LAB03-IT10			
					fibre ratio			furnace B-004	5	1/lot	LAB03-IT60		discard bars	
					water absorption			BT-001	5	1/lot	LAB03-IT46		discard bars	
					transverse shear			TO-004	5	1/lot	ACI 440.3R B4		discard bars	
					certificate of compliance		n/a	n/a	1	1/lot	n/a		create certificate	
				ship.	identification		n/a	n/a	1	1/bar mark	visual	PRD02-E11	create label	



# Appendix D

## Individual Experimental Results

This appendix supplements the results chapter to present the individual test results for every tested specimen and the corresponding statistical results that were determined for each control and test group (of relevant specimen sets). In general, the following tables are sorted by specimen age, exposure temperature, manufacturer, size, and lot. The tables with individual specimen results are further sorted by specimen count. Dependent on the test procedure, the tables for the individual test results list the most essential (e.g. maximum specimen strength, displacement at maximum strength, etc.) data, while the statistical tables present the minimum ( $\wedge$ ), maximum ( $\vee$ ), mean ( $\mu$ ), standard deviation ( $\sigma$ ), and coefficient of variation (CV) values.

For the purpose of this research project, a wide variety of tested material characteristics throughout numerous aging periods was favored over a large specimen count per evaluated material characteristic. This was an economical decision and in some cases led to reduced data sets, which consisted of no more than three specimens per test or control group. While the virgin material characteristics were evaluated for larger data sets (five specimens per group), all material characteristics that were measured after saltwater exposure were derived from specimen groups of three. It is emphasized that the authors are aware that some statistical values, for example, the standard deviation or coefficient of variation, have limited relevance under these circumstances. But decisions were made to determine these statistical values for all data sets, regardless, because the authors are of the opinion that the results provide additional insight on each tested characteristic, its sensitivity to saltwater exposure, and its general variability relative to the other material characteristics.

### D.1 Density and Cross-Sectional Dimension Test

The following Table D.1 lists all specimen measurements and results that were determined to derive the GFRP rebar diameters according to ASTM D 792 (ASTM International, 2008b). The diameter and the cross-sectional area of the rebars were calculated from the measured density and the individual specimen

volume and lengths.

Table D.1: Density and cross-sectional property test results for each individual specimen

Exposure		Specimen				Specific								
Age	T	Manuf.	Size	Lot	Spec.	Length	Gravity	Density	Volume		Area		Diameter	
d	°C	Type	#	No.	No.	mm	–	kg m <sup>3</sup>	mm <sup>3</sup>	in. <sup>3</sup>	mm <sup>2</sup>	in. <sup>2</sup>	mm	in.
0	23	A	3	1	1	25.4	2.02	2019	2096	0.128	82.6	0.128	10.3	0.404
0	23	A	3	1	2	24.9	2.03	2026	2030	0.124	81.4	0.126	10.2	0.401
0	23	A	3	1	3	25.4	2.03	2024	2064	0.126	81.4	0.126	10.2	0.401
0	23	A	3	2	1	25.1	2.06	2059	2062	0.126	82.0	0.127	10.2	0.402
0	23	A	3	2	2	25.0	2.07	2067	2057	0.126	82.3	0.128	10.2	0.403
0	23	A	3	2	3	24.9	2.06	2060	2032	0.124	81.7	0.127	10.2	0.402
0	23	A	3	3	1	24.4	2.04	2036	1948	0.119	79.9	0.124	10.1	0.397
0	23	A	3	3	2	25.7	2.06	2055	2041	0.125	79.4	0.123	10.1	0.396
0	23	A	3	3	3	25.3	2.08	2079	1993	0.122	78.7	0.122	10.0	0.394
0	23	B	3	1	1	26.5	1.83	1830	2292	0.140	86.5	0.134	10.5	0.413
0	23	B	3	1	2	26.2	1.84	1837	2254	0.138	86.1	0.134	10.5	0.412
0	23	B	3	1	3	27.3	1.84	1836	2345	0.143	85.9	0.133	10.5	0.412
0	23	B	3	2	1	27.5	1.85	1843	2370	0.145	86.1	0.133	10.5	0.412
0	23	B	3	2	2	27.3	1.85	1845	2353	0.144	86.3	0.134	10.5	0.413
0	23	B	3	2	3	25.1	1.85	1842	2172	0.133	86.5	0.134	10.5	0.413
0	23	B	3	3	1	27.1	1.88	1875	2310	0.141	85.2	0.132	10.4	0.410
0	23	B	3	3	2	27.0	1.86	1854	2324	0.142	86.0	0.133	10.5	0.412
0	23	B	3	3	3	27.7	1.85	1846	2386	0.146	86.2	0.134	10.5	0.413
0	23	C	3	1	1	25.6	1.99	1991	1945	0.119	76.0	0.118	9.8	0.387
0	23	C	3	1	2	25.1	2.03	2024	1893	0.116	75.3	0.117	9.8	0.386
0	23	C	3	1	3	25.4	2.00	1997	1923	0.117	75.8	0.118	9.8	0.387
0	23	C	3	2	1	24.9	2.04	2035	1891	0.115	75.9	0.118	9.8	0.387
0	23	C	3	2	2	25.3	2.01	2005	1912	0.117	75.7	0.117	9.8	0.386
0	23	C	3	2	3	25.6	2.00	1996	1942	0.119	75.8	0.117	9.8	0.387
0	23	C	3	3	1	24.9	2.03	2026	1880	0.115	75.5	0.117	9.8	0.386
0	23	C	3	3	2	25.7	2.01	2008	1955	0.119	76.0	0.118	9.8	0.387
0	23	C	3	3	3	24.9	1.99	1991	1905	0.116	76.5	0.119	9.9	0.389
0	23	A	5	1	1	24.7	2.05	2044	5341	0.326	216.0	0.335	16.6	0.653
0	23	A	5	1	2	25.5	2.05	2042	5536	0.338	216.8	0.336	16.6	0.654
0	23	A	5	1	3	25.0	2.05	2046	5383	0.329	215.6	0.334	16.6	0.652
0	23	A	5	2	1	25.3	2.09	2087	5440	0.332	215.0	0.333	16.5	0.651
0	23	A	5	2	2	24.8	2.09	2083	5334	0.326	214.8	0.333	16.5	0.651
0	23	A	5	2	3	24.8	2.08	2079	5313	0.324	214.2	0.332	16.5	0.650
0	23	A	5	3	1	25.4	2.04	2041	5401	0.330	212.7	0.330	16.5	0.648
0	23	A	5	3	2	25.1	2.05	2042	5376	0.328	214.5	0.332	16.5	0.651
0	23	A	5	3	3	25.7	2.05	2044	5468	0.334	212.7	0.330	16.5	0.648
0	23	B	5	1	1	27.5	1.87	1870	6049	0.369	219.9	0.341	16.7	0.659
0	23	B	5	1	2	27.5	1.87	1867	6055	0.369	220.4	0.342	16.8	0.660
0	23	B	5	1	3	27.3	1.87	1868	6037	0.368	221.1	0.343	16.8	0.661
0	23	B	5	2	1	27.6	1.86	1857	6095	0.372	221.1	0.343	16.8	0.661
0	23	B	5	2	2	27.7	1.87	1868	5892	0.360	212.7	0.330	16.5	0.648
0	23	B	5	2	3	27.4	1.87	1864	6052	0.369	220.6	0.342	16.8	0.660
0	23	B	5	3	1	27.0	1.91	1906	5849	0.357	216.4	0.335	16.6	0.653
0	23	B	5	3	2	27.7	1.87	1865	6085	0.371	219.9	0.341	16.7	0.659
0	23	B	5	3	3	27.8	1.87	1869	6104	0.372	219.8	0.341	16.7	0.659
0	23	C	5	1	1	25.8	2.17	2163	4880	0.298	188.9	0.293	15.5	0.611
0	23	C	5	1	2	25.3	2.15	2144	4760	0.290	188.2	0.292	15.5	0.609
0	23	C	5	1	3	24.9	2.15	2148	4670	0.285	187.3	0.290	15.4	0.608
0	23	C	5	2	1	25.4	2.17	2164	4761	0.291	187.2	0.290	15.4	0.608
0	23	C	5	2	2	25.3	2.18	2177	4952	0.302	195.5	0.303	15.8	0.621
0	23	C	5	2	3	25.8	2.15	2143	4832	0.295	187.5	0.291	15.5	0.608
0	23	C	5	3	1	24.9	2.15	2147	4675	0.285	187.5	0.291	15.5	0.608
0	23	C	5	3	2	26.0	2.16	2157	4876	0.298	187.3	0.290	15.4	0.608
0	23	C	5	3	3	25.6	2.16	2154	4801	0.293	187.8	0.291	15.5	0.609
0	23	A	8	1	1	27.5	2.08	2074	14398	0.879	524.2	0.813	25.8	1.017
0	23	A	8	1	2	27.0	2.08	2075	14158	0.864	524.4	0.813	25.8	1.017
0	23	A	8	1	3	26.6	2.08	2073	13989	0.854	525.2	0.814	25.9	1.018
0	23	A	8	2	1	25.2	2.10	2093	13102	0.800	520.6	0.807	25.7	1.014

Continued on next page ...

Table D.1: Density and cross-sectional property test results for each individual specimen

Exposure		Specimen				Specific								
Age	T	Manuf.	Size	Lot	Spec.	Length	Gravity	Density	Volume		Area		Diameter	
d	°C	Type	#	No.	No.	mm	–	kg m <sup>3</sup>	mm <sup>3</sup>	in. <sup>3</sup>	mm <sup>2</sup>	in. <sup>2</sup>	mm	in.
0	23	A	8	2	2	26.2	2.10	2094	13 653	0.833	521.1	0.808	25.8	1.014
0	23	A	8	2	3	26.5	2.08	2080	13 814	0.843	521.9	0.809	25.8	1.015
0	23	A	8	3	1	25.5	2.08	2071	13 962	0.852	547.5	0.849	26.4	1.040
0	23	A	8	3	2	25.4	2.06	2061	13 417	0.819	528.9	0.820	26.0	1.022
0	23	A	8	3	3	25.9	2.06	2059	13 627	0.832	526.8	0.817	25.9	1.020
0	23	B	8	1	1	27.5	1.87	1871	14 883	0.908	541.9	0.840	26.3	1.034
0	23	B	8	1	2	27.4	1.87	1868	14 518	0.886	529.9	0.821	26.0	1.023
0	23	B	8	1	3	28.1	1.88	1874	15 090	0.921	537.7	0.833	26.2	1.030
0	23	B	8	2	1	27.6	1.86	1852	15 060	0.919	545.0	0.845	26.3	1.037
0	23	B	8	2	2	27.5	1.85	1850	14 971	0.914	545.1	0.845	26.3	1.037
0	23	B	8	2	3	27.3	1.86	1859	14 831	0.905	543.9	0.843	26.3	1.036
0	23	B	8	3	1	27.2	1.86	1854	14 816	0.904	544.0	0.843	26.3	1.036
0	23	B	8	3	2	28.0	1.86	1857	15 180	0.926	542.8	0.841	26.3	1.035
0	23	B	8	3	3	26.9	1.86	1861	14 642	0.893	543.6	0.843	26.3	1.036
0	23	C	6	1	1	24.8	2.10	2094	6541	0.399	264.1	0.409	18.3	0.722
0	23	C	6	1	2	25.0	2.05	2050	6789	0.414	271.2	0.420	18.6	0.732
0	23	C	6	1	3	24.8	2.05	2050	6743	0.411	271.9	0.421	18.6	0.733
0	23	C	6	2	1	25.7	2.06	2059	6802	0.415	265.0	0.411	18.4	0.723
0	23	C	6	2	2	25.2	2.05	2046	6717	0.410	266.9	0.414	18.4	0.726
0	23	C	6	2	3	25.7	2.06	2053	6831	0.417	266.1	0.413	18.4	0.725
0	23	C	6	3	1	24.8	2.05	2044	6714	0.410	270.4	0.419	18.6	0.730
0	23	C	6	3	2	24.6	2.05	2048	6620	0.404	268.7	0.417	18.5	0.728
0	23	C	6	3	3	25.3	2.06	2057	6818	0.416	269.5	0.418	18.5	0.729

The specific gravity was calculated by dividing the measured dry mass of the sample by the weight of the submerged specimen. Subsequently, the density of the samples was determined by multiplying the specific gravity and the density of the water in which the specimen was submersed. Because the density of every substance depends on its temperature, the water temperature was monitored as described in ASTM. The water temperature measured 19.8 °C (67.6 °F) for this project, and hence, the distilled water had a density of 998.25 kg/m<sup>3</sup> (62.319 lbs./ft<sup>3</sup>). Then, the volume of the submerged rebar section was determined by dividing the dry mass of the sample by the density of the water. Afterwards, the volume of the rebar sample was divided by the average length of the sample to calculate the cross-sectional area. Finally, the diameter was calculated based on the assumption that the shape of the rebars was round.

## D.2 Fiber Content Test

The relative amount of constituent materials were determined based on weight measurements after lost on ignition tests. The percentage of fiber content is listed in Table D.2 along with the relative resin and sand (surface coating) quantities. If a rebar type included sand as part of the surface enhancement, the weight of sand was subtracted before the fiber and resin content percentage were calculated to achieve comparable results throughout all tested rebar types, independent on the surface enhancement.

Table D.2: Fiber content test results for each individual specimen

Exposure		Specimen				Contents		
Age d	T °C	Manuf. Type	Size #	Lot No.	Spec. No.	Fiber %	Resin %	Sand %
0	23	A	3	1	1	73.28	26.72	13.73
0	23	A	3	1	2	73.35	26.65	15.56
0	23	A	3	1	3	73.26	26.74	13.68
0	23	A	3	2	1	73.75	26.25	5.69
0	23	A	3	2	2	73.55	26.45	7.01
0	23	A	3	2	3	73.76	26.24	6.89
0	23	A	3	3	1	75.08	24.92	6.01
0	23	A	3	3	2	75.01	24.99	6.78
0	23	A	3	3	3	75.04	24.96	5.62
0	23	B	3	1	1	85.18	14.82	0.00
0	23	B	3	1	2	85.08	14.92	0.00
0	23	B	3	1	3	85.17	14.83	0.00
0	23	B	3	2	1	84.71	15.29	0.00
0	23	B	3	2	2	84.85	15.15	0.00
0	23	B	3	2	3	84.79	15.21	0.00
0	23	B	3	3	1	84.56	15.44	0.00
0	23	B	3	3	2	84.39	15.61	0.00
0	23	B	3	3	3	84.49	15.51	0.00
0	23	C	3	1	1	75.43	24.57	0.00
0	23	C	3	1	2	74.66	25.34	0.00
0	23	C	3	1	3	75.34	24.66	0.00
0	23	C	3	2	1	76.63	23.37	0.00
0	23	C	3	2	2	77.20	22.80	0.00
0	23	C	3	2	3	76.43	23.57	0.00
0	23	C	3	3	1	77.15	22.85	0.00
0	23	C	3	3	2	77.06	22.94	0.00
0	23	C	3	3	3	76.22	23.78	0.00
0	23	A	5	1	1	76.02	23.98	4.07
0	23	A	5	1	2	76.16	23.84	4.23
0	23	A	5	1	3	76.40	23.60	4.06
0	23	A	5	2	1	74.39	25.61	5.99
0	23	A	5	2	2	74.79	25.21	5.74
0	23	A	5	2	3	74.78	25.22	5.95
0	23	A	5	3	1	75.01	24.99	5.14
0	23	A	5	3	2	74.91	25.09	4.95
0	23	A	5	3	3	75.02	24.98	5.16
0	23	B	5	1	1	83.93	16.07	0.00
0	23	B	5	1	2	83.87	16.13	0.00
0	23	B	5	1	3	83.82	16.18	0.00
0	23	B	5	2	1	83.65	16.35	0.00
0	23	B	5	2	2	83.73	16.27	0.00
0	23	B	5	2	3	83.73	16.27	0.00
0	23	B	5	3	1	83.86	16.14	0.00
0	23	B	5	3	2	83.88	16.12	0.00
0	23	B	5	3	3	83.40	16.60	0.00
0	23	C	5	1	1	69.80	30.20	0.00
0	23	C	5	1	2	69.75	30.25	0.00

Continued on next page ...

Table D.2: Fiber content test results for each individual specimen

Exposure		Specimen				Contents		
Age d	T °C	Manuf. Type	Size #	Lot No.	Spec. No.	Fiber %	Resin %	Sand %
0	23	C	5	1	3	69.67	30.33	0.00
0	23	C	5	2	1	70.21	29.79	0.00
0	23	C	5	2	2	70.12	29.88	0.00
0	23	C	5	2	3	70.55	29.45	0.00
0	23	C	5	3	1	70.46	29.54	0.00
0	23	C	5	3	2	70.06	29.94	0.00
0	23	C	5	3	3	70.56	29.44	0.00
0	23	A	8	1	1	74.80	25.20	1.89
0	23	A	8	1	2	75.07	24.93	1.98
0	23	A	8	1	3	75.12	24.88	2.01
0	23	A	8	2	1	74.84	25.16	1.64
0	23	A	8	2	2	74.92	25.08	1.80
0	23	A	8	2	3	74.90	25.10	1.38
0	23	A	8	3	1	75.15	24.85	1.66
0	23	A	8	3	2	75.13	24.87	1.74
0	23	A	8	3	3	75.07	24.93	1.84
0	23	B	8	1	1	83.79	16.21	0.00
0	23	B	8	1	2	83.99	16.01	0.00
0	23	B	8	1	3	84.01	15.99	0.00
0	23	B	8	2	1	84.09	15.91	0.00
0	23	B	8	2	2	84.09	15.91	0.00
0	23	B	8	2	3	83.96	16.04	0.00
0	23	B	8	3	1	83.47	16.53	0.00
0	23	B	8	3	2	83.39	16.61	0.00
0	23	B	8	3	3	83.32	16.68	0.00
0	23	C	6	1	1	74.38	25.62	0.00
0	23	C	6	1	2	74.38	25.62	0.00
0	23	C	6	1	3	74.25	25.75	0.00
0	23	C	6	2	1	75.32	24.68	0.00
0	23	C	6	2	2	75.60	24.40	0.00
0	23	C	6	2	3	75.54	24.46	0.00
0	23	C	6	3	1	74.61	25.39	0.00
0	23	C	6	3	2	74.51	25.49	0.00
0	23	C	6	3	3	74.63	25.37	0.00

### D.3 Transverse Shear Test

The following Table D.3 displays the most important measurements and results related to the transverse shear strength test for every individual rebar specimen. The shear strength results (based on the nominal diameter) and the corresponding cross-head displacements (measured at the moment in time the maximum test load was recorded) are provided.

Table D.3: Transverse shear test results (ultimate values) for each individual specimen

Exposure		Specimen				Transverse		Displacement	
Age	T	Manuf.	Size	Lot	Spec.	Shear Strength		at Shear Strength	
d	°C	Type	#	No.	No.	ksi	MPa	in.	mm
000	23	A	3	1	1	30.1	207.4	0.14	3.57
000	23	A	3	1	2	34.4	237.1	0.13	3.34
000	23	A	3	1	3	32.2	221.9	0.14	3.50
000	23	A	3	1	4	28.2	194.7	0.13	3.25
000	23	A	3	1	5	31.0	213.8	0.12	3.03
000	23	A	3	1	6	31.3	216.1	0.13	3.27
000	23	A	3	2	1	30.9	213.1	0.15	3.77
000	23	A	3	2	2	30.5	210.5	0.14	3.51
000	23	A	3	2	3	31.2	214.9	0.15	3.76
000	23	A	3	3	1	30.2	208.2	0.14	3.62
000	23	A	3	3	2	30.0	206.8	0.14	3.67
000	23	A	3	3	3	31.3	215.9	0.15	3.87
000	23	B	3	1	1	24.1	166.3	0.10	2.63
000	23	B	3	1	2	24.5	168.9	0.10	2.61
000	23	B	3	1	3	24.3	167.6	0.11	2.80
000	23	C	3	1	1	29.5	203.1	0.14	3.55
000	23	C	3	1	2	31.0	213.8	0.13	3.25
000	23	C	3	1	3	30.3	209.0	0.14	3.66
000	23	C	3	2	1	30.7	211.6	0.14	3.65
000	23	C	3	2	2	31.5	217.1	0.15	3.75
000	23	C	3	2	3	32.0	220.5	0.14	3.59
000	23	C	3	3	1	30.5	210.5	0.14	3.54
000	23	C	3	3	2	29.9	206.2	0.14	3.46
000	23	C	3	3	3	31.7	218.7	0.13	3.29
000	23	A	5	1	1	24.9	171.9	0.19	4.80
000	23	A	5	1	2	27.2	187.8	0.18	4.51
000	23	A	5	1	3	26.1	179.7	0.20	5.05
000	23	A	5	1	4	26.5	183.0	0.24	6.15
000	23	A	5	1	5	25.0	172.0	0.20	5.02
000	23	A	5	1	6	25.2	173.8	0.18	4.50
000	23	A	5	2	1	26.4	182.0	0.21	5.43
000	23	A	5	2	2	25.9	178.6	0.20	5.20
000	23	A	5	2	3	26.6	183.7	0.20	5.16
000	23	A	5	3	1	28.8	198.6	0.21	5.28
000	23	A	5	3	2	28.4	195.9	0.21	5.27
000	23	A	5	3	3	28.4	195.5	0.19	4.84
000	23	B	5	1	1	22.3	153.8	0.15	3.71
000	23	B	5	1	2	23.0	158.9	0.14	3.52
000	23	B	5	1	3	23.1	159.1	0.13	3.24
000	23	C	5	1	1	33.5	230.7	0.20	5.21
000	23	C	5	1	2	30.6	210.8	0.21	5.28
000	23	C	5	1	3	30.5	210.1	0.19	4.89
000	23	C	5	2	1	31.3	216.0	0.19	4.88
000	23	C	5	2	2	30.2	208.3	0.19	4.85
000	23	C	5	2	3	32.1	221.1	0.18	4.47
000	23	C	5	3	1	32.5	224.2	0.19	4.74
000	23	C	5	3	2	31.8	219.0	0.18	4.54
000	23	C	5	3	3	32.1	221.3	0.19	4.78
000	23	C	6	1	1	26.9	185.7	0.19	4.86
000	23	C	6	1	2	30.8	212.5	0.23	5.92
000	23	C	6	1	3	28.6	197.1	0.22	5.50
000	23	C	6	2	1	28.6	197.5	0.22	5.47

Continued on next page ...

Table D.3: Transverse shear test results (ultimate values) for each individual specimen

Exposure		Specimen				Transverse		Displacement	
Age	T	Manuf.	Size	Lot	Spec.	Shear Strength		at Shear Strength	
d	°C	Type	#	No.	No.	ksi	MPa	in.	mm
000	23	C	6	2	2	26.4	181.9	0.22	5.47
000	23	C	6	2	3	29.2	201.6	0.20	5.20
000	23	C	6	3	1	27.8	191.7	0.21	5.40
000	23	C	6	3	2	28.0	193.1	0.26	6.69
000	23	C	6	3	3	27.7	190.7	0.22	5.64
000	23	A	8	1	1	24.8	171.3	0.27	6.79
000	23	A	8	1	2	24.0	165.7	0.24	5.99
000	23	A	8	1	3	25.0	172.6	0.23	5.84
000	23	A	8	1	4	25.0	172.6	0.23	5.84
000	23	A	8	1	5	24.3	167.8	0.25	6.33
000	23	A	8	1	6	25.3	174.4	0.24	6.07
000	23	A	8	2	1	25.3	174.5	0.29	7.31
000	23	A	8	2	2	24.7	170.4	0.32	8.02
000	23	A	8	2	3	24.3	167.4	0.28	7.23
000	23	A	8	3	1	24.7	170.4	0.28	7.03
000	23	A	8	3	2	24.3	167.5	0.25	6.42
000	23	A	8	3	3	24.8	170.7	0.31	7.77
000	23	B	8	1	1	22.3	154.0	0.18	4.49
000	23	B	8	1	2	22.3	154.0	0.18	4.49
000	23	B	8	1	3	22.4	154.7	0.14	3.61
060	23	A	3	1	1	36.3	250.0	0.17	4.28
060	23	A	3	1	2	39.4	271.9	0.17	4.34
060	23	A	3	1	3	34.8	239.7	0.18	4.57
060	23	B	3	1	1	28.8	198.4	0.11	2.89
060	23	B	3	1	2	30.9	213.4	0.12	3.00
060	23	B	3	1	3	28.3	195.3	0.12	3.14
060	23	C	3	1	1	41.2	284.1	0.16	4.18
060	23	C	3	1	2	36.5	251.7	0.16	4.15
060	23	C	3	1	3	39.9	274.9	0.17	4.24
060	40	A	3	1	1	39.5	272.2	0.16	4.00
060	40	A	3	1	2	35.8	246.7	0.19	4.92
060	40	A	3	1	3	36.7	253.3	0.16	4.02
060	40	B	3	1	1	30.9	213.1	0.11	2.91
060	40	B	3	1	2	28.0	193.3	0.12	3.02
060	40	B	3	1	3	31.8	219.1	0.12	3.05
060	40	C	3	1	1	37.4	257.9	0.17	4.44
060	40	C	3	1	2	40.2	277.0	0.17	4.25
060	40	C	3	1	3	38.1	263.0	0.16	3.95
060	60	A	3	1	1	33.4	230.4	0.16	4.04
060	60	A	3	1	2	35.6	245.3	0.17	4.22
060	60	A	3	1	3	32.9	226.5	0.16	4.03
060	60	B	3	1	1	28.2	194.1	0.12	3.00
060	60	B	3	1	2	29.2	201.1	0.12	2.94
060	60	B	3	1	3	29.6	204.0	0.12	2.94
060	60	C	3	1	1	35.5	245.1	0.17	4.27
060	60	C	3	1	2	36.3	250.0	0.15	3.71
060	60	C	3	1	3	34.4	237.3	0.16	4.03
120	23	A	3	1	1	39.7	273.7	0.17	4.35
120	23	A	3	1	2	37.1	255.8	0.20	5.12
120	23	A	3	1	3	37.2	256.5	0.21	5.29
120	23	B	3	1	1	27.6	190.3	0.13	3.25
120	23	B	3	1	2	30.2	208.1	0.14	3.45

Continued on next page ...

Table D.3: Transverse shear test results (ultimate values) for each individual specimen

Exposure		Specimen				Transverse		Displacement	
Age	T	Manuf.	Size	Lot	Spec.	Shear Strength		at Shear Strength	
d	°C	Type	#	No.	No.	ksi	MPa	in.	mm
120	23	B	3	1	3	28.1	193.7	0.13	3.40
120	23	C	3	1	1	33.4	230.5	0.15	3.92
120	23	C	3	1	2	36.1	248.6	0.15	3.76
120	23	C	3	1	3	36.0	248.4	0.18	4.50
120	40	A	3	1	1	35.5	244.5	0.22	5.56
120	40	A	3	1	2	35.8	246.7	0.19	4.94
120	40	A	3	1	3	35.2	243.0	0.26	6.61
120	40	B	3	1	1	27.2	187.5	0.10	2.62
120	40	B	3	1	2	31.1	214.8	0.12	2.98
120	40	B	3	1	3	28.9	199.5	0.13	3.25
120	40	C	3	1	1	35.1	241.8	0.15	3.83
120	40	C	3	1	2	42.9	295.9	0.16	3.94
120	40	C	3	1	3	43.8	301.7	0.15	3.74
120	60	A	3	1	1	29.0	199.9	0.15	3.72
120	60	A	3	1	2	27.6	190.1	0.16	3.99
120	60	A	3	1	3	29.1	200.8	0.15	3.75
120	60	B	3	1	1	29.3	201.8	0.13	3.30
120	60	B	3	1	2	30.2	208.3	0.13	3.18
120	60	B	3	1	3	29.8	205.2	0.13	3.41
120	60	C	3	1	1	39.6	272.8	0.16	4.00
120	60	C	3	1	2	39.3	270.9	0.15	3.69
120	60	C	3	1	3	36.2	249.5	0.14	3.58
210	23	A	3	1	1	30.2	208.1	0.14	3.65
210	23	A	3	1	2	28.5	196.4	0.15	3.73
210	23	A	3	1	3	31.6	217.6	0.14	3.64
210	23	B	3	1	1	27.8	191.5	0.10	2.53
210	23	B	3	1	2	25.7	177.4	0.09	2.41
210	23	B	3	1	3	24.6	169.7	0.11	2.78
210	23	C	3	1	1	29.5	203.2	0.13	3.28
210	23	C	3	1	2	33.2	229.2	0.15	3.80
210	23	C	3	1	3	33.7	232.1	0.15	3.74
210	40	A	3	1	1	32.4	223.3	0.17	4.27
210	40	A	3	1	2	32.2	222.1	0.14	3.55
210	40	A	3	1	3	31.1	214.4	0.17	4.37
210	40	B	3	1	1	27.0	185.9	0.11	2.83
210	40	B	3	1	2	28.3	195.4	0.13	3.19
210	40	B	3	1	3	25.4	175.3	0.11	2.68
210	40	C	3	1	1	35.7	246.0	0.13	3.38
210	40	C	3	1	2	35.0	241.1	0.14	3.51
210	40	C	3	1	3	32.3	222.6	0.13	3.19
210	60	A	3	1	1	31.7	218.7	0.15	3.87
210	60	A	3	1	2	31.5	217.0	0.15	3.72
210	60	A	3	1	3	31.8	218.9	0.17	4.36
210	60	B	3	1	1	29.1	200.7	0.10	2.46
210	60	B	3	1	2	23.0	158.3	0.11	2.68
210	60	B	3	1	3	8.2	56.4	0.04	1.10
210	60	C	3	1	1	30.8	212.2	0.15	3.75
210	60	C	3	1	2	31.1	214.5	0.15	3.82
210	60	C	3	1	3	31.8	219.2	0.11	2.75
365	23	A	3	1	1	37.6	259.1	0.18	4.59
365	23	A	3	1	2	35.9	247.4	0.17	4.26
365	23	A	3	1	3	39.6	272.8	0.17	4.32

Continued on next page ...



Table D.3: Transverse shear test results (ultimate values) for each individual specimen

Exposure		Specimen				Transverse		Displacement	
Age	T	Manuf.	Size	Lot	Spec.	Shear Strength		at Shear Strength	
d	°C	Type	#	No.	No.	ksi	MPa	in.	mm
365	23	B	3	1	1	29.7	204.7	0.12	3.03
365	23	B	3	1	2	24.3	167.7	0.11	2.71
365	23	B	3	1	3	25.8	178.2	0.13	3.26
365	23	C	3	1	1	38.9	268.0	0.18	4.69
365	23	C	3	1	2	35.1	242.2	0.13	3.41
365	23	C	3	1	3	36.0	248.4	0.14	3.55
365	40	A	3	1	1	35.5	244.4	0.18	4.46
365	40	A	3	1	2	34.1	235.2	0.17	4.32
365	40	A	3	1	3	32.2	221.8	0.17	4.28
365	40	B	3	1	1	29.1	200.7	0.14	3.52
365	40	B	3	1	2	29.6	204.1	0.10	2.64
365	40	B	3	1	3	28.7	197.9	0.13	3.41
365	40	C	3	1	1	34.3	236.3	0.17	4.25
365	40	C	3	1	2	41.7	287.6	0.15	3.86
365	40	C	3	1	3	32.6	224.4	0.15	3.84
365	60	A	3	1	1	34.6	238.7	0.14	3.46
365	60	A	3	1	2	33.6	231.5	0.16	4.18
365	60	A	3	1	3	34.7	239.1	0.16	4.15
365	60	B	3	1	1	26.9	185.5	0.11	2.86
365	60	B	3	1	2	25.7	176.9	0.11	2.74
365	60	B	3	1	3	28.3	195.4	0.12	2.97
365	60	C	3	1	1	31.0	213.9	0.12	3.09
365	60	C	3	1	2	31.4	216.5	0.14	3.54
365	60	C	3	1	3	32.4	223.5	0.13	3.35

Table D.4 lists the most essential results from the statistical analysis for the transverse shear test data. Each table row is based on the measurements for all specimens in the relevant data set.

Table D.4: Transverse shear test statistical values for each sample group

Exposure		Sample Group			Statistical Values								
Age	T	Manuf.	Size	Lot	Imperial				Metric				CV
					∧	∨	μ	σ	∧	∨	μ	σ	
d	°C	Type	#	No.	ksi	ksi	ksi	ksi	MPa	MPa	MPa	MPa	%
000	23	A	3	1	28.24	34.38	31.21	2.1	195	237	215	14.2	6.60
000	23	A	3	2	30.52	31.16	30.86	0.3	210	215	213	2.2	1.04
000	23	A	3	3	29.99	31.31	30.50	0.7	207	216	210	4.9	2.33
000	23	B	3	1	24.11	24.50	24.31	0.2	166	169	168	1.3	0.79
000	23	C	3	1	29.46	31.00	30.26	0.8	203	214	209	5.3	2.55
000	23	C	3	2	30.69	31.98	31.39	0.7	212	221	216	4.5	2.07
000	23	C	3	3	29.91	31.72	30.72	0.9	206	219	212	6.3	3.00
000	23	A	5	1	24.93	27.24	25.82	0.9	172	188	178	6.5	3.68
000	23	A	5	2	25.90	26.65	26.31	0.4	179	184	181	2.6	1.45
000	23	A	5	3	28.36	28.81	28.53	0.2	196	199	197	1.7	0.86
000	23	B	5	1	22.31	23.08	22.81	0.4	154	159	157	3.0	1.89
000	23	C	5	1	30.47	33.46	31.50	1.7	210	231	217	11.7	5.38
000	23	C	5	2	30.22	32.07	31.21	0.9	208	221	215	6.4	2.98
000	23	C	5	3	31.76	32.51	32.12	0.4	219	224	221	2.6	1.17

Continued on next page ...

Table D.4: Transverse shear test statistical values for each sample group

Exposure		Sample Group			Statistical Values								
Age d	T °C	Manuf. Type	Size #	Lot No.	Imperial				Metric				CV %
					$\wedge$ ksi	$\vee$ ksi	$\mu$ ksi	$\sigma$ ksi	$\wedge$ MPa	$\vee$ MPa	$\mu$ MPa	$\sigma$ MPa	
000	23	C	6	1	26.94	30.82	28.78	2.0	186	213	198	13.4	6.78
000	23	C	6	2	26.38	29.24	28.09	1.5	182	202	194	10.4	5.38
000	23	C	6	3	27.66	28.01	27.82	0.2	191	193	192	1.2	0.63
000	23	A	8	1	24.03	25.29	24.76	0.5	166	174	171	3.3	1.93
000	23	A	8	2	24.29	25.31	24.77	0.5	167	175	171	3.6	2.08
000	23	A	8	3	24.29	24.75	24.58	0.3	167	171	170	1.8	1.03
000	23	B	8	1	22.33	22.44	22.37	0.1	154	155	154	0.4	0.28
060	23	A	3	1	34.77	39.43	36.82	2.4	240	272	254	16.4	6.47
060	23	B	3	1	28.32	30.95	29.35	1.4	195	213	202	9.7	4.79
060	23	C	3	1	36.51	41.21	39.19	2.4	252	284	270	16.7	6.18
060	40	A	3	1	35.78	39.48	37.33	1.9	247	272	257	13.3	5.15
060	40	B	3	1	28.03	31.78	30.24	2.0	193	219	209	13.5	6.48
060	40	C	3	1	37.41	40.18	38.58	1.4	258	277	266	9.9	3.71
060	60	A	3	1	32.85	35.57	33.95	1.4	226	245	234	9.9	4.23
060	60	B	3	1	28.15	29.58	28.97	0.7	194	204	200	5.1	2.53
060	60	C	3	1	34.42	36.26	35.41	0.9	237	250	244	6.4	2.61
120	23	A	3	1	37.09	39.69	38.00	1.5	256	274	262	10.1	3.87
120	23	B	3	1	27.60	30.18	28.62	1.4	190	208	197	9.5	4.80
120	23	C	3	1	33.43	36.05	35.17	1.5	230	249	242	10.4	4.29
120	40	A	3	1	35.25	35.79	35.50	0.3	243	247	245	1.9	0.77
120	40	B	3	1	27.19	31.15	29.09	2.0	187	215	201	13.7	6.82
120	40	C	3	1	35.07	43.75	40.58	4.8	242	302	280	33.1	11.81
120	60	A	3	1	27.57	29.13	28.56	0.9	190	201	197	5.9	3.01
120	60	B	3	1	29.26	30.21	29.74	0.5	202	208	205	3.3	1.59
120	60	C	3	1	36.18	39.57	38.35	1.9	249	273	264	12.9	4.89
210	23	A	3	1	28.49	31.55	30.07	1.5	196	218	207	10.6	5.11
210	23	B	3	1	24.61	27.78	26.04	1.6	170	192	180	11.1	6.17
210	23	C	3	1	29.48	33.67	32.13	2.3	203	232	222	15.9	7.18
210	40	A	3	1	31.09	32.38	31.90	0.7	214	223	220	4.8	2.20
210	40	B	3	1	25.43	28.34	26.91	1.5	175	195	186	10.1	5.42
210	40	C	3	1	32.28	35.67	34.31	1.8	223	246	237	12.3	5.21
210	60	A	3	1	31.47	31.75	31.65	0.2	217	219	218	1.1	0.49
210	60	B	3	1	8.18	29.11	20.08	10.8	56	201	138	74.2	53.58
210	60	C	3	1	30.78	31.79	31.22	0.5	212	219	215	3.6	1.66
365	23	A	3	1	35.88	39.56	37.67	1.8	247	273	260	12.7	4.90
365	23	B	3	1	24.32	29.69	26.62	2.8	168	205	184	19.1	10.39
365	23	C	3	1	35.13	38.86	36.68	1.9	242	268	253	13.4	5.31
365	40	A	3	1	32.17	35.45	33.91	1.7	222	244	234	11.4	4.88
365	40	B	3	1	28.70	29.61	29.14	0.5	198	204	201	3.1	1.56
365	40	C	3	1	32.55	41.72	36.18	4.9	224	288	249	33.6	13.47
365	60	A	3	1	33.58	34.68	34.29	0.6	232	239	236	4.3	1.80
365	60	B	3	1	25.66	28.34	26.97	1.3	177	195	186	9.2	4.97
365	60	C	3	1	31.03	32.42	31.61	0.7	214	224	218	5.0	2.28

## D.4 Horizontal Shear Test

Similar to the previous section, the following Table D.5 lists the maximum measured data for all specimens that were tested for horizontal shear strength. The strength values were determined based on the measured

maximum loads and the nominal (not measured) cross-sectional dimensions. The displacement at shear strength represents the cross-head extension that was measured simultaneously with the maximum failure load. Accordingly, this value is indicative of the deflection of the shear specimen that lead to resin failure and slip between the fibers.

Table D.5: Horizontal shear test results (ultimate values) for each individual specimen

Exposure		Specimen				Horizontal		Displacement	
Age	T	Manuf.	Size	Lot	Spec.	Shear Strength		at Shear Strength	
d	°C	Type	#	No.	No.	ksi	MPa	in.	mm
000	23	A	3	1	1	6.9	47.7	0.10	2.61
000	23	A	3	1	2	6.5	44.8	0.09	2.39
000	23	A	3	1	3	6.6	45.3	0.09	2.25
000	23	A	3	2	1	6.1	42.2	0.10	2.62
000	23	A	3	2	2	6.3	43.7	0.10	2.54
000	23	A	3	2	3	5.3	36.6	0.08	2.09
000	23	A	3	3	1	6.0	41.2	0.09	2.25
000	23	A	3	3	2	6.9	47.7	0.12	2.96
000	23	A	3	3	3	6.0	41.2	0.08	2.02
000	23	B	3	1	1	6.3	43.2	0.07	1.88
000	23	B	3	1	2	6.1	42.2	0.06	1.55
000	23	B	3	1	3	6.1	41.9	0.06	1.50
000	23	B	3	2	1	6.8	47.2	0.07	1.72
000	23	B	3	2	2	6.1	41.9	0.06	1.64
000	23	B	3	2	3	6.4	44.0	0.06	1.52
000	23	B	3	3	1	6.9	47.3	0.06	1.58
000	23	B	3	3	2	6.5	44.5	0.05	1.30
000	23	C	3	1	1	7.3	50.3	0.10	2.64
000	23	C	3	1	2	6.9	47.4	0.09	2.35
000	23	C	3	1	3	6.9	47.7	0.08	2.03
000	23	C	3	2	1	7.6	52.3	0.10	2.50
000	23	C	3	2	2	7.4	50.7	0.12	3.04
000	23	C	3	2	3	8.0	55.0	0.09	2.33
000	23	C	3	3	1	8.3	57.0	0.09	2.39
000	23	C	3	3	2	7.4	51.0	0.08	2.05
000	23	C	3	3	3	7.3	50.2	0.08	2.10
000	23	A	5	1	1	5.6	38.5	0.13	3.30
000	23	A	5	1	2	6.0	41.6	0.15	3.68
000	23	A	5	1	3	6.4	43.8	0.12	3.02
000	23	A	5	2	1	5.6	38.9	0.11	2.71
000	23	A	5	2	2	6.2	42.4	0.13	3.22
000	23	A	5	2	3	5.8	40.2	0.12	3.09
000	23	A	5	3	1	6.7	46.4	0.13	3.39
000	23	A	5	3	2	6.0	41.5	0.13	3.29
000	23	A	5	3	3	6.6	45.2	0.15	3.80
000	23	B	5	1	1	6.1	41.7	0.09	2.40
000	23	B	5	1	2	6.3	43.3	0.11	2.68
000	23	B	5	1	3	5.9	40.9	0.10	2.49
000	23	B	5	2	1	5.9	40.4	0.10	2.54
000	23	B	5	2	2	6.1	42.1	0.09	2.28
000	23	B	5	2	3	6.2	42.8	0.10	2.43
000	23	B	5	3	1	5.8	40.2	0.07	1.76
000	23	B	5	3	2	5.7	39.1	0.11	2.78
000	23	B	5	3	3	5.9	40.4	0.10	2.58

Continued on next page ...

Table D.5: Horizontal shear test results (ultimate values) for each individual specimen

Exposure		Specimen				Horizontal		Displacement	
Age	T	Manuf.	Size	Lot	Spec.	Shear Strength		at Shear Strength	
d	°C	Type	#	No.	No.	ksi	MPa	in.	mm
000	23	C	5	1	1	6.8	47.0	0.14	3.52
000	23	C	5	1	2	7.2	49.8	0.12	3.10
000	23	C	5	1	3	7.4	50.8	0.15	3.84
000	23	C	5	2	1	7.8	54.0	0.15	3.80
000	23	C	5	2	2	7.0	48.5	0.11	2.86
000	23	C	5	2	3	7.5	51.9	0.12	2.99
000	23	C	5	3	1	6.9	47.3	0.13	3.39
000	23	C	5	3	2	7.7	53.3	0.14	3.50
000	23	C	5	3	3	7.5	51.8	0.11	2.87
000	23	C	6	1	1	6.3	43.4	0.15	3.90
000	23	C	6	1	2	6.9	47.7	0.15	3.92
000	23	C	6	1	3	7.0	48.1	0.15	3.88
000	23	C	6	2	1	5.9	40.9	0.13	3.32
000	23	C	6	2	2	6.6	45.4	0.15	3.80
000	23	C	6	2	3	6.5	45.0	0.16	4.04
000	23	C	6	3	1	6.0	41.7	0.21	5.29
000	23	C	6	3	2	6.0	41.7	0.21	5.29
000	23	C	6	3	3	6.5	44.8	0.13	3.26
000	23	A	8	1	1	6.2	42.5	0.19	4.88
000	23	A	8	1	2	6.3	43.5	0.19	4.77
000	23	A	8	1	3	6.3	43.6	0.22	5.64
000	23	A	8	2	1	4.6	31.5	0.20	5.03
000	23	A	8	2	2	6.2	42.7	0.18	4.67
000	23	A	8	2	3	6.2	42.5	0.20	5.10
000	23	A	8	3	1	6.3	43.4	0.20	5.04
000	23	A	8	3	2	6.6	45.3	0.22	5.48
000	23	A	8	3	3	6.7	46.2	0.23	5.78
000	23	B	8	1	1	5.4	37.1	0.14	3.49
000	23	B	8	1	2	5.5	38.1	0.15	3.69
000	23	B	8	1	3	6.0	41.7	0.14	3.44
000	23	B	8	2	1	6.6	45.2	0.16	3.98
000	23	B	8	2	2	5.5	38.1	0.14	3.67
000	23	B	8	2	3	6.2	42.5	0.15	3.73
000	23	B	8	3	1	3.7	25.8	-0.21	-5.27
000	23	B	8	3	2	5.9	40.8	0.15	3.81
000	23	B	8	3	3	5.8	40.0	0.14	3.68
060	23	A	3	1	1	6.5	45.0	0.07	1.81
060	23	A	3	1	2	6.7	46.1	0.09	2.38
060	23	A	3	1	3	6.4	44.2	0.09	2.39
060	23	B	3	1	1	6.6	45.6	0.09	2.23
060	23	B	3	1	2	5.4	37.5	0.05	1.31
060	23	B	3	1	3	7.3	50.4	0.07	1.66
060	23	C	3	1	1	7.0	47.9	0.08	2.01
060	23	C	3	1	2	6.7	46.1	0.08	2.01
060	23	C	3	1	3	6.9	47.6	0.07	1.87
060	40	A	3	1	1	6.4	43.9	0.09	2.41
060	40	A	3	1	2	6.3	43.2	0.09	2.23
060	40	A	3	1	3	6.1	42.0	0.08	2.15
060	40	B	3	1	1	6.6	45.7	0.05	1.19
060	40	B	3	1	2	7.2	49.9	0.06	1.44
060	40	B	3	1	3	7.1	48.8	0.06	1.52
060	40	C	3	1	1	6.9	47.4	0.07	1.83

Continued on next page ...

Table D.5: Horizontal shear test results (ultimate values) for each individual specimen

Exposure		Specimen				Horizontal		Displacement	
Age	T	Manuf.	Size	Lot	Spec.	Shear Strength		at Shear Strength	
d	°C	Type	#	No.	No.	ksi	MPa	in.	mm
060	40	C	3	1	2	6.6	45.6	0.07	1.66
060	40	C	3	1	3	7.1	48.7	0.10	2.57
060	60	A	3	1	1	6.5	45.0	0.09	2.40
060	60	A	3	1	2	6.5	45.0	0.07	1.88
060	60	A	3	1	3	6.3	43.4	0.06	1.50
060	60	B	3	1	1	6.6	45.8	0.05	1.22
060	60	B	3	1	2	7.4	51.1	0.06	1.47
060	60	B	3	1	3	5.6	38.4	0.04	1.05
060	60	C	3	1	1	6.7	46.2	0.06	1.60
060	60	C	3	1	2	6.7	46.3	0.06	1.55
060	60	C	3	1	3	7.2	49.9	0.08	2.07
120	23	A	3	1	1	6.5	44.9	0.08	2.05
120	23	A	3	1	2	7.2	50.0	0.11	2.88
120	23	A	3	1	3	7.1	48.9	0.08	2.13
120	23	B	3	1	1	7.5	51.9	0.07	1.73
120	23	B	3	1	2	7.0	48.0	0.05	1.37
120	23	B	3	1	3	6.5	44.8	0.05	1.40
120	23	C	3	1	1	6.6	45.2	0.07	1.84
120	23	C	3	1	2	6.5	44.9	0.07	1.82
120	23	C	3	1	3	7.5	52.0	0.09	2.18
120	40	A	3	1	1	6.3	43.4	0.08	2.00
120	40	A	3	1	2	6.7	46.3	0.08	2.01
120	40	A	3	1	3	6.1	42.3	0.09	2.20
120	40	B	3	1	1	6.8	46.8	0.05	1.32
120	40	B	3	1	2	7.1	48.8	0.06	1.46
120	40	B	3	1	3	7.3	50.0	0.06	1.57
120	40	C	3	1	1	6.8	46.7	0.08	2.05
120	40	C	3	1	2	6.8	47.1	0.08	2.05
120	40	C	3	1	3	8.5	58.8	0.11	2.70
120	60	A	3	1	1	6.6	45.7	0.08	2.06
120	60	A	3	1	2	6.6	45.6	0.08	1.98
120	60	A	3	1	3	6.1	42.3	0.09	2.21
120	60	B	3	1	1	7.4	51.1	0.06	1.47
120	60	B	3	1	2	7.3	50.5	0.06	1.42
120	60	B	3	1	3	6.7	46.4	0.05	1.19
120	60	C	3	1	1	7.4	50.9	0.07	1.88
120	60	C	3	1	2	6.9	47.5	0.06	1.54
120	60	C	3	1	3	7.6	52.4	0.09	2.28
210	23	A	3	1	1	6.2	42.6	0.08	1.91
210	23	A	3	1	2	6.4	44.2	0.09	2.25
210	23	B	3	1	1	6.0	41.6	0.04	1.10
210	23	B	3	1	2	6.7	45.9	0.06	1.42
210	23	B	3	1	3	7.0	48.0	0.06	1.59
210	23	C	3	1	1	7.0	48.3	0.08	2.11
210	23	C	3	1	2	6.5	44.7	0.09	2.22
210	23	C	3	1	3	6.5	44.7	0.08	2.14
210	40	A	3	1	1	6.1	41.9	0.09	2.17
210	40	A	3	1	2	6.5	45.1	0.10	2.45
210	40	A	3	1	3	6.4	43.9	0.08	1.92
210	40	B	3	1	1	7.1	48.8	0.06	1.60
210	40	B	3	1	2	7.1	49.1	0.05	1.33
210	40	B	3	1	3	6.2	43.1	0.05	1.32

Continued on next page ...

Table D.5: Horizontal shear test results (ultimate values) for each individual specimen

Exposure		Specimen				Horizontal		Displacement	
Age	T	Manuf.	Size	Lot	Spec.	Shear Strength		at Shear Strength	
d	°C	Type	#	No.	No.	ksi	MPa	in.	mm
210	40	C	3	1	1	7.2	49.9	0.10	2.57
210	40	C	3	1	2	6.8	46.6	0.07	1.87
210	40	C	3	1	3	6.8	47.0	0.08	2.10
210	60	A	3	1	1	6.8	46.8	0.10	2.51
210	60	A	3	1	2	6.7	46.2	0.08	2.15
210	60	A	3	1	3	6.7	46.0	0.11	2.76
210	60	B	3	1	1	6.6	45.8	0.05	1.22
210	60	B	3	1	2	5.9	40.5	0.05	1.30
210	60	B	3	1	3	6.4	43.9	0.05	1.31
210	60	C	3	1	1	6.8	46.7	0.08	2.03
210	60	C	3	1	2	7.2	49.6	0.08	2.00
210	60	C	3	1	3	6.9	47.3	0.08	1.97
365	23	A	3	1	1	6.0	41.6	0.09	2.21
365	23	A	3	1	2	6.8	47.1	0.09	2.32
365	23	A	3	1	3	5.9	40.8	0.09	2.20
365	23	B	3	1	1	7.8	53.5	0.07	1.82
365	23	B	3	1	2	7.0	48.0	0.06	1.53
365	23	B	3	1	3	6.6	45.7	0.06	1.49
365	23	C	3	1	1	6.6	45.7	0.08	1.96
365	23	C	3	1	2	6.7	46.1	0.08	2.13
365	23	C	3	1	3	6.8	46.9	0.08	2.02
365	40	A	3	1	1	6.5	44.6	0.11	2.81
365	40	A	3	1	2	6.8	47.1	0.08	2.02
365	40	A	3	1	3	6.4	44.4	0.10	2.44
365	40	B	3	1	1	6.2	42.6	0.05	1.26
365	40	B	3	1	2	6.5	45.0	0.08	1.94
365	40	B	3	1	3	7.3	50.3	0.06	1.42
365	40	C	3	1	1	6.4	44.2	0.08	1.97
365	40	C	3	1	2	7.3	50.6	0.09	2.25
365	40	C	3	1	3	7.1	48.6	0.09	2.25
365	60	A	3	1	1	6.7	46.3	0.08	1.99
365	60	A	3	1	2	5.9	40.8	0.08	1.99
365	60	A	3	1	3	6.8	46.6	0.08	2.03
365	60	B	3	1	1	5.4	37.4	0.05	1.20
365	60	B	3	1	2	5.5	37.8	0.04	0.95
365	60	B	3	1	3	4.0	27.7	0.04	1.13
365	60	C	3	1	1	6.5	44.9	0.06	1.61
365	60	C	3	1	2	6.5	44.5	0.07	1.77
365	60	C	3	1	3	8.4	58.1	0.10	2.50

Based on the strength values presented in the previous table, statistical values were determined, which are presented in Table D.6. Each row represents the data for a complete data set of numerous specimens (control and test groups).

Table D.6: Horizontal shear test statistical values for each sample group

Exposure		Sample Group			Statistical Values								
Age d	T °C	Manuf. Type	Size #	Lot No.	Imperial				Metric				CV %
					$\wedge$ ksi	$\vee$ ksi	$\mu$ ksi	$\sigma$ ksi	$\wedge$ MPa	$\vee$ MPa	$\mu$ MPa	$\sigma$ MPa	
000	23	A	3	1	6.50	6.92	6.66	0.2	45	48	46	1.5	3.37
000	23	A	3	2	5.30	6.34	5.92	0.5	37	44	41	3.8	9.25
000	23	A	3	3	5.97	6.91	6.29	0.5	41	48	43	3.7	8.63
000	23	B	3	1	6.08	6.27	6.16	0.1	42	43	42	0.7	1.66
000	23	B	3	2	6.08	6.85	6.44	0.4	42	47	44	2.7	6.01
000	23	B	3	3	6.45	6.86	6.66	0.3	44	47	46	2.0	4.35
000	23	C	3	1	6.87	7.29	7.03	0.2	47	50	48	1.6	3.25
000	23	C	3	2	7.35	7.98	7.64	0.3	51	55	53	2.2	4.17
000	23	C	3	3	7.29	8.26	7.65	0.5	50	57	53	3.7	7.00
000	23	A	5	1	5.58	6.36	5.99	0.4	38	44	41	2.7	6.53
000	23	A	5	2	5.64	6.16	5.88	0.3	39	42	41	1.8	4.42
000	23	A	5	3	6.02	6.73	6.44	0.4	42	46	44	2.5	5.73
000	23	B	5	1	5.93	6.27	6.09	0.2	41	43	42	1.2	2.87
000	23	B	5	2	5.85	6.21	6.06	0.2	40	43	42	1.3	3.03
000	23	B	5	3	5.67	5.86	5.78	0.1	39	40	40	0.7	1.77
000	23	C	5	1	6.82	7.37	7.14	0.3	47	51	49	1.9	3.94
000	23	C	5	2	7.03	7.84	7.47	0.4	48	54	51	2.8	5.42
000	23	C	5	3	6.85	7.73	7.37	0.5	47	53	51	3.1	6.17
000	23	C	6	1	6.30	6.97	6.73	0.4	43	48	46	2.6	5.57
000	23	C	6	2	5.94	6.58	6.35	0.4	41	45	44	2.5	5.61
000	23	C	6	3	6.05	6.50	6.20	0.3	42	45	43	1.8	4.23
000	23	A	8	1	6.17	6.33	6.27	0.1	43	44	43	0.6	1.35
000	23	A	8	2	4.58	6.20	5.64	0.9	32	43	39	6.4	16.39
000	23	A	8	3	6.29	6.70	6.52	0.2	43	46	45	1.5	3.23
000	23	B	8	1	5.38	6.05	5.65	0.3	37	42	39	2.4	6.20
000	23	B	8	2	5.53	6.56	6.08	0.5	38	45	42	3.6	8.56
000	23	B	8	3	3.74	5.91	5.15	1.2	26	41	36	8.4	23.75
060	23	A	3	1	6.42	6.69	6.55	0.1	44	46	45	1.0	2.13
060	23	B	3	1	5.44	7.31	6.46	0.9	38	50	45	6.5	14.66
060	23	C	3	1	6.68	6.95	6.85	0.1	46	48	47	1.0	2.13
060	40	A	3	1	6.09	6.37	6.24	0.1	42	44	43	1.0	2.27
060	40	B	3	1	6.62	7.24	6.98	0.3	46	50	48	2.2	4.55
060	40	C	3	1	6.62	7.07	6.85	0.2	46	49	47	1.5	3.27
060	60	A	3	1	6.30	6.53	6.45	0.1	43	45	44	0.9	2.07
060	60	B	3	1	5.57	7.40	6.54	0.9	38	51	45	6.3	14.07
060	60	C	3	1	6.70	7.23	6.88	0.3	46	50	47	2.1	4.41
120	23	A	3	1	6.52	7.25	6.95	0.4	45	50	48	2.6	5.52
120	23	B	3	1	6.50	7.52	7.00	0.5	45	52	48	3.5	7.28
120	23	C	3	1	6.52	7.55	6.87	0.6	45	52	47	4.0	8.48
120	40	A	3	1	6.13	6.71	6.38	0.3	42	46	44	2.0	4.66
120	40	B	3	1	6.78	7.26	7.04	0.2	47	50	49	1.7	3.43
120	40	C	3	1	6.77	8.52	7.38	1.0	47	59	51	6.9	13.47
120	60	A	3	1	6.13	6.63	6.46	0.3	42	46	45	2.0	4.39
120	60	B	3	1	6.73	7.41	7.15	0.4	46	51	49	2.6	5.18
120	60	C	3	1	6.89	7.60	7.29	0.4	48	52	50	2.5	4.99
210	23	A	3	1	6.17	6.41	6.29	0.2	43	44	43	1.2	2.68
210	23	B	3	1	6.03	6.96	6.55	0.5	42	48	45	3.2	7.18
210	23	C	3	1	6.48	7.01	6.66	0.3	45	48	46	2.1	4.55
210	40	A	3	1	6.08	6.54	6.33	0.2	42	45	44	1.6	3.73
210	40	B	3	1	6.25	7.13	6.82	0.5	43	49	47	3.4	7.23
210	40	C	3	1	6.76	7.23	6.93	0.3	47	50	48	1.8	3.74

Continued on next page ...

Table D.6: Horizontal shear test statistical values for each sample group

Exposure		Sample Group			Statistical Values								
Age d	T °C	Manuf. Type	Size #	Lot No.	Imperial				Metric				
					$\wedge$ ksi	$\vee$ ksi	$\mu$ ksi	$\sigma$ ksi	$\wedge$ MPa	$\vee$ MPa	$\mu$ MPa	$\sigma$ MPa	CV %
210	60	A	3	1	6.67	6.79	6.72	0.1	46	47	46	0.4	0.89
210	60	B	3	1	5.87	6.64	6.29	0.4	40	46	43	2.7	6.24
210	60	C	3	1	6.77	7.19	6.94	0.2	47	50	48	1.5	3.17
365	23	A	3	1	5.92	6.84	6.26	0.5	41	47	43	3.4	7.95
365	23	B	3	1	6.63	7.76	7.12	0.6	46	54	49	4.0	8.18
365	23	C	3	1	6.62	6.80	6.70	0.1	46	47	46	0.6	1.32
365	40	A	3	1	6.44	6.84	6.58	0.2	44	47	45	1.5	3.40
365	40	B	3	1	6.18	7.30	6.67	0.6	43	50	46	3.9	8.54
365	40	C	3	1	6.41	7.34	6.93	0.5	44	51	48	3.3	6.92
365	60	A	3	1	5.92	6.77	6.47	0.5	41	47	45	3.3	7.35
365	60	B	3	1	4.01	5.49	4.97	0.8	28	38	34	5.7	16.72
365	60	C	3	1	6.46	8.42	7.13	1.1	45	58	49	7.7	15.73

## D.5 Tensile Test

The longitudinal tensile properties for all tested specimens are listed in Table D.7. Specifically, the table presents the maximum tensile stresses and the corresponding elastic moduli, both based on the nominal cross-sectional dimensions. For a few specimens, the extensometer that measured the surface strain for elastic modulus calculations slipped on the rebar surface such that a true elastic modulus could not be determined. The following Table D.7 identifies these specimens through a “NA” in the last two columns.

Table D.7: Tensile strength test results (ultimate values) for each individual specimen

Exposure		Specimen				Tensile		Elastic	
Age d	T °C	Manuf. Type	Size #	Lot No.	Spec. No.	Strength		Modulus	
						ksi	MPa	ksi	GPa
000	23	A	3	1	1	148.8	1025.7	7704	53.12
000	23	A	3	1	2	146.6	1011.0	7850	54.13
000	23	A	3	1	3	146.8	1012.4	7908	54.52
000	23	A	3	3	1	139.3	960.1	7361	50.75
000	23	A	3	3	2	130.0	896.3	6923	47.73
000	23	A	3	3	3	136.7	942.7	7307	50.38
000	23	B	3	1	1	123.2	849.3	8904	61.39
000	23	B	3	1	2	117.8	812.4	8852	61.03
000	23	B	3	1	3	124.1	855.5	9284	64.01
000	23	B	3	3	1	109.4	754.4	NA	NA
000	23	B	3	3	2	110.9	764.3	NA	NA
000	23	B	3	3	3	124.8	860.2	8735	60.23
000	23	C	3	1	1	154.1	1062.6	8534	58.84
000	23	C	3	1	2	146.4	1009.7	8649	59.63
000	23	C	3	1	3	148.4	1023.2	8396	57.89
000	23	C	3	3	1	140.2	966.4	NA	NA

Continued on next page ...



Table D.7: Tensile strength test results (ultimate values) for each individual specimen

Exposure		Specimen				Tensile		Elastic	
Age	T	Manuf.	Size	Lot	Spec.	Strength		Modulus	
d	°C	Type	#	No.	No.	ksi	MPa	ksi	GPa
000	23	C	3	3	2	142.0	979.1	NA	NA
000	23	C	3	3	3	138.8	957.3	NA	NA
000	23	A	5	1	1	135.2	932.3	8118	55.97
000	23	A	5	1	2	134.7	928.9	8186	56.44
000	23	A	5	1	3	136.4	940.6	8074	55.67
000	23	A	5	3	1	132.6	913.9	7146	49.27
000	23	A	5	3	2	129.6	893.5	7698	53.08
000	23	A	5	3	3	132.9	916.2	7720	53.23
000	23	B	5	1	1	134.7	929.0	8559	59.01
000	23	B	5	1	2	136.7	942.8	8733	60.21
000	23	B	5	2	1	149.7	1031.9	27	0.18
000	23	B	5	2	2	136.5	941.1	8514	58.70
000	23	B	5	2	3	127.6	879.9	8059	55.57
000	23	B	5	3	1	134.7	929.0	8559	59.01
000	23	B	5	3	2	136.7	942.8	8733	60.21
000	23	C	5	1	1	117.9	813.0	6855	47.26
000	23	C	5	1	2	114.3	788.3	6858	47.29
000	23	C	5	1	3	115.9	798.9	759	5.23
000	23	C	5	3	1	107.3	740.0	6643	45.80
000	23	C	5	3	2	111.7	770.4	5663	39.04
000	23	C	5	3	3	106.6	734.9	6872	47.38
000	23	C	6	1	1	123.3	850.4	7032	48.48
000	23	C	6	1	3	121.9	840.2	11 412	78.68
000	23	C	6	3	1	118.9	819.5	7209	49.70
000	23	C	6	3	2	121.9	840.3	7148	49.28
000	23	C	6	3	3	122.3	843.1	7249	49.98
000	23	A	8	1	1	114.1	786.4	7731	53.30
000	23	A	8	1	2	112.0	772.5	7752	53.45
000	23	A	8	1	3	108.2	745.9	7931	54.68
000	23	B	8	1	1	129.9	895.6	8396	57.89
000	23	B	8	1	2	122.2	842.4	8334	57.46
000	23	B	8	1	3	123.0	848.0	8840	60.95
000	23	B	8	2	1	124.0	855.1	7813	53.87
000	23	B	8	2	2	125.9	867.8	8344	57.53
000	23	B	8	2	3	117.0	806.9	8411	57.99
060	23	A	3	1	2	137.1	945.6	7357	50.72
060	23	A	3	1	3	137.4	947.1	8025	55.33
060	23	B	3	1	1	151.5	1044.7	8112	55.93
060	23	B	3	1	2	125.5	865.3	9466	65.27
060	23	B	3	1	3	128.3	884.4	9022	62.21
060	23	C	3	1	1	146.8	1012.0	3934	27.13
060	23	C	3	1	2	143.7	990.5	7927	54.66
060	23	C	3	1	3	145.9	1006.0	7560	52.13
060	40	A	3	1	1	161.4	1112.9	7771	53.58
060	40	A	3	1	2	140.9	971.6	7643	52.70
060	40	A	3	1	3	137.5	947.7	7815	53.88
060	40	B	3	1	1	117.1	807.5	9116	62.85
060	40	B	3	1	2	123.2	849.4	8798	60.66
060	40	B	3	1	3	123.5	851.2	13 965	96.29
060	40	C	3	1	1	142.5	982.4	8114	55.94
060	40	C	3	1	2	140.8	970.7	7847	54.10
060	40	C	3	1	3	148.6	1024.3	7806	53.82

Continued on next page ...

Table D.7: Tensile strength test results (ultimate values) for each individual specimen

Exposure		Specimen				Tensile		Elastic	
Age	T	Manuf.	Size	Lot	Spec.	Strength		Modulus	
d	°C	Type	#	No.	No.	ksi	MPa	ksi	GPa
060	60	A	3	1	1	96.3	663.8	7801	53.78
060	60	A	3	1	2	95.8	660.3	7982	55.03
060	60	A	3	1	3	99.0	682.6	7837	54.04
060	60	B	3	1	1	109.1	752.3	8930	61.57
060	60	B	3	1	2	106.5	734.0	8865	61.12
060	60	B	3	1	3	106.9	737.3	8997	62.03
060	60	C	3	1	1	136.8	943.4	8085	55.75
060	60	C	3	1	2	140.6	969.3	8239	56.81
060	60	C	3	1	3	137.0	944.8	8027	55.34
120	23	A	3	1	1	136.8	943.4	329	2.27
120	23	A	3	1	2	130.8	902.1	7490	51.64
120	23	A	3	1	3	139.5	961.7	7563	52.14
120	23	B	3	1	1	119.7	825.0	8571	59.09
120	23	B	3	1	2	120.1	828.0	8910	61.43
120	23	B	3	1	3	119.5	823.7	8804	60.70
120	23	C	3	1	1	142.6	983.0	7942	54.76
120	23	C	3	1	2	143.3	988.2	7908	54.52
120	23	C	3	1	3	145.2	1000.9	8223	56.70
120	60	A	3	1	1	98.8	680.9	7560	52.13
120	60	A	3	1	2	77.0	531.0	7703	53.11
120	60	A	3	1	3	74.1	510.7	7640	52.68
120	60	B	3	1	1	174.8	1205.1	8813	60.76
120	60	B	3	1	2	115.8	798.4	9021	62.20
120	60	B	3	1	3	115.2	794.0	8836	60.92
120	60	C	3	1	1	108.7	749.2	9058	62.45
120	60	C	3	1	2	123.0	848.4	7587	52.31
120	60	C	3	1	3	132.9	916.2	7549	52.05
210	23	A	3	1	1	134.7	928.5	7559	52.12
210	23	A	3	1	2	131.5	906.4	7630	52.61
210	23	A	3	1	3	125.3	864.1	7391	50.96
210	23	B	3	1	1	114.4	788.4	8058	55.56
210	23	B	3	1	2	111.8	771.0	7908	54.53
210	23	B	3	1	3	112.0	772.4	8004	55.18
210	23	C	3	1	1	142.1	979.5	7678	52.94
210	23	C	3	1	2	137.2	945.7	7670	52.88
210	23	C	3	1	3	139.6	962.8	7607	52.45
210	40	A	3	1	1	124.7	859.8	6984	48.15
210	40	A	3	1	2	123.8	853.9	7266	50.10
210	40	A	3	1	3	123.1	848.7	7169	49.43
210	40	B	3	1	1	117.4	809.7	8811	60.75
210	40	B	3	1	2	121.4	837.1	8465	58.37
210	40	B	3	1	3	114.0	786.1	8504	58.63
210	40	C	3	1	1	131.9	909.3	7535	51.95
210	40	C	3	1	2	139.5	961.6	7399	51.01
210	40	C	3	1	3	142.7	983.5	7487	51.62
210	60	A	3	1	1	87.5	603.2	7295	50.30
210	60	A	3	1	2	80.4	554.4	7495	51.68
210	60	A	3	1	3	88.6	610.7	7252	50.00
210	60	B	3	1	1	100.6	693.7	8304	57.25
210	60	B	3	1	2	88.6	610.8	9042	62.34
210	60	B	3	1	3	89.2	615.1	8098	55.84
210	60	C	3	1	1	113.2	780.5	7572	52.21

Continued on next page ...

Table D.7: Tensile strength test results (ultimate values) for each individual specimen

Exposure		Specimen				Tensile		Elastic	
Age	T	Manuf.	Size	Lot	Spec.	Strength		Modulus	
d	°C	Type	#	No.	No.	ksi	MPa	ksi	GPa
210	60	C	3	1	2	116.8	805.3	7436	51.27
210	60	C	3	1	3	107.2	739.2	7596	52.37
365	23	A	3	1	1	126.2	870.2	6615	45.61
365	23	A	3	1	2	128.2	884.2	991	6.84
365	23	A	3	1	3	128.5	886.2	1018	7.02
365	23	B	3	1	1	119.1	820.8	8421	58.06
365	23	B	3	1	2	109.8	756.9	8411	57.99
365	23	B	3	1	3	121.5	837.4	8639	59.57
365	23	C	3	1	1	136.6	941.5	7634	52.64
365	23	C	3	1	2	143.0	986.2	5291	36.48
365	23	C	3	1	3	133.9	923.4	7544	52.02
365	40	A	3	1	1	110.7	763.4	6964	48.02
365	40	A	3	1	2	105.7	728.5	6980	48.13
365	40	A	3	1	3	111.9	771.5	7582	52.28
365	40	B	3	1	1	107.5	741.0	6670	45.99
365	40	B	3	1	2	114.7	790.7	8409	57.98
365	40	B	3	1	3	111.9	771.4	7945	54.78
365	40	C	3	1	1	135.7	935.6	7613	52.49
365	40	C	3	1	2	136.5	940.8	7554	52.09
365	40	C	3	1	3	131.8	908.5	7559	52.12
365	60	A	3	1	1	102.8	709.0	7011	48.34
365	60	A	3	1	2	87.6	604.0	7315	50.43
365	60	A	3	1	3	93.7	646.3	7263	50.08
365	60	B	3	1	1	104.9	723.3	8185	56.44
365	60	B	3	1	2	102.5	707.0	8080	55.71
365	60	B	3	1	3	101.7	701.5	8106	55.89
365	60	C	3	1	1	123.8	853.5	5656	38.99
365	60	C	3	1	2	124.6	858.8	7146	49.27
365	60	C	3	1	3	130.1	897.0	7651	52.75

The statistically reduced tensile property data is shown in Table D.8 for both the tensile strength and the elastic modulus. For clarity, this table lists all data in imperial units only. Each row is representative of one data set (control or test group) and lists the minimum, the maximum, the mean, the standard deviation, and the coefficient for both properties.

Table D.8: Tensile strength test statistical values for each sample group (Imperial Units)

Exposure		Sample Group			Statistical Values									
Age	T	Manuf.	Size	Lot	Tensile Strength					Elastic Modulus				
					∧	∨	μ	σ	CV	∧	∨	μ	σ	CV
d	°C	Type	#	No.	ksi	ksi	ksi	ksi	%	ksi	ksi	ksi	ksi	%
000	23	A	3	1	146.6	148.8	147.4	1.2	0.80	7704	7908	7821	105	1.3
000	23	A	3	3	130.0	139.3	135.3	4.8	3.53	6923	7361	7197	239	3.3
000	23	B	3	1	117.8	124.1	121.7	3.4	2.78	8852	9284	9013	236	2.6
000	23	B	3	3	109.4	124.8	115.0	8.5	7.37	NA	NA	NA	NA	NA
000	23	C	3	1	146.4	154.1	149.7	4.0	2.66	8396	8649	8526	126	1.5

Continued on next page ...

Table D.8: Tensile strength test statistical values for each sample group (Imperial Units)

Exposure		Sample Group			Statistical Values									
Age d	T °C	Manuf. Type	Size #	Lot No.	Tensile Strength					Elastic Modulus				
					$\wedge$ ksi	$\vee$ ksi	$\mu$ ksi	$\sigma$ ksi	CV %	$\wedge$ ksi	$\vee$ ksi	$\mu$ ksi	$\sigma$ ksi	CV %
000	23	C	3	3	138.8	142.0	140.3	1.6	1.14	NA	NA	NA	NA	NA
000	23	A	5	1	134.7	136.4	135.5	0.9	0.64	8074	8186	8126	57	0.7
000	23	A	5	3	129.6	132.9	131.7	1.8	1.38	7146	7720	7521	325	4.3
000	23	B	5	1	134.7	136.7	135.7	1.4	1.04	8559	8733	8646	123	1.4
000	23	B	5	2	127.6	149.7	137.9	11.1	8.04	27	8514	5533	4774	86.3
000	23	B	5	3	134.7	136.7	135.7	1.4	1.04	8559	8733	8646	123	1.4
000	23	C	5	1	114.3	117.9	116.0	1.8	1.55	759	6858	4824	3520	73.0
000	23	C	5	3	106.6	111.7	108.6	2.8	2.57	5663	6872	6392	642	10.0
000	23	C	6	1	121.9	123.3	122.6	1.1	0.86	7032	11412	9222	3097	33.6
000	23	C	6	3	118.9	122.3	121.0	1.9	1.55	7148	7249	7202	51	0.7
000	23	A	8	1	108.2	114.1	111.4	3.0	2.67	7731	7931	7805	110	1.4
000	23	B	8	1	122.2	129.9	125.0	4.2	3.39	8334	8840	8523	276	3.2
000	23	B	8	2	117.0	125.9	122.3	4.7	3.81	7813	8411	8189	327	4.0
060	23	A	3	1	137.1	137.4	137.3	0.2	0.11	7357	8025	7691	472	6.1
060	23	B	3	1	125.5	151.5	135.1	14.3	10.58	8112	9466	8867	690	7.8
060	23	C	3	1	143.7	146.8	145.4	1.6	1.11	3934	7927	6474	2207	34.1
060	40	A	3	1	137.5	161.4	146.6	12.9	8.83	7643	7815	7743	89	1.2
060	40	B	3	1	117.1	123.5	121.3	3.6	2.96	8798	13965	10626	2896	27.3
060	40	C	3	1	140.8	148.6	143.9	4.1	2.84	7806	8114	7922	167	2.1
060	60	A	3	1	95.8	99.0	97.0	1.7	1.79	7801	7982	7873	96	1.2
060	60	B	3	1	106.5	109.1	107.5	1.4	1.32	8865	8997	8931	66	0.7
060	60	C	3	1	136.8	140.6	138.1	2.1	1.53	8027	8239	8117	110	1.4
120	23	A	3	1	130.8	139.5	135.7	4.4	3.27	329	7563	5127	4156	81.1
120	23	B	3	1	119.5	120.1	119.7	0.3	0.27	8571	8910	8762	174	2.0
120	23	C	3	1	142.6	145.2	143.7	1.3	0.93	7908	8223	8024	173	2.2
120	60	A	3	1	74.1	98.8	83.3	13.5	16.19	7560	7703	7635	72	0.9
120	60	B	3	1	115.2	174.8	135.2	34.2	25.32	8813	9021	8890	114	1.3
120	60	C	3	1	108.7	132.9	121.5	12.2	10.02	7549	9058	8065	860	10.7
210	23	A	3	1	125.3	134.7	130.5	4.7	3.64	7391	7630	7527	122	1.6
210	23	B	3	1	111.8	114.4	112.7	1.4	1.25	7908	8058	7990	76	0.9
210	23	C	3	1	137.2	142.1	139.6	2.5	1.76	7607	7678	7652	39	0.5
210	40	A	3	1	123.1	124.7	123.9	0.8	0.65	6984	7266	7140	143	2.0
210	40	B	3	1	114.0	121.4	117.6	3.7	3.14	8465	8811	8593	190	2.2
210	40	C	3	1	131.9	142.7	138.0	5.5	4.01	7399	7535	7474	69	0.9
210	60	A	3	1	80.4	88.6	85.5	4.4	5.19	7252	7495	7348	130	1.8
210	60	B	3	1	88.6	100.6	92.8	6.8	7.30	8098	9042	8481	496	5.9
210	60	C	3	1	107.2	116.8	112.4	4.8	4.31	7436	7596	7534	86	1.1
365	23	A	3	1	126.2	128.5	127.7	1.3	0.99	991	6615	2875	3239	112.7
365	23	B	3	1	109.8	121.5	116.8	6.2	5.28	8411	8639	8490	129	1.5
365	23	C	3	1	133.9	143.0	137.8	4.7	3.40	5291	7634	6823	1328	19.5
365	40	A	3	1	105.7	111.9	109.4	3.3	3.03	6964	7582	7176	352	4.9
365	40	B	3	1	107.5	114.7	111.3	3.6	3.26	6670	8409	7675	901	11.7
365	40	C	3	1	131.8	136.5	134.6	2.5	1.87	7554	7613	7575	32	0.4
365	60	A	3	1	87.6	102.8	94.7	7.7	8.09	7011	7315	7196	163	2.3
365	60	B	3	1	101.7	104.9	103.1	1.6	1.60	8080	8185	8124	55	0.7
365	60	C	3	1	123.8	130.1	126.1	3.4	2.73	5656	7651	6817	1037	15.2

Similar to the table above, the following Table D.9 presents statistical results for the tensile properties of all relevant data sets. However, this table lists all values in metric units.

Table D.9: Tensile strength test statistical values for each sample group (Metric Units)

Exposure		Sample Group			Statistical Values									
Age d	T °C	Manuf. Type	Size #	Lot No.	Tensile Strength					Elastic Modulus				
					$\wedge$ MPa	$\vee$ MPa	$\mu$ MPa	$\sigma$ MPa	CV %	$\wedge$ GPa	$\vee$ GPa	$\mu$ GPa	$\sigma$ GPa	CV %
000	23	A	3	1	1011	1026	1016	8.1	0.80	53.12	54.52	53.92	0.72	1.34
000	23	A	3	3	896	960	933	33.0	3.53	47.73	50.75	49.62	1.65	3.32
000	23	B	3	1	812	855	839	23.3	2.78	61.03	64.01	62.15	1.63	2.62
000	23	B	3	3	754	860	793	58.4	7.37	NA	NA	NA	NA	NA
000	23	C	3	1	1010	1063	1032	27.5	2.66	57.89	59.63	58.79	0.87	1.48
000	23	C	3	3	957	979	968	11.0	1.14	NA	NA	NA	NA	NA
000	23	A	5	1	929	941	934	6.0	0.64	55.67	56.44	56.03	0.39	0.70
000	23	A	5	3	893	916	908	12.5	1.38	49.27	53.23	51.86	2.24	4.33
000	23	B	5	1	929	943	936	9.7	1.04	59.01	60.21	59.61	0.85	1.42
000	23	B	5	2	880	1032	951	76.5	8.04	0.18	58.70	38.15	32.92	86.28
000	23	B	5	3	929	943	936	9.7	1.04	59.01	60.21	59.61	0.85	1.42
000	23	C	5	1	788	813	800	12.4	1.55	5.23	47.29	33.26	24.27	72.97
000	23	C	5	3	735	770	748	19.2	2.57	39.04	47.38	44.07	4.43	10.04
000	23	C	6	1	840	850	845	7.2	0.86	48.48	78.68	63.58	21.35	33.58
000	23	C	6	3	820	843	834	12.9	1.55	49.28	49.98	49.66	0.35	0.71
000	23	A	8	1	746	786	768	20.5	2.67	53.30	54.68	53.81	0.76	1.41
000	23	B	8	1	842	896	862	29.2	3.39	57.46	60.95	58.77	1.91	3.24
000	23	B	8	2	807	868	843	32.1	3.81	53.87	57.99	56.46	2.26	4.00
060	23	A	3	1	946	947	946	1.1	0.11	50.72	55.33	53.03	3.26	6.14
060	23	B	3	1	865	1045	931	98.5	10.58	55.93	65.27	61.13	4.76	7.79
060	23	C	3	1	990	1012	1003	11.1	1.11	27.13	54.66	44.64	15.22	34.09
060	40	A	3	1	948	1113	1011	89.3	8.83	52.70	53.88	53.38	0.61	1.15
060	40	B	3	1	807	851	836	24.8	2.96	60.66	96.29	73.27	19.97	27.25
060	40	C	3	1	971	1024	992	28.2	2.84	53.82	55.94	54.62	1.15	2.11
060	60	A	3	1	660	683	669	12.0	1.79	53.78	55.03	54.28	0.66	1.22
060	60	B	3	1	734	752	741	9.8	1.32	61.12	62.03	61.58	0.45	0.74
060	60	C	3	1	943	969	952	14.6	1.53	55.34	56.81	55.97	0.76	1.35
120	23	A	3	1	902	962	936	30.6	3.27	2.27	52.14	35.35	28.65	81.05
120	23	B	3	1	824	828	826	2.2	0.27	59.09	61.43	60.41	1.20	1.98
120	23	C	3	1	983	1001	991	9.2	0.93	54.52	56.70	55.33	1.19	2.15
120	60	A	3	1	511	681	574	93.0	16.19	52.13	53.11	52.64	0.49	0.94
120	60	B	3	1	794	1205	933	236.1	25.32	60.76	62.20	61.29	0.79	1.28
120	60	C	3	1	749	916	838	84.0	10.02	52.05	62.45	55.60	5.93	10.67
210	23	A	3	1	864	929	900	32.7	3.64	50.96	52.61	51.89	0.84	1.63
210	23	B	3	1	771	788	777	9.7	1.25	54.53	55.56	55.09	0.52	0.95
210	23	C	3	1	946	979	963	16.9	1.76	52.45	52.94	52.76	0.27	0.51
210	40	A	3	1	849	860	854	5.6	0.65	48.15	50.10	49.23	0.99	2.01
210	40	B	3	1	786	837	811	25.5	3.14	58.37	60.75	59.25	1.31	2.21
210	40	C	3	1	909	984	951	38.2	4.01	51.01	51.95	51.53	0.47	0.92
210	60	A	3	1	554	611	589	30.6	5.19	50.00	51.68	50.66	0.90	1.77
210	60	B	3	1	611	694	640	46.7	7.30	55.84	62.34	58.48	3.42	5.85
210	60	C	3	1	739	805	775	33.4	4.31	51.27	52.37	51.95	0.59	1.15
365	23	A	3	1	870	886	880	8.7	0.99	6.84	45.61	19.82	22.33	112.67
365	23	B	3	1	757	837	805	42.5	5.28	57.99	59.57	58.54	0.89	1.52
365	23	C	3	1	923	986	950	32.4	3.40	36.48	52.64	47.05	9.15	19.46
365	40	A	3	1	728	772	754	22.9	3.03	48.02	52.28	49.47	2.43	4.91
365	40	B	3	1	741	791	768	25.1	3.26	45.99	57.98	52.92	6.21	11.73
365	40	C	3	1	909	941	928	17.3	1.87	52.09	52.49	52.23	0.22	0.43
365	60	A	3	1	604	709	653	52.9	8.09	48.34	50.43	49.62	1.12	2.26
365	60	B	3	1	702	723	711	11.4	1.60	55.71	56.44	56.01	0.38	0.68
365	60	C	3	1	854	897	870	23.7	2.73	38.99	52.75	47.00	7.15	15.22

## D.6 Bond-to-Concrete Test

The individual measured bond strength test results are shown in the following Table D.10 to report both the bond stresses and the rebar bond slippage for each specimen. Because ACI 440.3R suggests to document the slippage behavior through bond stress measurements at specific rebar slip instances, the table presents not just the ultimate bond stress (strength) but also the bond stresses that corresponded to a slip value of  $\frac{2}{1000}$  in.,  $\frac{4}{1000}$  in., and  $\frac{1}{100}$  in. For clarity, the table lists all results in imperial units only.

Table D.10: Bond-to-Concrete strength test results for each individual specimen (Imperial Units)

Exposure		Specimen				Bond Stress				Bond Slippage	
Age d	T °C	Manuf. Type	Size #	Lot Lot	Spec. No.	at Specific Slippage			Ult. ksi	at Maximum Stress	
						$\frac{2}{1000}$ in. ksi	$\frac{4}{1000}$ in. ksi	$\frac{1}{100}$ in. ksi		Free End in.	Load End in.
000	23	A	3	1	1	2.07	2.36	2.56	2.58	0.013	-0.013
000	23	A	3	1	2	2.51	2.78	2.84	2.85	0.008	0.066
000	23	A	3	1	3	2.43	2.62	2.69	2.69	0.010	0.059
000	23	B	3	1	1	0.40	0.51	0.75	2.08	0.182	0.234
000	23	B	3	1	2	0.28	0.39	0.55	1.74	0.237	0.269
000	23	B	3	1	3	0.55	0.74	1.05	1.75	0.280	0.316
000	23	C	3	1	1	0.95	1.74	2.59	3.03	0.023	0.082
000	23	C	3	1	2	1.70	2.10	2.62	2.99	0.022	0.102
000	23	C	3	1	3	1.37	1.86	2.61	3.22	0.028	0.093
060	23	A	3	1	1	1.22	1.43	1.69	1.83	0.038	0.105
060	23	A	3	1	3	2.50	2.69	2.86	2.87	0.014	0.003
060	23	B	3	1	1	0.84	1.02	1.37	2.44	0.263	0.366
060	23	B	3	1	2	0.49	0.87	1.45	2.59	0.239	0.361
060	23	B	3	1	3	0.31	0.40	0.61	1.62	0.214	0.311
060	23	C	3	1	1	1.50	1.87	2.30	2.45	0.019	0.018
060	23	C	3	1	3	1.02	1.43	1.93	2.31	0.029	0.128
060	40	A	3	1	1	2.18	2.50	2.57	2.73	0.016	0.088
060	40	A	3	1	2	2.34	2.47	2.58	2.58	0.012	0.105
060	40	A	3	1	3	2.56	2.76	2.87	2.87	0.009	0.102
060	40	B	3	1	1	1.03	1.25	1.67	2.49	0.119	0.214
060	40	B	3	1	2	0.55	0.83	1.32	2.43	0.256	0.366
060	40	B	3	1	3	0.74	0.94	1.38	2.46	0.284	0.391
060	40	C	3	1	1	0.72	1.08	1.73	2.76	0.032	0.150
060	40	C	3	1	2	1.10	1.52	2.14	2.77	0.028	0.134
060	40	C	3	1	3	1.31	1.96	2.66	2.99	0.021	0.132
060	60	A	3	1	1	2.30	2.56	2.30	2.62	0.007	0.117
060	60	A	3	1	2	0.61	0.92	1.41	2.04	0.282	0.359
060	60	A	3	1	3	2.72	2.88	2.96	2.96	0.010	0.094
060	60	B	3	1	1	0.64	0.83	1.27	2.52	0.219	0.373
060	60	B	3	1	2	0.87	1.16	1.57	2.73	0.200	0.329
060	60	B	3	1	3	0.53	0.77	1.27	2.68	0.235	0.328
060	60	C	3	1	1	1.20	1.59	2.14	2.69	0.026	0.147
060	60	C	3	1	2	1.13	1.62	2.33	2.90	0.028	0.132
060	60	C	3	1	3	1.23	1.68	2.34	2.87	0.034	0.139
120	23	A	3	1	1	1.24	1.50	1.84	2.07	0.021	0.111
120	23	A	3	1	2	1.87	2.15	2.33	2.34	0.013	0.102
120	23	A	3	1	3	2.12	2.37	2.48	2.48	0.011	0.094
120	23	B	3	1	1	0.86	1.09	1.55	3.03	0.248	0.377

Continued on next page ...

Table D.10: Bond-to-Concrete strength test results for each individual specimen (Imperial Units)

Exposure		Specimen				Bond Stress				Bond Slippage	
Age d	T °C	Manuf. Type	Size #	Lot Lot	Spec. No.	at Specific Slippage			Ult. ksi	at Maximum Stress	
						$\frac{2}{1000}$ in. ksi	$\frac{4}{1000}$ in. ksi	$\frac{1}{100}$ in. ksi		Free End in.	Load End in.
120	23	B	3	1	2	0.89	1.12	1.56	3.12	0.189	0.302
120	23	B	3	1	3	0.71	0.84	1.15	2.59	0.249	0.332
120	23	C	3	1	1	0.70	1.39	2.19	2.80	0.029	0.178
120	23	C	3	1	2	1.23	1.75	2.43	3.01	0.027	0.068
120	23	C	3	1	3	1.16	1.83	2.66	3.08	0.023	0.149
120	40	A	3	1	1	1.83	2.00	2.09	2.10	0.008	0.082
120	40	A	3	1	2	2.66	2.96	3.05	3.05	0.009	0.127
120	40	A	3	1	3	2.09	2.26	2.32	2.32	0.009	0.090
120	40	B	3	1	1	0.78	1.02	1.47	2.50	0.239	0.309
120	40	B	3	1	2	0.64	0.87	1.37	2.63	0.260	0.343
120	40	B	3	1	3	0.66	0.88	1.37	2.53	0.109	0.210
120	40	C	3	1	1	0.54	0.93	1.65	2.66	0.032	0.141
120	40	C	3	1	2	1.55	1.89	2.31	2.41	0.016	0.126
120	40	C	3	1	3	1.29	1.81	2.53	3.09	0.027	0.145
120	60	A	3	1	1	0.77	0.77	0.77	2.73	0.012	0.098
120	60	A	3	1	2	2.29	2.43	2.53	2.54	0.012	0.107
120	60	A	3	1	3	1.23	1.41	1.64	1.89	0.237	0.306
120	60	B	3	1	1	0.84	1.12	1.58	2.45	0.125	0.231
120	60	B	3	1	2	1.38	1.50	1.70	2.32	0.220	0.309
120	60	B	3	1	3	0.65	0.84	1.22	2.59	0.302	0.369
120	60	C	3	1	1	1.25	1.83	2.47	2.86	0.025	0.131
120	60	C	3	1	2	1.20	1.78	2.58	3.17	0.028	0.124
120	60	C	3	1	3	1.56	1.83	2.21	2.33	0.019	0.096
210	23	A	3	1	1	2.08	2.24	2.26	2.27	0.007	0.038
210	23	A	3	1	2	2.53	2.70	2.89	2.92	0.016	0.058
210	23	A	3	1	3	0.74	0.85	1.10	1.26	0.028	0.111
210	23	B	3	1	1	1.12	1.29	1.66	2.70	0.267	0.318
210	23	B	3	1	2	0.87	1.00	1.33	2.55	0.242	0.292
210	23	B	3	1	3	0.99	1.25	1.72	2.71	0.212	0.293
210	23	C	3	1	1	1.14	1.42	1.97	2.50	0.025	0.103
210	23	C	3	1	2	1.85	2.13	2.59	2.82	0.023	0.096
210	23	C	3	1	3	0.96	1.44	1.96	2.38	0.026	0.095
210	40	A	3	1	1	2.56	2.62	2.64	2.64	0.009	0.079
210	40	A	3	1	2	2.73	2.81	2.85	2.86	0.008	0.066
210	40	A	3	1	3	2.43	2.61	2.74	2.74	0.009	0.063
210	40	B	3	1	1	0.83	1.06	1.45	2.49	0.166	0.223
210	40	B	3	1	2	0.66	0.86	1.25	2.48	0.314	0.363
210	40	B	3	1	3	1.00	1.24	1.73	2.89	0.228	0.268
210	40	C	3	1	1	1.16	1.56	2.18	2.57	0.027	0.102
210	40	C	3	1	2	1.20	1.66	2.42	2.82	0.025	0.096
210	40	C	3	1	3	0.63	0.90	1.23	1.70	0.032	0.099
210	60	A	3	1	1	2.92	2.95	2.96	2.97	0.006	0.014
210	60	A	3	1	2	2.45	2.49	2.52	2.52	0.008	0.093
210	60	A	3	1	3	2.86	2.89	1.93	2.89	0.005	0.090
210	60	B	3	1	1	0.49	0.71	1.13	2.35	0.200	0.252
210	60	B	3	1	2	0.76	1.00	1.46	2.54	0.166	0.253
210	60	B	3	1	3	0.79	1.01	1.38	2.58	0.244	0.323
210	60	C	3	1	1	1.60	1.88	2.37	2.73	0.025	0.115
210	60	C	3	1	2	1.35	1.89	2.34	2.56	0.024	0.132
210	60	C	3	1	3	1.74	2.10	2.59	2.89	0.021	0.131
365	23	A	3	1	1	1.48	1.88	2.09	2.09	0.011	0.057

Continued on next page ...

Table D.10: Bond-to-Concrete strength test results for each individual specimen (Imperial Units)

Exposure		Specimen				Bond Stress				Bond Slippage	
Age d	T °C	Manuf. Type	Size #	Lot Lot	Spec. No.	at Specific Slippage			Ult. ksi	at Maximum Stress	
						$\frac{2}{1000}$ in. ksi	$\frac{4}{1000}$ in. ksi	$\frac{1}{100}$ in. ksi		Free End in.	Load End in.
365	23	A	3	1	2	1.96	2.33	2.62	2.65	0.016	0.061
365	23	B	3	1	1	1.62	1.77	2.10	2.89	0.015	0.185
365	23	B	3	1	2	0.75	0.98	1.52	2.67	0.186	0.224
365	23	B	3	1	3	0.79	0.99	1.39	2.63	0.246	0.320
365	23	C	3	1	1	0.38	0.91	1.77	2.62	0.030	0.099
365	23	C	3	1	2	0.75	1.37	2.38	3.11	0.028	0.098
365	23	C	3	1	3	1.53	1.82	2.33	2.94	0.033	0.103
365	40	A	3	1	1	2.43	2.51	2.55	2.55	0.010	0.054
365	40	A	3	1	2	1.64	1.90	2.13	2.14	0.013	0.050
365	40	A	3	1	3	1.64	1.83	1.94	1.94	0.011	0.061
365	40	B	3	1	1	1.54	1.68	2.33	2.43	0.009	0.133
365	40	B	3	1	2	1.11	1.31	1.68	2.60	0.157	0.265
365	40	B	3	1	3	1.06	1.32	1.76	2.65	0.057	0.357
365	40	C	3	1	2	1.27	1.85	2.48	3.02	0.025	0.095
365	40	C	3	1	3	0.66	1.18	1.90	2.71	0.032	0.104
365	60	A	3	1	1	1.43	1.67	1.91	1.99	0.023	0.062
365	60	A	3	1	2	2.46	2.61	2.67	2.67	0.009	0.062
365	60	B	3	1	1	1.07	1.35	1.86	2.91	0.104	0.254
365	60	B	3	1	2	0.60	0.78	1.14	2.51	0.217	0.322
365	60	B	3	1	3	0.40	0.46	0.65	1.93	0.314	0.352
365	60	C	3	1	2	1.29	1.75	2.30	2.64	0.023	0.098
365	60	C	3	1	3	1.38	2.12	2.72	3.01	0.023	0.108

Similar to the previous table, Table D.11 documents the bond-to-concrete measurement results for all tested specimens per ASTM requirements. However, other than the table above, Table D.11 offers the test results in metric units. Accordingly, the relevant bond stresses are tabulated for measurements corresponding to 0.05 mm, 0.10 mm, and 0.25 mm of rebar slip.

Table D.11: Bond-to-Concrete strength test results for each individual specimen (Metric Units)

Exposure		Specimen				Bond Stress				Bond Slippage	
Age d	T °C	Manuf. Type	Size #	Lot No.	Spec. No.	at Specific Slippage			Ult. MPa	at Maximum Stress	
						0.05 mm MPa	0.10 mm MPa	0.25 mm MPa		Free End mm	Load End mm
000	23	A	3	1	1	14.24	16.25	17.66	17.76	0.32	-0.33
000	23	A	3	1	2	17.28	19.18	19.59	19.62	0.20	1.68
000	23	A	3	1	3	16.77	18.05	18.54	18.56	0.24	1.49
000	23	B	3	1	1	2.76	3.55	5.20	14.33	4.63	5.94
000	23	B	3	1	2	1.92	2.66	3.77	12.00	6.01	6.84
000	23	B	3	1	3	3.82	5.12	7.26	12.07	7.11	8.02
000	23	C	3	1	1	6.53	11.99	17.87	20.92	0.57	2.08
000	23	C	3	1	2	11.70	14.48	18.09	20.63	0.57	2.60
000	23	C	3	1	3	9.45	12.82	17.97	22.21	0.70	2.35
060	23	A	3	1	1	8.39	9.89	11.65	12.63	0.95	2.67

Continued on next page ...



Table D.11: Bond-to-Concrete strength test results for each individual specimen (Metric Units)

Exposure		Specimen				Bond Stress				Bond Slippage	
Age d	T °C	Manuf. Type	Size #	Lot No.	Spec. No.	at Specific Slippage				at Maximum Stress	
						0.05 mm MPa	0.10 mm MPa	0.25 mm MPa	Ult. MPa	Free End mm	Load End mm
060	23	A	3	1	3	17.23	18.56	19.69	19.80	0.34	0.09
060	23	B	3	1	1	5.77	7.04	9.42	16.85	6.68	9.30
060	23	B	3	1	2	3.40	6.01	10.02	17.84	6.08	9.17
060	23	B	3	1	3	2.13	2.79	4.21	11.19	5.44	7.90
060	23	C	3	1	1	10.33	12.86	15.86	16.87	0.49	0.47
060	23	C	3	1	3	7.05	9.84	13.31	15.90	0.74	3.26
060	40	A	3	1	1	15.01	17.24	17.70	18.84	0.42	2.24
060	40	A	3	1	2	16.12	17.03	17.77	17.80	0.30	2.66
060	40	A	3	1	3	17.63	19.01	19.78	19.80	0.23	2.59
060	40	B	3	1	1	7.07	8.62	11.52	17.18	3.02	5.44
060	40	B	3	1	2	3.81	5.73	9.13	16.78	6.50	9.29
060	40	B	3	1	3	5.12	6.48	9.52	16.96	7.20	9.93
060	40	C	3	1	1	4.94	7.42	11.90	19.04	0.81	3.82
060	40	C	3	1	2	7.58	10.46	14.72	19.13	0.71	3.40
060	40	C	3	1	3	9.03	13.50	18.35	20.64	0.54	3.35
060	60	A	3	1	1	15.88	17.64	15.85	18.03	0.17	2.97
060	60	A	3	1	2	4.18	6.34	9.71	14.08	7.17	9.11
060	60	A	3	1	3	18.75	19.86	20.43	20.43	0.24	2.38
060	60	B	3	1	1	4.40	5.72	8.79	17.41	5.56	9.49
060	60	B	3	1	2	5.98	7.97	10.85	18.80	5.07	8.37
060	60	B	3	1	3	3.64	5.34	8.75	18.47	5.96	8.33
060	60	C	3	1	1	8.31	10.96	14.78	18.54	0.65	3.73
060	60	C	3	1	2	7.81	11.17	16.06	20.01	0.72	3.34
060	60	C	3	1	3	8.45	11.58	16.13	19.81	0.86	3.53
120	23	A	3	1	1	8.55	10.35	12.70	14.25	0.52	2.81
120	23	A	3	1	2	12.89	14.80	16.08	16.17	0.33	2.60
120	23	A	3	1	3	14.59	16.31	17.08	17.09	0.28	2.40
120	23	B	3	1	1	5.96	7.49	10.68	20.88	6.31	9.57
120	23	B	3	1	2	6.11	7.69	10.77	21.49	4.79	7.66
120	23	B	3	1	3	4.90	5.79	7.92	17.83	6.31	8.43
120	23	C	3	1	1	4.86	9.57	15.09	19.34	0.74	4.52
120	23	C	3	1	2	8.50	12.05	16.76	20.75	0.69	1.73
120	23	C	3	1	3	8.01	12.60	18.31	21.25	0.59	3.78
120	40	A	3	1	1	12.63	13.77	14.41	14.45	0.21	2.08
120	40	A	3	1	2	18.36	20.39	21.00	21.01	0.24	3.24
120	40	A	3	1	3	14.41	15.58	15.99	16.00	0.22	2.28
120	40	B	3	1	1	5.36	7.05	10.16	17.20	6.06	7.84
120	40	B	3	1	2	4.38	6.02	9.46	18.13	6.59	8.71
120	40	B	3	1	3	4.52	6.06	9.44	17.46	2.77	5.32
120	40	C	3	1	1	3.73	6.41	11.37	18.37	0.80	3.59
120	40	C	3	1	2	10.66	13.05	15.93	16.61	0.41	3.21
120	40	C	3	1	3	8.91	12.46	17.45	21.31	0.70	3.68
120	60	A	3	1	1	5.32	5.32	5.32	18.85	0.30	2.49
120	60	A	3	1	2	15.81	16.76	17.42	17.49	0.31	2.71
120	60	A	3	1	3	8.47	9.71	11.31	13.00	6.01	7.78
120	60	B	3	1	1	5.78	7.71	10.88	16.90	3.17	5.87

Continued on next page ...

Table D.11: Bond-to-Concrete strength test results for each individual specimen (Metric Units)

Exposure		Specimen				Bond Stress				Bond Slippage	
Age d	T °C	Manuf. Type	Size #	Lot No.	Spec. No.	at Specific Slippage				at Maximum Stress	
						0.05 mm MPa	0.10 mm MPa	0.25 mm MPa	Ult. MPa	Free End mm	Load End mm
120	60	B	3	1	2	9.49	10.37	11.70	15.97	5.59	7.85
120	60	B	3	1	3	4.51	5.77	8.40	17.84	7.67	9.37
120	60	C	3	1	1	8.59	12.61	17.06	19.69	0.64	3.34
120	60	C	3	1	2	8.30	12.31	17.76	21.85	0.70	3.16
120	60	C	3	1	3	10.73	12.64	15.22	16.06	0.48	2.45
210	23	A	3	1	1	14.36	15.43	15.59	15.66	0.19	0.96
210	23	A	3	1	2	17.44	18.63	19.92	20.10	0.40	1.48
210	23	A	3	1	3	5.07	5.88	7.59	8.72	0.70	2.82
210	23	B	3	1	1	7.72	8.91	11.48	18.62	6.79	8.08
210	23	B	3	1	2	6.02	6.89	9.20	17.57	6.15	7.43
210	23	B	3	1	3	6.82	8.62	11.87	18.65	5.39	7.45
210	23	C	3	1	1	7.85	9.79	13.57	17.22	0.64	2.63
210	23	C	3	1	2	12.76	14.70	17.82	19.42	0.58	2.44
210	23	C	3	1	3	6.61	9.94	13.49	16.42	0.66	2.42
210	40	A	3	1	1	17.68	18.04	18.19	18.21	0.22	2.00
210	40	A	3	1	2	18.82	19.40	19.64	19.70	0.22	1.68
210	40	A	3	1	3	16.76	17.97	18.91	18.91	0.24	1.60
210	40	B	3	1	1	5.74	7.29	10.00	17.15	4.22	5.66
210	40	B	3	1	2	4.54	5.95	8.59	17.07	7.97	9.21
210	40	B	3	1	3	6.90	8.53	11.90	19.92	5.78	6.80
210	40	C	3	1	1	7.98	10.79	15.05	17.69	0.69	2.60
210	40	C	3	1	2	8.26	11.46	16.72	19.47	0.62	2.44
210	40	C	3	1	3	4.32	6.20	8.51	11.69	0.81	2.51
210	60	A	3	1	1	20.10	20.37	20.38	20.46	0.16	0.36
210	60	A	3	1	2	16.89	17.17	17.35	17.36	0.21	2.37
210	60	A	3	1	3	19.73	19.94	13.32	19.95	0.12	2.29
210	60	B	3	1	1	3.37	4.87	7.76	16.18	5.08	6.41
210	60	B	3	1	2	5.24	6.90	10.06	17.52	4.22	6.43
210	60	B	3	1	3	5.46	6.95	9.48	17.77	6.19	8.21
210	60	C	3	1	1	11.07	12.94	16.33	18.81	0.63	2.92
210	60	C	3	1	2	9.30	13.06	16.10	17.67	0.62	3.34
210	60	C	3	1	3	12.03	14.47	17.84	19.93	0.53	3.34
365	23	A	3	1	1	10.20	12.94	14.41	14.42	0.27	1.44
365	23	A	3	1	2	13.50	16.09	18.06	18.30	0.40	1.55
365	23	B	3	1	1	11.19	12.21	14.48	19.92	0.37	4.69
365	23	B	3	1	2	5.15	6.77	10.50	18.43	4.72	5.68
365	23	B	3	1	3	5.47	6.85	9.57	18.10	6.25	8.13
365	23	C	3	1	1	2.65	6.30	12.19	18.09	0.77	2.52
365	23	C	3	1	2	5.15	9.47	16.39	21.47	0.70	2.48
365	23	C	3	1	3	10.54	12.52	16.07	20.30	0.83	2.62
365	40	A	3	1	1	16.75	17.31	17.61	17.61	0.24	1.38
365	40	A	3	1	2	11.34	13.09	14.70	14.78	0.34	1.28
365	40	A	3	1	3	11.31	12.64	13.36	13.36	0.29	1.54
365	40	B	3	1	1	10.64	11.59	16.05	16.77	0.22	3.38
365	40	B	3	1	2	7.63	9.03	11.59	17.95	3.99	6.73
365	40	B	3	1	3	7.32	9.12	12.13	18.24	1.44	9.08

Continued on next page ...

Table D.11: Bond-to-Concrete strength test results for each individual specimen (Metric Units)

Exposure		Specimen				Bond Stress				Bond Slippage	
Age d	T °C	Manuf. Type	Size #	Lot No.	Spec. No.	at Specific Slippage			Ult. MPa	at Maximum Stress	
						0.05 mm MPa	0.10 mm MPa	0.25 mm MPa		Free End mm	Load End mm
365	40	C	3	1	2	8.74	12.72	17.13	20.79	0.64	2.41
365	40	C	3	1	3	4.56	8.14	13.09	18.68	0.81	2.63
365	60	A	3	1	1	9.87	11.52	13.18	13.73	0.58	1.58
365	60	A	3	1	2	16.99	17.98	18.40	18.41	0.22	1.58
365	60	B	3	1	1	7.39	9.30	12.84	20.06	2.65	6.44
365	60	B	3	1	2	4.14	5.38	7.85	17.31	5.52	8.18
365	60	B	3	1	3	2.79	3.18	4.46	13.31	7.97	8.94
365	60	C	3	1	2	8.91	12.04	15.86	18.20	0.58	2.50
365	60	C	3	1	3	9.54	14.59	18.78	20.72	0.59	2.76

The ultimate bond strength values were further analyzed for statistical relevance and the minimum, maximum, mean, standard deviation, and coefficient of variation values were determined for each data set or each applicable specimen group. Table D.12 was created to systematically present the results from the statistical analysis.

Table D.12: Bond-to-Concrete strength test statistical values for each sample group

Exposure		Sample Group			Statistical Values									
Age d	T °C	Manuf. Type	Size #	Lot No.	Imperial				Metric					
					$\wedge$ ksi	$\vee$ ksi	$\mu$ ksi	$\sigma$ ksi	$\wedge$ MPa	$\vee$ MPa	$\mu$ MPa	$\sigma$ MPa	CV %	
000	23	A	3	1	2.58	2.85	2.70	0.14	17.76	19.62	18.65	0.93	5.01	
000	23	B	3	1	1.74	2.08	1.86	0.19	12.00	14.33	12.80	1.32	10.34	
000	23	C	3	1	2.99	3.22	3.08	0.12	20.63	22.21	21.25	0.84	3.95	
060	23	A	3	1	1.83	2.87	2.35	0.74	12.63	19.80	16.21	5.07	31.27	
060	23	B	3	1	1.62	2.59	2.22	0.52	11.19	17.84	15.29	3.59	23.45	
060	23	C	3	1	2.31	2.45	2.38	0.10	15.90	16.87	16.38	0.68	4.18	
060	40	A	3	1	2.58	2.87	2.73	0.14	17.80	19.80	18.81	1.00	5.31	
060	40	B	3	1	2.43	2.49	2.46	0.03	16.78	17.18	16.97	0.20	1.17	
060	40	C	3	1	2.76	2.99	2.84	0.13	19.04	20.64	19.60	0.90	4.60	
060	60	A	3	1	2.04	2.96	2.54	0.47	14.08	20.43	17.51	3.21	18.31	
060	60	B	3	1	2.52	2.73	2.64	0.11	17.41	18.80	18.22	0.73	3.98	
060	60	C	3	1	2.69	2.90	2.82	0.12	18.54	20.01	19.46	0.79	4.08	
120	23	A	3	1	2.07	2.48	2.30	0.21	14.25	17.09	15.84	1.45	9.14	
120	23	B	3	1	2.59	3.12	2.91	0.28	17.83	21.49	20.07	1.96	9.77	
120	23	C	3	1	2.80	3.08	2.97	0.14	19.34	21.25	20.45	0.99	4.84	
120	40	A	3	1	2.10	3.05	2.49	0.50	14.45	21.01	17.15	3.43	19.99	
120	40	B	3	1	2.50	2.63	2.55	0.07	17.20	18.13	17.60	0.48	2.70	
120	40	C	3	1	2.41	3.09	2.72	0.34	16.61	21.31	18.76	2.37	12.65	
120	60	A	3	1	1.89	2.73	2.39	0.44	13.00	18.85	16.45	3.06	18.63	
120	60	B	3	1	2.32	2.59	2.45	0.14	15.97	17.84	16.90	0.93	5.52	
120	60	C	3	1	2.33	3.17	2.78	0.42	16.06	21.85	19.20	2.92	15.23	
210	23	A	3	1	1.26	2.92	2.15	0.83	8.72	20.10	14.83	5.74	38.69	
210	23	B	3	1	2.55	2.71	2.65	0.09	17.57	18.65	18.28	0.62	3.38	

Continued on next page ...

Table D.12: Bond-to-Concrete strength test statistical values for each sample group

Exposure		Sample Group			Statistical Values									
Age d	T °C	Manuf. Type	Size #	Lot No.	Imperial				Metric				CV %	
					$\wedge$ ksi	$\vee$ ksi	$\mu$ ksi	$\sigma$ ksi	$\wedge$ MPa	$\vee$ MPa	$\mu$ MPa	$\sigma$ MPa		
210	23	C	3	1	2.38	2.82	2.57	0.22	16.42	19.42	17.69	1.55	8.77	
210	40	A	3	1	2.64	2.86	2.75	0.11	18.21	19.70	18.94	0.75	3.95	
210	40	B	3	1	2.48	2.89	2.62	0.24	17.07	19.92	18.05	1.63	9.01	
210	40	C	3	1	1.70	2.82	2.36	0.59	11.69	19.47	16.28	4.08	25.03	
210	60	A	3	1	2.52	2.97	2.79	0.24	17.36	20.46	19.26	1.66	8.62	
210	60	B	3	1	2.35	2.58	2.49	0.12	16.18	17.77	17.15	0.86	4.99	
210	60	C	3	1	2.56	2.89	2.73	0.16	17.67	19.93	18.81	1.13	6.02	
365	23	A	3	1	2.09	2.65	2.37	0.40	14.42	18.30	16.36	2.75	16.81	
365	23	B	3	1	2.63	2.89	2.73	0.14	18.10	19.92	18.82	0.97	5.13	
365	23	C	3	1	2.62	3.11	2.89	0.25	18.09	21.47	19.95	1.72	8.62	
365	40	A	3	1	1.94	2.55	2.21	0.31	13.36	17.61	15.25	2.16	14.17	
365	40	B	3	1	2.43	2.65	2.56	0.11	16.77	18.24	17.65	0.78	4.41	
365	40	C	3	1	2.71	3.02	2.86	0.22	18.68	20.79	19.73	1.49	7.55	
365	60	A	3	1	1.99	2.67	2.33	0.48	13.73	18.41	16.07	3.31	20.59	
365	60	B	3	1	1.93	2.91	2.45	0.49	13.31	20.06	16.89	3.39	20.08	
365	60	C	3	1	2.64	3.01	2.82	0.26	18.20	20.72	19.46	1.78	9.17	

It is emphasized again that, except for the virgin material characteristics, most of the statistical data in this appendix is based on sample sets of three specimens. Specifically values such as the standard deviation and the coefficient of variation have to be interpreted with caution because the specimen groups are technically too small for statistical relevance. However, for economical reasons and to cover a wider array of mechanical properties, it was decided to keep the sample sizes small and report the statistical values because they provide an insight on the general GFRP rebar behavior and are indicative of the test procedures or mechanical properties that suffers the most variabilities.